Politecnico di Milano

Scuola di Ingegneria Industriale e dell'Informazione

Dipartimento di Chimica, Materiali e Ingegneria Chimica "G. Natta"

Master of science in Chemical Engineering

Investigation of the reaction of $O(^3P)$ with alkenes: from *ab initio* kinetic constants to rate rules

---

Author:
Luna Pratali Maffei
876305

Supervisor:
Prof. Carlo Cavallotti
Co-Supervisor:
Prof. Giancarlo Cicero

Academic Year 2017-2018

Acknowledgements

I am deeply thankful to my supervisor prof. Carlo Cavallotti, for giving me the opportunity to elaborate this exciting project. Without him, this thesis would have never been possible. He introduced me to chemical kinetics and computational chemistry during my years as a master student, and transmitted to me his passion about these subjects. Thank you for sharing your knowledge with me, and for pushing me in the right way. Thank you for your guidance, but also for your constant enthusiasm, understanding, patience, and advice. I look forward to work together on future projects.

I want to express my gratitude to prof. Giancarlo Cicero, my co-supervisor from Politecnico di Torino, for his availability and his interest in this work, despite his expertise is in a different field.

I also want to thank the professors who contributed the most to my educational growth. Even though they are not directly involved in the project, they all -in their own way- contributed to my development as a student and to my growing passion in the field of my thesis project. First of all, I owe my gratitude to prof. Alberto Cuoci, who was the first professor I met at Politecnico di Milano, and continuously inspired me in the past two years. He was always open for suggestions and discussions, and taught me how to solve problems more independently and creatively. Then, I feel thankful to prof. Enrico Tronconi, for his brilliant lectures, for transmitting his immense experience, and for giving me the opportunity to attend the ISCRE conference in Florence, which had a great impact on my decisions for the future. I also want to thank prof. Matteo Tommasini, who gave me a different perspective on computational chemistry and started interesting discussions about this thesis project. I am also grateful to prof. Roberto Piazza, who introduced me to the world of statistical physics in an unconventional and fascinating way. Going back in the years, I feel thankful to prof. Armando Gennaro, who was the first one to raise my curiosity towards partition functions.

I would also like to thank some of my collegues of my MSc at Politecnico di Milano: Mattia, for making me feel welcomed when I arrived; Elena, for sharing passions at university, and risotti at home; and Francesco, for sharing dinners, ASP projects, and for risking emotional breakdowns together before ASP deadlines. I also want to mention the whole ASP XIII cycle community, without whom this MSc would not have been as valuable, especially Francesca, Luca and Andrea.

I feel grateful to those whom always supported me in my choices through the years, especially my old friends Davide, Matteo and Federica. But most of all, I want to express my gratitude to my parents Amina and Sergio, who always believed in me and helped me build my future in many ways. And finally, I am thankful to my twin sister Dalia, for being always by my side, boosting me, appreciating me, and without whom I could not imagine any of these years.

Sommario

La reazione di addizione di ossigeno tripletto O(^{3}P) ad alcheni terminali è rilevante nella chimica dei processi di combustione, atmosferici e interstellari. Formatosi l'addotto iniziale, il sistema può reagire sulla superficie di tripletto, oppure passare a quella di singoletto tramite una transizione di spin chiamata "intersystem crossing" (ISC). La reattività di sistemi che coinvolgono ISC non è compresa appieno, ed è dunque difficile predire con metodi teorici le frazioni dei prodotti finali, i.e. "branching ratios" (BRs). Ciononostante, grazie ad avanzate tecniche sperimentali supportate dalla chimica computazionale, il fenomeno dell'ISC risulta oggi meno oscuro, e la cinetica globale di piccoli sistemi quali O(^{3}P)+etilene, propilene e 1-butene è stata riprodotta in modo piuttosto accurato.

In questa tesi, è stato sviluppato un efficiente metodo teorico per lo studio di reazioni con ISC, determinando le costanti cinetiche di ogni percorso reattivo completamente *a priori*, i.e. *ab initio*, a partire dalle strutture elettroniche. Questo approccio è stato validato tramite lo studio dei principali cammini reattivi di tripletto e dell'ISC di O(^{3}P)+C_2H_4, il più studiato in questa classe di reazioni. Una volta calcolate strutture ed energie *ab initio*, i BRs sono stati ottenuti da un bilancio di popolazione, detto "master equation", includendo l'ISC con la teoria di Landau-Zener. La rispondenza dei BRs con dati teorici e sperimentali di riferimento prova la validità del metodo, e legittima l'utilizzo di leggi cinetiche derivate *ab initio* per predire la reattività di alcheni ad alto peso molecolare (PM), attualmente ignota. A questo proposito, è stata sviluppata una metodologia di "scaling" per leggi cinetiche. Essa è stata validata derivando i BRs dei prodotti di tripletto e dell'ISC di O(^{3}P)+1-butene a partire dalla reattività del propilene, ottenendo un'ottima corrispondenza con dati sperimentali e teorici. Dunque, si sono predetti anche i BRs di O(^{3}P)+1-pentene, finora ignoti. Estendendo questo approccio di scaling ai prodotti della superficie di singoletto sarà quindi possibile predire la reattività globale dell'addizione di O(^{3}P) ad alcheni ad alto PM.

Abstract

The reaction of triplet atomic oxygen O(^{3}P) with terminal alkenes plays an important role in combustion, atmospheric and interstellar chemistry. The initial triplet adduct may either react on the triplet potential energy surface (PES) or undergo a spin transition to the singlet PES, called "intersystem crossing" (ISC). The reactivity of systems involving ISC is poorly understood, and therefore it is difficult to predict theoretically the fraction of the final products of the reaction, i.e. the "branching ratios" (BRs). However, in the past decades, the coupling of advanced experimental techniques with computational quantum chemistry allowed both a better understanding of ISC and a representative characterization of the overall kinetics of small systems, i.e. O(^{3}P) addition to ethylene, propylene and 1-butene.

In the present thesis, an efficient theoretical methodology to study reactions involving ISC was developed. Its strength is that kinetic constants of each reaction pathway are determined completely *a priori*, i.e. *ab initio*, starting from electronic structures. First, the approach was validated on the most studied system in this reaction class, O(^{3}P)+C_2H_4. *Ab initio* calculations of the structures and energies for the main triplet reaction pathways and ISC were performed. The product branching ratios were then obtained solving a population balance, called "master equation", where ISC was included using Landau-Zener statistical theory. The results were comparable to benchmark calculations and experimental data, proving the validity of the method. This also legitimates the use of kinetic laws derived *ab initio* to predict the unknown reactivity of alkenes with higher molecular weight (MW). In this respect, a scaling methodology for the rate laws was developed and applied to derive the product branching of O(^{3}P)+1-butene from the reactivity of propylene, obtaining a good correspondence with theoretical and experimental data. Then, also the BRs of O(^{3}P)+1-pentene were derived, showing how the unknown behaviour of longer chain alkenes can be predicted. This scaling approach may be extended to the singlet product branching, so as to obtain predictions for the full reactivity of higher MW alkenes.

Preface

The reaction of triplet atomic oxygen O(^{3}P) with terminal alkenes plays an important role in combustion, atmospheric and interstellar chemistry. The main challenge for the study of the kinetics of this reaction class is related to the presence of "inter-system crossing" (ISC). ISC is a non-radiative transition from the triplet to the singlet potential energy surface (PES), attributed to spin-orbit interactions. Kinetic studies for the derivation of the product distribution, i.e. the "branching ratios" (BRs), were conducted with advanced experimental techniques like crossed molecular beam (CMB) coupled with theoretical *ab initio* calculations. At present, this methodology was applied to study the three smallest systems of this reaction class, i.e. O(^{3}P) addition to ethylene, propylene and 1-butene. These are all characterized by a similar kinetics. First, the triplet adduct is formed upon cleavage of C-C π bond, and in the case of propylene and 1-butene, the new σ C-O bond may form with either the terminal or the central carbon. Concerning ethylene and the terminal carbon adducts, the main reaction pathways on the triplet PES are the elimination of a hydrogen from the terminal carbon and the cleavage of C-C σ bond to produce formaldehyde CH_2O. The adduct can also undergo ISC to the singlet PES, then reacting to produce mostly formyl HCO or molecular hydrogen H_2. In propylene and 1-butene, the central carbon adduct reacts on the triplet PES mostly via C-C cleavage producing vinoxy CH_2CHO, or via H elimination, whereas ISC plays a minor role. The global reactivity was studied with *ab initio* calculations in a wide range of temperature, and compared with CMB experiments. In general, at higher temperature ISC decreases in favour of products from triplet reaction pathways, especially formaldehyde and vinoxy. In addition, its contribution to the reactivity increases from propylene to 1-butene, and it is expected to grow further in higher molecular weight (MW) hydrocarbons. However, *ab initio* calculations predict a faster drop of ISC with temperature compared to CMB experiments. The largest discrepancies are found in ethylene and propylene, in particular for the H elimination channel, and were mostly attributed to a non-thermal behaviour of the triplet adduct formed. This effect is expected to be less relevant in heavier systems, although this was not verified yet, because *ab initio* calculations are too computationally demanding for higher MW alkenes. In this framework, the present work validates an efficient *ab initio* theoretical methodology on O(^{3}P)+C_2H_4, the most studied of this reaction class. Then, a method for the prediction of the reactivity of O(^{3}P) with longer chain alkenes is developed and validated deriving the product branching of O(^{3}P)+1-butene from the rate laws of O(^{3}P)+propylene.

In the first part of this work, O(^{3}P)+C_2H_4 was considered. In particular, H elimination, CH_2O formation, and ISC were studied with *ab initio* calculations. The power of this theoretical method resides in the fact that the kinetic constants of each reaction are computed *a priori* from the electronic structures of the molecules involved, i.e. the reactants, the transition states, and the products. This requires solving the stationary Schrödinger equation with theories appropriately selected. In this case,

density functional theory (DFT) was used for a first determination of the structures, then CASPT2 was employed to compute the final geometries and frequencies, so as to capture the multi-reference character of each reactive channel. The energies were determined at CASPT2 level with higher accuracy, and it was shown how sensitive the energy barriers are to the level of theory used. ISC was treated with transition state theory (TST) as the other reactive pathways, considering as a transition state the point where the triplet and singlet PES have the same energy and the spin-orbit interaction is maximized. This choice is based on previous works on propylene and 1-butene: the resulting geometry and reactivity were similar, however it was found that the geometry of ISC point varies significantly with the method used to locate it. The global reactivity of the system was studied solving an overall population balance, called "master equation", with Monte Carlo methods. ISC was included using Landau-Zener statistical theory. The BRs thus obtained are in good agreement with benchmark theoretical and experimental data. This establishes the validity of the method and legitimates the use of kinetic constants determined *ab initio* to predict the reactivity of $O(^3P)$ with higher MW alkenes. In this respect, the scaling of kinetic laws was performed using an additional intrinsic temperature T^*, characteristic of each adduct. T^* was derived integrating the heat capacity of the adduct, computed *ab initio*, from a given temperature T to the T^* at which the internal energy corresponded to the depth of the adduct. With these scaling factors, the BRs for the main triplet reactive channels and ISC of 1-butene were derived from the phenomenological rate laws of 1-propylene. The predicted BRs did not correspond precisely to those obtained with previous *ab initio* calculations, due to differences in both the reactivity of the two systems and the computational methodology used. Hence, corrective factors were quantitatively determined on this basis, and a good matching was eventually obtained. This constitutes a first validation of the method proposed. Concerning higher MW alkenes for which no data are available, scaling relations were applied to predict the reactivity of 1-pentene from 1-butene: as expected, an overall increase of ISC was observed. Scaling factors from 1-butene to C_nH_{2n} with $n=6 \div 24$ were instead approximated with group additivity rules. For this set of alkenes, it was found that reliable predictions may be obtained above 600-700 K, i.e. in the temperature range of typical combustion studies. In order to attain predictions at lower temperatures, full *ab initio* calculations for 1-pentene are required. These are also desirable for a further validation of the scaling methodology proposed. Finally, the predictions may be extended to the full PES, including also the singlet product branching after ISC. This requires the computation of the heat capacities of the stable intermediates on the singlet PES. The overall reactivity obtained may be for instance included in combustion modelling in order to predict the effect of $O(^3P)$+alkenes on the properties of the flame.

Contents

List of Figures

List of Tables

List of Abbreviations

AITSTME	**A**b **I**nitio **T**ransition **S**tate **T**heory-based **M**aster **E**quation
AO	**A**tomic **O**rbital
BR	**B**ranching **R**atio
CMB	**C**rossed **M**olecular **B**eam
DFT	**D**ensity **F**unctional **T**heory
DOF	**D**egree **O**f **F**reedom
GTO	**G**aussian **T**ype **O**rbital
HF	**H**artree **F**ock
hl	**h**igh **l**evel
ISC	**I**nter**S**ystem **C**rossing
KMC	**K**inetic **M**onte **C**arlo
KMC-ME	**K**inetic **M**onte **C**arlo-**M**aster**E**quation
LCAO	**L**inear **C**ombination of **A**tomic **O**rbitals
ME	**M**aster **E**quation
MECP	**M**inimum **E**nergy **C**rossing **P**oint
MEP	**M**inimum **E**nergy **P**ath
MC	**M**onte **C**arlo
MO	**M**olecular **O**rbital
MW	**M**olecular **W**eight
PES	**P**otential **E**nergy **S**urface
QBD	**Q**uality **B**y **D**esign
QCT	**Q**uasi **C**lassical **T**rajectory
QCT-SH	**Q**uasi **C**lassical **T**rajectory-**S**urface **H**opping
RRHO	**R**igid **R**otor **H**armonic **O**scillator
RRKM	**R**ice **R**amsperger **K**assel **M**arcus
SD	**S**later **D**eterminant
SH	**S**urface **H**opping
SOC	**S**pin **O**rbit **C**oupling
STO	**S**later **T**ype **O**rbital
TS	**T**ransition **S**tate
TST	**T**ransition **S**tate **T**heory
VTST	**V**ariational **T**ransition **S**tate **T**heory

Physical Constants

Bohr Radius	$a_0 = 5.292 \times 10^{-11}\,\mathrm{m}$
Boltzmann Constant	$k_B = 1.380\,648\,53 \times 10^{-23}\,\mathrm{J\,K^{-1}}$
Permittivity of vacuum	$\epsilon_0 = 8.854\,187\,817 \times 10^{-12}\,\mathrm{F\,m^{-1}}$
Hartree	$E_h = 4.360 \times 10^{-18}\,\mathrm{J}$
Pi	$\pi = 3.141\,592\,653\,589\,793 -$
Planck Constant	$\hbar = 1.054\,571\,800 \times 10^{-34}\,\mathrm{J\,s}$
Planck Constant	$h = 6.626\,070\,040 \times 10^{-34}\,\mathrm{J\,s}$
Speed of Light	$c_0 = 2.997\,924\,58 \times 10^{8}\,\mathrm{m\,s^{-1}}$

List of Symbols

C	concentration	$\mathrm{mol\,cm^{-3}}$
E	energy	E_h or $\mathrm{J\,mol^{-1}}$
k	kinetic constant	$\mathrm{s^{-1}}$ or $\mathrm{cm^3\,mol^{-1}\,s^{-1}}$
m	mass	kg
T	temperature	K
P	pressure	Pa
Q	partition function	
λ	reaction coordinate	Å or $^\circ$
ν	vibrational frequency	cm

Chapter 1

Introduction

1.1 Reason for the study

The reaction class of O(^{3}P) with alkenes is of utmost importance in different fields. First, it is responsible for pollutant emissions in atmospheric chemistry [1]. Furthermore, it was recently found to be relevant in the chemistry of cold cores of interstellar clouds [2]. Finally, unsaturated hydrocarbons are oxidized by O(^{3}P) during combustion and this reaction was introduced in large kinetic mechanisms for the modeling of flames [3].

Despite the interest shared in literature towards this reaction class, multiple challenges hinder an accurate identification of the reaction channels and their associated products. In fact, being the fields of application extremely varied, a wide range of reaction conditions is to be explored, from prohibitively low interstellar temperatures (of about 20 K) to prohibitively high combustion temperatures (above 700 K), passing through atmospheric conditions hardly reproduced experimentally. Hence, the initial studies only included addition kinetic constants for limited temperature ranges, and no information about the product distribution [4, 5]. Then, technological advancements allowed significant progress thanks to both theoretical calculations such as *ab initio* electronic structure and trajectory studies, and new experimental techniques such as crossed molecular beam (CMB) [6]. Theory and experiments are in good agreement with respect to addition kinetic constants, and their combination also led to a better understanding of the reaction mechanism and the product branching [7–9]. Nevertheless, the complexity of these systems prevented from obtaining accurate correspondences and therefore in literature they are still a matter of debate [10].

The main reason behind the difficult reproducibility of the behavior of such reactions is intersystem crossing (ISC), a non-radiative transition between spin states: in this case, the transition from triplet to singlet after the formation of the first adduct[1]. Not only this phenomenon is poorly understood, but also its kinetics is usually treated with probabilistic theories which are difficult to integrate in kinetic schemes. A new approach was proposed in the past decade and yielded fairly accurate results [11], although it was applied to only few systems [7, 8, 10]. Hence, further validation is required before it can be used extensively. This should be achieved together with the

[1] Considering an even number of electrons, a triplet state has two electrons with parallel spin (and different energies), whereas in a singlet state half electrons have spin up and half have spin down.

validation of the MC-RRKM[2] method [12–14], used for the determination of kinetic constants and product branching ratios (BRs). Therefore, the first part of this study is dedicated to the reproduction of benchmark calculations [10] for the smallest system of this class, $O(^3P) + C_2H_4$. This is also needed to justify the use of data for heavier molecular weight unsaturated hydrocarbons considered later in this thesis and previously obtained in the same way [8, 15, 16].

Finally, despite the remarkable advancements in *ab initio* theoretical calculations and in computational tools [17] and the recent promising developments in quantum computing applied to chemistry [18], computational cost is still extremely demanding, thus limiting these studies to low molecular weight systems (with 2-4 carbon atoms) [19, 20]. However, for both interstellar and combustion chemistry, it is desirable to extend such studies to heavier alkenes. In fact, it was observed that the reactivity and the extent of ISC increase with molecular weight [2]. Therefore, the product distribution is expected to shift towards singlet species, even at high temperatures. This is particularly relevant in combustion systems, where fuels such as diesel contain mostly heavy hydrocarbons. The integration of these important reactions in kinetic schemes would most likely improve the prediction of the macroscopic properties of the flame (ignition delay time, flame speed, and pollutant emissions) [21], and would ultimately be useful for a *quality by design* (QBD) approach of new biofuels. For this purpose, it is necessary to find rate rules which allow to scale up the results obtained for light species. Hence, the second part of this thesis is dedicated to finding such rules for the main triplet reaction pathways. In the future, it will be possible to extend them to the whole PES [3], such that a solid prediction tool will be available.

1.2 Spin-forbidden reactions

Spin-forbidden reactions fall within the broader category of *non-adiabatic* reactions, for which the adiabatic approximation for Schrödinger breaks down. This happens when two different electronic states of the system are extremely close in energy and may therefore "cross": as a result, a single state "adiabatic" surface is insufficient for the description of the system. Collisional non-adiabatic reactions include electron transfer and charge transfer [22], and the most popular example is the avoided crossing from an ionic to a covalent state in the bond stretching of LiF. Spin-forbidden reactions are instead collisionless, and as the name suggests, they are characterized by a "hop" from the spin state of the reactants to that of the products. These reactions are relevant in combustion chemistry, but also in photochemistry, and are studied for both biomedical applications and electronics.

In $O(^3P)$ + alkenes, the change in spin state (ISC), only occurs from the triplet to the singlet energy surface, and it is considered irreversible, because the reverse process

[2] Acronym for Monte Carlo-Rice Rasperger Kassel Marcus.

[3] The **P**otential **E**nergy **S**urface describes the change in the potential energy of the system along its N reaction pathways as a function of N reaction coordinates, therefore it includes the full reactivity of the system.

is extremely slow. An example of such states is shown in Figure 1.1: the initial triplet state (with parallel spins, on the left) hops to a singlet state (with opposite spins), either open shell (on the right) or close shell (in the middle).

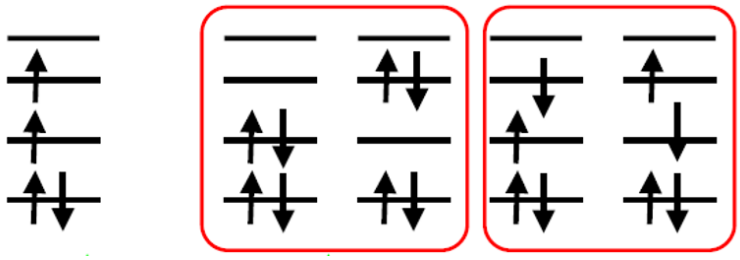

FIGURE 1.1: Possible transitions from a triplet state (left) to close shell singlets (middle) or open shell singlets (right)

The explanation of spin-forbidden reactions in relation with the PES is subtle and well presented by Harvey [11]. The change in spin state is associated with the coupling between the angular momentum of the electron and the intrinsic magnetic moment of its spin, which is called "Spin-Orbit Coupling" and is a relativistic effect. The corresponding Hamiltonian[4] H_{SO} is a part of the relativistic Breit-Pauli Hamiltonian [23] and is not usually included in the approximate solution of the Schrödinger equation. Harvey speaks of *adiabatic surface* when, still within the adiabatic approximation, H_{SO} is included, and of *diabatic surface* when this term is excluded. A possible spin-forbidden reaction is shown in Figure 1.2: diabatic surface 1 may be a triplet state, and diabatic surface 2 a singlet, crossing at the minimum energy crossing point (MECP); the resulting adiabatic surfaces (dotted lines) include spin state mixing. In case H_{SO} is high (Figure 1.2 a), as in heavy systems, the transition from singlet to triplet may be described as a regular TS[5]. This reaction can be seen as a sort of crossing from diabatic surface 1 to 2 induced by SOC. However, if the mixing is weak (Figure 1.2 b), the system "hops" from one surface to the other non-adiabatically, either hopping from the lower to the upper adiabatic surface, or remaining on the triplet diabatic surface and hopping when moving back to the reactants. These two descriptions are equivalent, however the latter is more easily implemented, and is therefore used in computations[6]. This weak coupling is present especially in light systems as those under study, and only gained attention in recent years [24].

The models used for the description of the hopping probability are statistical, and were first introduced in 1932 by Landau and Zener who came to similar conclusions [25, 26]. In these theories, the hopping probability between two adiabatic surfaces is

$$P_{LZ}(E) = \exp\left(-\frac{2\pi H_{SO}^2}{\hbar \Delta F}\sqrt{\frac{\mu}{2E}}\right) \tag{1.1}$$

[4]The Hamiltonian operator derives from the expression of the energy of the system by substituting the terms (e.g. momentum) with the corresponding operator.

[5]The transition state (TS) is defined within the framework of transition state theory (TST), as explained in section 2.3.2.

[6]A more detailed explanation is given in section 2.4.2.

where H_{SO} is the SOC diagonal Hamiltonian, ΔF is the relative slope of the diabatic curves at MECP, μ is the reduced mass, E is the kinetic energy with respect to the reactants (therefore $\sqrt{\frac{\mu}{2E}}$ is the nuclei velocity). A further explanation is given in section 2.4.2.

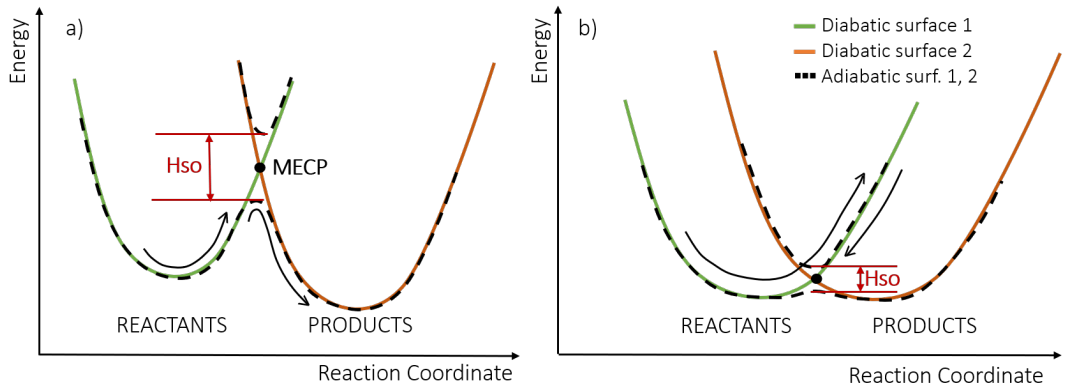

FIGURE 1.2: Diabatic and adiabatic curves for a spin-forbidden reaction with strong coupling a), and weak coupling b)

1.3 State of the art

1.3.1 Experimental approach: Crossed Molecular Beams

Nowadays, benchmark experiments for the analysis of the product BRs for O(^{3}P) addition to alkenes are performed using CMB technique. As the name suggests, this consists in colliding two supersonic beams (one for each reactant) at known velocity and angle, and therefore at known collision energy, in a vacuum chamber. Then, the direction and velocity of the products are measured and coupled with mass spectrometric data. A detailed explanation of the technique is behind the scope of this work and can be found in literature [27, 28].

The main advantage of CMB lies in the single-collision conditions, namely there are no secondary or wall collisions typical of bulk experiments. Hence, a consistent comparison with either dynamics or quantum mechanical simulations can be done. Furthermore, advanced spectroscopy techniques allow the identification of all product channels, including unexpected species. Finally, the analysis of the products let retrieve information about the internal energy distribution, which shades light on important features of the PES. Concerning O(^{3}P) + alkenes reactive systems, the first extensive study was done in 1989 [29]. However, the identification of products was ambiguous, and was only made accurate thanks to the recent developments in detection techniques [30–32]. Furthermore, such techniques also broadened the possible range of collision energies, which are set in comparison with a wider temperature range of theoretical calculations (see section 1.3.3).

1.3.2 Theoretical Approach

For the theoretical study of O(^{3}P) + alkenes reaction systems, two main theoretical approaches are currently used. The most recent one is QCT-SH calculations [33]: this is a molecular dynamics method, which therefore reproduces the trajectories of the nuclei by integrating the classical equations of motion at every timestep. It is called "Quasi Classical" because it can include "Surface Hopping" between potential energy surfaces, which is a purely quantum effect, and it can also be solved together with the time-dependent Schrödinger equation. These calculations require the integration of thousands of trajectories, and their interpolation on the PES requires months of work; furthermore, they are not always reliable since they fail to include important electronic effects. Finally, they require an available PES for the system, which can be fully reconstructed only using *ab initio* calculations.

Ab initio quantum chemical calculations are thus called because they involve the solution of the electronic Schrödinger equation from first principles, namely with only physical constants as an input. The main advantage is that, in principle, they converge to the exact solution. Such calculations allow to reconstruct the full multi-well[7] PES and to compute the kinetic constants of all the reaction pathways, as well as the BRs, completely *a priori*. For this purpose, several theories need to be integrated: the approach thus obtained is called "Ab Initio Transition State Theory-based Master Equation" (AITSTME) [34]. Within this framework, it is also possible to treat pathways of spin-forbidden reactions proceeding with an appropriate implementation of the statistical theories mentioned in section 1.2 [35]. This method is used in this work, and will therefore be explained in Chapter 2, however a short overview is provided here. Assuming that the reaction pathways on the PES are already known, the procedure is as follows:

1. AI: Each reaction pathway is considered singularly. The geometries of reactants, wells and products and TS are optimized *ab initio* and the corresponding energies are determined (sections 2.1, 2.2, 2.3.3). The wells undergoing ISC are considered, and the geometry and energy of the MECP is found according to the approach proposed by Harvey [35, 36] (section 2.4.1).

2. TST: microcanonical kinetic constants for the single reaction pathways are determined (section 2.3.2).

3. ME: phenomenological rate constants as a function of temperature and pressure are obtained with RRKM-ME calculations[12] (section 2.3.4). In the case of O(^{3}P)+alkenes, only the initial addition kinetic constant is necessary for the following calculations.

4. MC-RRKM: all the reaction pathways are considered together. Given a certain temperature and pressure, microcanonic kinetic constants are computed with

[7] With more stabilized intermediate complexes, called wells, between the reactant and the products.

RRKM, and statistical MC integration on thousands of reacted molecules allows to obtain the products BRs [13, 14] (section 2.3.5).

1.3.3 Merging experiments and theory: a warning

A deep insight into the kinetics and the PES can be gained upon comparison between CMB studies and *ab initio* electronic structure calculations. However, this is not straightforward. The main difficulty resides in finding the correspondence between the collision energy and the temperature used in the simulations, for which no specific rule can be found in literature. In fact, CMB experiments all occur at room temperature, and high temperatures are mimicked using high collisional energies. For instance, Peeters et al suggest that the collisional energy should be converted to additional vibrational energy of the first adduct formed [37]. However, the initial energy distribution in the systems is different: in fact, in *ab initio* calculations the gaseous system is considered thermal and has a Maxwell-Bolzmann velocity distribution

$$f(v) = \left(\frac{\mu}{2\pi k_B T}\right)^{\frac{3}{2}} e^{-\frac{1}{2}\frac{\mu v_{rel}^2}{k_B T}} \tag{1.2}$$

whereas velocity distribution in a collision of a CMB experiment is way narrower. This causes uncertainties in comparing theory and experiments, hence usually only trends are considered rather than the exact values of the BRs. The correlation with QCT-SH calculations is instead direct, and proved already successful in some systems [38].

1.3.4 Reaction of $O(^3P)$ with C_2H_4

Atomic oxygen addition to ethylene is the most studied reaction in the considered reaction class: in fact, it is a prototypical polyatomic non-adiabatic multichannel reaction involving two PES with different spin multiplicities. In addition, it is the fastest in terms of computational time, and also the most fascinating for its strong non-adiabatic character and complex reaction mechanism. Furthermore, it is strongly multi-reference, namely its electronic configurations are only described accurately by including multiple states, which makes the theoretical treatment extremely challenging. Most importantly, it is a relevant reaction in ethylene flames formation [39], in heavier hydrocarbons oxidation [40], and in interestellar chemistry [2]. For these reasons, numerous experimental (CMB) and theoretical studies (QCT-SH and AIT-STME) for the main product BRs were conducted, and the most accurate results were obtained since the 1990s [10, 29, 31, 32, 37, 38, 41]. The overall addition kinetic constant is now well established and expressed according to modified Arrhenius law as $k(T)=2.25\ 10^{-17}T^{1.88}\exp\left(-\frac{92}{T}\right)$ cm^3 $molecule^{-1}$ s^{-1} [42]. Nevertheless, the kinetics of this system is still a matter of debate, in particular with regards to the extent of ISC, which in theory and experiments appears to have different trends with temperature.

The reaction pathways to the main products and the corresponding reaction enthalpies at 0 K (taken from `https://webbook.nist.gov/chemistry/`) are listed in Table 1.1:

TABLE 1.1: Reaction pathways for $O(^3P) + C_2H_4$

$$
\begin{aligned}
O(^3P) + C_2H_4 \quad &\rightarrow CH_2CHO + H \quad \Delta H_0 = -17.0 \text{ kcal mol}^{-1} \quad (1)\\
&\rightarrow CH_2 + CH_2O \quad \Delta H_0 = -5.4 \text{ kcal mol}^{-1} \quad (2)\\
&\rightarrow CH_3 + HCO \quad \Delta H_0 = -27.9 \text{ kcal mol}^{-1} \quad (3)\\
&\rightarrow CH_3CO + H \quad \Delta H_0 = -23.5 \text{ kcal mol}^{-1} \quad (4)\\
&\rightarrow CH_2CO + H_2 \quad \Delta H_0 = -84.2 \text{ kcal mol}^{-1} \quad (5)
\end{aligned}
$$

After the formation of the first weakly-bound adduct upon $O(^3P)$ addition to ethylene, dissociation or rearrangement to several products can occur. In particular, the main pathways on the triplet PES involve the elimination of hydrogen H (1) or of methylene CH_2 (2), whereas the non-adiabatic transition to the singlet PES leads to the formation of acetaldehyde CH_3CHO, which dissociates (or isomerizes and dissociates) to methyl CH_3 (3), acetyl CH_3CO (4), or to ketene CH_2CO (5). Detailed descriptions of the full PES are found for instance in [10, 32, 37, 41]. If the main reaction pathways are now well determined, the BRs are not. This uncertainty is mostly related to the different results of theory and experiments and to the way ISC is treated, as explained below.

In Table 1.2, a summary of the most recent results is presented in chronological order. The comparison between CMB/QCT-SH and AI calculations is done considering that a collision energy of $6 \div 8$ kcal mol^{-1} corresponds to about $500 \div 700$ K, whereas $12 \div 13$ kcal mol^{-1} correspond to about 1000 K. In the table, the percentages of the main products are shown (for reasons of space, only the main molecule of each product channel is indicated), as well as the overall ratio between triplet and singlet products T:S.

Kinetic experiments at room temperature were performed for the triplet and singlet PES separately (in 1986 and 2009, respectively), and resulted in a T:S ratio of 45:55, which is considered correct and corresponds to a collision energy of about $3 \div 4$ kcal mol^{-1}.

In the initial CMB studies by Schmoltner et al [29] it was found that at room temperature the methyl channel, and therefore the singlet products, dominated, as in the kinetic experiments. According to CMB studies by Casavecchia et al in 2005 [43], T:S ratio (and therefore the extent of ISC) remained constant with temperature (at about 1000 K), and a shift from vinoxy to methylene was observed for the triplet products. However, the results of these experiments were revised in 2012 after the advancement of CMB techniques and findings about problems related to O(1D) and $O(^3P)$ mixing in the beam[31, 32]. In these studies, an increase in collision energy yielded a smaller ISC and a consequent T:S ratio of 55:45, which was attributed to the shorter lifetime of the initial adduct. Nonetheless, the first *ab initio* RRKM theoretical studies of this system by Peeters et al in 2005 [37] followed the initial findings. In

TABLE 1.2: $O(^3P) + C_2H_4$ main product BRs

Author	Date	Method	T (Ecoll)	T:S	CH_2CHO vinoxy	CH_2 methylene	CH_3 methyl	CH_3CO acetyl	CH_2CO ketene
Endo [44]	1986	Exp	290	-	39±10	6±3	-	-	-
Schmoltner [29]	1989	CMB	(6)	45:55	35.46	9.54	47.21	2.66	0.5
Casavecchia [43]	2005	CMB	(12.9)	43:57	27 ± 6	16 ± 6	43± 11	1± 0.5	13 ± 3
Peeters [37]	2005	AI	300	45:55	40.1	5.2	47.7	2.2	2.4
			1000	46:54	28	17.8	44.1	3.5	3.4
			2000	48:52	18.5	29.1	36.9	5.7	5.4
Schatz [41]	2008	QCT-SH	(12.9)	25:75	22 ± 12	3 ±2	55 ± 29	-	1-20
				20:80	14 ± 6	3 ± 2	62 ± 27	-	0-21
Miyoshi [45]	2009	Exp	295	-	-	-	0.53±4	-	19±0.1
Casavecchia [31]	2012	QCT-SH	(8.4)	36:64	28	8	49	10	5
Casavecchia [32]	2012	CMB	(8.4)	50:50	30± 6	20 ± 5	34 ± 9	3 ± 1	13 ±4
		CMB	(13.7*)	55:45	33± 7	22 ± 8	31 ± 8	2 ± 1	13 ±3
Casavecchia [38]	2015	QCT-SH	(13.7)	44:56	33	11	45	7	4
Klippenstein [10]	2016	AITSTME	(8.4)	56:44	48	8	37	4	3
			(12.9)	78:22	55	23	17	2	2
This work	2018	AITSTME	300	46:54	43.39	2.7	53.82	-	-
			500	61:39	52	9.04	38.49	-	-
			800	79:21	58.04	20.74	20.16	-	-
			1000	85:15	57.86	27.09	13.76	-	-

fact, the rate of ISC was simply considered constant with temperature ($1.5\ 10^{11} s^{-1}$), so as to obtain a T:S ratio of about 45:55 poorly varying with temperature, and product redistribution within each PES. The first theoretical study which made use of Landau-Zener statistical theory for ISC rate dates back to 2008 [41], and it consisted of QCT-SH calculations which were compared with the CMB results of 2005. However, due to uncertainties in the computation of SOC, two different values were tried and kept fixed (50 cm^{-1} and 70 cm^{-1}), resulting in a significant overestimation of ISC (up to 80 % for 70 cm^{-1}).

The most relevant contribution in the past years is by the group of professor Casavecchia, who combined advanced CMB and QCT-SH studies. Between 2012 and 2015, they shed new light on the experimental issues related to the spin-forbidden character of the reaction, and thus revised also the previous studies. In conclusion, CMB experiments highlighted a decrease of ISC at higher collision energies, which increases the triplet products BRs to 50 % and 55 % at 8.4 and 13.7 kcal mol^{-1} respectively. This trend is also present in the QCT-SH simulations, where the SOC was taken as an average among geometry configurations close to the MECP with a value of 35 cm^{-1}. However, in trajectory simulations the singlet products are always favored, whereas in CMB a shift from a prevailing triplet products fraction to a prevailing singlet products fraction is observed at 8.4 kcal mol^{-1}. Considering error bars of CMB experiments, the results are comparable.

The most recent studies of this system were conducted at Argonne National Labs in 2016 [10]. In this case, the AITSTME approach was used and is also validated in the present work. The main difference with respect to the previous AI calculations lie in the accurate treatment of ISC (approach as in Harvey [35]) which resulted in a smaller SOC value of 27 cm^{-1}, as well as the introduction of classical trajectory calculations for the study of the branching following ISC. In the table, results corresponding to

collision energies of the CMB experiments are provided: contrary to QCT-SH calculations, AITSTME predict a fast drop of ISC at high energies down to 22 % at about 12.9 kcal mol^{-1}. This was attributed to the fact that ISC rate is basically unaffected by temperature, whereas the rates of hydrogen and methylene elimination (pathways 1 and 2) increase of several orders of magnitude in the 300 ÷ 2000 K range. This trend is confirmed by the present work, and will be discussed later in this thesis. According to Li et al [10], the discrepancy with CMB experiments is essentially related to the treatment of ISC. Nevertheless, the general trend in the T:S product distribution is a decrease of ISC with temperature.

In the present work, it was decided to focus on the main triplet channels, and on the computation of ISC. Hence, in Table 1.2, the overall extent of ISC is reported as methyl, which is the main singlet product. The restricted PES considered is shown in Figure 1.3, along with the main TS, well and product energies computed with respect to the reactants.

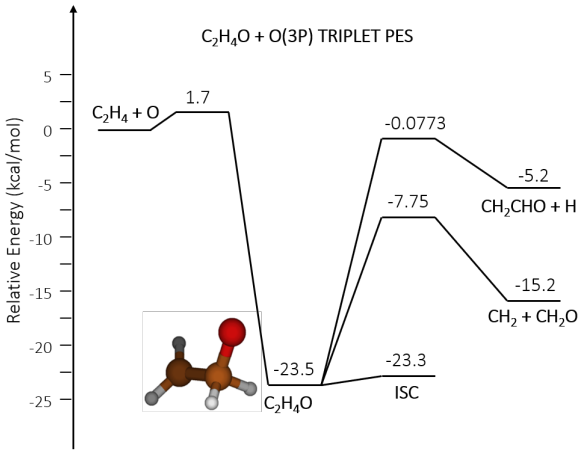

FIGURE 1.3: Sketch of the main reaction pathways of the triplet PES of the reaction of O(^{3}P) with ethylene

1.3.5 Reaction of O(^{3}P) with C_3H_6

As opposed to C_2H_4, very few studies were performed on product BRs in bigger systems. In the case of O(^{3}P) addition to propylene, the first comprehensive and synergistic theoretical and experimental work dates back to 2014 [8, 15]. In these works, the full PES was investigated with *ab initio* RRKM-ME simulation, and these calculations were validated with CMB experiments at 9.3 kcal mol^{-1}. In this case, an fairly good correspondence between theoretical and experimental results was achieved. The addition rate constant is well established and at room temperature has a value of 3.910^{-12} cm^3 molecule^{-1} s^{-1} [2].

The main difference between propylene and heavier hydrocarbons with respect to ethylene lies in the asymmetry in the behavior of O(^{3}P) addition to the double bond. In fact, considering only 1-alkenes, oxygen addition may occur to either the terminal carbon (about 70 %) or the central carbon (about 30 %), forming two initial wells

which can both undergo ISC. It was found that the main contribution to ISC comes from the terminal carbon addition, whereas for the central carbon the extent of ISC is never above 10 % and rapidly drops to 0 % with temperature. The main reaction pathways are listed in Table 1.3 (T indicates addition the the terminal carbon PES, C to the central one).

TABLE 1.3: Reaction pathways for $O(^3P) + C_3H_6$

$O(^3P) + C_3H_6$				
T	$\rightarrow$	$CH_3CHCHO + H$	$\Delta H_0 = -17.2$ kcal mol^{-1}	(1)
T	$\rightarrow$	$CH_3CH + H_2CO$	$\Delta H_0 = -5.4$ kcal mol^{-1}	(2)
C	$\rightarrow$	$CH_3COCH_2 + H$	$\Delta H_0 = -18.3$ kcal mol^{-1}	(3)
C	$\rightarrow$	$CH_3 + CH_2CHO/CH_3CO$	$\Delta H_0 = -25.1$ kcal mol^{-1}	(4)
T	$\rightarrow$	$CH_3CHCO + H_2$	$\Delta H_0 = -78.8$ kcal mol^{-1}	(5)
T/C	$\rightarrow$	$CH_2CH_2 + H_2CO$	$\Delta H_0 = -76.3$ kcal mol^{-1}	(6)
T/C	$\rightarrow$	$CH_3CH_2 + HCO$	$\Delta H_0 = -24.8$ kcal mol^{-1}	(7)

The well CH_3CHCH_2O formed via terminal carbon addition can undergo eliminaiton of either hydrogen (1) or formaldehyde (2), which are the main triplet channels and are the same as those investigated in $O(^3P)$ addition to ethylene. Concerning instead the central carbon addition, CH_3CHOCH_2 undergoes similar processes, namely hydrogen loss (3) and decomposition to methyl and vinoxy (4). Hence, (1-4) are all products of the triplet surface, and are those of interest in this work. A sketch of these channels together with the potential energies of reactants, TS, wells and products is shown in Figure 1.4. Here, also the energies of ISC points are shown. After ISC, the terminal carbon addition well may decompose to methylketene and molecular hydrogen (5), which is the most relevant channel, or convert to other stable intermediates, namely methyloxirane and propanal. After ISC of the central carbon addition well instead, either methyloxirane or acetone are formed. Methyloxirane can decompose to ethylene and formaldehyde (6) or isomerize to propanal or acetone. Finally, propanal mostly decomposes to ethyl and formyl (7) or to methyl and acetyl (4), which is also the main product of acetone decomposition. Hence, pathways (5-7) are derived from the singlet PES, whereas (4) has significant contributions from both the triplet and the singlet PES. Only an accurate integration of the BRs obtained experimentally with RRKM-ME simulations allows a full understanding of the mechanism [15].

A comparison between experimental and theoretical values for the BRs at both low and high temperature is found in Table 1.4. For reasons of space, only the one molecule of each product channel is indicated. At room temperature, kinetic data were available [46]. Despite the agreement in the predictions of methylketene and ethyl channels (5) and (7), a strong difference in both the methyl and methylvinoxy channels (4) and (1) is present. In the former case, this depends on the fact that in the experiments only contribution from the vinoxy was considered, which in RRKM-ME simulations was 25 %. The latter difference would instead be due to a systematic error in the prediction of the H loss channel, as explained by Leonori et al [15]. At higher energy, the main difference lies again in the BR of the methylvinoxy channel

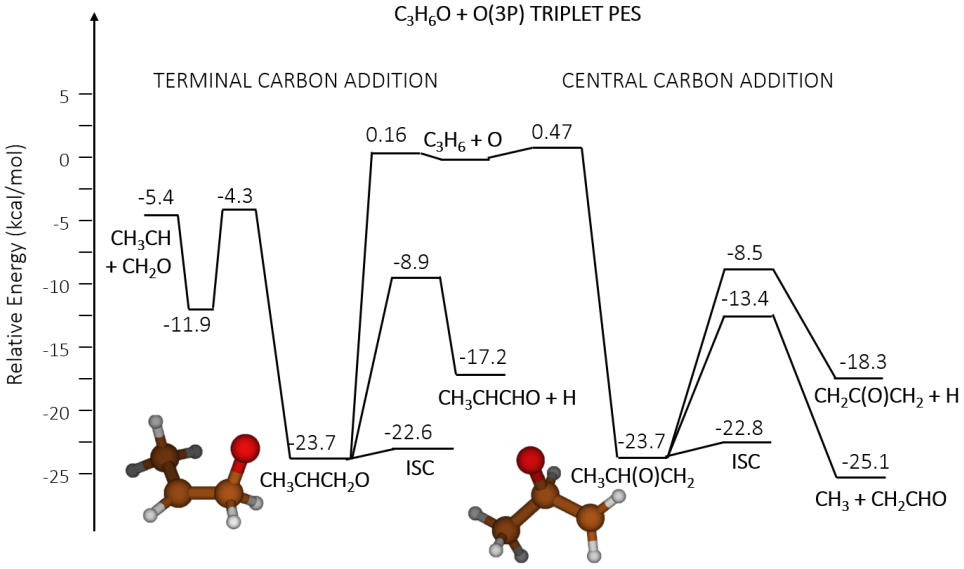

FIGURE 1.4: Sketch of the main reaction pathways of the triplet PES of the reaction of $O(^3P)$ with propylene

(1), which may be due to dynamic effects not accounted for in the RRKM-ME simulations. Despite this, there is good agreement on the ISC fraction, which is about 20 %. Concerning the trend with temperature, modified Arrhenius expressions for hydrogen loss (1)+(3), formaldehyde formation (2), methyl formation (4) and ISC were computed by Cavallotti et al [8]. As in the case of C_2H_4, ISC fraction drops with temperature, however its extent is always smaller than in ethylene. This is related to the peculiar behavior of ethylene, in fact it is in general true that ISC fraction increases in heavier molecules, as in 1-butene.

TABLE 1.4: $O(^3P) + C_3H_6$ main product BRs

Method	**T (Ecoll)**	CH_3CHCHO **methylvinoxy**	CH_3COCH_2 **oxopropyl**	CH_3CHCO **methylketene**	CH_3 **methyl**	C_2H_5 **ethyl**	H_2CO **formaldehyde**
Exp [46]	300	46±11	-	1.4±1.1	28±7	25±	-
RRKM-ME [15]	300	15.9	3	1.8	44.2	28.3	6.5
CMB [15]	(9.3)	7±2	5± 2	3 ± 1.5	32± 10	9± 4	44 ± 5
RRKM-ME[15]	(9.3)	26.1	1.0	1.1	32.6	7.0	32.1

1.3.6 Reaction of $O(^3P)$ with C_4H_8

Atomic oxygen addition to 1-butene was studied essentially for its importance in the combustion of biobutanol, where it is generated by the pyrolysis of 1-butanol. As in the case of the smaller systems, the kinetic constant was well assessed and at room temperature is 4.14 10^{-12} cm^3 $molecule^{-1}$ s^{-1} [47]. The main reaction channels and PES were studied with spectroscopy techniques together with trans-2-butene and isobutene in 2004 [48], however the first theoretical[8] PES comprehensive of most reaction channels was built in 2012 [49]. Recent coupled CMB and RRKM-ME studies shed

[8]Investigated with density functional theory (DFT).

light on new reaction pathways and determined BRs accurately [16, 50]. The work on the full PES is still in preparation, and further details will be presented in the result section 4.1.

The PES mirrors the one of propylene, as shown from the pathways listed in Table 1.5:

TABLE 1.5: Reaction pathways of $O(^3P) + C_4H_8$

$O(^3P) + C_4H_8$				
T	$\rightarrow$	$CH_3CH_2CHCHO + H$	$\Delta H_0 = -18.2$ kcal mol^{-1}	(1)
T	$\rightarrow$	$CH_3CH_2CH + H_2CO$	$\Delta H_0 = -6.0$ kcal mol^{-1}	(2)
C	$\rightarrow$	$CH_3CH_2COCH_2 + H$	$\Delta H_0 = -19.9$ kcal mol^{-1}	(3)
C	$\rightarrow$	$C_2H_5 + CH_2CHO/CH_3CO$	$\Delta H_0 = -26.9$ kcal mol^{-1}	(4)
T	$\rightarrow$	$CH_3CH_2CHCO + H_2$	$\Delta H_0 = -31.1$ kcal mol^{-1}	(5)
T/C	$\rightarrow$	$C_2H_5CO + CH_3$	$\Delta H_0 = -33.4$ kcal mol^{-1}	(6)
T/C	$\rightarrow$	$C_3H_7 + HCO$	$\Delta H_0 = -25.8$ kcal mol^{-1}	(7)

It is evident that the reaction pathways are the same as those analyzed in the propylene PES, with the exception of (6). Clearly, all the products are characterized by an extra methyl group. Some differences are however present: in particular, in this system the proportion between the central and terminal carbon addition is lower with respect to propylene ($0.30 \div 0.40$ instead of $0.35 \div 0.41$), and the extent of ISC from the central carbon is even smaller. These features will be further discussed in the result section 4.1. Given the similarity between the two systems, it would be natural to find a simple relation between the reaction rates of the corresponding pathways so as to be able to make predictions for heavier systems. In this study, only the triplet reaction channels and the ISC rates were analyzed for the determination of rate rules. The triplet PES used is shown in Figure 1.5.

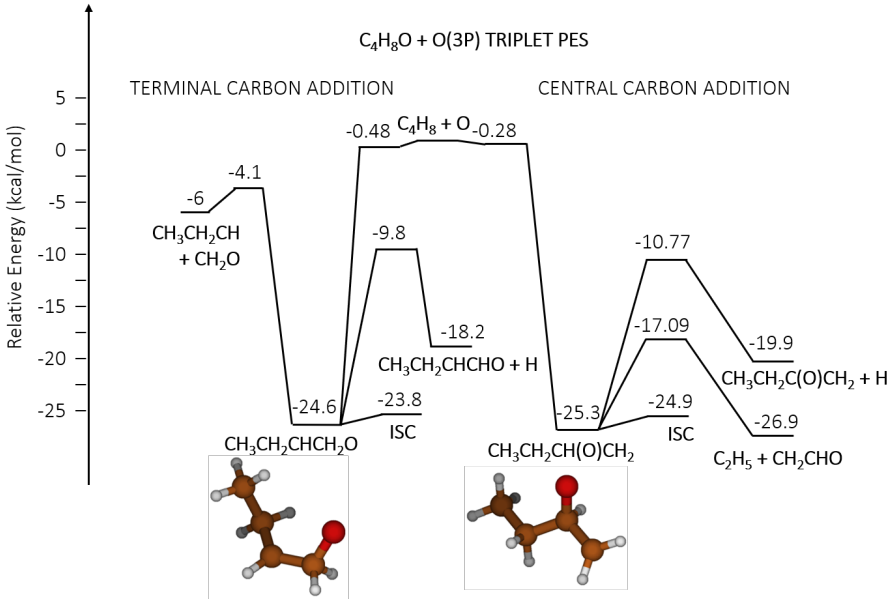

FIGURE 1.5: Sketch of the main reaction pathways of the triplet PES of the reaction of $O(^3P)$ with 1-butene

1.4 Aim of the work and approach

After this brief overview of the state of the art of $O(^3P)$ reaction with alkenes, it is evident that several challenges remain. Synergistic experimental and theoretical studies are necessary for the understanding of these systems, and despite a fair agreement between the two approaches was recently achieved, inaccuracies still remain. As far as theoretical calculations are concerned, the most reliable and successful approach to date is the integration of *ab initio* calculations with TST and RRKM-ME simulations, although it was adopted for the study of few systems only and further validation is required. In any case, *ab initio* calculations of such accuracy cannot be used for heavier systems, since adding a single carbon atom results in prohibitive computational times. Hence, an efficient predictive model of reaction rates for heavier alkenes would allow to obtain at minimal effort an entire set of kinetic constants to be used in kinetic models of atmospheric, interstellar, or combustion chemistry.

In light of these considerations, the aim of this work is to provide a validation and an insight into the AITSTME-MC method for the calculation of the kinetic constants and BRs of these systems, and to present possible scaling relations for heavier alkenes. For both tasks, only the triplet PES and ISC were considered, in view of a future extension to the singlet PES in case the approach proves successful. An outline of the main steps of this thesis is reported herein.

In the first part of this work, the method validation was conducted on $O(^3P) + C_2H_4$ (Chapter 3). In fact, benchmark theoretical calculations and experimental results can be used as comparison, and this system was never studied at Politecnico di Milano. Furthermore, it is the smallest and therefore the fastest computationally. An analysis of the reaction pathways of the triplet PES will be presented, with a focus on the difficulties encountered in the determination of energies and frequencies (Section 3.1). Then, the obtained BRs and phenomenological rate constants are listed and compared to the data available in literature for the final method validation. The discussion will also concern the challenges which still remain, speculating on possible future directions.

After the method validation, the determination of rate rules is tackled (Chapter 4). The systems considered are $O(^3P) + C_3H_6$ and $O(^3P) + C_4H_8$: data and simulations were retrieved from previous works and revised. Clearly, these simulations were performed with the method validated in the first part. Hence, the main focus is on the determination of scaling factors for the kinetic constants of propylene to determine those of butene on the basis of considerations about kinetics and energy redistribution, without the use of any fitting parameters. These rules will then be used for the prediction of the behavior of $O(^3P) + C_5H_{10}$, and calculations on this system will also be presented.

Chapter 2

Methods

In this chapter, an overview of the methods used in this thesis is presented. The structure of the different sections is organized as the series of calculations that must be performed in order to apply AITSTME to spin-forbidden reactions.

Section 2.1 will focus on the theoretical methods of *ab initio* calculations, namely the theories used for the optimization of the structures and the computation of frequencies and energies. First, an overview of Hartree-Fock (HF) theory will be presented in section 2.1.1, followed by a brief illustration of the basis sets used in 2.1.2. Then, the correlation methods used in this work for the improvement of HF solution are considered in sections 2.1.3, 2.1.4, 2.1.5. Finally, also density functional theory (DFT) is treated in section 2.1.6. The approach adopted to perform these tasks will then be presented in section 2.2.

Section 2.3 explains the methods for the determination of the kinetic constants for the single reaction pathways. First, the general concept of potential energy surface is explained in section 2.3.1. Then, an overview of TST is provided in section 2.3.2, together with considerations about the inclusion of hindered rotors in section 2.3.3. This is followed by a discussion about the intrinsic kinetic constant calculations with RRKM theory in section 2.3.4. Finally, the overall approach for the solution of the ME is illustrated in section 2.3.5.

The AITSTME calculations for the single reaction pathways were computed using a new code called EStokTP, which aims at automating the *a priori* determination of rate constants. This code will thus briefly presented in section 2.3.6.

The calculation of the product BRs and of phenomenological rate laws is briefly illustrated in section 2.3.7.

ISC is considered separately and the methods for both the search of MCEP and the integration of this reaction pathway in the RRKM-ME simulations are discussed in section 2.4.

As far as the determination of rate rules is concerned, section 2.5 delineates the idea behind the approach proposed and presents the equations used. A further focus on thermochemistry is provided in section 2.6, as the computation of heat capacities was essential for the estimation of the scaling factors for the rate constants.

2.1 Computational quantum chemistry

In this section, a brief overview of the computational methods used for the calculation of the energies, structures and frequencies is given. A complete description can be found in computational chemistry books. For this thesis, the main references were "Modern quantum chemistry" by Szabo and Ostlund [51] and "Introduction to computational chemistry" by Jensen [52].

Ab initio calculations allow the determination of structures, energies and frequencies *a priori*, and this is the reason why they constitute such a powerful tool. The computation of the energy is the most important task, in particular for the calculation of the energy barriers for the reactions, and therefore the kinetic constants. The energy is obtained solving the time independent Schrödinger equation $H\Psi=E\Psi$, where E is the total energy, H is the Hamiltonian and Ψ is the wavefunction. The wavefunction provides a complete description of the system, as Ψ^2 is the probability to find a particle in the phase space where the wavefunction is defined. The system in question is made of nuclei identified by spatial nuclear coordinates $\mathbf{R}=(\mathbf{R}_1, \mathbf{R}_2, ..., \mathbf{R}_I, ..., \mathbf{R}_{Nn})$ and electrons identified by electronic spatial coordinates $\mathbf{r}=(\mathbf{r}_1, \mathbf{r}_2, ..., \mathbf{r}_i, ..., \mathbf{r}_{Nel})$. Spin coordinates for each electron $\boldsymbol{\omega}$ do not appear in the Hamiltonian, but they are needed in the wavefunction for a complete description of electrons: the complete set of electronic coordinates is therefore $\mathbf{x} = (\mathbf{r},\boldsymbol{\omega})$. The Hamiltonian operator includes the terms of the kinetic energy $\mathbf{T}$ and the potential energy $\mathbf{V}$ of electrons and nuclei, as in equation (2.1), where n subscript refers to nuclei, e subscript refers to electrons:

$$\mathbf{H}_{tot} = \mathbf{T}_n + \mathbf{T}_e + \mathbf{V}_{ne} + \mathbf{V}_{ee} + \mathbf{V}_{nn} \tag{2.1}$$

The nuclei kinetic energy is

$$\mathbf{T}_n(\mathbf{R}) = \sum_{I=1}^{N_n} -\frac{\hbar^2}{2M_I}\nabla_I^2 \tag{2.2}$$

where M is the mass of the nuclei.

The kinetic energy of the electrons is

$$\mathbf{T}_e(\mathbf{r}) = \sum_{i=1}^{N_{el}} -\frac{\hbar^2}{2m}\nabla_i^2 \tag{2.3}$$

where m is the mass of the electron. The kinetic energy operators are both one-body operators, whereas all the potential energy operators are two-body, as they express electrostatic interactions. The nuclei-electron electrostatic potential is

$$\mathbf{V}_{ne}(\mathbf{r},\mathbf{R}) = \sum_{i,I=1}^{N_e,N_n} -\frac{e^2 Z_I}{4\pi\epsilon_0|\mathbf{R}_I - \mathbf{r}_i|} \tag{2.4}$$

where Z_I is the nuclear atomic mass number. The nuclei-nuclei and electron-electron potentials are expressed in the same way as

$$\mathbf{V}_{nn}(\mathbf{R}) = \sum_{I<J}^{N_n} \frac{e^2 Z_I Z_J}{4\pi\epsilon_0 |\mathbf{R}_I - \mathbf{R}_J|} \tag{2.5}$$

$$\mathbf{V}_{ee}(\mathbf{r}) = \sum_{i<j}^{N_e} \frac{e^2}{4\pi\epsilon_0 |\mathbf{r}_i - \mathbf{r}_j|} \tag{2.6}$$

In (2.5) and (2.6), the sum is a double summation where one index (j or J) runs on all the particles, whereas the other one (i or I) runs only on values smaller than those considered for the first index. In other words, it is a summation over all the couples of nuclei or electrons. The Hamiltonian can be re-written in atomic units[1], namely normalized with respect to the physical constants appearing in the operators.

The stationary Schrödinger equation is usually treated according to the adiabatic and Born-Oppenheimer approximations. The adiabatic approximation restricts the solution of the Schrödinger equation to a single electronic surface, neglecting the coupling between different electronic states. Then, within the validity limits of the adiabatic approximation, the Born-Oppenheimer approximation allows the decoupling between nuclear and electronic wavefunctions. In fact, since the mass of an electron is at least four orders of magnitude smaller than that of a nucleus, its kinetic energy is extremely higher. Hence, $\mathbf{T}_n$ can be neglected and $\mathbf{V}_{nn}$ may be considered constant. This results in two different equations, the electronic Schrödinger equation (2.7) and the nuclear Schrödinger equation (2.8):

$$\mathbf{H}_{el}\Psi_{el}(\mathbf{x};\mathbf{R}) = (\mathbf{T}_e + \mathbf{V}_{ne} + \mathbf{V}_{ee})\Psi_{el} = E_{el}\Psi_{el}(\mathbf{x};\mathbf{R}) \tag{2.7}$$

$$\mathbf{H}_n\Psi_n(\mathbf{R}) = (\mathbf{T}_n + \mathbf{V}_{nn} + E_{el})\Psi_n = E_n\Psi_n(\mathbf{R}) \tag{2.8}$$

In the electronic Schrödinger equation, the dependence on nuclei is only parametric, namely nuclei are considered fixed. The nuclear Schrödinger equation instead describes the state of the nuclei in a potential field generated by the electronic configuration with energy E_{el}. In *ab initio* calculations, only (2.7) is solved, hence nuclei are always considered fixed and the total energy of the calculation output is $E_{el,tot} = E_{el} + V_{nn}$. In the following, the theories used for the solution of this equation are presented.

2.1.1 Hartree-Fock theory and electron correlation

Hartree-Fock theory was the most common method for the solution of the electronic Schrödinger equation until DFT spread in the past decades. Nowadays, HF is indeed useful for the understanding of all the methods developed afterwards, and it is often used in calculations to obtain an initial guess for the wavefunction of the system.

[1] The distances are expressed in Bohrs, the energy is expressed in Hartree (see the physical constants.)

The basic assumption of Hartree-Fock theory is the mean field approximation: in equation (2.7), $\mathbf{T}_e$ and $\mathbf{V}_{ne}$ are one-electron operators, namely they are summations running over a single electronic index; $\mathbf{V}_{ee}$ is instead a two-electrons operator, as it includes the interactions between all the possible pairs of electrons in the system. Therefore, electrons should be in principle considered all together. The mean field approximation instead considers each electron as immersed in a field generated by all the other electrons, such that they can be treated as independent. The final aim is in fact to obtain an equation for a single electron, easier to solve. Under the mean-field approximation, the wavefunction can be written as a *Hartree product* of spin-orbitals $\chi_i(\mathbf{x}_i)$ which are the product of the spatial part $\psi_i(\mathbf{r}_i)$ and the spin part $\alpha(\omega_i)$ of the wavefunction. A simple product however is an unphysical description of the system, because it does not fulfill neither the indistinguishableness of electrons nor Pauli exclusion principle[2]. This issue can be solved by writing the wavefunction in the form of a Slater Determinant (SD):

$$\Psi_{el} = \frac{1}{\sqrt{N!}} \begin{vmatrix} \chi_1(\mathbf{x}_1) & \chi_2(\mathbf{x}_1) & \cdots & \chi_N(\mathbf{x}_1) \\ \chi_1(\mathbf{x}_2) & \chi_2(\mathbf{x}_2) & \cdots & \chi_N(\mathbf{x}_2) \\ \vdots & \vdots & \ddots & \vdots \\ \chi_1(\mathbf{x}_N) & \chi_2(\mathbf{x}_N) & \cdots & \chi_N(\mathbf{x}_N) \end{vmatrix} \tag{2.9}$$

where the rows correspond to the N electrons and the columns to the N spin-orbitals.

The Hartree-Fock equations are derived from this formulation using the variational principle. Basically, considering that the ground-state configuration of the system minimizes its energy, any trial wavefunction approximating the exact solution will yield a higher energy. In other words, the expectation value of the Hamiltonian $< \Psi_{el}|H_{el}|\Psi_{el} >$ is an upper bound to the ground state energy. Hence, the electronic wavefunction and energy are found by minimizing the E_{el} with respect to every spin-orbital. The minimization is done using the Lagrange multipliers method: the energy variation δE_{el} with respect to each spin-orbital variation $\delta\chi_i$ is constrained with the orthonormality of the varied spin-orbital $(\chi + \delta\chi_i)$. The multiplier results as the energy of the corresponding spin orbital ϵ_i. In this way, N_{el} equations are derived of the kind

$$f(i)\chi_a(\mathbf{x}_i) = \left[h_0(i) + \sum_{b=1}^{N} \left(J_b(i) - K_b(i) \right) \right] \chi_a(\mathbf{x}_i) = \epsilon_a \chi_a(\mathbf{x}_i) \tag{2.10}$$

where $f(i)$ is the Fock operator for a generic electron i, constituted of the one-body term $h_0(i)$ and the two-body terms $J_b(i)$, the coulomb operator accounting for electrostatic interactions, and $K_b(i)$, the exchange operator accounting for the effect of switching electrons in a quantum system. $K_b(i)$ has no classical correspondence. It is noted that in this case the indexes used for the orbitals are a and b instead of i,

[2]Switching two electrons must yield the same probability density, and the wavefunction must change sign because it must be antisymmetric.

so as to make the distinction between electrons and orbitals clear. The resulting set of equations is an eigenvalue problem where all the equations are coupled due to the presence of the two-body terms. Furthermore, the system is strongly non-linear, since the Fock operator contains the orbitals themselves, which however can only be found solving the eigenvalue problem. The solution procedure is therefore iterative, and it is called "self consistent field" (SCF) because the spin-orbitals obtained are consistent with the electric field generated by themselves. Convergence is reached when the energy and the spin-orbitals undergo no change from one iteration to the following one.

It is noted that the spin-orbitals χ_a are constituted both by the spatial and the spin part. However, since spin does not appear in $f(i)$, it is possible to integrate the equations over the spin coordinates ω_i, such that only the spatial part ψ_a is to be determined. ψ_a physically corresponds to the molecular orbitals where electrons are allocated. In a closed-shell system, each spatial molecular orbital is occupied by two electrons with opposite spin, hence only $\frac{N_{el}}{2}\psi_a$ are found and only half of the equations are solved: this is referred to as "Restricted" HF because two electrons are restricted to occupy the same spatial orbital. If a system is instead open-shell, N_{el} different solutions for the spatial part of the molecular orbitals are found and therefore the procedure is called "Unrestricted" HF.

In Hartree-Fock equations, the molecular orbitals ψ_a have no defined form. However, it is more convenient to express them in a physically meaningful form, namely as a linear combination of atomic orbitals (LCAO):

$$\psi_a(\mathbf{r}_i) = \sum_{\lambda=1}^{N_\lambda} (c_{\lambda a}\phi_\lambda(\mathbf{r}_i)) \tag{2.11}$$

where ϕ_λ are the atomic orbitals and $c_{\lambda a}$ are the coefficients of the combination. Once (2.11) is substituted inside (2.10) and integration over the atomic orbitals (AOs) is performed, N_λ "Roothan-Hall" equations are obtained

$$\sum_{\lambda=1}^{N_\lambda} (F_{\nu\lambda}c_{\lambda j}) = \epsilon_j \sum_{\mu=1}^{N_\mu} (S_{\sigma\mu}c_{\mu j}) \tag{2.12}$$

where $F_{\nu\lambda}$ is the Fock matrix $\int d\mathbf{r}_i \phi^*_\nu(\mathbf{r}_i) f(i) \phi_\lambda(\mathbf{r}_i)$, and $S_{\sigma\mu}$ is the overlap matrix $\int d\mathbf{r}_i \phi^*_\sigma(\mathbf{r}_i)\phi_\mu(\mathbf{r}_i)$, unitary if the AOs are orthonormal, and the indexes $\lambda\nu\mu\sigma$ refer to atomic orbitals. This means that the number of equations to be solved increases to the number of AOs considered N_λ, and therefore an equal number of molecular orbitals (MOs) is found as a solution. However, only the MOs with the lowest energy are occupied (from $\frac{N_{el}}{2}$ for RHF to a maximum of N_{el} for an UHF system), whereas the others are called virtual. The main advantage of the new set of equations is that in the solution procedure no more functions have to be determined, but simply sets of coefficients. The size of the set of AOs should be chosen so as to obtain a trade-off between the accuracy in the representation (the MOs are exact only if an infinite set

is used) and computational cost (which scales with N_λ^4).

An overview of the solution procedure for the electronic Schrödinger equation with Hartree-Fock method has been presented. The question arising at this point is how accurate this solution is. The main approximations introduced are the mean field and the representation of the wavefunction as a single ground-state SD. In terms of wavefunction, the resulting electronic density underestimates the distance between electrons. This is due to a missing repulsion effect which derives from the correlation between their motion: for instance, in Hartree-Fock equations it is possible that two electrons with anti-parallel spins occupy the same position in space, whereas in reality a coulomb hole prevents this. This effect however is also found for electrons with the same spin. By definition, the difference between Hartree-Fock energy and the exact energy (using the same basis set) is called "correlation energy". Although it only corresponds to 1 % of the total energy, it is essential for the description of chemical phenomena and bond formation. For instance, in a HF single determinant wavefunction, when a bond is stretched the electrons of the breaking bond will always have equal probabilities to be on either of the two nuclei, and the bond will have equal ionic and covalent characters: the missing repulsion effect is called "static correlation". Instantaneous repulsion effects between electrons are instead referred to as "dynamic correlation".

A lot of effort was put in the development of electron correlation methods. Since the main limit in HF arises from the representation of the wavefunction with a single SD, HF wavefunction is used as a reference and expanded using excited SDs[3] to obtain the many-electron wavefunction:

$$\Psi = a_0\Phi_{HF} + \sum_i a_i\Phi_i \tag{2.13}$$

The number of included SDs Φ_i determines the accuracy of the description of the electron correlation, whereas the size of the basis set for the AOs ϕ_λ determines the accuracy of the description of the MOs ψ_a, as explained in the following.

2.1.2 Basis sets

The LCAO expansion of MOs according to equation (2.11) can be seen as a change of basis from the space of electrons spatial coordinates to that of AOs, which can therefore be regarded as basis functions. Every atomic orbital can in turn be represented by one or more functions, and the complete set of functions is called a basis set. The accuracy of the basis set is essential to achieve a solution as close as possible to the exact one. This depends on both the kind of functions and the number of basis functions used.

The two main categories of basis functions are STO and GTO. Slater-type orbitals are exponential functions, whereas gaussian-type orbitals are gaussian functions, as

[3] According to Lödwin theorem, the exact solution can be obtained as an expansion of infinite SDs.

the name suggests; both kinds are centered at the nucleus. GTOs provide a poorer representation of the electron density both close and far from the nucleus, hence more functions are required for an accurate representation of the AOs. Nevertheless, they are preferred to STOs because of their computational efficiency related to their easy integration.

GTO basis sets usually describe AOs by a contraction of N_G gaussian functions of the kind

$$\phi_\lambda = \sum_{i=1}^{N_G} d_{\lambda i} g_{\lambda i}(\alpha_{\lambda i}) \tag{2.14}$$

where $d_{\lambda i}$ are the coefficients of the contraction and $g_{\lambda i}$ are gaussian functions with exponents $\alpha_{\lambda i}$. Contraction coefficients and exponents are fitted semi-empirically on selected properties (e.g. the energy). Due to the vicinity to the nucleus, the overall number of functions required for the representation of core orbitals is higher than for valence orbitals. However, since the latter are involved in the formation of bonds and are therefore more important energetically, they are ofter represented with more sets of basis functions, split according to the distance from the nucleus. Such basis sets are called "split valence", and the most used ones are the DZ, TZ, QZ (double, triple and quadruple zeta[4]). Further improvements in the description of bonds can be achieved by adding functions of different orbitals characterized by a higher angular momentum: for instance, p functions can be added to s orbitals. Since the effect is to introduce a polar component in the electron density, these additional functions are denoted "polarization functions". Another possibility to improve the bond description is to introduce diffuse functions[5] in the basis set, which thus becomes "augmented". The basis sets used in this work have all these features. In particular, the most used were cc-pVDZ, cc-pVTZ, cc-pVQZ and aug-cc-pVTZ, where "p" indicates the polarization, "VXZ" the kind of valence splitting, "aug" the augmentation. "cc" instead stands for "correlation consistent", which refers to the fact that functions contributing in the same way to the correlation energy are introduced at the same stage, and this is particularly suitable when considering bond formation. For initial geometry optimizations, also a Pople Style basis set of the kind 6-311G+g(d,p) was used: this is an STO basis set (still using primitive gaussians, but fitted to STO) with triple split valence (6 primitives for the core orbitals, and 3 functions contracting 3, 1 and 1 primitives respectively for the valence orbitals), s diffuse functions (indicated by the +), and d, p polarization functions.

An infinite number of basis functions leads to the exact solution of the equation considered: this is called "basis set limit". Clearly, only finite basis sets are used and therefore the aim is to converge to the basis set limit in a systematic fashion by increasing the size and quality of the basis set. Several extrapolation procedures which combine different basis sets and levels of theory are available: the aim is always to recover the missing correlation energy of the Hartree-Fock solution. The biggest

[4]The denomination "zeta" derives from the name of the exponents of the STO basis functions.
[5]With very small exponents, therefore slowly decaying.

advantage of correlation methods based on HF wavefunction and these basis sets is the systematic improvement of the predicted properties: a qualitative description of this is shown in Figure 2.1. The exact solution is achieved by using a complete basis set (CBS) and a full-CI expansion (FCI), as clarified in the following sections.

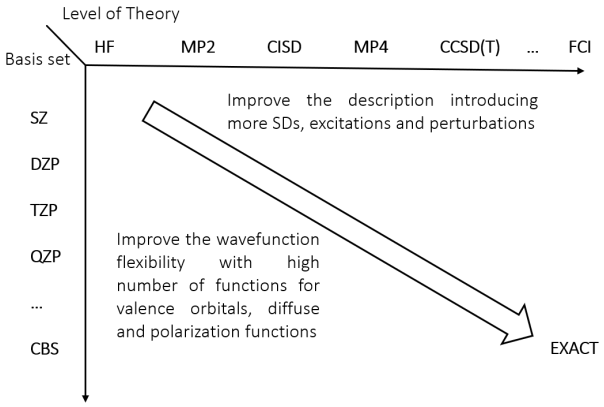

FIGURE 2.1: Systematic convergence to the exact multi-electron wavefunction improving the basis set size and the level of theory.

2.1.3 MCSCF method

The simplest electron correlation method is *configuration interaction* (CI). This is a post-HF method, as it exploits a ground-state HF calculation to build also excited SDs, such that the resulting wavefunction is

$$\Psi_{CI} = a_0\Phi_{HF} + \sum_S a_S\Phi_S + \sum_D a_D\Phi_D + \sum_T a_T\Phi_T + \cdots \tag{2.15}$$

where S, D, T indicate all the possible single, double, and triple excitations within the space of MOs. Once Φ_{HF} is computed, excited SDs are built using the MOs obtained: virtual MOs of Φ_{HF} will thus become occupied in the excited determinants, and the number of virtual MOs included depends on the kind of excitation considered. To compute the final Ψ_{CI}, the energy is minimized with respect to the coefficients a_i under orthonormality constraint. Clearly, a full CI expansion is prohibitive but for extremely small systems, and is therefore usually truncated to CISD (including single and double excitations). However, this causes problems of size consistency[6], and therefore other methods as MCSCF are preferred.

Multiconfiguration self-consistent field method (MCSCF) is simply a CI where also the MO coefficients of every SD are optimized. Hence, the method is not post-HF, because both $c_{\lambda j}$ of equation (2.11) and a_i of equation (2.15) are computed in the same step. It is understood that this method is computationally more demanding than CI, therefore the number of configurations included is smaller and the hardest challenge is the selection of the set which best represents the properties of the system

[6]The energy of two atoms at a large distance is different if computed considering them together or as separate entities.

of interest. The most popular approach to this problem is to use the *complete active space self consistent field* (CASSCF): instead of considering all excitations of one kind, the complete set of excitations within a selected active space is included. The active MOs are typically some of the highest occupied and lowest unoccupied MOs, because this choice provides a good description of bond-cleavage or bond-forming processes. In this work, CASSCF method is the one used most extensively, especially in its perturbed form CASPT2. In fact, MCSCF shows convergence problems due to the fact that $c_{\lambda j}$ and a_i are optimized together, therefore it is not guaranteed that the energy is minimized with respect to the $c_{\lambda j}$. This issue is solved using perturbation theories, as explained in the following section 2.1.4.

2.1.4 Perturbation theories

Perturbation theories are based on the principle that the approximate solution of HF equations is anyway close to the exact one, therefore by applying a small variation (a perturbation) $\mathbf{H'}$ to the reference Hamiltonian $\mathbf{H}_0$ should lead to the exact solution:

$$\mathbf{H}\Psi = (\mathbf{H}_0 + \lambda\mathbf{H'})\Psi = W\Psi \tag{2.16}$$

where λ is the perturbation parameter which indicates the extent of the perturbation. W and Ψ are written as an expansion of λ as

$$W = \sum_i \lambda^i W_i \tag{2.17}$$

$$\Psi = \sum_i \lambda^i \Psi_i \tag{2.18}$$

and i therefore indicates the order of the correction. Substituting (2.17) and (2.18) in (2.16) and collecting together the terms of the same order, perturbation equations are obtained, and the generic nth order one reads

$$\mathbf{H}_0\Psi_n + \mathbf{H'}\Psi_{n-1} = \sum_{i=0}^{n} W_i\Psi_{n-i} \tag{2.19}$$

In general, the nth wavefunction is expressed as an expansion of the solutions of the zero-th order Schrödinger equation Φ_i, with expansion coefficients depending on the order of the perturbation. This approach is called *Rayleigh-Schrödinger* (RS) perturbation theory. Perturbation theories differ in the way the perturbation Hamiltonian $\mathbf{H'}$ is expressed. The most common one is *Moller-Plesset* theory (MP), where $\mathbf{H'} = \mathbf{V}_{ee} - 2 < \mathbf{V}_{ee} >$ is called "fluctuation potential". Although $\mathbf{V}_{ee}$ of (2.6) is unknown in principle, the correction for the energy only contains expectation values which can be computed starting from the unperturbed wavefunction and MOs. The main advantages of perturbation methods are that they have no problems of size consistency and they can be applied to any zero-th order wavefunction, including already

correlated functions such as CI and CASSCF. In the latter, the aim of MP2 is to retrieve the dynamic part of the correlation energy, as CASSCF retrieves the static one. The main disadvantage is instead the oscillating behavior in terms of convergence to the exact solution[7], which led to questioning the convergence itself. Nevertheless, low orders of MP are computationally inexpensive and MP2 continues to be used, as it was done in this work.

Concerning the application of MP2 to CASSCF wavefunction, this results in a method called CASPT2 which was extensively used in this thesis. CASPT2 was implemented using MOLPRO, which takes as reference the procedure of Andersson et al [53], where $\mathbf{H}_0$ is chosen so as to obtain contributions to the perturbation energy only from the single and double excitations. It is noted that CASPT2 method may give rise to problems. In particular, if the eigenvalues of the perturbed Hamiltonian are close to those of the unpertubed one, singularities in the potential emerge, and the corresponding perturbed states are called "intruder states". This is particularly frequent when Rydberg orbitals are present, as in the case of O(^{3}P). A possible solution is to add a shift parameter in $\mathbf{H}_0$ and introduce a level shift correction in the perturbed energy which removes this effect, as proposed by Roos et Aal [54]. Another problem is the systematic underestimation of bond energies, caused by an asymmetric treatment of closed and open shell configurations. It is possible to correct $\mathbf{H}_0$ with a shift parameter based on the difference between the ionization potential and the electron affinity of the molecule, called "IPEA shift" [55]. These theories can be applied using suitable MOLPRO packages, and were adopted in the present work for the computation of high-level energies.

2.1.5 Coupled Cluster theory

Coupled cluster (CC) is probably the most used correlation method nowadays. The idea behind it is similar to CI, however the way excited SDs are obtained is different: in fact, in CC the wavefunction is obtained by applying to the reference wavefunction Φ_0 an operator $\exp(\mathbf{T})$ which generates the excitations. In fact, $\mathbf{T} = \mathbf{T}_1+\mathbf{T}_2+\mathbf{T}_3+\cdots$ where the number corresponds to the order of the excitation, and $\mathbf{T}_i\Phi_0$ has the same form as the CI excitations of (2.15). The Taylor expansion of this exponential results in

$$\begin{aligned}\exp(\mathbf{T}) = 1 + \mathbf{T}_1 + \left(\mathbf{T}_2 + \frac{1}{2}\mathbf{T}_1^2\right) + \left(\mathbf{T}_3 + \mathbf{T}_2\mathbf{T}_1\frac{1}{6}\mathbf{T}_1^3\right) \\ + \left(\mathbf{T}_4 + \mathbf{T}_3\mathbf{T}_1\frac{1}{2}\mathbf{T}_2^2 + \frac{1}{2}\mathbf{T}_2\mathbf{T}_1^3 + \frac{1}{24}\mathbf{T}_1^4\right) + \cdots\end{aligned} \tag{2.20}$$

where states of the same order are grouped together. The inclusion of mixed terms with non-interacting (disconnected) excited states such as $\mathbf{T}_2\mathbf{T}_1$ solves the problem

[7] Even orders of MP decrease the energy, whereas odd orders increase it. The addition of all MPn perturbations should lead to the exact solution, although there is little experience beyond MP4.

of size consistency of methods like CI. The resulting Schrödinger equation is

$$\mathbf{H}\exp(\mathbf{T})\Phi_0 = E_{CC}\exp(\mathbf{T})\Phi_0 \tag{2.21}$$

E_{CC} is obtained by projecting (2.21) onto Φ_0 instead of using the variational principle: in this way, $\mathbf{H}\exp(\mathbf{T})$ is considered as a single operator, and since the Hamiltonian only contains one and two-electrons terms, only singly and doubly excited states remain in $\exp(\mathbf{T})$. The expansion coefficients of each $\mathbf{T}_i$ are instead determined by projecting (2.21) onto slater determinants of each ith excitation Φ_S, Φ_D, etc.

As in CI expansion, truncation is needed. Usually, CCSD with $\mathbf{T} = 1 + \mathbf{T}_1 + \mathbf{T}_2$ is used, and its computational cost scales with N_λ^6: this also includes triple excitations as combinations of $\mathbf{T}_1$ and $\mathbf{T}_2$. The lack of connected triples is compensated for by adding terms from perturbations computed with MP4 and MP5, resulting in CCSD(T), which is considered the "golden standard" of electronic structure theory for energy calculation. This method was used for the computation of several energies, as clarified in section 2.2.

2.1.6 Density Functional Theory

HF and post-HF methods find a solution to the Schrödinger equation by minimizing the energy of the system with respect to the choice of the wavefunction. However, the information really needed is not the wavefunction, but the energy and the electron density. In light of this consideration, density functional theory proposes a completely different approach than HF: the energy of the system is derived as a functional of the electron density $E_{el}[\rho]$[8]. This representation is allowed by Hohenberg-Kohn theorem, which establishes a one-to-one correspondence between the electron density and the energy. Hence, the variational principle can be extended and $E_{el}[\rho]$ is obtained by minimizing it with respect to the electron density. The main advantage is that the electron density is only function of three spatial coordinates, thus reducing significantly the computational cost. The energy is still derived as the expectation value of the Hamiltonian $< \Psi|\mathbf{H}|\Psi >$, however all the terms are expressed in terms of electron density.

The most used model for the computation of the energy is Kohn-Sham theory. This method is based on the introduction of a set of fictitious independent non-interacting molecular orbitals ψ_i which by definition produce the same density of the real system:

$$\rho(\mathbf{r}) = \sum_{i=1}^{N_{el}} |\psi_i| \tag{2.22}$$

[8] A functional produces a number from a function, in this case the electron density ρ, which in turn depends on variables, in this case the spatial coordinates $\mathbf{r}$.

and the same set of orbitals is also used to express the kinetic energy T_S[9], which will therefore be an approximation of the exact one. The total energy can be written as a sum of different contributions:

$$E_{DFT}[\rho] = T_S[\rho] + E_{ne}[\rho] + J[\rho] + E_{XC}[\rho] \tag{2.23}$$

where E_{ne} derives from the external potential accounting for nuclei-electrons interactions (2.4), J accounts for the coulomb interactions, whereas E_{XC} is the exchange-correlation functional accounting for the missing part of the kinetic energy and the non-classical contribution to the electron-electron interactions:

$$E_{XC}[\rho] = (T[\rho] - T_S[\rho]) + (E_{ee}[\rho] - J[\rho]) \tag{2.24}$$

The main advantage of DFT is that if the expression of E_{XC} is exact, the solution is in principle exact, and this is why a lot of research is still focused on the development of these functionals. Furthermore, the computational cost of DFT is extremely smaller than HF, thanks to the reduced number of degrees of freedom (3 instead of $3N_{el}$). Nevertheless, the improvement in the description of the system with E_{XC} is not systematic, and there may be the risk of overcorrelation. This is the reason why in this work, DFT was used only for initial steps of geometry optimization, checks on the energies and other rapid calculations. The E_{XC} functionals used were B3LYP, ωB97XD, and M06-2X.

2.2 Geometries, frequencies and energies calculations

The computation of geometries, frequencies and energies was performed using the program EStokTP, presented in section 2.3.6. This in turn calls GAUSSIAN or MOLPRO when CASSCF is needed. The initial input requires first guesses for the geometry in the form of a z-matrix, spin multiplicity, and symmetry, for reactants and products, and indications for the kind of TS to be searched. The z-matrix lists the atoms of the system defining the geometry in terms of internal coordinates, namely distances, angles and dihedral angles, for a total of ($3N$-6) internal degrees of freedom (DOFs), or ($3N$-5) for linear molecules (where N is the number of atoms). In the following, the level of theory and the basis used for calculations is indicated as theory/basis, according to customary conventions. Three different levels of optimization with increasing accuracy are identified:

1. Level0: a first geometry optimization is performed at DFT level, usually at ωb97xd/6-311+g(d,p). This only provides a more accurate guess for the following levels, and no frequencies are computed.

[9]The S subscript refers to the fact that the wavefunction can be written as a SD composed of the fictitious MOs ψ_i.

2. Level1: further geometry optimization and frequency calculation is performed using a bigger basis set with either ωb97xd/aug-cc-pVTZ or CASPT2/aug-cc-pVTZ. The latter was used for most optimizations, and particular attention was put in the determination of the active space. It is important that the active space is opened gradually, trying to include at each step both the bonding and the corresponding antibonding orbitals of interest, such that the correct excitations are captured by the representation of the system considered. CASSCF is implemented using MOLPRO program MULTI, and perturbations are added using MRCI program using RS2 command. In several cases, it was necessary to use state averaging for CASSCF, namely the ground and the first excited state were considered as equally contributing to the Fock operator, and the Hamiltonian resulting from this state mixing was considered as the zero-th order for perturbation calculations.

3. High level (hl): a more accurate estimation of the energy is performed in this step using MOLPRO. In case of CASPT2 calculations, the energy was improved by increasing the size of the active space, and including level shifts mentioned in section 2.1.4 using MRCI program. The perturbation theory at high level was implemented using the command RS2C, which computes gradients numerically and does not include core excitations, such that it is less computationally expensive. Coupled cluster calculations were also performed at level CCSD(T)/aug-cc-pVTZ. The energy was then corrected using MP2/aug-cc-pVTZ and MP2/aug-cc-pVQZ to converge to the basis set limit, such that the final value obtained was

$$E_{CBS} = E_{cc} + E_{MP2/TZ} - E_{MP2/QZ} \tag{2.25}$$

The geometry optimizations of GAUSSIAN and MOLPRO are based on a quasi-Newton algorithm [56, 57]: the total energy $E_{el,tot}$ is minimized with respect to the set of nuclear coordinates ($\mathbf{R}$) according to a Newton-Raphson scheme, so that the displacement is obtained as $\mathbf{R'} = \mathbf{R} - \mathbf{H}^{-1}\mathbf{g}$, where $\mathbf{g}$ is the gradient and $\mathbf{H}$ is the Hessian. The latter is only approximated by inexpensive methods for numerical reasons, which is why the method is called "quasi"-Newton. Convergence criteria are based on the maximum and RMS force and displacement.

The vibrational frequencies of the system were treated according to the rigid rotor harmonic oscillator (RRHO) approximation: the molecule is considered as a set of ($3N$-6) independent quantum harmonic oscillators moving rigidly around their fixed positions. The degrees of freedom are ($3N$-5) for linear molecules. The Hamiltonian of the Schrödinger equation $\mathbf{H}\psi = E\psi$ for each oscillator contains the regular kinetic operator and the potential operator expressed as an elastic potential $-k\frac{1}{2}\nabla^2$, where k is the elastic constant. Considering one dimension with coordinate x for simplicity, the equation to be solved becomes

$$\frac{\partial^2\psi}{\partial x^2} + \psi\left[\frac{2mE}{\hbar^2} - \frac{kmx^2}{\hbar^2}\right] = 0 \tag{2.26}$$

and the resulting energy levels of each oscillator are

$$E = \frac{\hbar}{2}\sqrt{\frac{k}{m}}(2n+1) = h\nu\left(\frac{1}{2}+n\right) \tag{2.27}$$

where n indicates the number of the quantized level, and $\nu = \frac{1}{2\pi}\sqrt{\frac{k}{m}}$ are the vibrational frequencies of the normal modes of the system. The elastic constant k is found from the computation of the Hessian matrix. From equation (2.27), it is noted that also for $n = 0$ at 0 K the energy of the oscillator is not null but corresponds to $ZPE = \frac{1}{2}h\nu$, called for this reason "zero point energy". This is the lowest possible energy of a quantum mechanical system and has no classical correspondence, since it stems from Heisenberg uncertainty principle. The total ZPE is clearly the sum of all these terms

$$ZPE = \sum_{i=1}^{3N-6} \frac{1}{2}h\nu \tag{2.28}$$

The energies calculated with GAUSSIAN and MOLPRO do not automatically include the ZPE, which is therefore added manually. Since the frequencies are computed at level1, the same ZPE is considered for both level1 and hl calculations. It is also possible that the RRHO approximation does not hold for all normal modes, and in these cases the ZPE is modified according to a different approximation treated in section 2.3.3.

2.3 Determination of rate constants

Chemical kinetics is the study of the evolution of a reacting system in time: the transformation of chemical species via the formation and cleavage of bonds is a chemical reaction. The reaction rate r quantifies the velocity at which this transformation occurs, and for homogeneous reactions, as those considered here, the reaction rate is the number of moles of a certain species i produced per unit time and volume. The simplest reactions to be treated from a kinetic point of view are elementary reactions, where the stoichiometry, which is the ratio between reacting molecules, coincides with the molecularity, namely the number and nature of the molecules physically involved in the phenomenon. In other words, the mathematical description of the reaction corresponds to its physics, and thanks to this it is possible to express the reaction rate r as a function of the concentration C_i and the stoichiometric coefficients ν_i of the reactant species N_{reac}:

$$r = k(T,P)\prod_{i=1}^{N_{reac}} C_i^{|\nu_i|} \tag{2.29}$$

where $k(T,P)$ is the kinetic constant as a function of temperature and pressure and it is the intrinsic quantity that must be determined. Elementary reactions are classified in uni-molecular, bi-molecular, and ter-molecular on the basis of the number

of reactant molecules involved N_{reac}. In this work, only uni and bi-molecular reactions were considered, and the corresponding kinetic constants have the units of s^{-1} and $cm^3mol^{-1}s^{-1}$ respectively. Elementary reactions usually occur in a single step, like the simple separate pathways from the well to the various products shown for $O(^3P) + C_2H_4$ in section 1.3.4. These elementary steps were treated with TST, as presented in section 2.3.2. Global non-elementary reactions can still be treated with laws such as (2.29), however the summation extends to all the species involved in the reaction and the powers of the C_i are not necessarily the stoichiometric coefficients. In this work, the global reactions are treated using the law for elementary reactions, as it provides a correct description of the kinetics. In particular, the kinetic constants are derived from the addition kinetic constant scaled with the BR of each channel, hence the resulting reactions are bi-molecular.

2.3.1 The concept of PES

Any elementary reaction involves the rearrangement of atoms from the configuration of the reactants to that of the products. These relative motions can be described in terms of the internal ($3N$-6) or ($3N$-5) DOFs of the system, namely distances, angles and dihedral angles, collected in a vector $\mathbf{a}$. The change in the energy of the system as a function of these internal coordinates (or a subset of them) is called potential energy surface. The elementary reaction in question will follow a specific path on the PES which minimizes the energy of the system when moving from the configuration of the reactants to that of the products: this is called "minimum energy path" (MEP). The projection of this MEP onto the space of coordinates is called "reaction coordinate" λ, and is extremely useful because it allows to describe the physical evolution of the positions of the atoms in the reaction in question with a single curvilinear coordinate. In other words, λ is a one-dimensional curvilinear coordinate along the PES which brings the reactants to the configuration of the products along the MEP. Mathematically, the variation of the internal coordinates $\mathbf{a}$ with respect to λ is described by the energy gradient, namely the slope of the PES: $d\mathbf{a}/d\lambda = -\nabla E$. An example of this is shown in Figure 2.2. A generic abstraction reaction of atom A_2 from molecule A_2A_3 by atom A_1 is represented. In this case, the system is composed of three aligned atoms, therefore the internal DOFs are 3, two distances and one angle. The angle is considered fixed as the atoms are aligned, therefore the only DOFs involved in the reaction are the distance between A_1 and A_2, r1, and the distance between A_2 and A_3, r2. These are the coordinates of the PES. The system evolves along the MEP from a large r1 and small r2 to a large r2 and small r1, increasing its energy to a maximum and then decreasing it again to that of products. Also the representation of the reaction coordinate λ projected onto the space of internal coordinates is shown.

A possible illustration of generic one-dimensional MEPs as a function of λ is found in Figure 2.3. The total energy is indicated as H, namely the enthalpy corresponding to $E_{el,tot} + ZPE$. In Figure 2.3a), an exothermic reaction with barrier is shown. This kind of MEP is characterized by an increase in energy up to a maximum, followed

by a decrease in energy to products. This maximum along λ is however a relative minimum with respect to all the other coordinates on the PES, and is therefore a saddle point. Uni-molecular reactions with barrier include isomerization, elimination and beta-scission, whereas bi-molecular ones include abstraction, substitution, and dissociative recombination. The difference in energy between reactants and products is ΔH_R (usually taken as the standard one at 0 K), whereas the energy barriers with respect to the maximum are $E_{A,FW}$ and $E_{A,BW}$, namely the activation energies for the forward and for the backward reactions[10]. This last point implies that the same MEP on the PES describes both the forward and the backward processes: in the example above, $A_1 + A_2A_3 \rightarrow A_1A_2 + A_3$ and $A_1A_2 + A_3 \rightarrow A_1 + A_2A_3$, respectively. This is called "microscopic reversibility principle", and it allows to compute the forward and backward kinetic constants on the same MEP using thermodynamic consistency. In Figure 2.3b), an endothermic barrierless reaction is shown. Uni-molecular reactions of this kind are single bond breaking reactions, where the ΔH_R corresponds to the energy of the bond which is broken. Bi-molecular barrierless reactions follow instead the reverse path and are always exothermic; they involve bond formation, such as radical recombination. In this case, the identification of the reaction barrier and the saddle point is not as simple as in reactions with barrier, and the kinetic treatment is more complex, as explained in the following section.

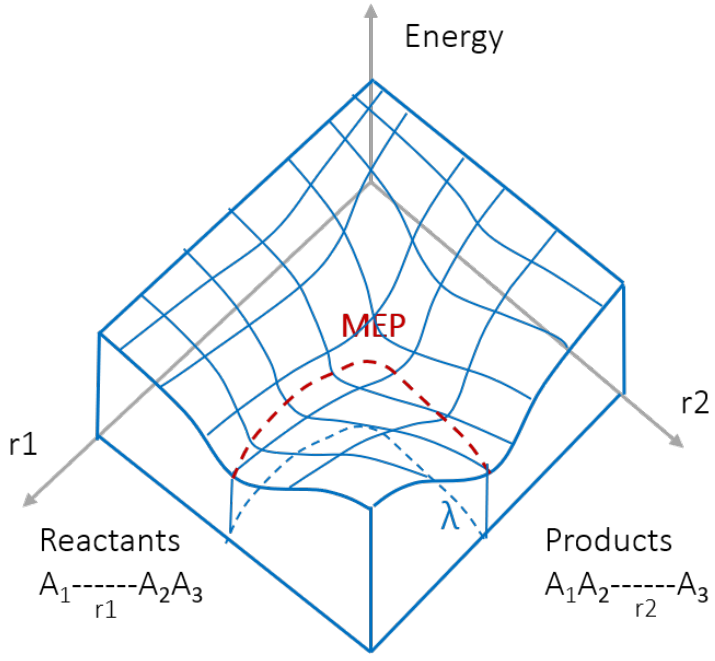

FIGURE 2.2: Example of PES for an abstraction reaction of atom A_2 from the molecule A_2A_3 by atom A_1 to form molecule A_1A_2

[10]The definition of activation energy is technically different: E_A corresponds to the slope of the Arrhenius plot $\log k(\frac{1}{T})$. Here the activation energies are taken as the energy barriers for simplicity.

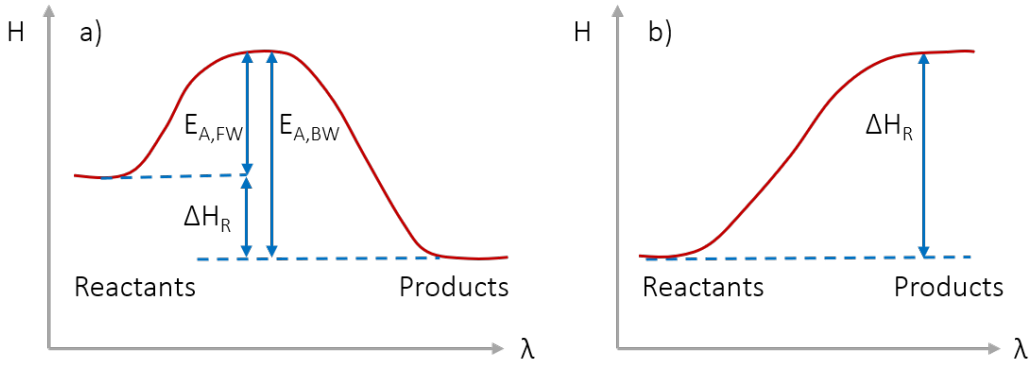

FIGURE 2.3: Example of MEPs for a reaction with energy barrier a) and a barrierless reaction b).

2.3.2 Classical and Variational TST

Transition state theory was first theorized in 1935 by Evans, Eyring and Polanyi [58, 59]. Despite the initial skepticism about this theory, it constitutes now the main method for treating the kinetics of elementary reactions, and further developments allowed also its extension to peculiar reaction classes, such as barrierless ones with variational TST [60]. A general treatment of TST can be found in chemical kinetics books.

The basic assumptions of TST are that the system can be treated according to Born-Oppenheimer approximation and that the velocity of the molecules follows Maxwell-Boltzmann distribution function (1.2). These are generally valid, however for the systems under study some difficulties may be encountered in this respect, as explained in the results. Classical TST treats MEPs with energy barriers, of the kind shown in Figure 2.3a). The basic idea is that the reaction rate is controlled by the frequency of passing through the saddle point, which is called transition state and is indicated using the symbol $\neq$. The configuration at the transition state is also called "activated complex", as the barrier $E_{A,FW}$ must be overcome for its formation, and it is considered as a bottleneck for the reactive flux. More specifically, the restrictive assumptions of TST describing these concepts and the consequent formulation of TST are listed below:

1. Non-recrossing assumption: according to this hypothesis, once the reactants overcome the TS configuration, they can only proceed to products, without the possibility of moving back to the configuration of reactants. This allows to express the reaction rate as the product between the frequency at which molecules pass the TS and the concentration of molecules at TS configuration, which therefore plays the role of a reactant:

$$r = \nu C_{\neq} \tag{2.30}$$

2. In a small region of length δ around the TS, the motion of the system along λ can

be separated from the other internal coordinates and treated as a translation. In this region, the potential is considered flat and therefore at the TS half of the molecules will evolve towards products at velocity v and half will move back to the reactants. Hence, the frequency of passing the TS is $v(2\delta)^{-1}$, resulting in

$$r = \frac{v}{2\delta} C_{\neq} \tag{2.31}$$

3. The TS is in equilibrium with the reactants: this allows to express $C_{\neq}$ in terms of the concentration of the reactants C_R and the respective partition functions according to $C_{\neq} C_R^{-1} = Q_{\neq} Q_R^{-1}$, such that expression (2.31) becomes

$$r = \frac{v}{2\delta} \frac{Q_{\neq}}{Q_R} C_R = k\ C_R \tag{2.32}$$

and therefore an expression for the kinetic constant is derived. R indicates generic reactants, and can therefore be referred to either a uni or bi-molecular reaction.

As far as the partition functions are concerned, these are the fundamental feature of statistical mechanics and they allow to express the macroscopic properties of a system as a function of its energy states. In fact, the most general definition of a partition function is

$$Q = \sum_{i=1}^{\infty} \exp\left(-\frac{E_i}{k_B T}\right) \tag{2.33}$$

where E_i are all the possible energy states of the system. The partition function is therefore related to how the energy is distributed in the system in question. The energy states are obtained by solving the Schrödinger equation. However, for an isolated molecule of ideal gas, the total energy can be regarded as the sum of independent translational, rotational, vibrational, and electronic contributions, whose product will result in the total Q. The energy states and the resulting partition functions for each are found by solving independent Schrödinger equations for a single particle in a box (Q^{tr}), a quantum rigid harmonic oscillator (Q^{vib}), a rotating molecule in 3D (Q^{rot}), and the electronic Schrödinger equation (Q^{el}). The resulting expressions are

$$Q^{tr} = \left(\frac{2\pi m k_B T}{h^2}\right)^{\frac{3}{2}} \tag{2.34}$$

$$Q^{rot} = \frac{8\pi^2 (2\pi k_B T)^{\frac{3}{2}} \sqrt{I_x I_y I_z}}{\sigma h^3} \tag{2.35}$$

$$Q^{vib} = \exp\left(-\frac{ZPE}{k_B T}\right) \prod_{i=1}^{3N-6} \frac{1}{1 - \exp\left(-\frac{h\nu_i}{k_B T}\right)} \tag{2.36}$$

$$Q^{el} = g^{el} \exp\left(-\frac{E_{el,tot}}{k_B T}\right) \tag{2.37}$$

where I_x, I_y, I_z are the principal moments of inertia, σ is the rotational symmetry number, g_{el} is the electronic degeneracy.

The final expression for the kinetic constant is derived as follows: v is expressed as the average velocity of Maxwell-Boltzmann distribution; then, the partition functions are expressed according to their independent contributions $Q^{tr}Q^{vib}Q^{rot}Q^{el}$; finally, the internal motion along the reaction coordinate is separated from $Q^{vib}_{\neq}$ (which thus includes only $3N$-7 DOFs and is indicated as $Q^{vib*}_{\neq}$) and expressed as a 1D translation. In this respect, it is noted that the vibrational frequency corresponding to the motion along λ at the TS is imaginary: in fact, considering that the energy gradient according to RRHO approximation is $\nabla E = k\ d\lambda$ and at the TS the energy decreases for any displacement along λ, the elastic constant k must be negative, hence the resulting frequency $\nu = \sqrt{k\ m^{-1}}$ will be imaginary. This allows to identify the TS with certainty in electronic structure calculations. The resulting expression of the kinetic constant is

$$k_{TST} = \frac{k_B T}{h} \frac{Q^{tr}_{\neq} Q^{rot}_{\neq} Q^{vib^*_0}_{\neq} g^{el}_{\neq}}{Q^{tr}_{R} Q^{rot}_{R} Q^{vib_0}_{R} g^{el}_{R}} \exp\left(-\frac{E_A}{k_B T}\right) \tag{2.38}$$

where Q^{vib_0} indicates that the ZPE exponential appearing in (2.36) is not included, and the activation energy is

$$E_A = (E_{el,tot} + ZPE)_{\neq} - (E_{el,tot} + ZPE)_R \tag{2.39}$$

At this point, a general overview of TST has been presented. However, this theory is not suitable for barrierless reactions, as anticipated. These are instead treated according to a modified version of TST, called variational (VTST). In order to explain the concept lying at the basis of VTST, the difference between tight and loose transition states is to be explained. A TS is defined "tight" when the configuration of the TS is geometrically similar to that of the reactants, hence the ratio between rotational and vibrational partition functions in (2.38) is close to 1. This is in general typical of reactions whose energy barrier is high and narrow. On the other hand, a loose TS is characterized by a very different configuration with respect to the reactants, with very elongated and distorted bonds. In this case, the vibrational frequencies of these bonds ν_i are small and therefore lead to high $Q^{vib^*_0}_{\neq}$, thus increasing the kinetic constant. This is typical of reactions with small and wide energy barriers, namely with large δ. Barrierless reactions are the extreme case in this category: according to classical TST, the configuration of the TS would coincide with that of the products, as they correspond to the maximum energy. In these cases, the non-recrossing assumption breaks down, as well explained by Truhlar and Garrett when introducing VTST [60], and this leads to an overestimation of k_{TST}. In order to tackle this issue, the kinetic constant k_{TST} is computed according to (2.38) along the full MEP, and its minimum value is taken as the upper limit for the real kinetic constant, as sketched qualitatively in Figure 2.4. The presence of the minimum in k_{TST} derives from the competition between E_A, which increases along λ thus decreasing k_{TST}, and ν_i associated with loose vibrations,

which decrease along λ thus increasing k_{TST}. Hence, in VTST, the minimum reactive flux is taken as the bottleneck for the reaction. When the barrierless reaction is bi-molecular and thus proceeds in the reverse direction, the kinetic constant is simply derived as the backward constant with thermodynamic consistency.

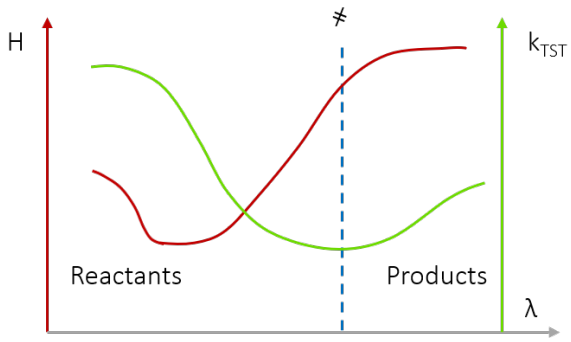

FIGURE 2.4: Sketch of the determination of the pseudo-TS and the kinetic constant in variational TST

In this work, both TST and VTST were used. In particular, VTST was used for addition and scission reactions. The TS was searched by scanning the reaction coordinate according to a predefined step, and the geometry with the highest energy was used as a guess for further optimizations. This was performed according to specific algorithms of GAUSSIAN and MOLPRO which ensure that the configuration always corresponds to a saddle point. As in the case of the reactants and products, different levels of optimization were adopted, namely level0 and level1 for the geometry, level1 for the frequencies, and hl for the energy. The rationale behind the optimization is the same as illustrated in section 2.2. When CASPT2 was used, the active spaces were selected starting from the configuration of the TS, and the same one was used for the study of the reactants and products of the reaction considered, so as to derive the energy barriers consistently. An extensive explanation will be provided in the results.

2.3.3 The Hindered Rotor Approximation

In TST, all the vibrational frequencies are treated according to RRHO approximation. However, this may break down when the vibrational frequencies associated with internal motions are low (in general, below 150 cm^{-1}), which is the case for some internal torsions. In fact, the potential of rotation around these bonds is periodic and therefore poorly described by the harmonic potential of RRHO. This leads to errors in the calculation of Q^{vib}, whose main contribution derives from small frequencies. Hence, k_{TST} may be inaccurate, in particular in the case of reactions with loose TS.

This concept is explained with an example of a reaction path treated in this thesis, the elimination of CH_2O from C_2H_4O, corresponding to the cleavage of C-C bond. The MEP of the reaction of Figure 2.5a) clearly shows the looseness of the TS. The internal torsion is the rotation of the moieties around the breaking C-C bond, and its potential has a periodicity of 2. During the bond cleavage, this motion becomes looser,

changing its ν calculated with RRHO from 182 cm^{-1} at the reactants to 87 cm^{-1} at the TS. The PES for a rotation of 180° around this bond at the configuration of the TS is shown in Figure 2.5b). The superimposed dotted orange line is a qualitative sketch of how the harmonic potential would instead behave starting from a stable configuration at about 70°. It is intuitive that, once an energy higher than about 0.1 kcal mol^{-1} is available to this internal motion, the system would switch to a configuration of 0°, whereas according to RRHO approximation the energy would be retained inside the motion and the system would just oscillate around the equilibrium position at 70°. This generally leads to an overestimation of the frequencies, although this effect is temperature dependent.

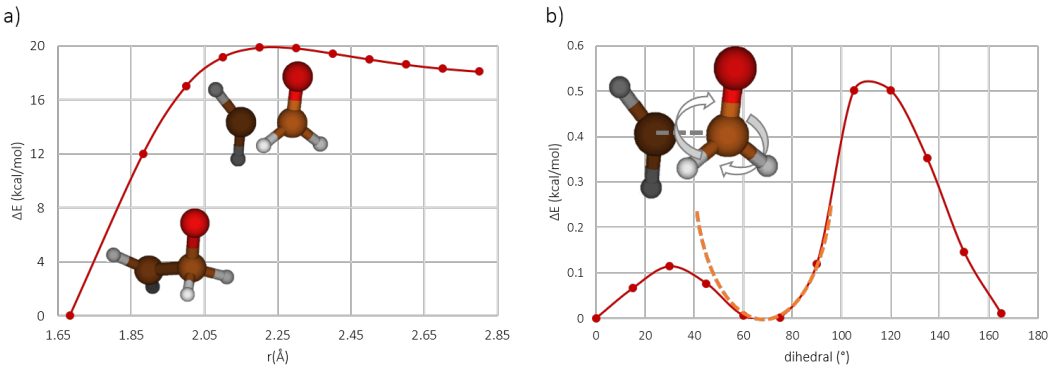

FIGURE 2.5: MEP for the elimination of CH_2 from C_2H_4O a), and PES of the hindered rotor of the TS b)

A solution to this problem is to treat internal torsions as independent one-dimensional hindered rotors [61]. This requires the solution of the one-dimensional Schrödinger equation for internal rotations

$$-\frac{\hbar^2}{2I_{red}}\frac{\partial^2\psi}{\partial\theta^2}+V(\theta)\psi=E\psi \tag{2.40}$$

where I_{red} is the reduced moment of inertia calculated according to the approach proposed by East and Radorn [62], θ is the dihedral angle describing the torsion and $V(\theta)$ is the corresponding potential, as the one in Figure 2.5b). The energy levels resulting from the solution of this equation are then used to calculate the corresponding partition function

$$q^{1DHR}=\sum_{i=1}^{\infty}\exp\left(-\frac{\epsilon_i}{k_BT}\right) \tag{2.41}$$

In this work, the number of levels included in q^{1DHR} was 300. This partition function is thus substituted to the corresponding q^{vib} in the overall Q^{vib}. For the molecules considered in this work, the procedure adopted is the following: first, the DOF corresponding to the HR to be treated was identified looking at the low ν_i; then, a PES scan along the selected coordinate was performed with constrained geometry optimizations at CASPT2/cc-pVDZ or ωb97xd-m062x/6-311+g(d,p), considering a single rotational period according to the rotor symmetry; finally, I_{red} was computed

and equation (2.41) was solved numerically for its first 300 eigenvalues; these were then used to compute q^{1DHR} at different temperatures, which was eventually substituted to the corresponding q^{vib} for the calculation of the kinetic constant. It is noted that also the contribution of ν_{1DHR} had to be removed from ZPE.

The effect of the inclusion of HRs in the reaction $C_2H_4O \rightarrow CH_2O + CH_2$ is illustrated in Table 2.1: $q_{\neq}^{vib}$ underestimates $q_{\neq}^{1DHR}$ at low temperature, and almost doubles it at high temperature; q_R^{vib} instead always underestimates q_R^{1DHR}, although its prediction is better at higher temperatures since ν_{1DHR} is higher than at the TS. The effect of these errors is highlighted by comparing k_{TST} with the one resulting from the inclusion of hindered rotors k_{HR}: if HRs are neglected, k is overestimated by a factor of 1.67 at 300 K, which increases to almost 2 at high temperatures. This is worsened by the looseness of the TS, as shown in the last columns: if the reaction is treated according to classical TST instead of its variational form, k is further overestimated by$1.1 \div 1.5$. Hence, k_{TST} is $1.8 \div 2.9$ times higher than its more accurate counterpart treated with HRs and VTST. The necessity of including both hindered rotors and variational effects in *ab initio* determination of kinetic constants is then apparent, as it allows a significant increase in the accuracy of predictions with relatively small additional complexity and computational effort.

Table 2.1: Corrections of the kinetic constant with HR and VTST

$\mathbf{T(K)}$	$\mathbf{q_{\neq}^{vib}}$	$\mathbf{q_{\neq}^{1DHR}}$	$\mathbf{q_R^{vib}}$	$\mathbf{q_R^{1DHR}}$	$\frac{\mathbf{q_{\neq}^{1DHR}}}{\mathbf{q_R^{1DHR}}}$	$\frac{\mathbf{q_{\neq}^{vib}}}{\mathbf{q_R^{vib}}}$	$\frac{\mathbf{k_{TST}}}{\mathbf{k_{HR}}}$	$\frac{\mathbf{k_{TST}}}{\mathbf{k_{VTST}}}$	$\frac{\mathbf{k_{TST}}}{\mathbf{k}}$
300	2.92	3.88	1.72	3.80	1.02	1.70	1.67	1.06	1.76
500	4.50	5.07	2.45	4.89	1.04	1.84	1.77	1.09	1.94
700	6.08	6.05	3.20	5.80	1.04	1.90	1.82	1.14	2.08
900	7.67	6.89	3.96	6.58	1.05	1.94	1.85	1.19	2.20
1200	10.05	7.99	5.10	7.61	1.05	1.97	1.88	1.26	2.36
1500	12.44	8.95	6.24	8.52	1.05	1.99	1.90	1.32	2.51
1700	14.03	9.54	7.00	9.08	1.05	2.00	1.91	1.37	2.61
2000	16.41	10.37	8.14	9.86	1.05	2.02	1.92	1.43	2.74
2200	18.01	10.88	8.90	10.34	1.05	2.02	1.92	1.47	2.82
2500	20.39	11.61	10.05	11.03	1.05	2.03	1.93	1.52	2.94

2.3.4 RRKM-ME theory

TST assumes that the reacting system is in equilibrium with the surrounding environment: namely, it is developed in a canonical distribution framework, where T and P are fixed. The resulting kinetic constant k has no dependence on pressure, which leads to overestimations of k. In fact, as noted first by Lindemann in 1922, the reactant molecule R of a uni-molecular reaction may acquire the energy needed to overcome the barrier via intermolecular collisions, such that the translational energy of the colliding body M is transferred to the reactant in the form of vibrational energy. This translational-vibrational energy transfer forms an activated complex R^*[11], which transforms into products D once the energy accumulated in the vibrational mode of

[11]The activated complex in this context is not related with the one formed at the TS, although the denomination is the same.

λ overcomes the barrier:

$$R + M \underset{k_{\overleftarrow{E}}}{\overset{k_{\overrightarrow{E}}}{\rightleftharpoons}} R^* \xrightarrow{k_R} D \tag{2.42}$$

The generic third body M may be a reactant, a product, or an inert. Assuming that the activated complex R^* is at steady state, the final expression for the reaction rate is derived as

$$r = \frac{k_R k_{\overrightarrow{E}} C_R C_M}{k_{\overleftarrow{E}} C_M + k_R} \tag{2.43}$$

where C_M contains the dependence on pressure[12]. In particular, the high and low pressure limits for $C_M \to \infty$ and $C_M \to 0$ are derived as

$$r_\infty = \left(\frac{k_R k_{\overrightarrow{E}}}{k_{\overleftarrow{E}}} \right) C_R = k_\infty C_R \tag{2.44}$$

$$r_0 = \left(k_{\overrightarrow{E}} C_M \right) C_R = k_0 C_R \tag{2.45}$$

where k_0 contains a linear pressure dependence via C_M, whereas k_∞ is pressure independent. Hence, at low P k decreases due to the poor energy transfer to the reactants, and this is called "fall-off regime". This effect is shown for the reaction $C_2H_4O \to CH_2 + CH_2O$ in Figure 2.6: k decrease with P is enhanced at high T, because the higher kinetic energy of the molecules and the broader energy distribution hinder the energy transfer to the DOF of the reaction coordinate. These curves however were not calculated with Lindemann theory, which is inaccurate in the intermediate fall-off regime. In fact, this theory does not account for the effects of the energy redistribution among the different energy states upon a collision, and for how the the population of each state affects the reactivity. This requires a switch to a microcanonical representation of the system, developed in RRKM-ME theory: RRKM estimates the microcanonical kinetic constant $k(E)$ for a uni-molecular reaction, whereas ME integration determines the population balance of each energy level E which eventually allows to determine the reactive behavior.

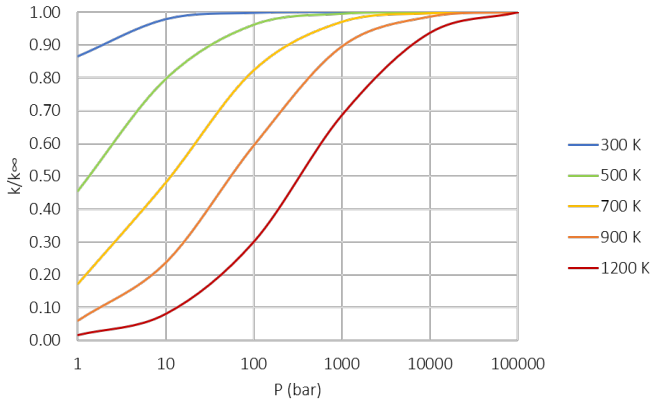

FIGURE 2.6: P and T dependence of k in $C_2H_4O \to CH_2 + CH_2O$

[12]In the case of an ideal gas, the concentration of the third body will simply correspond to $\frac{P}{k_B T}$

In RRKM theory, it is considered that the total energy of the system E is redistributed among the harmonic vibrational motions of the molecule and the translational motion associated with the reaction coordinate as in TST. The reaction can only occur when $E > E_A$, providing that this energy is retained as translational kinetic energy along λ. This energy state has a probability of existence $P(E^*)$, and will proceed with a velocity $v(E^*)(2\delta)^{-1}$, as in equation (2.31). Therefore, the kinetic constant at a certain energy E is

$$k(E) = \int_{E_A}^{E} \frac{v(E^*)}{2\delta} P(E^*) dE^* \tag{2.46}$$

The velocity $v(E^*)$ is simply expressed in terms of the kinetic energy E^*. $P(E^*)$ will instead be the probability that the total energy E is split among the states of the system such that E^* goes into the internal translation and $E - E^*$ goes into the other vibrational DOFs. Mathematically:

$$P(E^*) = \frac{\rho^{vib^*}(E - E^*)\rho^{tr}(E^*)}{\rho^{vib^*}(E)} \tag{2.47}$$

where $\rho(E)$ is the number of ways the energy redistributes among the considered motions of the molecule. An extensive treatment is found in Steinfeld [63]. ρ^{tr} can be expressed explicitly as the density of states of a particle moving in a box, and substituted in (2.46), eventually obtaining

$$k(E) = \frac{\int_{E_A}^{E} \rho^{vib}(E - E^*) d(E^*)}{h\rho^{vib}(E)} \tag{2.48}$$

With RRKM theory, $k(E)$ can be computed. However, the actual population $n(E)$ of a certain excited level E is unknown. This is found solving a population balance known as "master equation" (ME). A qualitative sketch of the phenomena represented in the ME is shown in Figure 2.7, where the MEP of $C_2H_4O \rightarrow CH_2 + CH_2O$ is taken as a reference. The ME describes the evolution of $n(E)$ as

$$\frac{dn(E)}{dt} = Z \sum_{E^I=0}^{E_{max}} \left(P(E, E^I) n(E^I) - P(E^I, E) n(E) \right) - k(E) n(E) \tag{2.49}$$

Z is the number of collisions per unit time and volume, which retains the pressure dependence since it is a function of C_M. The expression for Z used in this work can be found in Barbato et al [12]: Z contains Lennard-Jones parameters of the inert bath gas where the molecules are immersed (Ar in this case) which were therefore required as input. $P(E, E^I)$ is the probability that a molecule with energy E^I moves to energy E upon collision, hence $ZP(E, E^I)n(E^I)$ can be regarded as an inlet term of molecules at energy E, whereas $P(E^I, E)$ represents an outlet term. These probabilities were

determined according to the collisional exponential-down model

$$P(E, E^I) = \frac{1}{C(E^I)} \exp\left(-\frac{E^I - E}{\Delta E_{down}}\right) \tag{2.50}$$

where $C(E^I)$ is the normalization constant. ΔE_{down} represents the energy lost in a collision, which may for instance lead to collisional stabilization of intermediates. This was computed as a function of temperature according to $\Delta E^0_{down}(T\ 298^{-1})^{\alpha}$, where ΔE^0_{down} was set to 260 cm^{-1}, and α was set to 0.875. $P(E^I, E)$ ca be obtained from $P(E, E^I)$ imposing thermodynamic consistency, namely using $f(E^I)P(E, E^I) = f(E)P(E^I, E)$, where $f(E) = \rho(E)\exp(-E(k_B T)^{-1})\ Q^{-1}$ is the Boltzmann vibrational distribution function. The resulting problem is a complex integral-differential equation. The final kinetic constant at the considered T and P will be obtained as

$$k|_{T,P} = \sum_{E_A}^{E_{max}} n(E)k(E) \tag{2.51}$$

where E_{max} was set to 400 kcal mol^{-1} (the exact result is obtained with an infinite summation).

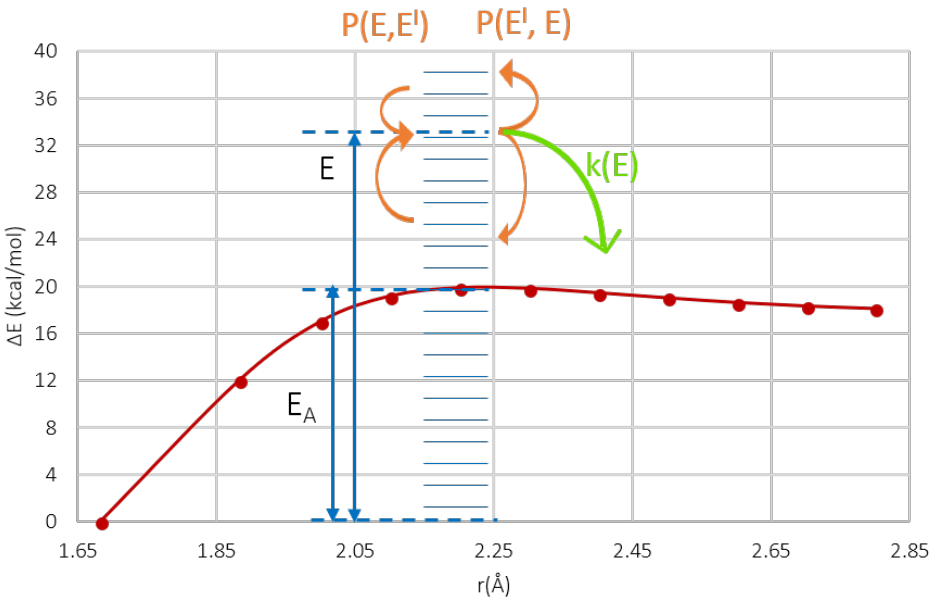

FIGURE 2.7: Sketch of population balance and jumps among energy levels in $C_2H_4O \rightarrow CH_2 + CH_2O$

2.3.5 ME and MC-RRKM simulations

Several approaches were proposed for the solution of the ME. In this work, two different methods were adopted for single reaction channels and for the global rates of the multi-well PES. In particular, for single reactions (basically the initial additions of

O(^{3}P) to alkenes), MESS[13] code was used (`http://tcg.cse.anl.gov/papr/codes/mess.html`, [64]). The solution method is based on the so called "chemically significant eigenstates", namely eigenvalues of equation (2.49) which can be directly related to phenomenological rate constants $k|_{T,P}$. The code input only requires the structures and the vibrational frequencies of the reactants and TS, and some parameters related to energy thresholds and integration steps.

Despite MESS is extremely fast and allows a direct prediction of $k|_{T,P}$, it is not suitable for the treatment of multi-well reactions. In fact, when treating a full PES it is difficult to associate single eigenvalues to the reaction pathways. Furthermore, since all the wells are connected, well-skipping reactions may occur, when for instance the energy of the system is enough to jump from a configuration to another without following any pathways described by reaction coordinates. Another phenomenon peculiar of multi-well reactions is collisional stabilization, which may occur when a molecule at the configuration of the well collides and transfers its energy to another complex, thus stabilizing: these stable intermediates may also not react further and are in this case considered as products. A sketch of these phenomena is shown in Figure 2.7.

Stochastic methods are more appropriate for the description of the collisional energy transfers typical of a multi-well PES. In this work a code developed by Barbato et al was used [12], as it was applied successfully to multi-well reactions of O(^{3}P) with alkenes in previous works [7, 8, 13, 14, 16]. As far as $k(E)$ is concerned, in this approach also the dependence on the angular momentum J was considered. Expression (2.48) would thus include an additional contribution of rotational energy and rotational density of states, resulting in $k(E, J)$. $k(E)$ is obtained by an average of J-resolved $k(E, J)$, whose details can be found in the corresponding paper. The ME is instead solved with a kinetic monte carlo (KMC) approach, which is why the method is referred to as KMC-ME. The main advantage of a stochastic solution method is that ME does not need to be integrated directly. The principle is that many independent reactive molecules are let move stochastically, and the resulting behavior is representative of the average reactivity of the system. In this work, 10000 independent reactive molecules were considered. The reaction is started by a collisional event, upon which the first complex is formed, containing a certain energy. At this point, the system evolves to a random event chosen among excitation, de-excitation, and reaction to a well or to a product with the respective probabilities. Time is updated and a new simulation is started only if a reactive event occurs. Finally, the energy distribution is computed on the basis of the time spent by the molecule in each energy configuration. The output of the simulation also contains the final number of molecules of every product and well, and the uni-molecular kinetic constants $k(E)$. Further details about the structure of the input are provided in Appendix E.

[13] Acronym of "master equation system solver."

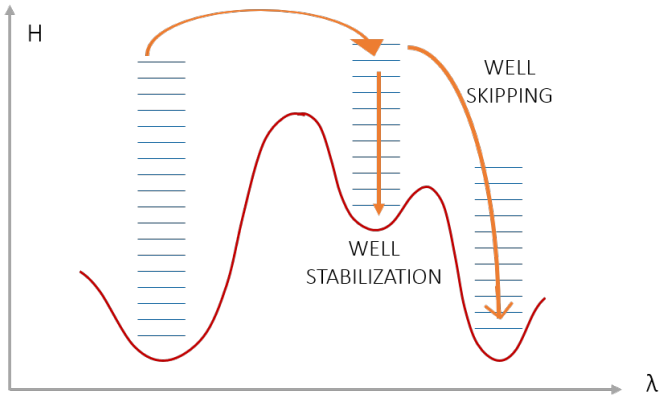

FIGURE 2.8: Example of phenomena of well stabilization and well skipping on a multi-well PES

2.3.6 Automatic determination of rate constants: EStokTP

The geometry optimization, frequency and energy calculations, and the determination of rate constants for the single channels were performed in an almost fully automated way using the program EStokTP[14] [65]. The steps illustrated in the previous paragraphs were undertaken in order. In the input, it is required to provide the level of theory and the basis sets for each kind of calculation, along with separate files for MOLPRO inputs in case CASPT2 is used. The data needed also include a first guess for the geometry of reactants and products in the form of a z-matrix, as well as indications about the reaction coordinate for the TS. Most importantly, each kind of reaction is treated differently and therefore the inputs change. For the $O(^3P)+C_2H_4$ PES, only addition and beta-scission reactions were treated, where all the elimination channels were considered as beta-scissions. The general steps performed by the code for each reaction class are listed below.

1. Optimization of reactants at level0: a first geometry optimization is performed as explained in section 2.2. This also allows for the stochastic search of the minimum configuration according to a MC sampling on dihedral angles chosen appropriately by the user.

2. Optimization of products at level0: this option is only needed in case of beta-scission reactions, and proceeds in the same way as step 1.

3. Optimization of the TS: a first guess of the TS is generated with a constrained scan along the reaction coordinate specified, usually in steps of 0.2 Å or as indicated by the user; the configuration for the guess is chosen as the one with the maximum energy. Then, a TS geometry optimization is performed with the level of theory chosen. Finally, appropriate dihedral angles are scanned stochastically for a further check on the correctness of the configuration found.

[14] Acronym of "electronic structure to $k(T,P)$".

This is particularly important for bigger molecules (above 3 carbon atoms), as several local minima are present.

4. Optimization of geometries at level1: all the structures found are optimized further, usually improving the basis set and the active space in case of CASSCF calculations. Also vibrational frequencies are computed at this point. For addition reactions, it is possible to find and optimize the adduct formed automatically. The algorithm used in the code uses as a starting point the geometry of the TS, therefore it is necessary to have a good initial structure, which is why the well geometry is only determined at level1. Further stochastic scans on the configuration found can also be performed.

5. Inclusion of hindered rotors: for all the reactive molecules, hindered rotors can be considered. The number of dihedral angles to be scanned, the number of points, and the HR symmetry are indicated in the input, therefore vibrational frequencies found should be checked first. The HR PES is derived and the energy is modified accordingly. The ZPE should instead be modified manually. The inclusion of HRs is extremely delicate and must be carefully checked: in fact, the HR PES may have negative energies indicating that the initial configuration found does not correspond to the absolute energy minimum, and this clearly requires to restart a part of the calculations. In the code, it is also possible to include coupled hindered rotors. This may be necessary for large molecules such as C_5H_{10}.

6. High level energy calculations: the energy of each reactive molecule is computed according to what explained in section 2.2.

7. Intrinsic reaction coordinate scan: in case variational calculations are needed, this step reconstructs the MEP at level1, computing the Hessian at every step, and allows the implementation of VTST. It is also useful for TS checks of classical TST.

8. Kinetic constant calculation: this step launches MESS code. All the required input data are automatically generated, however careful checks are needed. The output provides the kinetic constant in the selected range of temperature and pressure.

Since in most cases EStokTP output was only needed in order to compute the input values to the KMC-ME code, further packages were added in order to retrieve all the information needed in an appropriate format. It is noted that EStokTP does not treat spin-forbidden reactions, therefore all the calculations for MECP and H_{SO} were performed manually, as explained in section 2.4.

2.3.7 Determination of BRs and phenomenological rate constants

The final aim of the calculations is the *a priori* determination of the product distribution and the corresponding phenomenological rate constants as a function of T and P. However, the output of KMC-ME simulations only provide $k(E)$ and the number of molecules obtained of each product and well. Therefore, $k(T)$ for each reaction channel was determined in the post-processing of the results. First, the branching ratio of each product and well i was simply calculated as the fraction of product molecules N_i with respect to the total molecules N_{tot}. Then, the kinetic constant at each T and P was calculated by multiplying the BR by the addition kinetic constant computed with MESS:

$$k_i|_{T,P} = BR_i \; k_{add}|_{T,P} = \frac{N_i}{N_{tot}} k_{add}|_{T,P} \tag{2.52}$$

It is noted that in the case of O(^{3}P) addition to propylene and 1-butene, the PES related to the central and terminal carbon addition were considered separately. Hence, the final kinetic constant accounted for the BRs of each surface was multiplied by the respective addition constant:

$$k_i|_{T,P} = (\mathrm{BR}_i \; k_{add}|_{T,P})_{term} + (\mathrm{BR}_i \; k_{add}|_{T,P})_{centr} \tag{2.53}$$

and the total branching ratio for each component was then determined as

$$\mathrm{BR}_i = \frac{k_i}{\sum_{i=1} k_i} \tag{2.54}$$

Finally, phenomenological rate laws for each channel as a function of temperature and at fixed pressure were derived fitting a modified Arrhenius expression:

$$k_i(T;P) = k_0 \; (T)^{\alpha} \; \exp\left(-\frac{E_A}{RT}\right) \tag{2.55}$$

where k_0, α and E_A were the fitting parameters determined. It is noted that E_A does not correspond to the real energy barrier of the reaction considered. The procedure explained also includes the treatment of ISC, however some modifications are required, as explained in the following section 2.4.

2.4 Intersystem Crossing

ISC is rarely treated in chemical kinetics, therefore few methods for the computation of ISC kinetic constant are available in literature. Furthermore, ISC is not generally included in chemical kinetics codes such as EStokTP or MESS. The basic assumption for the the integration of ISC in kinetic models is that MECP may be treated as a transition state, with a specific reaction coordinate and corresponding imaginary vibrational frequency. The main difference is that $k(E)$ is computed in terms of hopping probability. Furthermore, MECP is usually assumed to be unique, whereas in reality

the hopping occurs in a certain region of the phase space. The same assumption concerns spin orbit coupling, which is regarded as independent on the nuclear coordinates in the MECP region. It is recalled that BO approximation is still considered valid, and the surfaces considered are the diabatic ones as described in section 1.2.

2.4.1 Determination of MECP

The determination of MECP was performed with the "partial optimization method", widely used in literature and described for instance by Harvey [36]. This method was also successfully applied in other studies of O(^{3}P) addition to alkenes and alkynes [7, 8]. MECP is defined as the point with minimum energy where the ground state singlet and triplet energies are the same, namely $E_{T_1} - E_{S_0} = 0$. This was found with a constrained optimization scan on the triplet surface T_1 at CASPT2 level with 2-state averaging, and the energy of the singlet state was then computed on the same geometry using the same active space. The scanned coordinates, comparable to reactions coordinates, were the C-C-O angle (aabs1) and the dihedral corresponding to CHO rotation (b1), as sketched in Figure 2.9. As expected, a full set of coordinates (aabs1,b1) yielded a null energy difference. For this set, also the frequencies and H_{SO} were computed. Spin orbit coupling calculations were performed with MRCI program of MOLPRO. Since CASPT2 is not supported by MRCI program, the orbitals were computed at CASSCF level for the triplet state, then computed again with CI, and eventually used as a guess for a singlet CI calculation for the energy of the singlet state. At CI level, $E_{T_1} - E_{S_0}$ was not exactly null, however this should not affect the results significantly [35]. SOC calculations result in three off-diagonal $H_{SO,i}$ matrix elements of the Breit-Pauli operator, which were averaged as suggested by Hu et al [41] for the evaluation of the final H_{SO}:

$$H_{SO} = \left(\frac{H_{SO,1}^2 + H_{SO,2}^2 + H_{SO,3}^2}{3} \right)^{\frac{1}{2}} \tag{2.56}$$

In the systems already analyzed in literature with this method [7, 8, 16], it was found that the point of minimum energy corresponded to the maximum H_{SO}, thus maximizing the hopping probability. In O(^{3}P) + C_2H_4 instead, the maximization of SOC occurred at a different points, as shown in Figure 2.9. However, upon frequency analysis no negative frequency was found at the minimum energy (at 110°), as opposed to the higher energy (at 112.6°). Furthermore, the total enthalpy $H = E_{el,tot} + ZPE$ was found to be lower at 112.6°. Hence, the point of maximum H_{SO} was reasonably considered as the MECP. These considerations are not in line with the assumption of H_{SO} independence of nuclear coordinates, which is instead valid in heavier systems. Finally, it is noted that for MECP calculations only the triplet and singlet ground states T_1 and S_0 were included in the calculations, contrary to what was done by Li et al [34] for the same system. In this work, several attempts of excited states computations were performed, however they were eventually rejected

for reasons discussed in the results. The validity of the approach is confirmed by the final kinetic constants and BRs obtained.

The "partial optimization" method proved effective in the determination of MECP, however it is extremely time consuming. Several other methods are available, among which the most popular is probably the "hybrid energy gradient method" proposed by Harvey [35] and used also by Li et al [34]. This is based on the idea that the search of the intersection should follow the direction where the higher energy grows less than the smaller one. In this work, a simplified version was adopted to find the conical intersection between the ground and excited triplet states T_1 and T_2 of the initial adduct. This kind of calculation was performed to check the involvement of the excited triplet state in ISC reactivity at high temperatures, as it will be further explained in the results. The method used for MECP was not adopted as the coordinates to be selected for a constrained scan were unknown. In this case, a first guess for the geometry of the intersection was generated at lower level with 2 state-average CASSCF using MOLPRO program for conical intersections. From this geometry, a Newton-Raphson method was implemented manually for the minimization of the function

$$f = (E_1 - E_2)\left(\frac{dE_1}{dq} - \frac{dE_2}{dq}\right) \tag{2.57}$$

where q indicates an internal coordinate. All computations were performed at CASPT2 level. The energy gradients were computed numerically, with the available options of MOLPRO. The step sizes for the gradients were set to 0.01 Bohr and 0.1°. The coordinates q to be updated minimizing (2.58) were chosen as those with the highest difference between the gradients. The chosen coordinates were thus updated according to

$$q' = q - \alpha\frac{f}{df} = q - \alpha\frac{(E_1 - E_2)\left(\frac{dE_1}{dq} - \frac{dE_2}{dq}\right)}{\left(\frac{dE_1}{dq} - \frac{dE_2}{dq}\right)^2 + (E_1 - E_2)\left(\frac{d^2E_1}{dq^2} - \frac{d^2E_2}{dq^2}\right)} \tag{2.58}$$

where α is a scaling parameter set too 0.1. The second derivatives were taken from the Hessian computed during the geometry optimization.

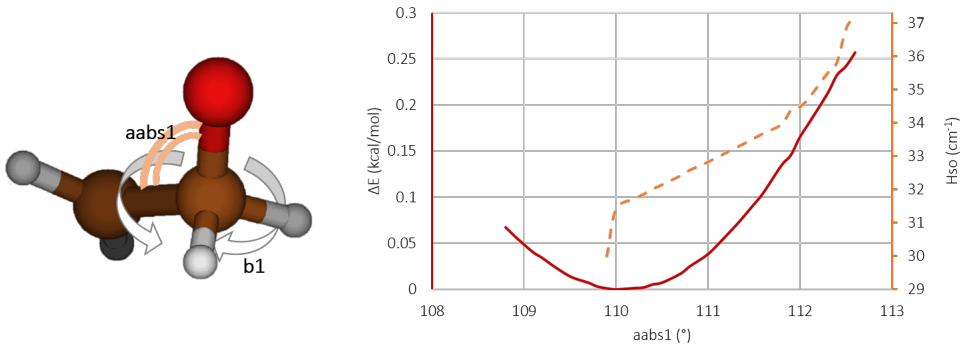

FIGURE 2.9: PES of the T_1S_0 crossing points and corresponding H_{SO} for C_2H_4O scanned along aabs1 and b1 coordinates

2.4.2 Landau-Zener theory and integration in KMC-ME simulations

Once the MECP has been located, the ISC is to be integrated in the KMC-ME model. In fact, ISC rate cannot be computed using MESS, and is therefore calculated directly in KMC-ME simulations. The approach used for the calculation of the microcanonical kinetic constant $k(E)$ is again the one proposed by Harvey [11], and implemented in KCM-ME code in 2010 [13]. In the input, MECP is indicated as a TS, with the corresponding imaginary frequency, and the value of H_{SO} computed according to (2.56) is also added. As in regular RRKM theory of equation (2.46), the kinetic constant is given by the total state density at an energy E above the MECP, with respect to the total rovibrational density of states of the reactant ρ^{vib}:

$$k(E,J) = \frac{\int_{E_{MECP}}^{E} p_{sh}(E^*)\rho^{vib}(E-E^*,J)dE^*}{h\rho^{vib}(E,J)} \tag{2.59}$$

where the dependence on J is removed by weighted averaging. Hence, surface hopping occurs when a certain energy E^* above E_{MECP} is retained in the reaction coordinate, and the remaining energy $E-E^*$ is distributed among the other rovibrational DOFs. In this case, the reaction coordinate corresponds to a combination of (aabs1,b1), namely the C-C-O angle and the O-C-C-H dihedral, respectively. When the O gets closer to the opposite C and an internal rotation makes the molecule roughly symmetric with respect to the O-C-C-H plane, the singlet state becomes favoured and ISC occurs, finally leading to the configuration of ethylene oxide. These two coordinates are clearly excluded from ρ^{vib} and instead included in p_{sh}, the surface hopping probability. According to the description of Harvey, p_{sh} refers to the hopping between diabatic surfaces, and is computed from the hopping probabilities between adiabatic surfaces P_{LZ}, as shown in Figure 2.10 and explained below. P_{LZ} is computed according to Landau-Zener theory [25, 26]:

$$P_{LZ}(E) = \exp\left(-\frac{2\pi H_{SO}^2}{\hbar\Delta F}\sqrt{\frac{\mu}{2E}}\right) \tag{2.60}$$

and the relative slope of the two surfaces at the seam was computed by a simple gradient averaging of the slopes with respect to the two coordinates:

$$\Delta F = \frac{1}{2}\left(\frac{dE}{d\text{aabs1}} + \frac{dE}{d\text{b1}}\right) \tag{2.61}$$

As shown in Figure 2.10, the motion described by P_{LZ} between the adiabatic surfaces is equivalent to the path described by an evolution along λ where the molecule remains on diabatic surface 1. Hence, P_{LZ} is the probability of staying on diabatic surface 1 and $(1-P_{LZ})$ is the probability of hopping from diabatic surface 1 to diabatic surface 2, as in Figure 2.10 on the right. The total p_{sh} is described as a double pass across the seam, namely as the sum of the probability of hopping at pass 1 $(1-P_{LZ})$ and the one of hopping at pass 2 without hopping at pass 1, $P_{LZ}(1-P_{LZ})$, resulting

in

$$p_{sh}(E) = (1 - P_{LZ}) + P_{LZ}(1 - P_{LZ}) = (1 - P_{LZ}^2) \tag{2.62}$$

The form of equation (2.62) also gives reason of why an increase in H_{SO} leads to an increase in ISC: in fact, if the exponential of (2.60) increases, P_{LZ} decreases and p_{sh} increases. P_{LZ} decreases because the distance between the adiabatic surfaces increases, as shown in the introduction in Figure 1.2.

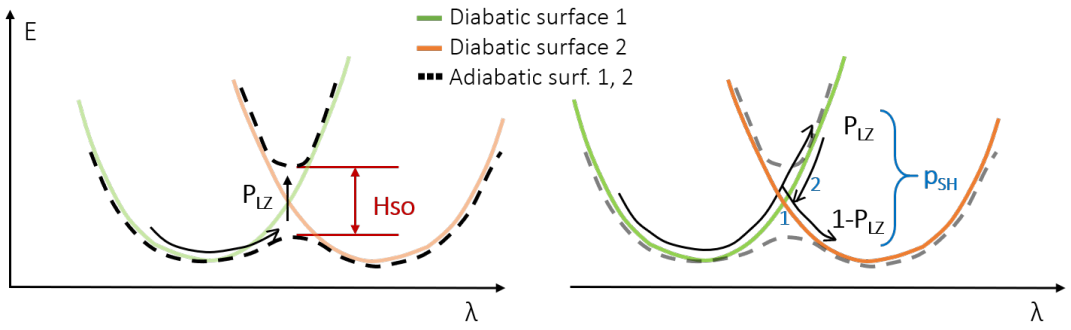

FIGURE 2.10: Hopping probability between adiabatic surfaces P_{LZ} (left) and diabatic surfaces p_{sh} (right)

2.5 Determination of rate rules

As explained in the introduction, the determination of rate rules for the scaling of phenomenological rate constants to heavier compounds is essential for applications in both interstellar and combustion chemistry. Rate rules would allow the transition from basic to applied research, as the integration of these kinetic constants in combustion modeling would contribute to the estimation of the flame properties. Usually, rate rules are determined with fitting parameters, once data for a series of species with increasing molecular weight is available [66]. In this work instead, a different approach was adopted, based on considerations about the behavior of the system.

In order to search a common trend in the reactivity of $O(^3P)$+alkenes, the PES of propylene and 1-butene were considered. Ethylene was excluded because its reactivity is not fully representative of that of heavier hydrocarbons: in fact, no distinction between terminal and central carbon can be done, and the ISC is higher than in heavier systems, contrary to the trends. Furthermore, complete data for propylene and 1-butene were available at the same level of theory, and also KMC-ME simulations were performed again with inputs prepared in other works, with slight modifications [8, 16, 50]. Hence, the scaling of C_3H_6 phenomenological rate constant to obtain those of C_4H_8 was performed. Rates for the addition of $O(^3P)$ to C_5H_{10} were then predicted, and will be validated in a future work. It is also recalled that the scaling was applied only to the main triplet channels and ISC, however KMC-ME simulations included the full PES. The same approach will probably be used in the future to derive rate rules for the singlet channels.

The idea behind the scaling is that all the PES for $O(^3P)+C_nH_{2n}$ with n>2 have the same structure and the same reactive channels, with the addition of methyl groups when n increases. The additional channels corresponding to C-C scissions are less reactive, therefore they may be neglected or grouped together as a single channel. This problem is mostly relevant on the singlet PES, whereas on the triplet PES only the channels of H and CH_2O elimination are highly reactive, also with increasing molecular weight. All the reactive channels are accessed upon the formation of two initial wells resulting from $O(^3P)$ addition to either the terminal or the central carbon. The well depth with respect to the reactants is roughly the same at different molecular weights, namely about 23.7 kcal mol^{-1} (which is the exact value for propylene terminal carbon addition). What instead really differs is the energy distribution among the DOFs of the system: in particular, as n increases, the internal energy of the adduct will be distributed among a larger number of internal motions $(3N-6)$. As a consequence, the energy retained in the DOFs corresponding to the reaction coordinates decrease, together with the reactivity of the channels. The kinetic constants of these channels will therefore decrease at higher molecular weight for the same internal energy. In other words, the reactivity of the heavier system will be comparable to that of the lighter system at a colder temperature, since the energy available to each channel is smaller. This concept can be expressed mathematically by associating to each well at a given T an intrinsic temperature T^* at which the internal energy corresponds to the well depth. This relation is written in terms of the heat capacity of the system:

$$\Delta E_{WELL} = 23.7 \text{ kcal mol}^{-1} = \int_T^{T^*} C_V(T')dT' \tag{2.63}$$

where C_V is the heat capacity of the well at constant volume accounting for the rovibrational contributions. Heat capacities were computed *ab initio*, as explained in detail in section 2.6. Equation (2.63) is a non-linear equation, and it was solved numerically for every species using a Matlab code written from scratch for the purpose. It is evident that, as the molecular weight and the heat capacity increase, the intrinsic temperature decreases, as an indication of the "colder reactivity" of the molecule. Now let us consider two generic wells with n and m carbon atoms. It is assumed that the reactivity of n is known, and the reactivity of m is to be predicted on the basis of the phenomenological rate constants of n. This can be done by scaling them on the basis of the difference in the intrinsic temperatures $\Delta T^*_{m-n}(T)$:

$$k_m(T) = k_n\left(T + \Delta T^*_{m-n}(T)\right) = k_n\left(T + T^*_m(T) - T^*_n(T)\right) \tag{2.64}$$

Therefore, the reactivity of m will be described by the laws of n but considering a different temperature, $k_m(T_{sc}) = k_0 T_{sc}^{\alpha} e^{-\frac{E_A}{RT_{sc}}}$, where $T_{sc} = T + \Delta T^*_{m-n}(T)$ and k_0, α and E_A are the parameters of the laws of n. The resulting BRs are simply computed according to (2.54). An important remark is that the quantity which is actually of interest are the BRs: in fact, the prediction of the $k(T)$ is unlikely to be accurate,

however the addition kinetic constants for heavier species are usually available in databases, therefore the final constants can be derived in a second moment.

By looking at expression (2.64), if $m > n$, $\Delta T^*_{m-n} < 0$, and the behavior of m will be that of n at a temperature lower by this intrinsic temperature difference. Also the product distribution represented by the BRs will be shifted to lower temperatures, resulting in an increase in the importance of ISC. In this work, $n = 3$ and $m = 4$, as the scaling was done from propylene to 1-butene. First, the correspondences between the reactive channels were established. KMC-ME simulations were launched again, high pressure phenomenological rate constants for these channels were derived and rate laws parameters were computed with non-linear regression functions in Matlab. Then, scaling factors were determined on the structure of the wells on the basis of the heat capacities computed *ab initio*. Finally, rate laws for 1-butene were predicted with (2.64) and compared to those calculated *ab initio*. Some corrective factors were also imposed on the basis of some differences between the two PES. All these points will be further discussed in the result section.

The method proposed for the determination of rate rules is innovative and extremely powerful. In fact, the computational effort for the determination of the kinetic constants for the main reaction channels for heavier hydrocarbons is reduced to the *ab initio* calculation of the heat capacity of the well, which can also be done with DFT. Although the application of these scaling relations was limited to the triplet PES and to ISC channel, possible further extensions to the full singlet PES would allow the complete *a priori* prediction of the BRs for heavier species.

2.6 Thermochemistry: computation of heat capacities

The heat capacities for each well were computed *ab initio* at DFT ωb97xd/aug-cc-pVTZ level, which was also used for the geometry optimization. This allowed fast calculations of the vibrational frequencies, at the cost of small errors in the computations which mostly cancel out in ΔT^*. The hindered rotors of each well were computed at the same level, with a PES constructed at steps of 10°. It is noted that only the well resulting from the terminal carbon addition was considered. In fact, the well depths for the terminal and central carbon additions are similar, and the few differences in the vibrational frequencies are only related to low ν which contribute the least to the overall heat capacity. Furthermore, differentiating the contributions would have required separate rate constants, which would increase the complexity of the method.

C_V is defined as the derivative of the internal energy U with respect to temperature at constant volume:

$$C_V = \left(\frac{\partial U}{\partial T}\right)_V \tag{2.65}$$

where in this case $U = E_{el,tot} + E_{vib} + E_{rot} + E_{trasl}$. The contributions to the heat capacity are only $C_{V,vib}$ and $C_{V,rot}$, as it is assumed that no translational energy is

retained upon well formation. The internal energy for a canonical ensemble is given by

$$U = -\left(\frac{\partial \ln Q}{\partial \beta}\right)_V \tag{2.66}$$

where $\beta = (k_B T)^{-1}$. This formula allows an easy derivation of the C_V for each contribution, which is fully treated in textbooks like McQuarrie [67]. The total rotational heat capacity is simply

$$C_{V,rot} = \frac{3}{2}R \tag{2.67}$$

where the gas molecule is assumed ideal. $C_{V,vib}$ is instead derived from the vibrational partition function (2.36) excluding the ZPE exponential, and is computed as the sum of the independent contributions of each normal mode:

$$C_{V,vib} = k_B \sum_{i=1}^{3N-6} \exp\left(\frac{hc\nu_i}{k_B T}\right) \left(\frac{1}{k_B T} \frac{hc\nu_i}{\exp\left(\frac{hc\nu_i}{k_B T}\right) - 1}\right)^2 \tag{2.68}$$

As far as hindered rotors are concerned, the contribution of their corresponding vibrational DOF was removed from (2.68) and substituted with the one derived from the 1DHR partition function (2.41), which is

$$C_{V,1DHR} = \frac{1}{k_B T^2}\left(\frac{1}{q_{1DHR}} \sum_{i=1}^{\infty} \epsilon_i^2 \exp\left(-\frac{\epsilon_i}{k_B T}\right) - U_{1DHR}^2\right) \tag{2.69}$$

where the internal energy is

$$U_{1DHR} = \frac{1}{q_{1DHR}} \sum_{i=1}^{\infty} \epsilon_i \exp\left(-\frac{\epsilon_i}{k_B T}\right) \tag{2.70}$$

and number of eigenvalues considered for each hindered rotor was 300. The HR potentials and eigenvalues were computed as explained in section 2.3.3.

Chapter 3

Results: $O(^3P)+C_2H_4$

The first part of the results regards the study of the addition of $O(^3P)$ to C_2H_4, whose main reaction channels and previous studies were presented in the introduction. The aim of these calculations was an understanding of the method and its validation for the following rate predictions on the basis of previous *ab initio* studies. Hence, in this section a deeper focus on the methods used and the difficulties found for each reaction channel will be presented. In particular, all the details about addition, ISC, H and CH_2O elimination will be provided in section 3.1. The main points highlighted will be the choice of the active space, which was the most delicate step, and the determination of high level energies. Furthermore, the addition rate constant will be discussed in comparison to experimental data and other theoretical works. Then, the results of KMC-ME simulations will be presented in section 3.2, together with the BRs obtained for the channels considered and the phenomenological rate laws thus derived. Finally, the validation of the approach and the partial disagreement of the BRs obtained with experimental data are discussed in section 3.3.

3.1 Reaction Channels

3.1.1 Addition

The most important reaction channel to analyze is the addition step. In fact, this is the entrance channel, and its rate determines those of all the following ones. However, this is also the most delicate to treat at CASPT2 level especially in relation to the choice of the active space. For this reason, several different trials were performed, and the reaction was treated at different levels of theory. In particular, the system was optimized at both CCSD(T)/CBS//ωb97xd/aug-cc-pVTZ and CASPT2(8e,7o)/aug-cc-pVTZ//CASPT2(6e,5o)/aug-cc-pVTZ, where // indicates the separation between the level for the energy and the one for geometries and frequencies. In the notation CASPT2(n_e,m_o) n_e and m_o indicate the number of electrons and orbitals included in the active space, respectively. When using DFT and CC, no problems were encountered, therefore here only the computations with CASPT2 will be treated. The final properties obtained for reactants, TS and product are listed in Table A.1 in Appendix A.

Concerning the input data, the only critical point is the state degeneracy of $O(^3P)$: in fact, its three energy levels are 1, 3 and 5 times degenerate respectively, and this has to be indicated explicitly. It is also noted that ethylene has a symmetry factor of 4. After the optimization of reactants and products at level0, the TS was searched with a constrained scan along the C1-O distance: the PES obtained at ωb97xd/cc-pVDZ is shown in Figure 3.1. The distance C1-O at the TS is about 2.14 Å. The TS is clearly loose, as expected from an addition reaction. Since the reaction can be considered almost barrierless, the kinetic constants were computed with both conventional and variational theories. Despite the low theoretical level of these initial calculations, the structure of the TS is already clear, as shown in Figure 3.2: the TS is symmetric with respect to the O-C1-C2 plane, with both angle "aabs1" and dihedral "babs1" of about 90°.

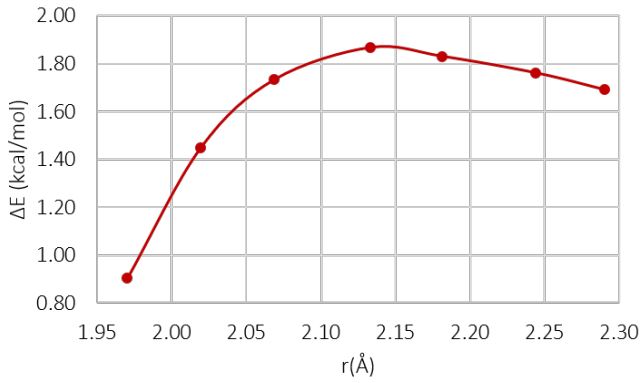

FIGURE 3.1: PES of the TS search for the addition of $O(^3P)$ to C_2H_4 at ωb97xd/cc-pVDZ level

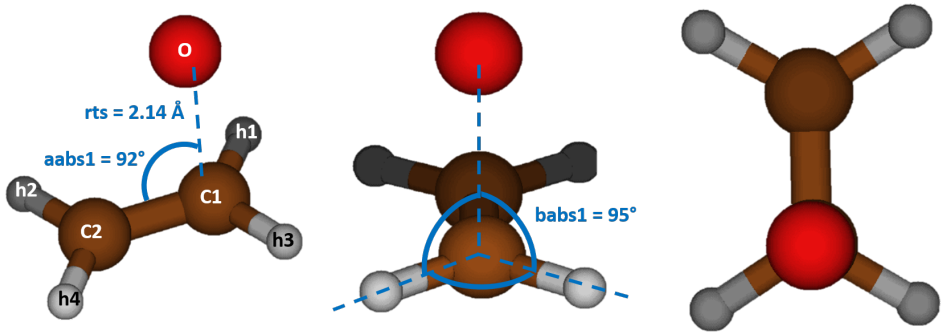

FIGURE 3.2: Different perspectives of the TS for the addition reaction with indications of the relevant internal coordinates

At this point, level1 computations at CASPT2 require the selection of an active space. The active space was selected from the configuration of the transition state, as it must include all the orbitals and electrons relevant to the bond formation and cleavage. A sketch of the electrons involved is shown in Figure 3.3: the electrons strictly required in the AS are those of the C1-C2 *pi* bond, which is being cleaved, and the unpaired electron of O forming the C1-O bond. The second unpaired electron of O must be

included because it is indistinguishable from the other, and it determines the existence of two different electronic states, as it may be either parallel or orthogonal to the O-C1-C2 plane. This also means that for an accurate representation of the electrons two states must be included in the CASSCF wavefunction, which will therefore be two-state averaged. Finally, the lone pair of oxygen should be included because of its interaction with the rest of the system. As far as the orbitals are concerned, it is clearly essential to include the C1-C2 *pi* orbital, its corresponding anti-bonding orbital, and the orbitals of the unpaired electrons and lone pair of oxygen. Hence, an active space with 6 electrons in 5 orbitals is required. The AS was selected gradually, using first (4e,4o) with cc-pVDZ, which captures the electrons of C1-C2 bonds and the lone pair of oxygen. The inclusion of the unpaired electron of O forming the bond was the last and most delicate step, as it also required the rotation between orbitals in the CASSCF calculations. The electron density obtained for such orbitals and the corresponding occupancy is shown in Figure 3.4. The C1-C2 bonding and anti-bonding orbitals are clearly 10.1 and 14.1, whereas the forming C1-O bond is partially captured in 13.1, whereas the other electrons of O(^{3}P) are in 11.1 and 12.1 with occupancy of 1.5 each. Hence, the lone pair and the unpaired electron of the initial O(^{3}P) configuration are now delocalized in these two orbitals, and this feature stems from the two-state averaging at CASSCF level. Finally, it is noted that despite in CASSCF two states were included, only the ground state was used for the calculation of energies and frequencies with RS2. Furthermore, to avoid state mixing, a shift of 0.2 was applied already at level1. The frequencies computed at this level are found in Table A.1.

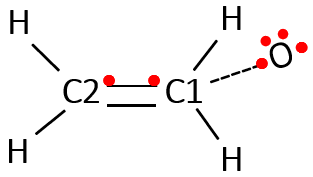

FIGURE 3.3: Sketch of the molecule with the forming C-O bond and the electrons involved in the reaction indicated in red

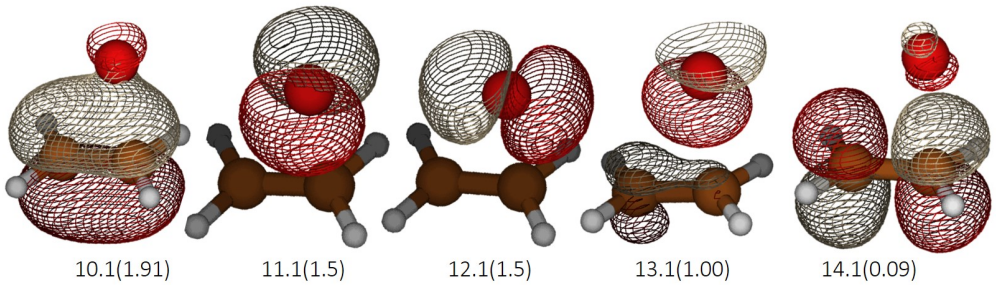

FIGURE 3.4: Electron density and orbital occupancy of the active space chosen for the TS of the addition

In order to treat the well at the same level of the TS, the same active space must be used, namely the same electrons must be included. The orbitals cannot be exactly the same, as once the C1-O bond is formed the electron density changes. Hence, the well optimization was done in the following way: first, CASSCF(6e,5o)/cc-pVDZ calculations were performed on the optimized structure of the TS; then, the structure of the well optimized at level0 was selected, and geometry optimization was done at CASPT2(6e,5o)/cc-pVDZ, using as a guess the orbitals of the TS just saved. In this way, the correct active space was retained. Finally, the level1 optimization was conducted and frequencies were computed. The resulting properties are in Table A.1, and the active space obtained is shown in Figure 3.5. In this case, the C1-O bonding and anti-bonding correspond to orbitals 10.1 and 14.1, whereas the unpaired electron of C2 is in orbital 13.1. The three remaining electrons of O are in orbitals 11.1 and 12.1, both with occupancy of 1.5.

As regards the reactant, the structure of ethylene was clearly optimized separately from that of $O(^3P)$ with DFT. However with CASSCF the reactants must be considered as a single entity, such that the same active space of the TS is used. Hence, a guess for the orbitals was generated from the structure of the TS as in the previous case; then, the distance C1-O was fixed to 10Å, and a CASPT2(6e,5o) optimization was launched. However, the number of states considered in the CASSCF averaging was increased to three, so as to account properly for the electronic states of $O(^3P)$. This level of optimization is to be considered useful only as a basis for energy calculations. In fact, the vibrational frequencies of the set thus obtained lose their meaning, as it becomes apparent from their values in Table A.1.

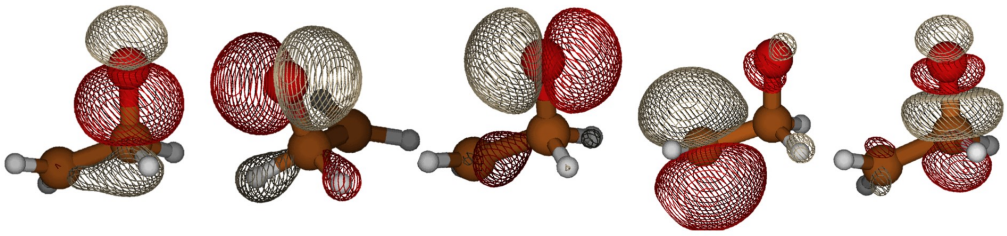

FIGURE 3.5: Electron density and orbital occupancy for the well of the addition

In this reaction, hindered rotors were not included. In fact, the lowest vibrational frequency associated with the rotation of $(C1)H_2O$ moiety around C1-C2 bond is about 150 cm^{-1} at the TS, which is the limit for the inclusion of HRs. Furthermore, this operation proved particularly difficult due to the nature of the z-matrix defined, where oxygen was the last atom. For this reason, the z-matrix was redefined for the optimization of the well and the study of the following reaction pathways.

The last step before the master equation simulations for the kinetic constant was the calculation of high level energies. In case of DFT structures, this was done with

coupled cluster theory and the procedure of convergence to CBS, as explained in the method section 2.2. For CASPT2 instead, the active space was increased as much as possible keeping the basis set of aug-cc-pVTZ. An ideal complete active space would be made of 16 electrons in 15 orbitals: with respect to the 6 electrons of the AS at level1, it would include all the electrons of C-C σ orbital (2e,2o) and in C-H σ orbitals (8e,8o). However, only the C-C σ orbital was introduced at high level. In fact, further increasing of the AS only led to the selection of Rydberg excited state (Figure 3.6), which is an excited state of oxygen only and it is not representative of the reactivity of the system under study. Hence, for the calculation of the high level energies, a CASPT2(8e,7o)/aug-cc-pVTZ was used. The same space was adopted for both the product and the reactant, and in the latter three states were used, as in the calculations at level1.

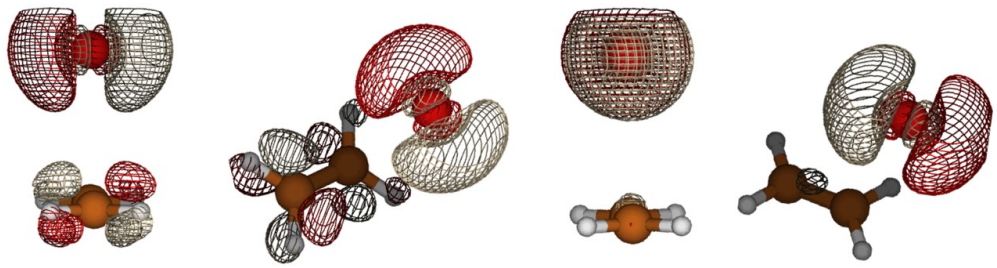

FIGURE 3.6: Rydberg orbital on the TS

The energies obtained at high level are shown in Table 3.1. The reactants are indicated as "reac1" and "reac2" because the former includes also CASPT2 calculations done for the reactants considered together at a distance of 9 Å. The hl CASPT2 calculations were done with MOLPRO using the commands indicated in the table, namely RS2, shift=0.2 and IPEA=0.25. These refer to the theories used and explained in the methods section 2.1.4. As far as the forward energy barrier is concerned, it is possible to compute it in two ways. In fact, the activation energy can be computed directly as the difference between the enthalpy of the transition state and that of the reactants as

$$E_{A,FW} = (H_{TS})_{CASPT2} - (E_{reac1})_{CASPT2} - (ZPE_{reac1} + ZPE_{reac2})_{CC} \qquad (3.1)$$

Alternatively, $E_{A,FW}$ can be computed indirectly from the backward energy barrier. In order to do this, the backward barrier $E_{A,BW}$ was computed at CASPT2 level as in equation (3.2) and the reaction enthalpy ΔH_{CC} was calculated at coupled cluster level as in equation (3.3). Finally, $E_{A,FW}$ was obtained adding ΔH_{CC} to $E_{A,BW}$ as in equation (3.4).

$$E_{A,BW} = (H_{TS})_{CASPT2} - (E_{well})_{CASPT2} - (ZPE_{well})_{CC} \qquad (3.2)$$

$$\Delta H_{CC} = (H_{well} - H_{reac1} - H_{reac2})_{CC} \tag{3.3}$$

$$E_{A,FW} = E_{A,BW} + \Delta H_{CC} \tag{3.4}$$

In all cases, a correction factor of -0.22 kcal mol^{-1} was applied to the reactants in order to account for the stabilization of atomic oxygen due to spin-orbit coupling effects. The activation energies thus obtained are listed in Table 3.2. The values have an estimated uncertainty of about 1 kcal mol^{-1}, which is significant in the case of the forward barrier: for instance, the value of the kinetic constant at 300 K computed using rs2c is 5 times higher than k_{add} computed with an IPEA shift of 0.25. It is noted that values obtained using IPEA shift differ the most with respect to the other ones, and also among themselves, and were therefore not considered. The $E_{A,FW}$ obtained with the first direct method is close to the values reported in Nguyen et al [37], where the resulting addition rate constant is in very good agreement with experimental values. The barriers computed with the second method instead are similar to those of Li et al of $E_{A,FW} = 1.5$ and $E_{A,BW} = 25.3$ kcal mol^{-1}. However, in their work it is explicitly declared that the resulting barrier led to an underestimation of the addition rate constant by 50 %, and therefore the properties of the TS were adjusted to fit the recommended values. Hence, in this work the barriers obtained with rs2c and method 1 were used, and are reported in Table 3.1. In this table, also the values for the activation energies computed with a full coupled cluster treatment are shown. The resulting E_{A,FW_CC} is more than 0.6 kcal mol^{-1} higher than the barrier at CASPT2, and the resulting k_{add} is therefore expected to be about 3 times lower at room temperature. Finally, it must be mentioned that, as opposed to the reference theoretical works [10, 37], the contribution of the excited state was not included in the computations, and this may lead to an underestimation of the kinetic constant at high temperatures. Furthermore, also the extraction channel on the triplet PES forming $C_2H_3 + OH$ was neglected. In any case, the final addition rate constant does not affect the product branching ratios, which are the actual target, and a perfect reproduction of experimental data or recommended values is beyond the scope of this work.

Table 3.1: High level energies for the addition step

High level energies (Hartree)						
	RS2	**shift=0.2**	**IPEA=0.25**	**CC**	**ZPE$_{CC}$**	**ZPE$_{CASPT2}$**
reac1	-153.3765	-153.3748	-153.3701	-78.4667	0.0513	0.0509
reac2				-74.9964	0.0000	
TS	-153.3751	-153.3732	-153.3671	-153.4612	0.0520	0.0515
well	-153.4151	-153.4132	-153.4062	-153.5009	0.0512	0.0522
final energies						
	ΔE$_{CC}$	**ΔH$_{CC}$**	**E$_{A,FW}$**	**E$_{A,FW_CC}$**	**E$_{A,BW}$**	**E$_{A,BW_CC}$**
(Hartree)	-0.0374	-0.0375	0.0020	0.0030	0.0395	0.0405
(kcal mol^{-1})	-23.49	-23.53	1.25	1.87	24.78	25.40

TABLE 3.2: Activation energies of the addition step computed with different methods

method 1	**rs2c**	**shift=0.2**	**IPEA=0.25**
$E_{A,FW}$	1.25	1.38	2.28
$E_{A,BW}$	24.78	24.92	25.81
method 2	**rs2c**	**shift=0.2**	**IPEA=0.25**
$E_{A,FW}$	1.76	1.78	1.17
$E_{A,BW}$	25.30	25.31	24.70

At this point, MESS simulations were launched and the kinetic constants in the selected range of T and P were computed. Two different simulations were performed: a first one without any variational treatment, which included the reactant properties at DFT level, the TS and product properties at CASPT2 level, and the $E_{A,FW}$ and $E_{A,BW}$ of Table 3.1; a second simulation instead was conducted with VTST-MESS, and all the input properties were at DFT level, and energies at CC level. The temperature range was $300 \div 2500$ K with a step size of 100 K. The high pressure kinetic constants are in Appendix B in Table B.1, whereas the properties along the variational selected path are in Table A.6 of Appendix A.

The plot of the kinetic constants in comparison with experiments and recommended values is shown in Figure 3.7. The experimental data were taken from Khaled et al [68], whereas the recommended values for the kinetic constant were more recently listed by Baulch et al [42]. The kinetic constant computed at CASPT2 is in good agreement with both experiments and recommended values, especially in the range of combustion temperatures of interest. There seems to be only a slight underestimation of the kinetic constant above 1500 K, for the reasons explained above. As regards the variational computations, the resulting k_{add} is 3 times smaller at room temperature and 2 times smaller in the high temperature range, due to both the higher barrier and the variational effects. A correction factor based on the activation energy difference with respect to Nguyen et al [37] may be applied at every temperature as

$$corr_{E_A} = \exp\left(-\frac{E_{A,REF} - E_{A,FW\_CC}}{RT}\right) \tag{3.5}$$

where R is the universal gas constant, $E_{A,REF}$ is 1.3 kcal mol^{-1}. This correction yields values which are almost superimposed to the experimental ones in the $300 \div 1500$ K range. At higher temperatures k_{add} has a larger difference with respect to Baulch et al which however is always below a factor of 1.6. As a conclusion, considering either the CASPT2 computations or the variational ones with the appropriate corrections, k_{add} differ from the recommended values by a factor of at most 1.25 or 1.64, respectively.

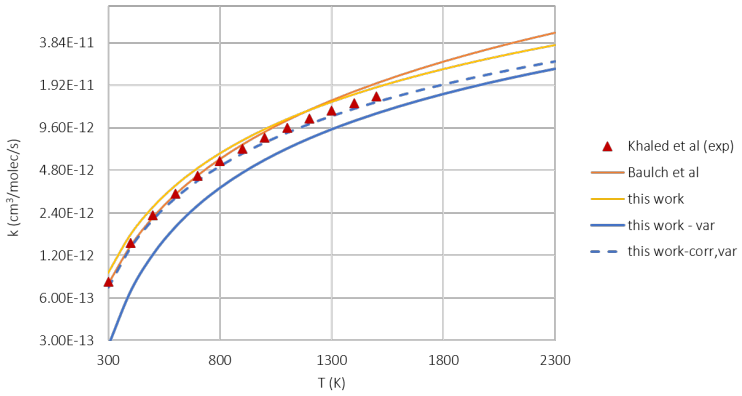

FIGURE 3.7: High P limit kinetic constant for the addition reaction in comparison with theoretical and experimental benchmark data

3.1.2 H elimination

For the study of the pathways following the formation of the initial well, the z-matrix was redefined so as to make the treatment of the hindered rotors easier. Hence, the oxygen was set as the third atom in the z-matrix, also following the convention according to which the heavier atoms are introduced first. The structure was optimized at DFT level simply setting as a guess the optimized well from the addition reaction, and then changing the z-matrix. The structure thus obtained was also considered as a guess for the optimization of the reactant at CASPT2 level. The procedure followed was similar to that adopted for the addition reaction, using both CCSD(T)/CBS//ωb97xd-mo62x/aug-cc-pVTZ and CASPT2(10e,9o)/aug-cc-pVTZ//CASPT2(4e,4o)/aug-cc-pVTZ for variational and conventional calculations, respectively. VTST aimed at capturing the barrierless character of the cleavage of C1-H1 σ bond. DFT calculations were performed with both ωb97xd and m062x basis sets, however only the former are reported here, as the energies, frequencies and kinetic constants obtained show only negligible changes. No particular criticality was encountered in DFT calculations, hence only those performed at CASPT2 level are treated in detail in this section.

The reaction considered is the elimination of a hydrogen from the (C1)H_2O group: this elimination reaction proceeds via the homolytic cleavage of C1-H1 σ bond, leaving on (C2)H_2(C1)HO three unpaired electrons, on C2, C1 and O. These will form a π bond on either C1-C2 or C1-O. Most likely, this will result in a delocalized π bond on the C2-C1-O group rather than a localized one. The interaction among these electrons will lower the product energy, such that the reaction will not be barrierless. The level0 optimization was performed at ωb97xd/6-311+g(d,p). After the optimization of the reactant and the products H and CH_2CHO, the TS structure was searched by a constrained optimization along C1-H distance. The resulting TS structure is shown in Figure 3.8: the C1-H1 distance is about 1.7 Å, highlighting a tighter TS compared to the addition reaction. It might be guessed that the variational effects in this case will be less evident than in the previous channel.

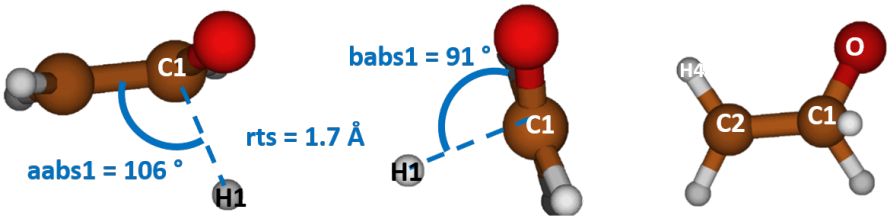

FIGURE 3.8: Structure of the TS for the H elimination step

For optimization at level 1, the AS must be chosen starting from the structure of the TS. The electrons to be included are highlighted in Figure 3.9: clearly, the electrons involved in C1-H1 scission must be considered, together with the unpaired electrons on C2 and O which form the delocalized π bond. The orbitals included will therefore be C1-H1 σ bonding and antibonding, and a delocalized π C2-C1-O bonding and antibonding, for a total of four. In this case, the lone pair of O was not included in the AS, because it is not relevant to the study of the reaction, and Rydberg orbital were selected when it was tried to do so. In this case, there was no state-averaging in CASSCF. In fact, the state averaging was related to the symmetry of the configuration of the TS for the addition, which is lost in the well and is therefore inconsistent with the physics of this reaction. The AS was increased gradually, first including the electrons of the breaking bond, then the unpaired ones, using CASSCF(2e,2o)/cc-pVDZ and CASSCF(4e,4o)/cc-pVDZ, then including perturbations and optimizing the structure at CASPT2(4e,4o)/cc-pVDZ; the final geometry and frequencies were computed upon increasing the basis set to aug-cc-pVTZ. The electron density and the occupancies of these orbitals are in Figure 3.10. Orbitals 11.1-14.1 clearly show the delocalization of the unpaired electrons and some density of the breaking C1-H1 σ bond. Orbitals 12.1 and 13.1 are characterized by a prevailing contribution from the unpaired electron on C2 and from the radical on H1. Once the AS was selected, both the reactant (the well) and the products were optimized at the same level. As in the case of the addition step, the correct guess for the orbitals was set on the optimized TS geometry, which was then updated to that of the well or the products with frozen C1-H1 distance of 9 Å. The final geometry optimization was then performed. The results of energies and frequencies obtained are listed in Table A.2 in Appendix A.

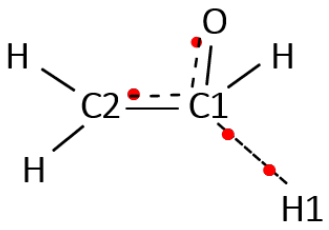

FIGURE 3.9: Sketch of the molecule with the cleaving C1-H1 bond and electrons involved in the reaction in red

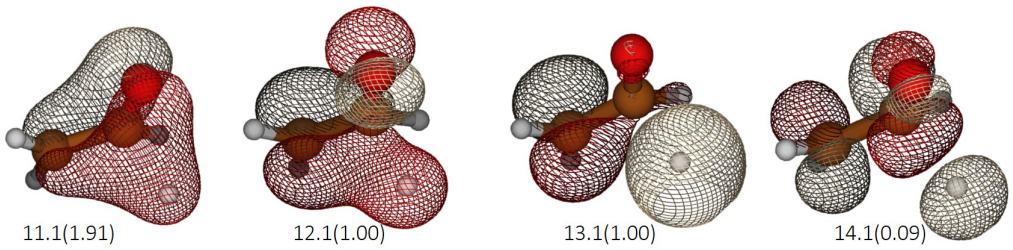

FIGURE 3.10: Electron density and orbital occupancy for the TS of the H elimination

Once level1 optimization was completed, hindered rotors were considered. In the well, only the frequency associated with the rotation around C1-C2 bond is below 150 cm^{-1}. This was therefore treated as 1DHR, and the PES for the rotation was computed at CASPT2(4e,4o)/cc-pVDZ at steps of 15°. The PES obtained for the well is shown in Figure 3.11a): the potential has a periodicity of 2, hence only the range $0 \div 180°$ is shown in the plot. Also the main configurations are superimposed on the plot: the two maxima correspond to symmetric configurations where CH_2 is either parallel or perpendicular to C1-O bond, whereas the minima are characterized by an alignment between one H of CH_2 with one of CH_2O. The PES obtained for the TS is instead shown in Figure 3.11b): the HR has again a periodicity of 2, as expected. However, it is clear that the potential barrier is not the one typical of a low barrier torsional motion, as it is as high as 10 kcal mol^{-1}. In fact, the vibrational frequency associated to this motion is about 400 cm^{-1}. Hence, no HRs were included in the TS. This also highlights how the TS is not particularly loose.

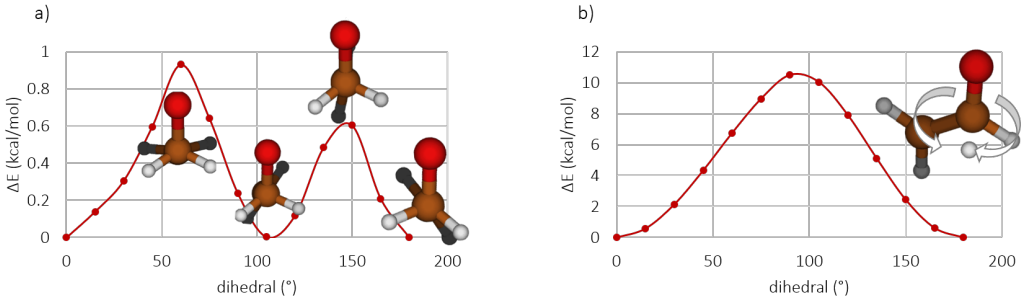

FIGURE 3.11: MEP of the 1DHR of the reactant (the well) a) and of the TS b)

Eventually, high level energies were computed. For CASPT2 calculations, the active space was increased as much as possible. The first bonds to be included at high level were the C1-C2 σ and σ*. At this point, the inclusion of the lone pair on oxygen required two-state averaging, which also changed the occupancy of the orbitals considered thus far. A gradual increase of the AS followed by second order perturbation calculations allowed to select 10 electrons in 9 orbitals, as shown in Figure

3.12, where bonding and anti-bonding orbitals are aligned vertically. It is evident how the AS of level1 is maintained, however a higher occupancy of orbital 12.1 is observed, due to a partial contribution from the oxygen lone pair, mostly contained in orbital 11.1. Orbitals 8.1-16.1 and 9.1-15.1 correspond instead to the C1-C2 and C1-O σ bonding and antibonding, respectively. The hl energies for the well and the products at fixed distance were computed using the AS of the TS: the AS was fully increased to CASSCF(10e,9o)/aug-cc-pVTZ on the TS structure, then the geometry was updated and perturbation theory applied. In all cases, also shifts were included.

The results are in Table 3.3. "prod2" is the H radical, whereas "prod1" indicates either CH_2CHO at CC or the two products together considered at a fixed distance of 9 Å for CASPT2 calculations. For the calculation of the energy barriers, $E_{A,FW}$ was computed directly as in equation (3.1): since ZPE_{CASPT2} for prod1 is meaningless, in this case $E_{A,FW}$ using the energies of IPEA=0.25, and ZPE_{CASPT2} for the TS, ZPE_{CC} for the reactant, which provided close values to those of Li et al [10]. The backward barrier was instead computed as $E_{A,BW} = E_{A,FW} - \Delta H_{CC}$. It is noted that all the barriers are extremely sensitive to the level of theory used, with an estimated uncertainty of 1 kcal mol^{-1}, which impacts the kinetic constant.

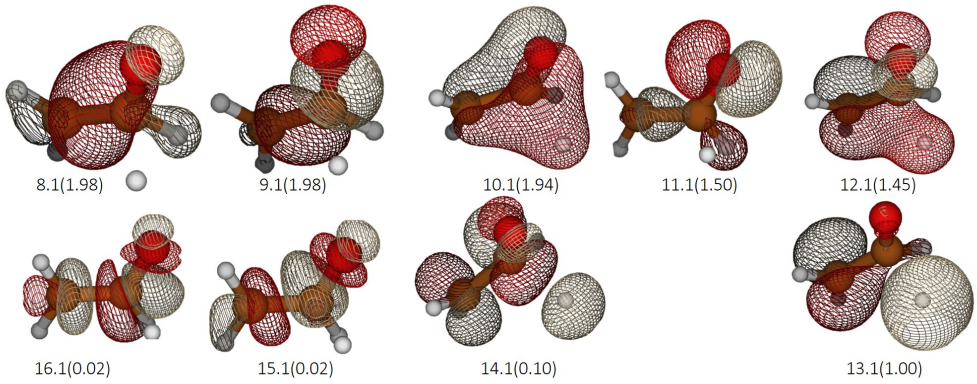

FIGURE 3.12: Electron density and orbital occupancy at high level for the TS of H elimination at CASPT2(10e,9o)/aug-cc-pVTZ

TABLE 3.3: High level energies for the H elimination step

high level energies (Hartree)						
	RS2	**shift=0.2**	**IPEA=0.25**	**CC**	**ZPE_{CC}**	**ZPE_{CASPT2}**
well	-153.4183	-153.4166	-153.4090	-153.5009	0.0513	0.0519
TS	-153.3862	-153.3843	-153.3780	-153.4691	0.0448	0.0455
prod1	-153.3960	-153.3943	-153.3896	-152.9792	0.0428	0.0431
prod2				-0.4999	0.0000	
Final energies						
	ΔE_{CC}	**ΔH_{CC}**	**$E_{A,FW}$**	**E_{A,FW_CC}**	**$E_{A,BW}$**	**E_{A,BW_CC}**
(Hartree)	0.0217	0.0131	0.0252	0.0253	0.0121	0.0121
(kcal/mol)	13.63	8.24	15.81	15.86	7.58	7.61

Kinetic constants were determined at two different levels of theory: conventional

TST was implemented using CASPT2(4e,4o)/aug-cc-pVTZ for the geometries and frequencies of reactant and TS, ωb97xd/aug-cc-pVTZ for the product, and the $E_{A,FW}$ and $E_{A,BW}$ of Table 3.3; a full coupled cluster treatment with DFT structures was instead used for variational calculations. The results of $k|_{T,P}$ in the $300 \div 2500$ temperature range at 1, 10, 100, 1000 and 10000 bar are listed in Tables B.2 and B.3 of Appendix B, whereas the properties along internal reaction coordinate for the variational path are found in Table A.7 of Appendix A. The plot of the conventional $k|_{T,P}$ and the comparison with its variational counterpart are shown in Figure 3.13 a) and b), respectively. It is evident that including P dependence is necessary, as at low pressure the kinetic constant at intermediate and high temperatures may be smaller by orders of magnitude. Concerning the ratio between variational and conventional rate constants, the scaling factor is not as low as in the addition step, as expected. The effect is stronger as temperature and pressure increase, and the lowest value is about 0.8. In fact, by looking at the TST kinetic constant of equation (2.38), it is apparent that at high T the rate constant increases due to the increase of both the activation energy exponential and of $Q_{\neq}^{vib_0^*}$. However, in VTST the kinetic constant is governed by the competition between E_A and ν varying along the reaction coordinate: at high T, the increase in E_A is smoothened in the exponential due to the high T, therefore its effect of decrease in the kinetic constant is less pronounced, and its minimum is found at smaller distances. This clearly is also valid for the variation of ν, however its variation along the reaction coordinate is smaller than that of E_A. A quantification of this is found by looking at the properties of the molecule as it evolves along λ in Table A.7. The TS is anyway tighter than in the addition step, as the vibrational motion of C1-H1 has a high vibrational frequency, and this is also mirrored in the high magnitude of the imaginary frequency at the TS (about 970 cm^{-1}). These kinetic constants were not used directly in the KMC-ME simulations, however the ratio between the variational and conventional ones was taken as a scale factor for the H elimination pathway at different temperatures.

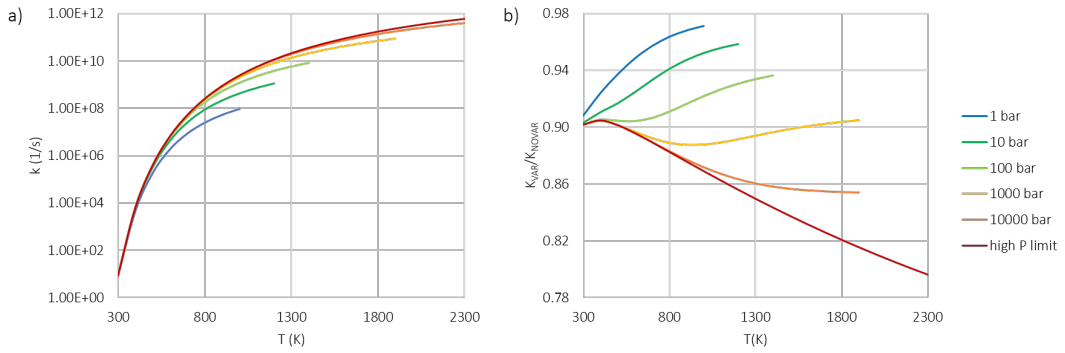

FIGURE 3.13: $k(T)$ at different pressures a) and ratio between $k(T)$ variational and non variational b)

3.1.3 CH_2O elimination

The other main reaction pathway considered on the triplet energy surface was the formation of formaldehyde. The approach adopted for the study of this reaction was the same as that of H elimination, therefore only the critical points are considered here, in particular concerning the treatment of the active space. The reaction considered is the homolytic cleavage of C1-C2 bond, which results in the formation of formaldehyde and the triplet CH_2 diradical. Upon rupture, the electron on C1 forms a π C1-O bond, whereas the electron on C2 is left unpaired. Hence, the reaction is not barrierless, as in the previous case. The level0 optimization was performed at ωb97xd/6-311+g(d,p). After the optimization of the reactant and the products CH_2 and CH_2O, the TS structure was searched by a constrained optimization along C1-C2 distance. The obtained MEP and TS structure are shown in Figure 3.14: the C1-C2 distance is about 2.2 Å, which is a looser configuration than for H elimination. Hence, variational effects will probably be more enhanced, also in light of the looser internal torsion around the breaking bond.

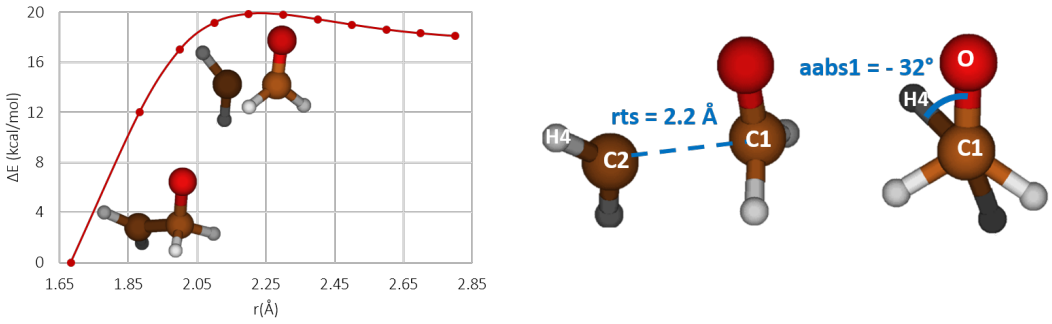

FIGURE 3.14: Structure of the TS for the CH_2O elimination step

For the level1 optimization, the AS was again chosen so as to capture the reactivity of the TS structure. As in the H elimination step, no state averaging was considered, and the lone pair on O was not included in the AS due to the interference of Rydberg states. In Figure 3.15, the electrons participating to the reaction are highlighted in red, namely those of the C1-C2 σ breaking bond, the unpaired electron on C2, and the unpaired electron on O forming a π bond upon scission. The orbitals will certainly include C2 unpaired electron, and the other orbitals may have a prevailing contribution of either C1-C2 σ bond and anti-bond and the unpaired electron on O, or of C1-O forming σ bond and anti-bond and another unpaired electron on C2. The latter configuration was found, as expected from the looseness of the TS, and the resulting electron density is shown in Figure 3.16. The calculations were done directly at CASSCF(4e,4o)/cc-pVDZ, then the basis was improved to aug-cc-pVTZ and perturbations were included, thus optimizing the structure at CASPT2(4e,4o)/aug-cc-pVTZ. Also in this case, no state averaging was used at level1 optimization. By looking at the electron density, it is clear that the couple of orbitals 11.1-14.1 is characterized by the major contribution of C1-O forming σ bond, whereas 12.1 and 13.1

are orbitals of the unpaired electrons on C2, with occupancy of 1.00 each. After the selection of the appropriate AS, the reactant and product were optimized at the same level, with the steps explained in the previous section. The energies (at high level) and frequencies obtained are listed in Table A.3 in Appendix A. It is noted that magnitude of the imaginary frequency of the TS is about 320 cm^{-1}, similarly to the addition step. This is a clear indication of the looseness of the TS with respect to the H elimination pathway.

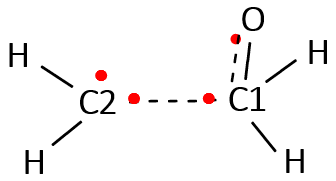

FIGURE 3.15: Sketch of the molecule with the cleaving C1-C2 bond and electrons involved in the reaction in red

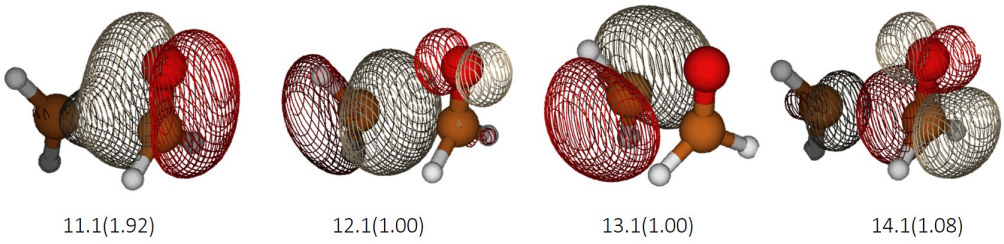

FIGURE 3.16: Electron density and orbital occupancy for the TS of the CH_2O elimination

Once level1 optimization was completed, hindered rotors were considered. With the AS used, the vibrational frequency for the internal torsion around C1-C2 bond of the well is about 180 cm^{-1} (as in A.3 in Appendix A), higher than what previously found; however, this was treated as 1DHR using CASPT2(4e,4o)/cc-pVDZ and the resulting potential has the same shape of the one shown in Figure 3.11a), with the highest peak lower by 0.1 kcal mol^{-1}. What really differs is the hindered torsion of the TS, which has an extremely low vibrational frequency of 87 cm^{-1}. The PES obtained at CASPT2(4e,4o)/cc-pVDZ for this rotation is shown in Figure 3.17, together with the configurations found at the maxima and minima: the shape of the potential is the same as in the well, however the barrier is reduced by roughly half, therefore in this case the inclusion of 1DHR in the rovibrational partition function is strictly necessary. The effect of this on the determination of the kinetic constant was already discussed in the method section 2.3.3. It is also noted that the structures of the two minima are optical isomers, therefore this shall be considered in the computation of the rate constant (as explained in Appendix E).

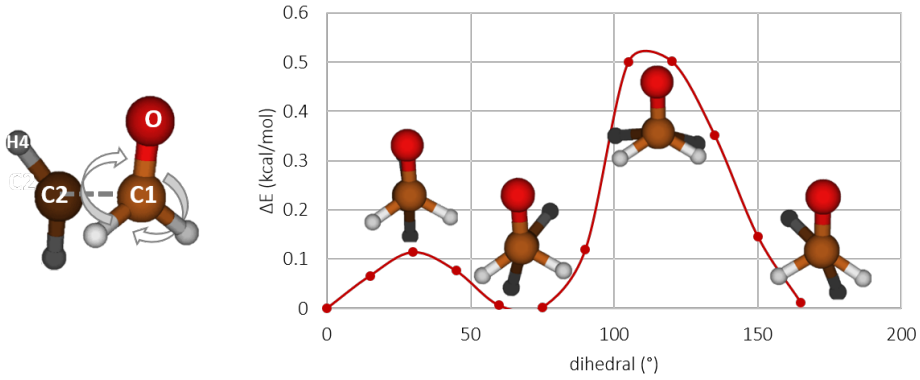

FIGURE 3.17: MEP of the 1DHR of the TS of CH_2O elimination

The reaction considered proved particularly challenging for the determination of high level energies at CASPT2 level. In fact, orbital mixing effects were frequent, and the electron density was particularly sensitive to the basis set used. Hence, the AS was fully selected using cc-pVDZ, and then the basis was increased to aug-cc-pVTZ. In this case, no state averaging was used, and the lone pair was not included. With several orbital rotations and freezings, a CASPT2(10e,10o)/aug-cc-pVTZ was obtained, as shown in Figure 3.18. C1-O σ and σ* orbitals 10.1-15.1 are contaminated with some C1-H σ bonding orbital, and the C-H σ and σ* orbitals are 8.1-16.1 and 9.1-17.1. Apart from the AS presented here, two other cases were considered, fully described in Appendix C. In particular, another possible active space of the same size includes the C-H σ and σ* bonding and anti-bonding orbitals of CH_2, resulting in similar energies. When instead two-state averaging was considered, an AS of 12 electrons in 11 orbitals was obtained. In this section, only the first AS is discussed, since it was the one actually used for the computation of the energy barriers. The hl energy for the well was computed from the TS structure, as explained in the previous section.

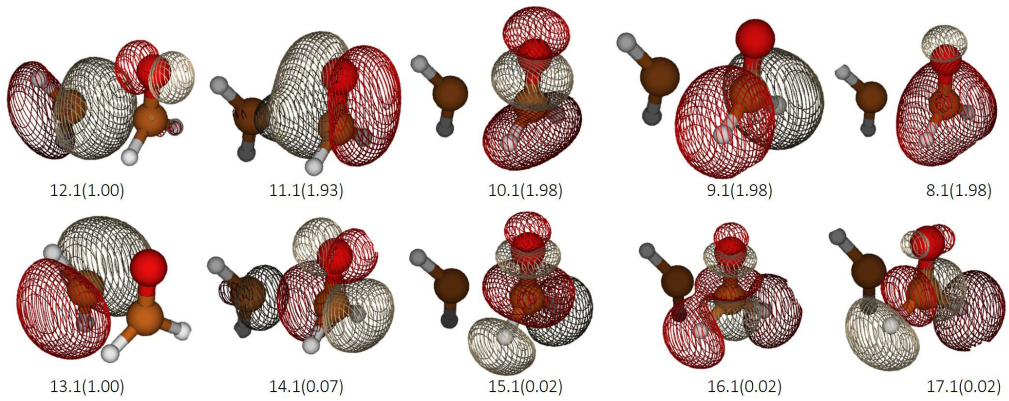

FIGURE 3.18: Electron density and orbital occupancy at high level for the TS of CH_2O elimination at CASPT2(10e,10o)/aug-cc-pVTZ

The results obtained for the hl energies are reported in Table 3.4. "prod1" is CH_2O and "prod2" is CH_2. $E_{A,FW}$ was calculated at CASPT2 level using an IPEA shift of 0.25. The backward barrier was instead computed as $E_{A,BW} = E_{A,FW} - \Delta H_{CC}$. It is noted that the barriers obtained differ by about 0.5 kcal mol^{-1} from those at CC level, possibly due to the different treatment of the TS. There is anyway an agreement within 0.5 kcal mol^{-1} with the energies by Li et al [10].

TABLE 3.4: High level energies for the CH_2O elimination step

high level energies (Hartree)						
	RS2	**shift=0.2**	**IPEA=0.25**	**CC**	**ZPE_{CC}**	**ZPE_{CASPT2}**
well	-153.4319	-153.4206	-153.4144	-153.5009	0.0513	0.0521
TS	-153.3897	-153.3786	-153.3722	-153.4598	0.0469	0.0474
prod1				-114.3750	0.0268	
prod2				-39.0895	0.0172	
Final energies						
	ΔE_{CC}	**ΔH_{CC}**	**$E_{A,FW}$**	**E_{A,FW_CC}**	**$E_{A,BW}$**	**E_{A,BW_CC}**
(Hartree)	0.0364	0.0291	0.0374	0.0366	0.0083	0.0075
(kcal/mol)	22.86	18.26	23.45	22.98	5.20	4.73

MESS simulations were performed in the same way as H elimination. The results of $k|_{T,P}$ are listed in Tables B.4 and B.5 of Appendix B, whereas the properties along internal reaction coordinate for the variational path are found in Table A.8 pf Appendix A. The plot of the conventional $k|_{T,P}$ and the ratio with its variational counterpart are shown in Figure 3.19 a) and b), respectively. Compared to the rate constant computed for H elimination, in formaldehyde formation there is higher sensitivity to both temperature and pressure. In particular, at low temperature k_{CH_2O} is several orders of magnitude smaller than k_H due to the activation energy, which is almost 10 kcal mol^{-1} higher than in the previous channel, whereas at high temperature it even overcomes k_H. It is therefore expected that in the KMC-ME simulations the relative importance of these channels in the BRs will switch at high temperature. Furthermore, at intermediate temperatures the difference between the low and high P rate constants is as high as two orders of magnitude. Concerning the ratio between the variational and conventional rate constants, a lower scaling factor was obtained compared to the H elimination step, especially at the high P limit where the variational rate constant may be 0.66 times lower than its conventional counterpart. This is due to the effect of the higher E_A and looser path with lower associated vibrational frequency $\nu^{\neq}$, which therefore prevails faster than E_A along the reaction coordinate at higher temperature, as explained in the previous section. A quantification of this is found by looking at the properties of the molecule along the reaction coordinate λ (namely C1-C2 distance) in Table A.8 of Appendix A. As in the case of H elimination, these kinetic constants were not used directly in the multi-well KMC-ME simulations, however the ratio between the variational and the conventional rate constants was taken as a scale factor for the treatment of this pathway at different temperatures.

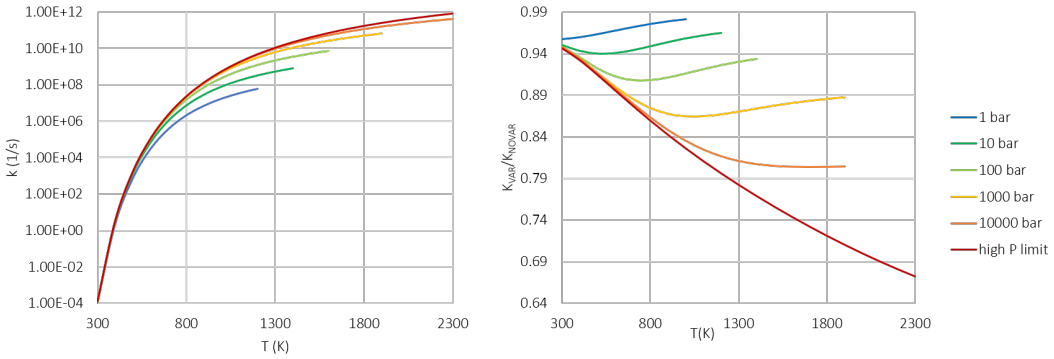

FIGURE 3.19: $k(T)$ at different pressures a) and ratio between $k(T)$ variational and non variational b)

3.1.4 Intersystem Crossing

The last reaction pathway analyzed on the triplet PES was intersystem crossing. The starting point was the optimized configuration of the well considered as the reactant, in the same way as the previous reaction channels. However, in this case geometries and frequencies for the ISC point were directly optimized with the final active space, and no high level energy calculations were performed. Therefore, also the energy barriers were computed with respect to the level1 well energy. The active space used for the search of ISC point was the same of the addition, namely two-state averaged CASPT2(6e,5o)/aug-cc-pVTZ as done by Cavallotti et al [8, 16]. The state averaging was included not only for consistency with the previous calculations, but also because it is expected that the MECP point is characterized by a symmetric structure, as in the case of propylene and 1-butene, as further discussed in section 3.3.1. Furthermore, the inclusion of the two states was necessary for the computation of the geometries and energies of the excited states S1 and T2. In every calculation, the addition TS structure was set as a guess and the AS selected at CASSCF(6e,5o)/aug-cc-pVTZ; then, the structure was updated to that of the optimized well, and various constrained geometry optimizations were conducted at CASPT2(6e,5o)/aug-cc-pVTZ. The active space of the well was shown in Figure 3.5 of section 3.1.1, whereas the same AS applied to the MECP structure found is shown in Figure 3.20 below for clarity. The orbitals 11.1 and 13.1, corresponding to unpaired electrons on O and a radical on CH_2, respectively, show different occupations depending on the state considered (1.59 and 0.91 are the occupations for the singlet state).

In Li et al [10], the search for the MECP proceeded via Harvey's hybrid optimization method at different levels: in fact, MECP points for the coupling of states S0/T1, S0/T2 and S1/T2 were found[1] and the final H_{SO} was computed as the average of the single $H_{SO,i}$ weighted on the state density at the respective energies. The total H_{SO} was 29 cm^{-1}, almost identical to the highest $H_{SO,i}$ of 30 cm^{-1} found for S1/T2. It is recalled that states T1/T2 indicate the ground and first excited triplet states,

[1]The MECP point corresponding to S1/T1 instead could not be located, and the same applies to the present work.

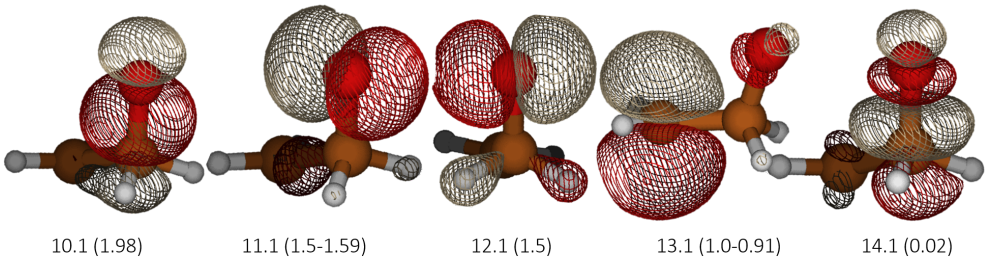

FIGURE 3.20: Orbital density used to find the MECP point

whereas S0/S1 indicate the ground and first excited singlet states. The denomination S0 and T1 refer to the fact that the singlet PES lie almost everywhere below the triplet one. In this work, it was tried to locate these three MECP points with a partial optimization method, proceeding via constrained scans of the PES starting from the well configuration as a function of the angle O-C1-C2 "aabs1" and the dihedral O-C1-C2-H2 "babs1". In fact, as explained in the methods, these coordinates are the most relevant for the change of the energy difference between the two states. A sketch of the physical reason of this is shown in Figure 3.21: the idea is that as O-C1-C2 angle decreases and O approaches C2, the interaction between the two unpaired electrons will favor a singlet state in which a C2-O bond is formed to give ethylene oxide. This interaction is strongest when the oxygen is aligned with C2, namely when the structure is symmetric and the dihedral is about 90°, whereas at the well babs1 = −40°. For all MECP points, the geometry optimization was conducted on the T1 PES, so as to be consistent with the physical motion of the molecule; some trials were also performed at S1 level, whereas no convergence was obtained at T2 level, probably due to the poor representation of this state with the AS used. After the geometry optimization, a CASPT2 calculation for the other states of interest was performed, and the corresponding energies saved. In this case, no hindered rotors were considered, since the dihedral torsion corresponds to the reaction coordinate. In the final KMC-ME simulations, only the S0/T1 intersection was included. Hence, in the following only a detailed presentation of the results for S0/T1 is given, whereas the S1/T2 and S0/T2 intersections are illustrated in Appendix D.

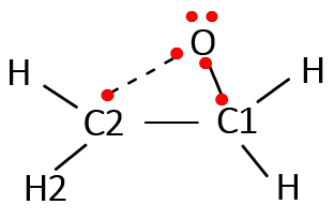

FIGURE 3.21: Sketch of the electrons included in the ISC active space as the geometry changes

The first step was the scan of the PES of T1 state around the well configuration. At the same geometry, also S0 energy was computed. As found from the dihedral scan on the well, the potential of the internal torsion has a periodicity of two; hence, babs1 was scanned in the range $0 \div 180°$ with steps of 10°. The angle aabs1 is about 113° in the optimized well structure, and a smaller value is expected for the MECP. The scan was thus performed in the $104 \div 115°$ range. Bigger values were also considered both for completeness and because at the beginning of the calculations also ISC points in that region were found. Values smaller than 104° were not scanned due to the prohibitive increase in energy. In fact, the O-C1-C2 bending motion is clearly characterized by higher energy barriers compared to the internal torsion, as also indicated by its higher vibrational frequency of about 430 cm^{-1}. The resulting two-dimensional PES is shown in Figure 3.22a), and the corresponding data are listed in Table D.3 and D.5 in Appendix D: S0 is in red, T1 in blue, and the circles indicate the points which were eventually considered as MECP. The projection of the difference between S0 and T1 energies in the shape of isoenergy lines is found in Figure 3.22b). The most evident feature of these two plots is the symmetry of the potential of both the singlet and triplet PES with respect to the central position of oxygen at about 90°. The intersection line between the two PES is extremely clear, and it is characterized by a decrease in the structure symmetry as the angle decreases. Despite the presence of intersection points at larger angles (114 and 115°), these were not analyzed further due to their higher energy, smaller SOC, and smaller extension of the crossing region. In is noted that, as anticipated in the methods, the intersection between S0 and T1 occurs in a certain region, not at a single point. However, for a consistent inclusion of ISC in TST and ME calculations, a single point must be selected. Hence, the points along the intersection line were analyzed further.

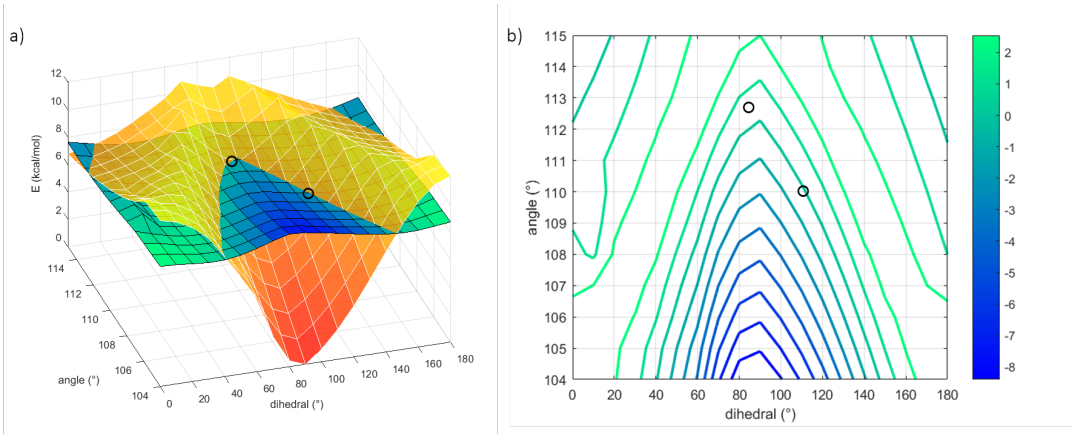

FIGURE 3.22: a) PES around MECP as a function of C2-C1-O angle and O-C1-C2-H2 dihedral (S0 in red and T1 in blue), b) Isoenergy level lines for (S0-T1) around MECP

In order to select the MECP, a more detailed scan was performed. First, the points of the intersection line were located with a precision of 0.1° and a difference in energy between the two states always smaller than 0.01 kcal mol^{-1}. The coordinates

(aabs1,babs1) of such points are in Table D.2 of Appendix D. Then, for each of these points, H_{SO} was computed as the average of the off-diagonal matrix elements of Breit-Pauli operator (obtained using MOLPRO), as explained in the method section 2.4.1. The resulting energy and H_{SO} are shown in Figure 3.23. It is evident that the point of minimum energy is not symmetric and does not correspond to the maximum coupling. As explained in the methods, the point of maximum H_{SO} was taken as the MECP, since it maximizes the hopping probability, it has a negative frequency and it also minimizes the enthalpy difference with respect to the well. As far as the other state couplings are concerned, these were found in the same way. However, for S0/T2 there was no significant difference in the H_{SO} in the crossing region, and the MECP was taken as the minimum of energy, either of T1, at which the geometry was optimized, or at the considered state. Both options were considered, although probably the former is more consistent with the physics of the problem. For S1/T2 instead, the H_{SO} varied a lot in the broad MECP region found, therefore also the point maximizing the coupling was considered. The properties found for all these points are listed in Table A.4.

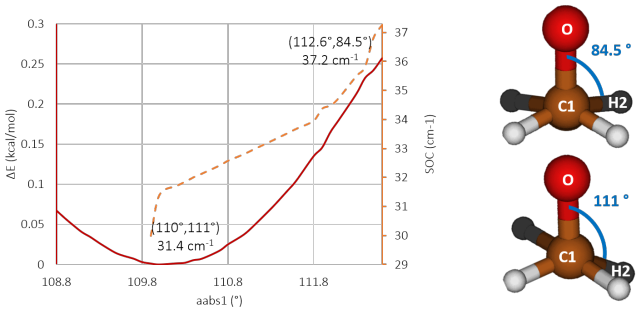

FIGURE 3.23: Energy and H_{SO} of the intersection points of S0/T1 and relative structures

A possible MEP with the corresponding reaction coordinate for ISC is shown in Figure 3.24, which zooms the two PES in the crossing region. A possible projection of the MEP on the (aabs1,babs1) plane as reaction coordinate λ is also shown. The MEP is characterized by a simultaneous change in the angle and the dihedral; the TS is located at a maximum of the T1 PES with respect to the dihedral angle, in fact the imaginary vibrational frequency found ($i273.73$ cm^{-1}) corresponds to its torsional motion. After crossing to the singlet surface, the MEP will proceed with a reduction of aabs1 only, towards the geometry of ethylene oxide (the product). Recalling Harvey's description of ISC, the black MEP is an adiabatic path, whereas the single S0 and T1 PES are the diabatic surfaces involved. For the calculation of the hopping probability, also the relative gradients at the MECP were needed. These were computed separately with a constrained optimization along each coordinate keeping the other one fixed to the value of MECP. The result is in Figure 3.25: the gradient of T1 is almost null, whereas that along S0 is higher, especially with respect to aabs1 variation.

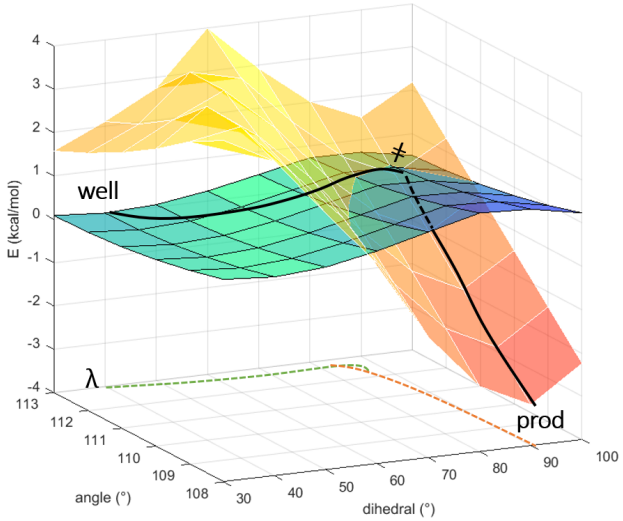

FIGURE 3.24: Representation of the MEP on the 2D PES for the S0/T1 crossing (well energy taken as reference)

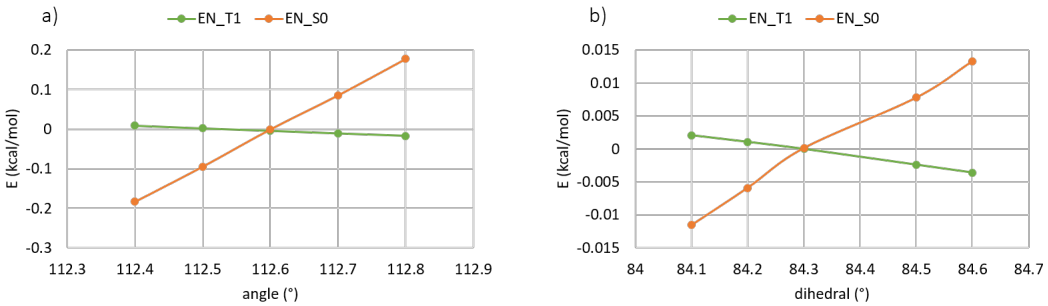

FIGURE 3.25: Energy gradients at the MECP for S0T1 with respect to angle aabs1 a) and dihedral babs1 b)

The results for all the MECP points found according to different methods and the relative energies with respect to the well are summarized in Table 3.5 and set in comparison with those of Li et al [10] in terms of both energy and H_{SO}. More details can be found in Table D.1 in Appendix D. It is noted that the geometries of minimum energy found for S1/T2 and S0/T2 coupling are extremely distorted, and in both cases one H of CH_2 moiety is almost aligned with O. The H_{SO} found for S0/T2 is comparable to that of S0/T1, however the corresponding energy barrier with respect to the well is almost 4 kcal mol^{-1}. The S1/T2 intersection maximizing H_{SO} is instead symmetric and the H_{SO} found is comparable to that of Li et al; nevertheless, the energy barrier with respect to the well is more than 1 kcal mol^{-1} higher. Overall, remarkable discrepancies are found with respect to the calculations presented here. According to their work, the MECP point for the ground state corresponds to the well structure, and the coupling found are extremely different, in particular because their coupling for S0/T2 is the lowest, whereas in this work it is the highest. This highlights the high sensitivity

of the computations performed to the level of theory and the method of MECP location. In Li et al, a recently introduced perturbation theory was used (QD-NEVPT2), and the MECP point was located using hybrid gradient method implemented in an open source code called NST (`http://tcg.cse.anl.gov/papr/codes/nst.html`). A comparison among MECP structures found with different methods is presented in section 3.3.1 of the discussion. As regards spin-orbit coupling, Li et al computed it with a software called ORCA at CASSCF level. As also stated in their work, the coupling parameter is a major source of a priori uncertainty, as it was found that H_{SO} was extremely sensitive to the geometry, contrary to what expected. In this work, the S0/T1 MECP point is the most consistent with what found in heavier systems, and its H_{SO} value is close to those indicated in literature. Hence, it was decided to use it as the only MECP for the following KMC-ME simulations. Furthermore, the interconversion from T2 to T1 is extremely fast, and this allows to neglect the contribution of T2 to the reactivity, as explained in the following paragraph.

Table 3.5: MECP points found for different couplings

aabs1 (∘)	**b1** (∘)	**states** -	**MECP** -	***i* freq** -	$\mathbf{\Delta H_{T1-well}}$ **(kcal/mol)**	$\mathbf{\Delta H_{well}}$ **(kcal/mol)**	$\mathbf{\Delta H_{well}}$[10] **(kcal/mol)**	$\mathbf{H_{SO}}$ $\mathbf{cm^{-1}}$	$\mathbf{H_{SO}}$[10] $\mathbf{cm^{-1}}$
112.6	84.5	S0/T1	max SOC	Y (babs1)	0.251	0.251	0	37.3	19.0
110	111	S0/T1	min S0/T1	N	0.449	0.449	0	31.4	19.0
108	81	S1/T2	max SOC	Y (babs1)	1.196	4.771	3.4	30.9	30.0
107.3	159.9	S1/T2	min S1/T2	N	0.658	4.421	3.4	5.4	30.0
113.4	143.2	S1/T2	min T1	N	-0.009	5.603	3.4	11.3	30.0
107	1.5	S0/T2	min S0/T2	Y (aabs1)	0.730	2.980	3.8	35.6	6.7
106	9.4	S0/T2	min T1	Y (aabs1)	0.822	3.768	3.8	37.9	6.7

Following the approach of Li et al, for the search of MECP also intersection points with states other than T1 were considered, in particular MECP points S1/T2 and S0/T2. In fact, the contribution from the excited state T2 may become relevant at high temperature, as it happens in the case of the addition step. A qualitative sketch of T2 and T1 MEPs including the entrance channel, ISC and H elimination channels is shown in Figure 3.26. On the excited triplet PES T2, the ISC with the high H_{SO} of S0/T2 or S1/T2 reported in Table 3.5 competes with H elimination, which is characterized by a higher energy barrier with respect to the T1 PES (as in Li et al [10]). Therefore, on this excited PES the relative contribution of ISC with respect H elimination will be higher than on T1 PES, and this may result in an overall higher branching ratio for ISC than the one computed in this work. Nevertheless, both pathways are also in competition with the well interconversion from T2 to T1, namely the non-radiative decay of the system to the lower triplet state T1. Hence, the contributions of H elimination and ISC on the T2 PES are relevant only if the interconversion is extremely slow, such that T2 well is long-lived. This happens when the difference in energy between T1 and T2 is high. Instead, in case an intersection point between T1 and T2 PES close to the well configuration exists, the interconversion may be fast and the contribution of the T2 PES to the reactivity negligible. Clearly, this would be the case only if this intersection point lied at an energy comparable to

that of T2 well. In order to investigate this, the T1/T2 intersection was searched, as described in section 2.4.1. The intersection point was found 2.7 kcal mol^{-1} above the well, which roughly corresponds to the T2 well energy. Therefore, interconversion from T2 to T1 is extremely fast. This means that the reactivity of the well is represented simply by the T1 PES, and this justifies the choice of considering only S0/T1 coupling for ISC and T1 reactivity for all the reaction pathways.

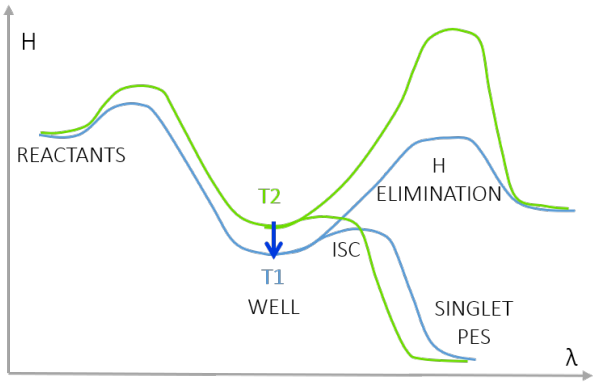

FIGURE 3.26: Sketch of a qualitative behavior of the MEP for addition, H elimination and ISC at T1 and T2

3.2 ME simulations and Branching Ratios

Once all the single reaction pathways were analyzed, the KMC-ME simulations were set, such that the kinetics on the multi-well PES could be derived. Setting the KMC-ME input is non-trivial and requires extreme attention. The first and probably most important point is setting the energies for transition states and products. These are listed in Table 3.6, where the the final enthalpies H are computed with respect to the reactant. H_{TS} is the enthalpy of the TS associated with the product in the table. It is noted that for ISC, no product was computed, and therefore the energy was set as that of the well. However, this does not affect the calculations. Furthermore, the TS enthalpy for ISC was computed with respect to the well at level1, as in Table 3.5. All the other barriers were instead taken as the $E_{A,FW}$ considered in the previous sections. The frequencies were taken at CASPT2 level with the active spaces used for each pathway, with the exception of the reactant, for which DFT frequencies were used. The full KMC-ME input is provided and explained in Appendix E.

TABLE 3.6: Energies used in KMC-ME simulations

SPECIES -	**E** (hartree)	**ZPE** (hartree)	**H** (hartree)	**H** (kcal/mol)	$\mathbf{E_A}$ (kcal/mol)	$\mathbf{H_{TS}}$ (kcal/mol)
C_2H_4+O(^{3}P)	-153.4631	0.0513	-153.4122	0.00		
WELL	-153.5009	0.0512	-153.4497	-23.53	1.76	1.76
ISC	-153.4131	0.0513	-153.3618	-23.53	0.25	-23.28
CH_2CHO+H	-153.4792	0.0428	-153.4364	-15.21	15.81	-7.72
CH_2O+CH_2	-153.4645	0.0440	-153.4205	-5.20	23.45	-0.08

The simulations were conducted at 0.0076 torr (1E-05 bar), such that the reaction conditions are comparable to the single collision conditions used in CMB experiments. Also other simulations at 1, 10, 30 and 100 bar were done. Anyway, the BRs change by maximum 15 % at 300 K. This is also pointed out by Li et al [10], who however do not say which is the pressure used in the laws presented. Hence, BRs at both 1E-05 and 100 bar are shown in comparison to theirs in Figure 3.27. The full set of data is reported in Appendix F in Table F.1 and F.2.

In the figure it is clear that the trends of each channel with temperature are well captured, and a perfect correspondence is not expected for both the intrinsic uncertainty of about ±10 % in the computations and for the differences in the methods used, further analyzed in the discussion. Anyway, the ISC channel at 100 bar shows a perfect overlap, whereas the slight mismatch of the elimination channels at high temperature might be due to the secondary channels (excited states and other pathways to the same products) which were not considered in this work. As expected, the importance of ISC decreases significantly with temperature, from about $60 \div 70$ % at room T to about $30 \div 20$ % already at 800 K, where the relative importance of the ISC and formaldehyde formation switch. As regards the H elimination channel, this shows a peak at about $55 \div 60$ % at 800 K, and then slightly decreases to less than 50 %. As anticipated in the previous sections, at high temperature the relative importance of H and CH_2O elimination channels switches.

In the figure, also data of kinetic experiments at 300 K and CMB experiments are plotted [29, 32, 44, 66]. A first comparison between *ab initio* calculations and experimental data was provided in Table 1.2 in the introduction. In the plot, it is evident that the trend of decreasing ISC and increasing formaldehyde formation at higher temperatures is captured. At 300 K, there is perfect correspondence with data of kinetic experiments. Nevertheless, at higher temperatures a strong discrepancy is observed: only formaldehyde channel is well represented by the BRs obtained, whereas ISC and H elimination differ from experimental data by more than 20 %. In fact, in the same way as Li et al, a faster drop with temperature of the ISC channel is found in comparison to both CMB experiments and trajectory calculations. In CMB experiments, ISC always prevails over H elimination, as opposed to what predicted *ab initio*. In this respect, the possibly increasing importance of the T2 surface in ISC was investigated, however it was found that this does not play a relevant role due to the fast interconversion, as already discussed. This missing ISC contribution at high temperature might however be due to the different thermal behavior of the system in the simulations and experiments, as explained in the following section.

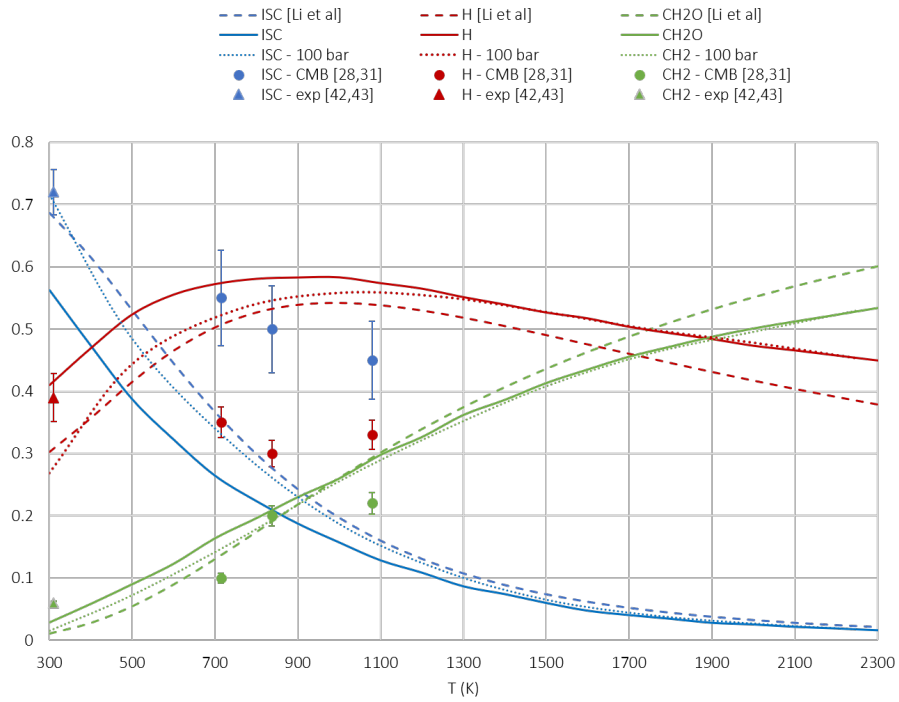

FIGURE 3.27: Plot of the main product channel BRs obtained for $O(^3P) + C_2H_4$ in comparison with those of Li et al [10]

3.3 Discussion and conclusions

In this section, further insight into the quality of the results obtained is provided. The two most critical points in the computations performed are the determination of MECP and spin-orbit coupling, and the differences obtained in the BRs with respect to experimental data. Hence, in subsection 3.3.1, the difference between MECP obtained at different levels is discussed. Then, in subsection 3.3.2 some qualitative considerations about the intrinsic discrepancies between experimental and theoretical techniques used for the study of this system are presented. Final remarks about the validation of the theoretical approach used are found in subsection 3.3.3.

3.3.1 Determination of MECP and SOC

The determination of MECP is extremely critical. The first assumption was related to the active space used, which was the same of the addition reaction. No significant change in the occupation of the orbitals from the well to MECP was found. This is due to the fact that the electronic configuration of the triplet state cannot possibly capture the C2-O forming bond, as this is spin forbidden. It was also tried to switch to a smaller AS of 4 electrons in 4 orbitals. This is shown in Figure 3.29: the pair of orbitals 12.1-13.1 would suggest a higher density and electronic interaction in the C2-O region compared to the original set, however a strange electron density was obtained in the close shell. It was thus inferred that this space was not representative of the configuration under study.

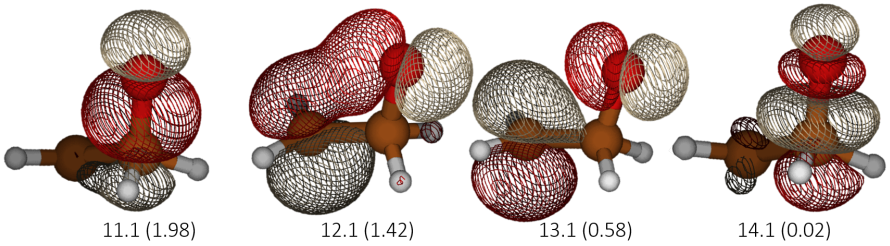

FIGURE 3.28: Orbital density on the MECP structure using CASPT2(4e,4o) and a single state

As far as the final MECP geometry is concerned, it was tried to understand whether this can be actually considered independent of the level of theory used, as claimed by Harvey [35] with regards to the hybrid gradient method. The optimized geometry was not reported in Li et al [10], however on the NST code used (`http://tcg.cse.anl.gov/papr/codes/nst.html`) the C_2H_4O crossing point is available as an example. Nevertheless, the level of theory used here for the optimization is mo62x/6-311+g(d,p), which is clearly different from that of this work and from QD-NEVPT2/aug-cc-pVTZ used by Li et al [10]. A further investigation was also performed trying to locate MECP using MOLPRO program for conical intersections at level CASSCF(6e,5o)/6-31+g(d,p) and CASSCF(6e,5o)/6-311+g(d,p). For all the geometries found, energies were computed at CASPT2(6e,5o)/aug-cc-pVTZ, so as to compare them with those obtained in this work. Also H_{SO} was determined using MOLPRO CI program at CASSCF(6e,5o)/aug-cc-pVTZ level. The results obtained are listed in Table A.5 in Appendix A, and the geometries are shown in Figure 3.29, where the dihedral O-C1-C2-H2, the angle O-C1-C2 and the distance C1-O are highlighted. It is immediately noted that the geometries are different, in particular in terms of dihedral angle and therefore of symmetry of the structure. In particular, the MECP of this work and of the first MOLPRO conical intersection calculation are characterized by a symmetry plane defined by O-C1-C2 atoms, and a smaller angle; on the other hand, MECP of Li et al and of the other MOLPRO calculation are asymmetric, with a closer geometry to that of the well, and a larger angle. The enthalpies found are significantly higher for MOLPRO geometries, whereas in the case of MECP found with NST program the configuration is only about 0.3 kcal mol^{-1} above the the well. Finally, the values of H_{SO} computed on these geometries are extremely different from one another. The main remark is that the MECP found with NST program results in a H_{SO} which is half of what declared by Li et al. Hence, it is inferred that either the geometry optimized at QD-NEVPT2 level is different and has a different coupling, or the calculation of H_{SO} at CASSCF with the ORCA software provides different H_{SO} values. It might be argued that this comparison is inconsistent, because in this work the final S0/T1 structure was found maximizing the coupling elements instead of minimizing the T1 energy. However, even considering the latter structure

(as in Figure 3.23), both the dihedral and the angle are different from what found in the configurations of Figure 3.29, and the only point in common is the asymmetry.

No final conclusion about the correctness of the MECP location can be drawn. The present discussion aims at highlighting how delicate this point is and how the whole set of BRs depends on a parameter which is extremely sensitive. Furthermore, a significant dependence of the MECP on the level of theory was found. This does not disrupt the basis of the methods used and validated in literature on multiple systems, but simply stresses the peculiarity of the system under study.

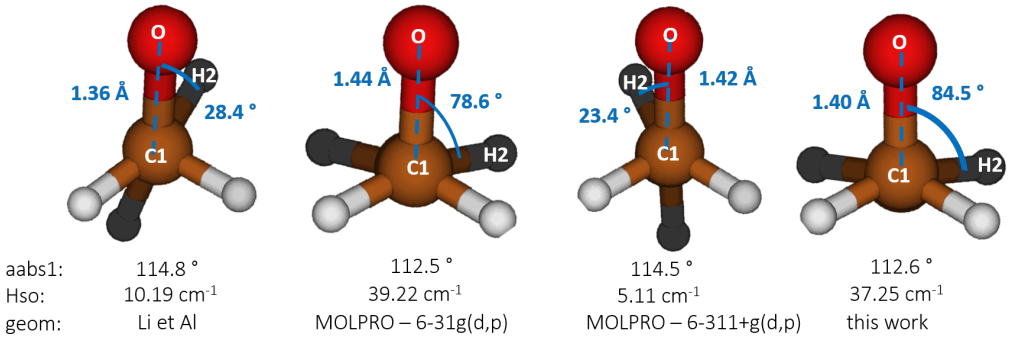

FIGURE 3.29: Comparison between the geometries of MECP obtained at different levels of theory

3.3.2 Thermalisation problem

In order to compare experiments and theory consistently, further insight in the correspondences between them is necessary. The main point was anticipated in section 1.3.3: CMB experiments occur at 300 K, and it is assumed that the the energy of the colliding reactants is redistributed among the rovibrational degrees of freedom of the well, such that this extra energy is equivalent to additional thermal energy. The correspondence between collisional energy E_{coll} and temperature T is therefore found as

$$E_{coll} = \int_{300\ \mathrm{K}}^{T} C_V^{rovib}(T')dT' \tag{3.6}$$

similarly to what already considered in equation (2.63). This equation was solved for C_2H_4O considering the collisional energies used in experiments, namely 6, 8.4, 12.9 and 13.7 kcal mol^{-1}: these are equivalent to 714, 837, 1043, 1079 K respectively. However, this correspondence is valid only as long as the energy redistribution in the system is fast, namely if the thermalization of the molecule upon collision is fast. A sketch of a qualitative comparison between collisional and thermal behavior relative to the well formation at 1000 K is shown in Figure 3.30: in CMB experiments, the system is at 300 K and therefore the initial energy distribution is narrower than that at 1000 K. Upon collision, it is assumed that the average energy is the one at 1000 K, where the energy distribution is wider. At this point, the entrance well is formed. However, in reality the well formation occurs fast after the collision, therefore at the beginning the well

still has an energy distribution at 300 K and all the collisional energy is retained in the single C1-O vibrational degree of freedom. Hence, there must be a certain lag time dt in which this redistribution occurs and the system thermalizes. The presence of this lag time causes the system to behave in a non-thermal way, unless it is significantly smaller than the characteristic reaction times for the various channels. In particular, the most affected channels would be those associated with higher vibrational frequencies and consequently higher energy barriers, because the state density at these high energies is way smaller at lower temperatures, and the energy redistribution takes longer. At the configuration of the well, the C1-H1 stretching has a frequency of about 3000 cm^{-1}, whereas both C1-O and C1-C2 stretching frequencies are about 2000 cm^{-1} and the frequency of the torsional motion associated with ISC is about 150 cm^{-1}. If the characteristic times of thermalization and reactivity are comparable, the system will behave as non-ergodic, namely its behavior averaged over time will not correspond to that averaged over the phase space, and the results of *ab initio* calculations will not be representative of the dynamic CMB experiments or QCT-SH calculations. As a consequence, in *ab initio* simulations the shortest times will not provide a realistic description of the system, because of high energy reactivity which should be cut off from the simulations. In this respect, it must be recalled that also in the case of propylene [8, 15], the reactivity to vinoxy is overestimated by *ab initio* calculations at high temperatures, likely for a similar reason. However, in heavier systems the discrepancy is smaller, since the molecule has an overall higher energy and energy redistribution effects are less relevant.

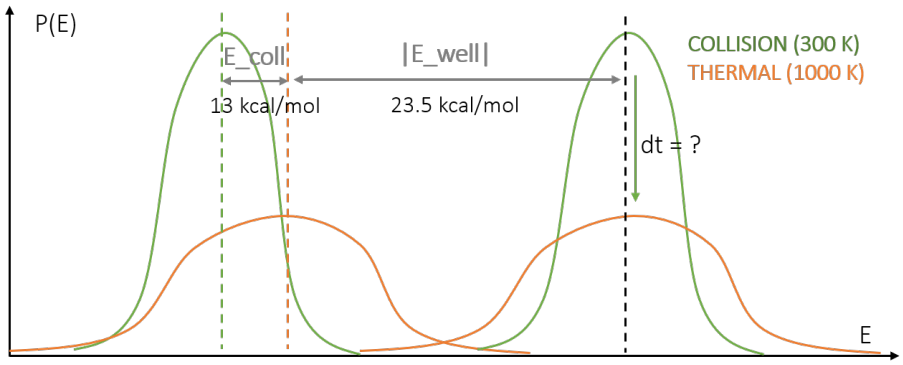

FIGURE 3.30: Sketch of the difference in energy distribution between a thermal system at 1000 K and a system at 300 K undergoing a collision to the same average energy

A further remark about the different behavior of collision conditions with respect to *ab initio* calculations regards the initial adduct lifetime. Casavecchia et al [32, 38] explain how the decrease of ISC with temperature is related to the decrease in the lifetime of the initial adduct: at 13.7 kcal mol^{-1} this is comparable to the molecular rotational period of 2.8 ps, whereas at smaller energies of 3 kcal mol^{-1} (corresponding to about 500 K) it is 5-6 times higher, hence about 15 ps. In *ab initio* calculations, this is equivalent to saying that at higher temperatures the reactivity of H and CH_2O elimination pathways is higher, however this cannot be in any way related to collisional

energy redistribution effects. By looking at the species lifetimes of KMC-ME output at 0.0076 torr, it is noted that at 300 K only about 27 % of the reactive events occur before 2.7 ps, whereas at 1000 K this number rises to more than 73 %.

A first possibility for a modification of the obtained BRs at 1000 K to produce results which actually mirror the CMB experiments behavior is a simple post processing. The basic consideration is in CMB the thermal energy distribution upon collision will be at 300 K before the collisional energy actually spreads among all the vibrational DOFs. If this time lag was known, it would be possible to substitute the *ab initio* reactivity in this interval with that computed at 300 K. This threshold τ_{thr} is unknown, therefore only speculations can be done. Considering that all molecules reacted before τ_{thr} would actually behave as at 300 K, the new BRs would be obtained as

$$BR_{i,new} = \frac{N_i(300\text{ K})|_{t<\tau_{thr}} + N_i(1000\text{ K})|_{t>1\ \tau_{thr}}}{N_{tot}(300\text{ K})|_{t<\tau_{thr}} + N_{tot}(1000\text{ K})|_{t>\tau_{thr}}} \tag{3.7}$$

This would result in an averaging between the BRs at the temperature of the simulations and room temperature on the basis of the characteristic time of energy redistribution, which depends on the molecule heat capacity and on the collisional energy. Considering that at 1000 K the complex lifetime in CMB experiments was about 2.8 ps, shorter threshold times were tried, and the results for 1 and 2 ps are shown in Table 3.7. In both cases, an increase in ISC is obtained, as expected. In particular, for $\tau_{thr} = 2$ ps, ISC is 41 %, which is almost identical to the CMB prediction of 45 %. Since the actual lag time is unknown, this result shall not be taken as a quantitative proof and only supports the hypothesis of the non-ergodicity of the system. Finally, this scaling of the BRs would only be meaningful if a considerable amount of the reacted molecules at the given temperature is retained. Otherwise, simulations with a higher number of reacted molecules should be performed.

TABLE 3.7: BRs of $O(^3P) + C_2H_4$ at 1000 K averaged with 300 K reactivity

molec	**t > 1ps N_i(1000 K)**	**t < 1 ps N_i(300 K)**	**$BR_{i,new}$**	**t > 2 ps N_i(1000 K)**	**t < 2 ps N_i(300 K)**	**$BR_{i,new}$**
reac	80	2	0.01	44	6	0.01
H	3293	431	0.56	2116	827	0.47
CH_2	1173	30	0.18	656	61	0.11
ISC	1079	570	0.25	1431	1153	0.41
tot	5625	1033		4247	2047	

An accurate modification of KMC-ME simulations in order to include the non-ergodicity of the system would require a change in the theoretical treatment of the kinetics. In particular, a time dependent vibrational density $\rho^{vib}(E,t)$ should be introduced, such that the microcanonical kinetic constant of equation (2.48) would change in time, affecting KMC-ME simulations. Clearly, time dependence would differ on the basis of the DOF considered. In order to obtain such a law, dynamic trajectory calculations are needed. For instance, *ab initio* molecular dynamics (AIMD) implemented

in programs such as CP2K would allow to obtain appropriate trajectories. Then, with post processing of data, the velocity autocorrelation function might be computed and associated with the energy stored in each vibrational DOF. This task was beyond the scope of this work, and the present discussion is only qualitative and aims at giving an idea of the reasons behind discrepancies and of further steps to be taken to explain them quantitatively.

3.3.3 Approach validation

The main aim of the study of the reactivity of $O(^3P) + C_2H_4$ was the validation of the *ab initio* approach used for the calculation of the branching ratios, as well as a full understanding of the methodology. The same approach as in the study of $O(^3P)$ reaction with propylene and 1-butene [8, 16] was adopted, so as to obtain consistent results for the series of the first three alkenes. This sets the basis for the scaling of the kinetic constants with rate rules.

The approach validation is based on the comparison with theoretical benchmark calculations as well as experimental data, which was done in the previous paragraphs and briefly summarized here.

The addition rate constant was computed *ab initio* with variational and non-variational calculations with an accuracy within a factor of 2, without the need of corrections on the energy barriers. Almost exact values are instead reached imposing a corrective factor which accounts for the contribution of the excited state.

As far as ISC is concerned, the results presented and the comparisons with the state of the art highlight that a lot of uncertainty is still present, in particular as regards the location of MECP. In fact, this seems to be extremely sensitive to changes in the level of theory and the basis set, as opposed to what should be achieved with hybrid gradients methods. This clearly does not invalidate the theories, but reveals how peculiar the system under study is, to the point that approaches which usually work are not likely to provide the most accurate results in this case. Even so, the MECP geometry found resembles that of the heavier systems, and the H_{SO} obtained is close to the recommended values.

Finally, the BRs obtained with KMC-ME simulations well reproduce the benchmark *ab initio* calculations of Li et al [10], as shown in Figure 3.27. Even higher accuracy in the predictions can be achieved: for instance, variational computations can be introduced explicitly in KMC-ME simulations, and further analysis in the MECP region may lead to the introduction of secondary MECP points upon hopping to the excited T2 surface. However, this was behind the scope of this work. Experimental data are not in full agreement with the results obtained, as they predict a less significant drop of ISC with temperature. As explained in the previous paragraphs, this might be due to an incorrect treatment of ISC with the statistical theories currently used, or more likely to a non-ergodicity of the system in question. In fact, the predictions of BRs are more accurate for heavier compounds, where non-ergodic effects are less relevant. It is also recalled that the $O(^3P)$ reaction with ethylene is

one of the most debated in literature in terms of product distribution, as explained in the introduction.

Overall, the calculations performed for the $O(^3P)$ reaction with ethylene are satisfactory and can be considered as a valid basis for the method understanding and for its application to heavier systems of the same kind or to similar kinetic schemes involving ISC.

Chapter 4

Determination of rate rules

In this section, the results obtained for the determination of rate rules will be presented. As explained in section 2.5 of chapter 2, the scaling from C_3H_6 to C_4H_8 was chosen, due to both the availability of data at the same level of theory and the similarity of the systems, as opposed to C_2H_4. This case study is presented in section 4.1. First of all, the comparison between both the PES structure and the reactivity of the systems is provided in subsections 4.1.1 and 4.1.2. Then, the determination of the scaling factors is discussed in subsection 4.1.3. Finally, subsection 4.1.4 illustrates the predictions obtained and the comparison with the calculated values.

Since the results were promising, the possibility of scaling the laws to heavier alkenes was also investigated, as they were never studied experimentally. Hence, in section 4.2 predictions for the BRs of O(^{3}P) addition to 1-pentene are shown and used as a basis for general considerations about scaling to longer chains. Finally, the main conclusions and future challenges are discussed in section 4.3.

4.1 From C_3H_6 to C_4H_8

4.1.1 PES in comparison

The first step for the scaling of rate rules from one PES to another is the full understanding of their differences and of how this may affect the results. An overview of the main product channels considered for both PES was already provided in the introduction, and a complete description is found in Cavallotti et al [8, 16]. As anticipated, in this case only the triplet PES was studied, and all the singlet channels were simply merged together as ISC. These channels and the energies of their TS and respective products are shown in Figure 4.1: a) is the propylene PES, b) is the 1-butene PES. The different colors show how the products were grouped together in different channels, and this color code is also used in the plots of the BRs of the following sections. The main channels identified are H elimination, formaldehyde formation, the production of vinoxy, and ISC. H elimination and ISC have contributions of both the central and terminal carbon additions.

For the analysis of the differences in the PES, energy barriers should be considered. First of all, it is noted that in propylene the entrance barriers for the addition are small but larger than 0, whereas in 1-butene the entrance barriers are submerged. This will

clearly affect the kinetic constants, however the aim of these rules is not the accurate determination of addition constants, but that of BRs. Hence, this difference becomes relevant only in case it results in a different ratio between central and terminal total branching in the two systems.

The second main difference is related to the well depths. It is recalled that in the determination of the scaling factors only the heat capacity of the terminal carbon addition well was computed. This is correct on propylene PES, as the wells have the same energy with respect to the reactants, namely -23.7 kcal mol^{-1}. This value was taken as a reference for the computation of the scaling temperatures T^*. However, on the PES of 1-butene the two wells have an energy difference of 0.7 kcal mol^{-1}. Furthermore, they both have a lower energy than the propylene wells, namely -24.6 kcal mol^{-1} for the terminal carbon and -25.3 kcal mol^{-1} for the central one. Nevertheless, the scaling relations lose their meaning if different energies are considered. In order to test the effect of this factor, the scaling temperature T^* for 1-butene terminal addition well was computed with a well depth of both 23.7 kcal mol^{-1} and 24.6 kcal mol^{-1}. The resulting T^* differ by less than 20 K, namely less than 2 %, which has an irrelevant effect on the scaling of rate laws. Furthermore, the exact value of the well depth of heavier hydrocarbons is unknown, and will always be assumed as -23.7 kcal mol^{-1}.

Finally, the most relevant difference in terms of energy is found in the vinoxy channel. This consists in a C-C scission which produces a methyl radical in the case of propylene, and an ethyl radical in the case of 1-butene. The barrier of the former system is more than 2 kcal mol^{-1} higher than the latter, which brings evidence of a different reactivity. In fact, the C-C stretching mode associated with the elimination of the methyl will be characterized by a higher frequency, since the detaching moiety is smaller. This will result in a smaller reactivity and smaller overall BR of vinoxy. This observation will be considered in the determination of the rules, so as to derive corrective factors for the predictions from propylene. However, this problem is only significant when scaling from propylene to 1-butene. In fact, the behavior of alkenes with more than 5 carbon atoms will be simply derived from that of 1-butene: when the detaching moiety changes from ethyl to propyl to heavier radicals, the difference in the energy barrier and the stretching mode will be irrelevant.

The only significant difference in terms of reaction pathways is the formation of formaldehyde. In fact, the path is extremely loose in the case of 1-butene, whereas in propylene it is characterized by an intermediate well: this will probably decrease the reactivity, although it might be balanced by an increase in tunneling effects, typical of tight pathways.

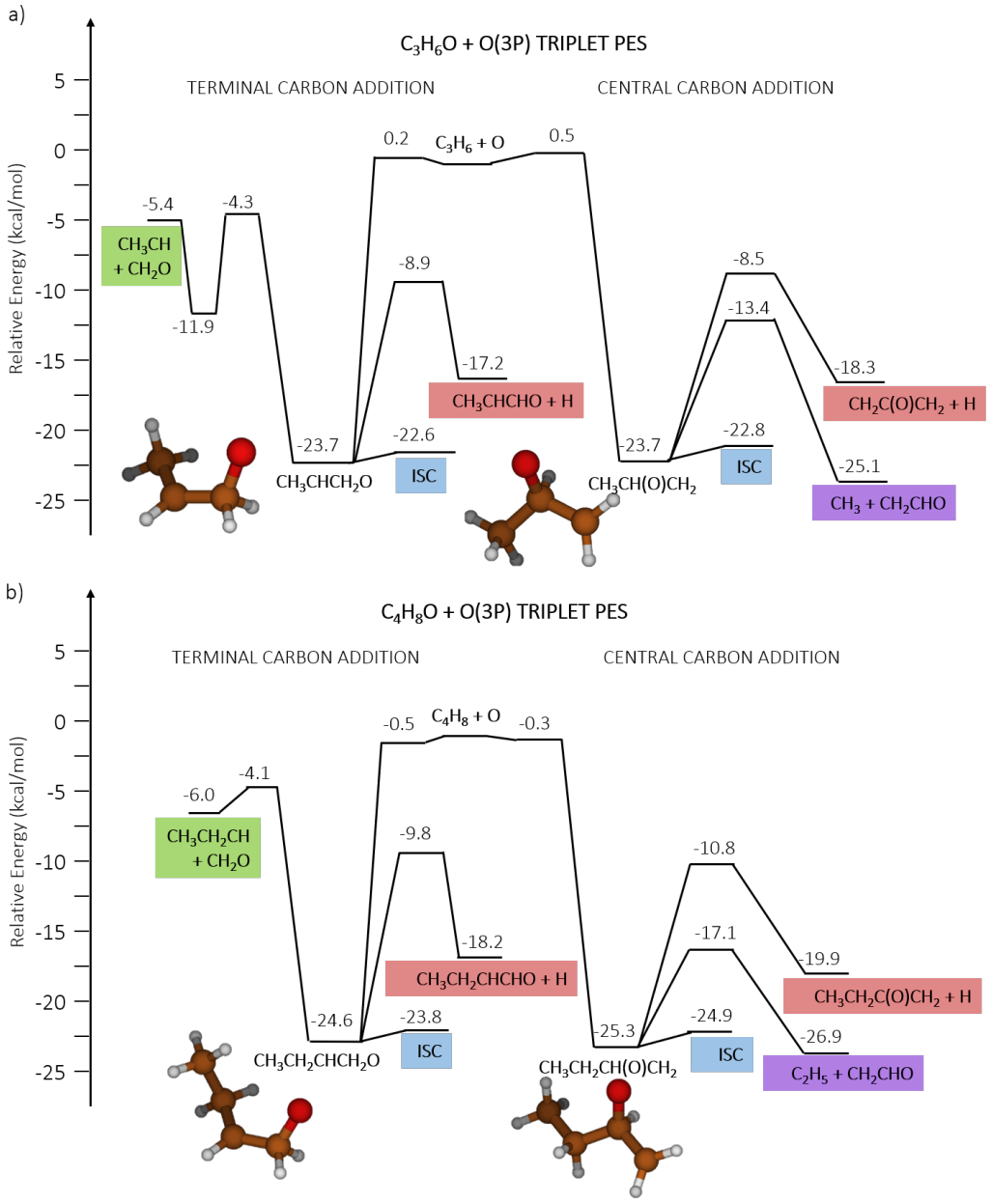

FIGURE 4.1: Channels used for the rate rules in propylene PES (a) and 1-butene PES (b)

4.1.2 Reactivity of $O(^3P)$+C_3H_6 and C_4H_8

For the calculation of the product distribution, master equation simulations were conducted. These were performed again only for 1-butene, whereas for propylene data were already available in the $500 \div 2250$ K range. Hence, this was the final range considered for both the BRs and the phenomenological rate constants. KMC-ME simulations were done at 1E-05 bar for 1-butene, instead data at 0.1 bar were available for propylene. The change of the BRs between these pressures is anyway negligible. The simulations included the full singlet and triplet PES, and the sketch of the considered species, reaction channels and their energies is found in Appendix E. The reactivity of the terminal and central carbon additions was studied separately.

Therefore, the relative importance of these two PES was determined by ratio between the kinetic constants of the entrance channels. The addition rates for the terminal and central carbon were computed with EStokTP using CCSD(T)/CBS//ωb97xd/aug-cc-pVTZ for the reactants and the well, and CCSD(T)/CBS//CASPT2(6e,5o)/aug-cc-pVTZ for the transition state. The potentials of the hindered rotors were instead computed at ωb97xd/6-311+g(d,p) level. The details are not reported here, as these calculations were done in previous works [8, 16]. Once the relative importance of the two PES was derived, the BRs for the product channels highlighted in Figure 4.1 were computed.

The data of the final branching ratios obtained for the two systems are found in Table F.3 and F.4 in Appendix F. In these tables, also the parameters derived for the phenomenological rate laws are listed, together with kinetic constants for the terminal and central carbon addition and their proportion. The rate constants for each channel are simply derived by multiplying the final BR by the total addition constant $k_{term} + k_{centr}$. First of all, it was found that despite the differences in the entrance barriers the relative fractions of the central and terminal carbon addition are roughly the same in the two systems, with discrepancies of 3 % maximum: the latter always prevails, contributing to almost 70 % of the reactivity at 500 K, and decreasing to about 60 % at 2000 K. Concerning instead the product branching ratios, these are plotted in Figure 4.2 a) for propylene, b) for 1-butene. The most striking difference in the behavior of the two systems resides in the trend described by ISC: in fact, at 500 K it increases from 40 % in propylene to 60 % in 1-butene, and this gap would be probably larger at room temperature. This is expected, because in heavier molecules the extent of ISC increases as a consequence of the slower reactivity of the other channels. As already pointed out, this is due to the fact that the energy of the well is redistributed among a larger number of degrees of freedom, and the states of each rigid oscillator are therefore less populated. ISC instead is poorly affected by this because its TS is associated with a low barrier torsion and its probability follows different laws (Landau-Zener theory). The idea of rate rules is that, by translating the plot of C_4H_8 on that of C_3H_6, there should be an almost perfect superposition of BRs which should also give an idea of the intrinsic temperature which will be actually computed. It is noted that when the rates of C_4H_8 are derived from those of the lighter system, the scaling factor ΔT^* is negative, hence the behavior of 1-butene corresponds to that of propylene at a lower temperature. However, the fit for the phenomenological laws of propylene was done in the 500÷2250 range, which means that at low T the BRs of 1-butene will be an extrapolation of these laws, and should therefore be interpreted carefully. Concerning instead the high T range, the asymptotes of the BR of the products should be the same, as these will not change by scaling the rates. However, by comparing Figure 4.2 a) and b), it is evident that the only asymptote which shows a perfect correspondence in the two systems is ISC, whose lines have exactly the same shape. The H and CH_2O elimination asymptotes instead differ by more than 0.5, whereas the vinoxy shows a better agreement. These discrepancies are due

to both physical reasons and to the way calculations were conducted. These are presented in this section, and serve as a justification of the more detailed analysis for the quantitative determination of corrective factors considered in subsection 4.1.4.

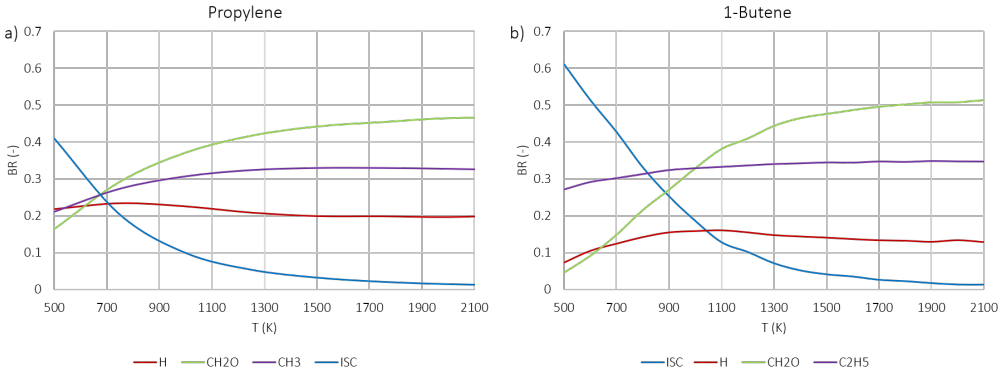

FIGURE 4.2: Branching ratios obtained with AITSTME calculations for O(^{3}P) addition to propylene (a) and to 1-butene (b)

In terms of computations, the calculations of the propylene PES did not include a variational treatment of the H elimination pathway, as opposed to those of 1-butene. As a result, the asymptote of the H elimination channel is about 0.07 lower in 1-butene, hence it almost halves. Since usually variational treatment for this kind of pathways decreases the constant by a factor of about 1.5, a first correction can be imposed on the kinetic constants obtained for propylene by dividing k_H by 1.5. In this way, the asymptotes almost coincide, as shown in Figure 4.3 a). This is clear also in Figure 4.3 b), where the superposition of the BRs for the two systems is achieved by an arbitrary shift of 200 K. Nevertheless, this factor of 1.5 was not used immediately, because all the corrections were introduced gradually on a quantitative basis. Finally, it is noted that no variational correction should be imposed on the formaldehyde pathway of propylene, because it is characterized by the formation of a stable intermediate, as opposed to 1-butene.

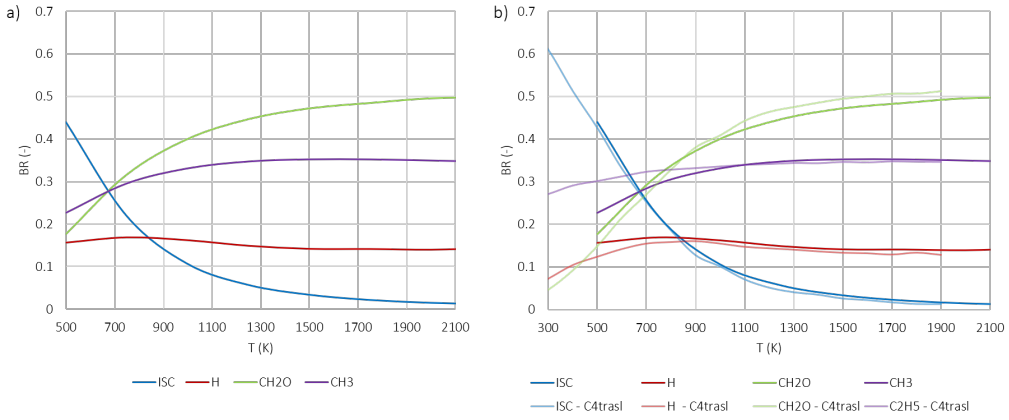

FIGURE 4.3: a) Branching ratios for O(^{3}P) addition to propylene corrected with variational factor of 1.5 on H elimination and b) superposition of BRs with a shift of 200 K

Concerning instead physical differences in the reactivity of the two systems, these mostly regard the PES of the central carbon addition. Therefore, it is easier to spot them by looking at the results of the KMC-ME simulations for the terminal and central carbon addition separately, fully reported in Table F.5 and F.6 in Appendix F. It is pointless to make a detailed quantitative comparison, since it is known that the behavior with temperature changes from propylene to 1-butene, however it is interesting to observe trends. In fact, there is a striking difference in the trends described by ISC, in particular in relation to its contribution from the central carbon PES. In particular, at 500 K in 1-butene the central carbon well undergoes almost no ISC, with a contribution to the total product branching below 5 %, whereas in propylene this is more than 13 %. This difference is amplified when considering the fractional contributions to ISC from the terminal and central carbon addition. In the case of terminal carbon for instance, this would be

$$FR_{term} = \frac{(k_{ISC})_{term}}{(k_{ISC})_{term} + (k_{ISC})_{centr}} \tag{4.1}$$

such that

$$BR_{ISC} = \frac{(k_{ISC})_{term} + (k_{ISC})_{centr}}{k_{add}} = \frac{(k_{ISC})_{tot}}{k_{add}} \tag{4.2}$$

The comparison of the FR_{term} and FR_{centr} between propylene and 1-butene is shown in Figure 4.4, whereas the corresponding data are reported in Table F.7 in Appendix F. In both systems, the relative importance of ISC from the central carbon increases with temperature. However, in in 1-butene it is always smaller than that of the terminal carbon, and is below 10 % for a wide temperature range. In propylene instead, it overcomes that of the terminal carbon already at 900 K. At this temperature, the total ISC in propylene is still 10 % (5 % from terminal, 5 % from central), whereas in 1-butene it is almost 20 %, although less than 2 % comes from the central carbon. When scaling the rates, this difference in ISC will only be relevant at low temperature, since at high temperature its BR tends to 0 in both cases. This discrepancy in the ISC behavior is a direct consequence of the different reactivity of the vinoxy channel, as anticipated. This is highlighted by looking at the product branching for the central carbon only, as shown in Figure 4.5 a) for propylene, b) for 1-butene. At 500 K, the vinoxy channel constitutes about 60 % of the total central branching in propylene, whereas it is already higher than 80 % in 1-butene. In the former system, the missing vinoxy product branching goes instead to ISC, and this is why ISC shows such an important contribution from the central carbon in propylene. This behavior will not be captured by the rate rules, and therefore corrective factors will be necessary. At the same time, it is recalled that such corrections will not be required for the scaling of 1-butene laws to heavier hydrocarbons.

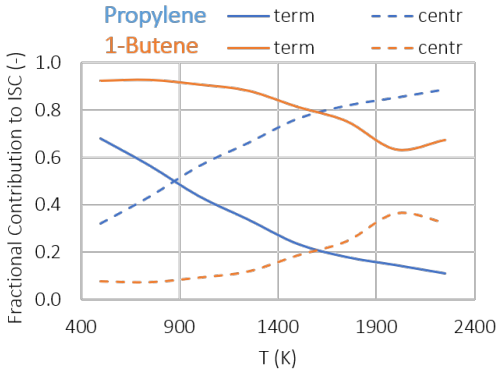

FIGURE 4.4: Fractional contribution to ISC from the terminal and central carbon addition for propylene (blue) and 1-butene (orange)

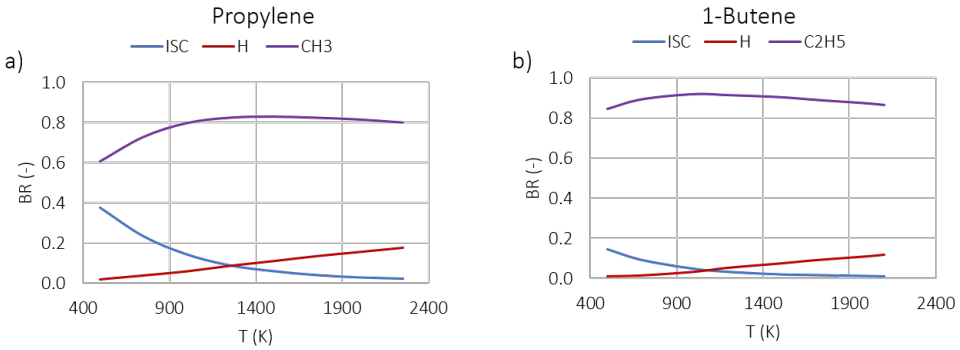

FIGURE 4.5: BRs of the central carbon addition in propylene (a) and 1-butene (b)

4.1.3 Determination of scaling factors

The determination of scaling factors requires the computation of intrinsic temperatures T^* and therefore of the heat capacities of the wells considered, as explained in sections 2.5 and 2.6 in chapter 2. In order to observe the trend of the heat capacities and scaling factors for a full set of adducts and not simply those of propylene and 1-butene, also the wells formed upon O(^{3}P) addition to ethylene and 1-pentene were considered. Clearly, for a consistent scaling all heat capacities must be computed at the same level of theory. Hence, in all cases the optimization was done at ωb97xd/aug-cc-pVTZ level, whereas hindered rotors were treated at ωb97xd/6-311+g(d,p) level. Especially for the larger molecules, an extensive stochastic scan was conducted on the dihedrals considered as hindered rotors, so as to ensure an accurate localization of the absolute minimum of the structure. The properties of each well are listed in Table G.1 of Appendix G. Then, constrained geometry optimizations were performed to compute the PES of the hindered rotors: all the plots with the relative structures are shown in section G.2 in Appendix G. All these data were generated using ESTokTP, whereas the eigenvalues associated with the HR partition function and the heat capacities were computed with programs written specifically for this purpose.

Once the vibrational frequencies and HR eigenvalues were obtained, the heat capacities were computed using the equations presented in the methods in section 2.6. These were then integrated between a temperature in the range of $300 \div 2500$ K, and an upper limit at which the energy of the system reached 23.7 kcal mol^{-1}, namely the well depth. The resulting temperature was thus saved as T^*. The heat capacities Cv and the resulting $\Delta T^* = (T^* - T)$ are listed in Table G.2 in Appendix G, and plotted in Figure 4.6 a) and b), respectively. In plot a), it is easily seen that there is a stable increase in the value of the heat capacity when adding CH_3 groups to the molecule. This is expected, since each CH_3 adds 8 degrees of freedom at a time, and therefore the increase in the heat capacity will be roughly the same from a well to the heavier one. Nevertheless, the relative importance of this additional contribution with respect to the total heat capacity decreases at higher molecular weight, and this is why this even increase in Cv from $C_nH_{2n}O$ to $C_{n+1}H_{2(n+1)}O$ is not associated with an even decrease of T^*, as shown in Figure 4.6 b). The intrinsic temperature T^* needed to reach the well energy decreases in heavier systems, because the capacity of the molecule to absorb heat rises. Furthermore, at high temperature ΔT^* reaches an asymptote, mirroring the behavior of Cv. However, contrary to the heat capacity, the difference between the curves is not even. This is due to the fact that as the system grows heavier the contribution of the additional methyl group becomes less and less relevant with respect to the overall Cv. This results in a smaller change in T^* and ΔT^*. In fact, considering the percent change in Cv with respect to the previous alkene in the series, this results as more than 30 % in C_3H_6O, $25 \div 30$ % in C_4H_8O and only $20 \div 25$ % in $C_5H_{10}O$. Following this trend, there should be a certain chain length above which the change in the heat capacity will be insignificant, and therefore the change in T^* will be irrelevant, too. Following this line of thoughts, above a certain threshold n also the reactivity of the system will be unchanged, therefore all the $O(^3P) + C_nH_{2n}$ reactions may be treated in the same way. This may only be done upon a quantitative definition of the "insignificant" change of the heat capacity.

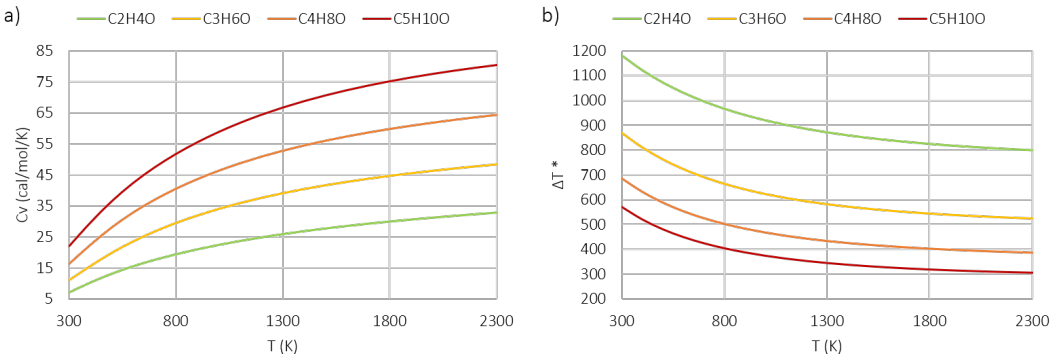

FIGURE 4.6: a) Heat capacities of the species considered b) ΔT^* computed for each species

By looking at Figure 4.6 b), the ΔT^* appears to be simply shifted vertically, keeping the same shape. This would be an extremely useful feature, since it would

allow to use a single value as a scaling factor at every temperature. Unluckily, this is not the case. This is evident in Figure 4.7, where the values of the T^* for the analyzed wells are plotted with respect to that of $C_5H_{10}O$. These differences can vary by more than 100 K, and are characterized by a higher sensitivity at low temperature and for shorter chains; this may have a significant effect on the BRs predicted on this basis. This point explains why the simpler option of a constant scaling factor was rejected.

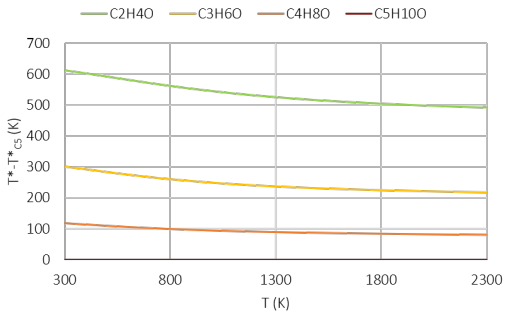

FIGURE 4.7: ΔT^* with respect to that of 1-pentene

A final important point which must be addressed in this section regards the justification of using only the terminal carbon well for the determination of the heat capacities. In fact, as anticipated in section 2.5 of the methods, it is simpler to consider one of the two wells for the computations. The terminal one was chosen for its higher contribution to the total reactivity. If this were not done, the BRs for the central and terminal carbon addition should be scaled separately, and this would be more time consuming and computationally demanding. Nevertheless, it can be proved that the assumption made is actually correct. For this purpose, the same calculations performed for the C_4H_8O terminal well were also done for the central well. The properties obtained are listed in Table G.3 in Appendix G, together with the T^*, in comparison with those of the terminal addition well. As far as the T^* is concerned, there is a difference of less than 30 K between the two configurations, which is less than 8 % of the final ΔT^*. Furthermore, considering that the central well lies about 1 kcal mol^{-1} below the terminal one, the T^* of the central well was computed again taking this difference into account, by setting the well formation energy to 24.7 kcal mol^{-1}. In this way, the sets of T^* achieved differ by a maximum of 10 K with respect to the terminal well, which has a negligible impact on the final scaling. The possibility of separate scalings for the terminal and central reactivity was therefore not considered further.

4.1.4 Predictions with rate rules

In this section, the results of the predictions of the branching ratios of O(^{3}P) addition to C_4H_8 on the basis of the phenomenological rate laws of the main product channels of O(^{3}P) addition to C_3H_6 are presented and compared with the calculated values. The scaling of the kinetic constants was done adding to the considered temperature

the factor $(T^*_{C4} - T^*_{C3})$, as explained in section 2.5 of the methods. All the data are reported in Appendix F, whereas here only the plots of the BRs obtained are shown. Several corrective factors were used with respect to the initial scaling, based on the considerations about the PES and reactivity of the previous subsections 4.1.1 and 4.1.2. The effect of each of these corrections will be highlighted and presented step by step.

The first result obtained with the scaling relations is shown in Figure 4.8, and the full set of data is found in Table F.8 in Appendix F. Solid lines are the predictions, whereas dotted lines are the calculated values. The predicted temperature scaling imposes a shift of the propylene rate laws of about -180 K at 500 K, and a smaller shift of about -150 K at high temperatures. In the $500 \div 650$ K range the effective temperature $T_{eff} = (T + T^*_{C4} - T^*_{C3})$ is below 500 K, therefore the predictions represent a sort of extrapolation of the behavior of propylene at low temperatures, since the fit of the phenomenological rates was obtained with data in the $500 \div 2250$ K range. Low temperature results should therefore be interpreted carefully. By looking at the plot, it is evident that there are several discrepancies between the predicted and the calculated values. The shift in the asymptotes are due to the non-variational treatment of the H elimination channels in 1-propylene, as already pointed out. Therefore, only the trends with temperature should be considered here. The behavior of ISC seems well represented, and predictions undergo a maximum underestimation of less than 5 % with respect to the calculations. The behavior of the vinoxy channel shows instead significant deviations, especially below 1000 K: in particular, the predictions mirror the trends of propylene, with a consistent contribution of ISC from the central carbon addition well at the expenses of the vinoxy channel. In this way, the missing ISC contribution from the terminal carbon is instead accounted as H elimination. However, this is compensated by the higher importance of ISC from the central carbon, hence ISC prediction is extremely close to calculations. This first plot was the starting point for the determination of corrective factors. Corrections should not be regarded as impositions that aim at finding an agreement between predictions and calculations, but as necessary to reach a consistent comparison. Furthermore, this will not be required when scaling 1-butene rate laws to heavier systems. In fact, 1-butene laws will be used instead of propylene ones to predict the behavior of 1-pentene and longer chains, because of the smaller scaling factor and the higher accuracy of these calculations. In addition, calculated BRs of 1-butene show better agreement with experimental data and are therefore expected to produce more reliable predictions.

The first correction to be introduced is related to the variational treatment of H elimination. The quantitative scaling was based on the assumption that the ratio between the variational and conventional kinetic constants in propylene would be the same as in 1-butene, for which the data of both pathways were available. This resulted in a corrective factor of $1.55 \div 1.65$, slightly varying with temperature. In the initial corrections, this temperature dependence was maintained; then, a constant factor of 1.6 was applied. This allowed to simply scale the pre-exponential factor of the rate law

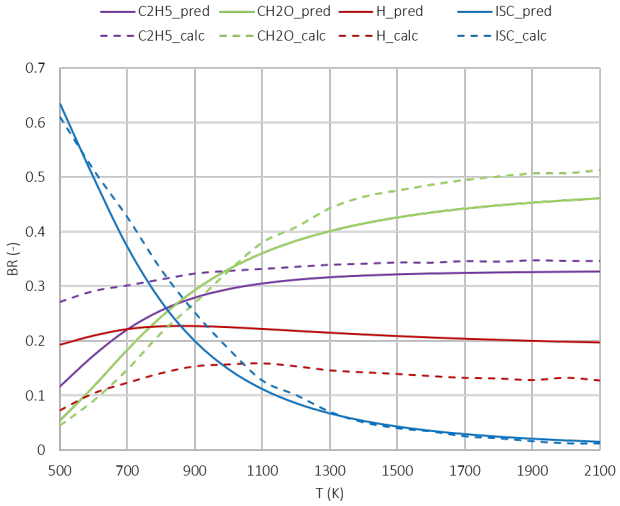

FIGURE 4.8: Prediction for the BRs of $O(^3P) + C_4H_8$ in comparison with calculated values

of propylene for the H elimination channel. This is expected to generate more correct results also for the BRs of the lighter system. In fact, in the high temperature KMC-ME simulations of Leonori et al [15] the H elimination channel was overestimated by more than 50 % with respect to CMB experiments, and the scaling would partially help reduce this difference, although it is mostly due to non-ergodic effects. The kinetic constants and BRs obtained with this scaling are in Table F.9 of Appendix F, whereas the plot of the BRs in comparison with the calculations is shown in Figure 4.9. The asymptotes are captured perfectly, supporting the validity of this correction. Nevertheless, a strong disagreement remains at low temperature, as a consequence of the different behavior of the addition to the central carbon. The underestimation of the C_2H_5 channel causes the overestimation of both H elimination and ISC from the central carbon.

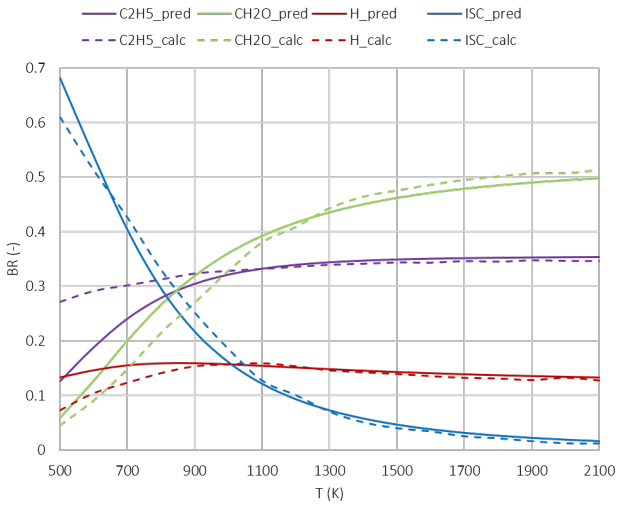

FIGURE 4.9: Prediction for the BRs of $O(^3P) + C_4H_8$ with corrections on H elimination channel in comparison with calculated values

In order to tackle this issue, a different approach was used. The main observation is that in C_4H_8O, and certainly also in heavier systems, the main contribution to the products of the central carbon addition comes from the vinoxy channel, contrary to what happens in propylene. Therefore, it may be tried to derive the BR of C_2H_5 from the fraction of the central carbon addition, which is the almost identical in the two systems. However, the asymptote for this total fraction is 0.4, which is clearly higher than the vinoxy BR of 1-butene. This is due to several reasons, which can be quantified as corrections to the central carbon addition fraction to derive a more accurate prediction for the vinoxy channel:

1. In the computation of the BRs, the fraction of molecules which dissociate back to the reactants were included in the total number of reacted molecules, but not accounted for as a reaction channel. This means that, when deriving the kinetic constants as $k_i = (\mathrm{BR}_i\ k_{add})_{term} + (\mathrm{BR}_i\ k_{add})_{centr}$, the total sum of $(\mathrm{BR}_i)_{term}$ and of $(\mathrm{BR}_i)_{centr}$ was less than 1. If the total addition kinetic constant is computed again as the sum of these k_i, it will be slightly smaller than the original value. This effect is irrelevant in the BRs and their scaling if the proportion of molecules which dissociate back is the same in the two systems. In the terminal carbon addition, the fraction of molecules reacted back is negligible in both systems. However, this is not the case of the central carbon addition, and their amount is much higher in propylene than in 1-butene. As a result, the central carbon fraction of the overall products would be lower than what initially indicated. A correction is therefore imposed multiplying the central carbon fraction by the ratio of the actually reacted molecules with respect to the total ones, as shown in the first column of Table 4.1. This correction has no effect at low temperature, whereas it decreases C_2H_5 precent fraction by more than 5 % at high temperature.

2. The second correction is naturally based on the contribution of the H elimination channel, which would otherwise be counted twice. In both propylene and 1-butene, the relative contribution of CH_3 and C_2H_5 with respect to H elimination in the central carbon addition is the same, as shown by the BRs of Table F.5 and F.6 in Appendix F. Hence, it is possible to further rescale the fraction of central carbon addition with the factor $\mathrm{N}_{\mathrm{CH_3}}\,(\mathrm{N}_{\mathrm{H}} + \mathrm{N}_{\mathrm{CH_3}})^{-1}$. The result at different temperatures is shown in the second column of Table 4.1. Also in this case, the major correction is at high temperature and reduces the fraction by a further 10 %. In the last columns of the table, the overall correction and the final BR obtained as a prediction of C_2H_5 are indicated.

Using this correction, the kinetic constant associated with the vinoxy channel does not need to be computed for the derivation of the BRs. Therefore, the BRs of the

other channels are simply derived as

$$BR_i = \frac{k_i}{\sum_{i=1}^{3} k_i} \; (1 - BR_{\mathrm{C_2H_5}}) \tag{4.3}$$

The results of the predictions thus obtained are found in Table F.10 in Appendix F and are shown in Figure 4.10: the plot highlights a very good agreement between the predictions and the calculations, in fact there is a mismatch in the branching ratios of less than 0.1. This can be already considered a success, since the uncertainty of *ab initio* calculations is in this range. The biggest difference is found at low temperature, where the ISC is underestimated by the predictions, and C_2H_5 is overestimated. This depends on the fact that the contribution of ISC from the central carbon was completely omitted, whereas in 1-butene at 500 K it is 14.5 % of the central fraction, which results in about 5 % total, as reported in Table F.6. This is exactly the additional fraction of C_2H_5 predicted with the method just described. It clearly does not make sense to add also this correction, as it would imply a complete knowledge of the system to be predicted. It is finally recalled that in the scaling from 1-butene to heavier alkenes the C_2H_5 fraction would simply be fixed to that of 1-butene, considering a temperature scaling in the behavior of the BR instead of the kinetic constants. This would require also simulations at lower temperature. The data available for 1-butene were anyway in the $300 \div 2500$ K range, and the full set is reported in the appendices.

TABLE 4.1: Corrective factors

T (K)	$\frac{\textbf{reacted}}{\textbf{all}}$	$\frac{\textbf{CH}_\textbf{3}}{\textbf{centr}}$	**corr**	$\frac{\textbf{centr}}{\textbf{tot}}$	$\mathbf{BR_{C_2H_5}}$
500	1.000	0.982	0.982	0.347	0.341
750	0.998	0.969	0.968	0.374	0.362
1000	0.995	0.957	0.952	0.383	0.365
1250	0.988	0.939	0.928	0.391	0.363
1500	0.980	0.924	0.906	0.396	0.359
1750	0.969	0.908	0.879	0.400	0.351
2000	0.958	0.894	0.856	0.402	0.345
2250	0.946	0.890	0.842	0.406	0.342

In light of the consideration just made, a final scaling was obtained by simply fixing the BR of the vinoxy channel to that of 1-butene, such that no prediction is applied to this, and the scaling of the other channels was evaluated independently, as in equation (4.3). The full set of kinetic constants and BRs is listed in Table F.11 in Appendix F, ad the comparison with the calculated values is shown in Figure 4.11. In this case, the prediction is almost perfect, with slight discrepancies smaller than 0.05 in the medium-low temperature range. This sets the validity of the approach for the scaling of rate laws from propylene to 1-butene. In the following paragraphs, the results and further possibilities for the scaling to heavier hydrocarbons is discussed.

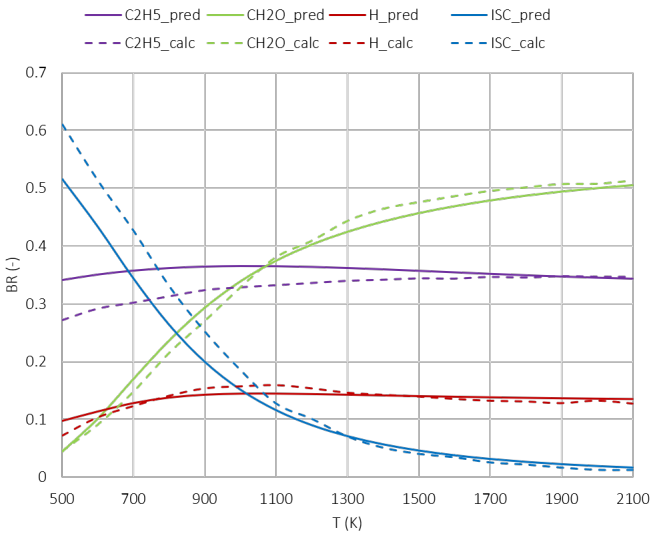

FIGURE 4.10: Prediction for the BRs of $O(^3P) + C_4H_8$ with fixed and rescaled central BR in comparison with calculated values

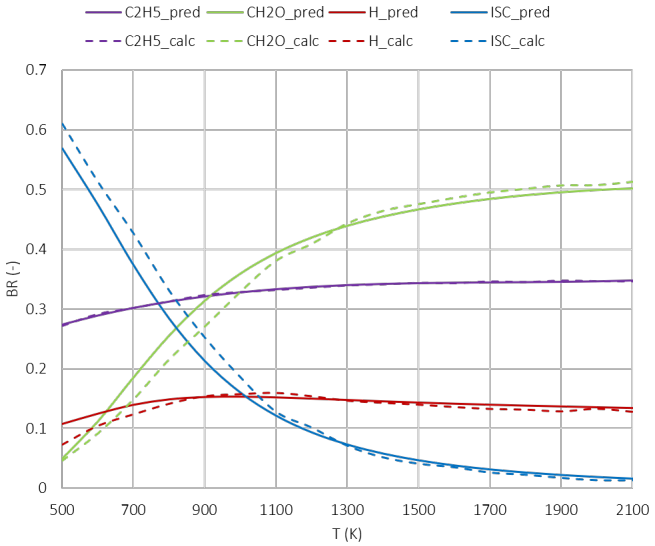

FIGURE 4.11: Prediction for the BRs of $O(^3P) + C_4H_8$ with C_2H_5 BR equal to the calculated value in comparison with calculated values

4.2 From C_4H_8 to heavier alkenes

The final aim of the scaling relations is certainly not the prediction of BRs between species whose behavior is already known. In fact, the power of these rules is to consider a full set of heavier hydrocarbons and to determine the BRs for all of them. The scaling proposed requires the heat capacity of the well, here determined *ab initio* at a relatively small computational effort compared to the full set of KMC-ME simulations. Furthermore, for the heaviest species like C_{10+}, group additivity rules may be used. In this work, a first prediction for the BRs of $O(^3P)$ addition to 1-pentene C_5H_{10} was conducted. The properties were computed as for the other hydrocarbons considered

in the series, and the heat capacity thus derived was integrated for the determination of T^*. The results of the well properties, heat capacities and intrinsic temperatures are in Table G.1 and G.2 of Appendix G, whereas the plots of the hindered rotor potentials are in section G.2. For the determination of the BRs, both propylene and 1-butene rate laws were scaled. In the first case, the ΔT^* was clearly set as $(T^*_{C5} - T^*_{C3})$, which vary between -280 and -220 K. The last version of the rules with the fixed BR for the vinoxy channel was used. This BR was interpolated in the $300 \div 2500$ K range with a polynomial expression, and it was scaled with respect to 1-butene with a factor of $(T^*_{C5} - T^*_{C4})$. The results are in Table F.12 in Appendix F, whereas the plot of the predictions obtained is in Figure 4.12 a). The shaded portion represents unreliable predictions, as the effective temperature is below the lower limit of the original fitting range. For instance, the scaling factor at $T = 500$ K is $(T^*_{C5} - T^*_{C4}) = -280$ K: this means that 1-pentene is assumed to behave like propylene at $T_{eff} = 220$ K, which is largely outside the range of propylene fit ($500 \div 2250$ K). Then, it was also tried to obtain the same predictions using the phenomenological rate laws of $O(^3P) + C_4H_8$, which were interpolated in the $300 \div 2100$ K range. In this case, the scaling parameter was $(T^*_{C5} - T^*_{C4})$, which ranges from -110 and -80 K. The results are in Table F.13 in Appendix F, and the plot is in Figure 4.12 b). The trends are consistent with the expectations. In fact, the BR of ISC in 1-pentene is $0.65 \div 0.7$ at 500 K, about 0.05 above the calculated BR of ISC in 1-butene. Furthermore, the switch in the importance of ISC and formaldehyde channels occurs at a higher temperature with respect to the smaller system. This latter prediction is more reliable, because the calculations used for the fit are more accurate and the scaling factor is smaller, therefore the behavior of 1-pentene will be represented better.

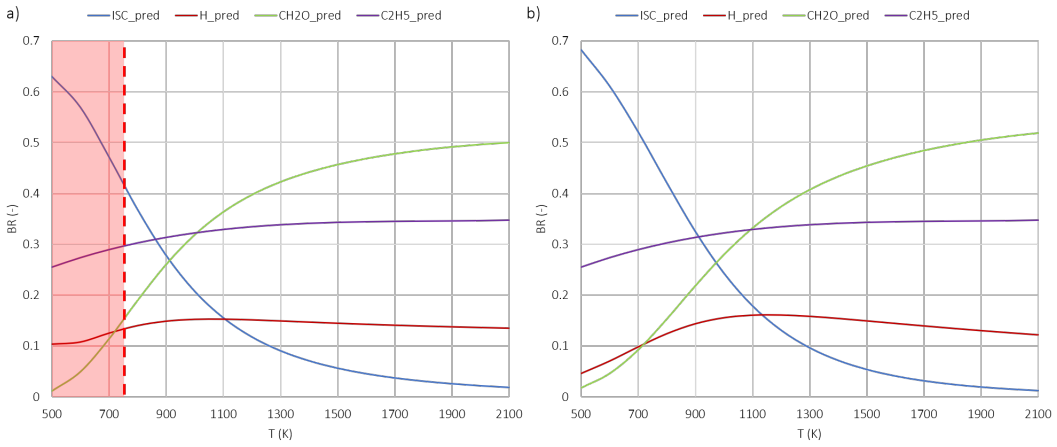

FIGURE 4.12: Predictions for the BRs of $O(^3P) + C_5H_{10}$ from C_3H_6 (a) and C_4H_8 (b)

It is worth stressing further in which temperature range the predictions should be considered valid. It must be considered that scaling the rates for higher molecular weights is equivalent to considering these rates at lower temperatures. Therefore, the predictions are reliable only if the effective temperature T_{eff} at which the rates are

considered is still within the range where the original rate laws were fitted, otherwise they are extrapolations. In the case of propylene, the rate laws were fitted in the $500 \div 2250$ K range, therefore any scaling with an effective temperature T_{eff} below 500 K should be checked carefully: $T_{eff} = (T + T^*_{C5} - T^*_{C3})$ is 500 K at $T = 765$ K, hence predictions are reliable only above 765 K. The same applies to 1-butene, which however was fitted in the $300 \div 2100$ K range. In this case, $T_{eff} = (T + T^*_{C5} - T^*_{C4})$ is 300 K at $T = 406$ K, therefore predictions are reliable above 406 K. As a result, it makes more sense to predict BRs for 1-pentene from 1-butene, as in Figure 4.12 b).

The risks related to the extrapolation of rate laws at low temperatures become evident when considering a wider temperature range for the predictions obtained from propylene. For instance, one might wonder what happens in 1-butene or 1-pentene below 500 K. By looking at the scaling factors in Table F.11 and F.12 in Appendix F, it is seen that for 1-butene the scaling factor at 300 K is -180 K, hence T_{eff} is 120 K, whereas for 1-pentene it is -300 K, which makes the T_{eff} equal to 0 K and any prediction completely meaningless. The results for this full temperature range are plotted in Figure 4.13 a) for 1-butene, and b) for 1-pentene. The shaded portions indicate the ranges where BRs are extrapolated, as explained in the previous paragraph. In both cases, below $T_{eff} = 220$ K, there is a complete inversion of the BR trends for ISC and H elimination. Hence, for $T_eff = 220 \div 300$ K, predictions may be unreliable, however below 220 K they lose their meaning. What would be required is a fitting which includes T below room temperature, which is not often analyzed in KMC-ME simulations. Even so, the fit of modified Arrhenius law generally becomes less accurate at low temperatures: for instance, the fit of 1-butene phenomenological rate laws in the $300 \div 1500$ K range has a R^2 of 0.975 for ISC and 0.985 for H elimination, whereas generally the fitting is considered good only with R^2 above 0.99. Furthermore, at low temperature the dependence on pressure is more significant, and extra attention must be paid also in this respect. Further investigations in this direction may be an interesting subject of work for the future.

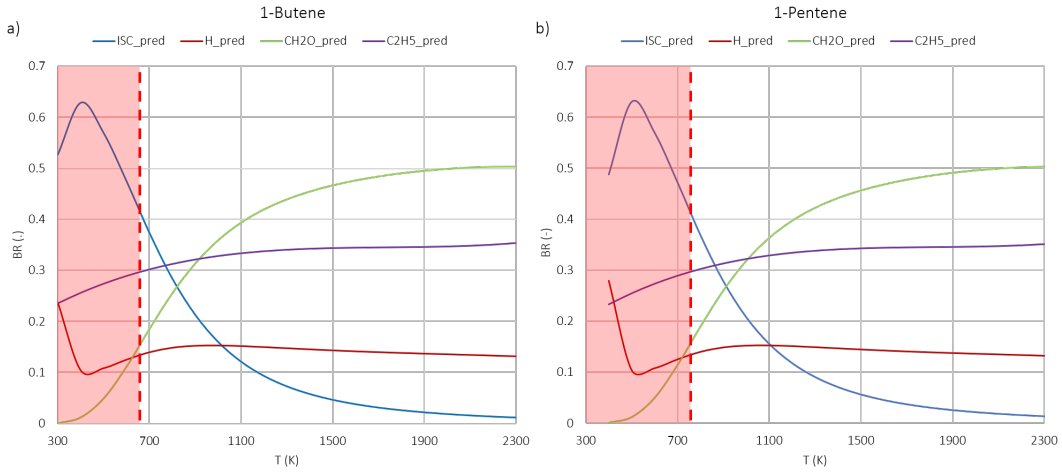

FIGURE 4.13: Predictions for the BRs of $O(^3P) + C_4H_8$ (a) and $O(^3P) + C_5H_{10}$ (b) from C_3H_6 in the $300 \div 2300$ K range

It is also interesting to look at a larger temperature range for the predictions of 1-pentene from the laws of 1-butene: as explained in the previous paragraphs, the BRs thus predicted should be accurate above 406 K. The result is shown in Figure 4.14 a). Also in this case, the shaded portion below 406 K represents the range where BRs are extrapolated. The predictions look smoother and more consistent at low temperature compared to what shown in Figure 4.13. Nevertheless, this should not be attributed to a better quality of the laws or an actual legitimacy of the extrapolation. In fact, in this case the BRs were derived with equation (4.3), and the BR of the vinoxy channel was directly scaled from the polynomial fit, which is the reason for this smoother behavior. The "regular" predictions obtained scaling all the kinetic constants are instead shown in Figure 4.14 b), again highlighting the unreliable temperature range of the predicted BRs. Above 500 K, the behavior is the same as that of Figure 4.14 a), but for some minor discrepancies. At 300 K instead (T_{eff} = 185 K), the extrapolation is completely meaningless and should not be considered. This inversion in ISC and C_2H_5 BRs is attributed to the effect of the exponential terms of the Arrhenius laws for the kinetic constants. In fact, by looking at the activation energies and α parameters of the fit for 1-butene laws in Table F.4 in Appendix F, it is noted that ISC has a high activation energy of about 3 kcal mol^{-1} which causes the rate to drop at low T, whereas C_2H_5 has a slightly negative E_A, such that the rate increases significantly at low T. The contribution of the other channels instead tends to zero.

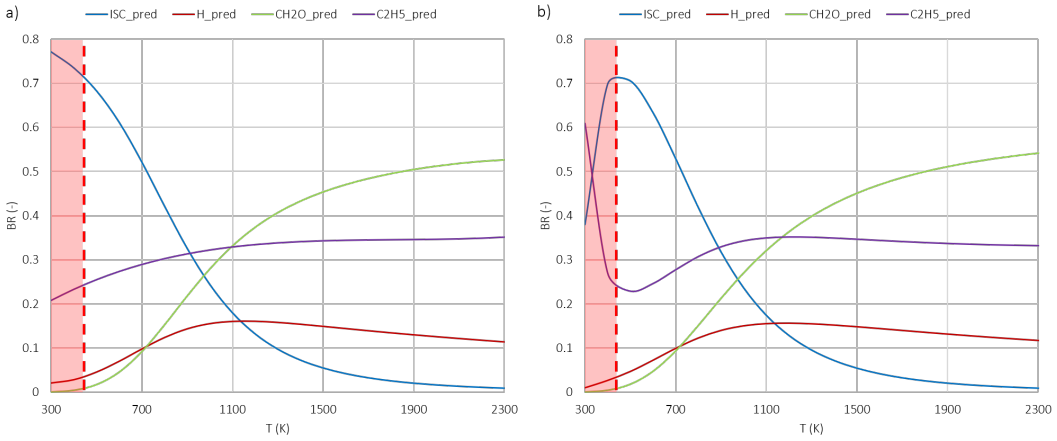

FIGURE 4.14: Predictions for the BRs of $O(^3P) + C_5H_{10}$ from C_4H_8 in the full temperature range using C_2H_5 BR prediction (a), or using all the scaled kinetic constants(b)

In the previous paragraph, it was pointed out how the Arrhenius fit has poorer quality at lower temperatures. This can be further investigated by comparing the BRs obtained from the fits of the rate laws with the original calculations for both 1-butene and propylene, as in Figure 4.15. In particular, on the plot of 1-butene a) it is highlighted how ISC and C_2H_5 are not fitted accurately at low T, anticipating the abrupt changes in BRs observed in Figure 4.14 b). The vinoxy channel shows the biggest discrepancies with respect to the calculated values, and this is another reason why it is wiser to keep its branching fixed and fitted with a polynomial expression.

This also serves as a general warning about the fit quality of Arrhenius expressions, which causes issues even when R^2 is above 0.99. Concerning instead the BRs obtained from propylene fitted rate laws in plot b), BRs look smoother even at low temperature, and are perfectly superimposed on the calculated values in the whole fitting range. Nevertheless, extrapolations with T_{eff} below 200 K causes the inversion of ISC and H elimination trends, as observed in Figure 4.13.

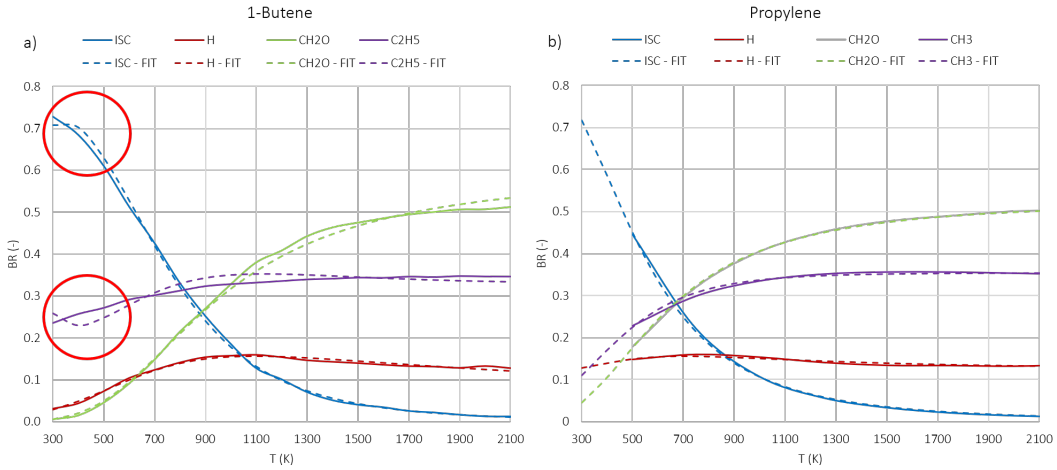

FIGURE 4.15: Data fitting for the BRs of $O(^3P) + C_4H_8$ (a) and $O(^3P) + C_3H_6$ (b) in comparison with the calculated values

All the elements discussed may rise doubts about the validity of these scaling relations. The main problems highlighted regard low temperature behavior. In particular, it was considered that scaling to heavier alkenes leads to use the scaled rate laws outside the original range of data fitting, and therefore represent risky extrapolations. Hence, KMC-ME simulations for 1-butene at very low T would be required to extend the original fitting range and that of reliable predictions as a consequence. Even so, below room T Arrhenius fitting is less accurate, and pressure dependence is more significant and should be accounted for. Most importantly, when scaling from C_4 to $C_{n>5}$ the ΔT^* will be lower and lower, resulting in uncertain predictions in an even larger range of temperature than the one found for 1-pentene. Nevertheless, as pointed out in subsection 4.1.3, the growth of ΔT^* is smaller and smaller as the chain length increases, because the additional heat capacity of the methyl becomes less and less significant with respect to the overall one. Therefore, it would be very useful to be able to make at least approximate predictions of the heat capacities and ΔT^* at increasing molecular weights. In this way, it would be possible to identify the smallest chain length above which the reactive behavior can be considered the same. Furthermore, the associated maximum ΔT^* would allow to derive the smallest temperature at which the calculated values for 1-butene or any other species need to be available to obtain reliable predictions at a given temperature. In this way, the next steps for future studies would be more structured and useless computations may be spared.

A first approximation in this direction can be done as follows: it can be assumed that the increase in the heat capacity from $C_nH_{2n}O$ to $C_{n+1}H_{2(n+1)}O$ is the same as that from C_4H_8O to $C_5H_{10}O$. Then, the heat capacity can be interpolated with a simple polynomial expression as Cv = a1 + a2 T + a3 T^2 + a4 T^3, and the T^* can be determined integrating the Cv thus obtained between T and the unknown T^* such that the final energy is 23.7 kcal mol^{-1}. The results are reported in Table G.4 and G.5 in Appendix G. The plot of the ΔT^* for n = $4 \div 24$ is shown in Figure 4.16. As n increases, the difference in ΔT^* with respect to n-1 decreases more and more. Nevertheless, by looking at this plot it cannot be stated that above a certain n the reactivity behaves in the same way, because ΔT^* keeps decreasing, although it will indeed differ less in the $10 \div 20$ than in the $2 \div 10$ range of n. In any case, the scaling of rate laws is strongly limited by the large difference in ΔT^* between the lightest and the heaviest compounds shown. For instance, when studying combustion of diesel oil, the reactivity of chains with $10 \div 20$ carbon atoms should be included. However, in the approximation proposed the ΔT^* for $C_{10}H_{20}O$ at 300 K is $325 \div 143$ K. This means that, if 1-butene is used as a reference for the predictions, at 300 K the effective temperature $T_{eff} = (T + \Delta T^*_{C_{10}} - \Delta T^*_{C_4})$ is -60 K. In the case of $C_{20}H_{40}O$, this value decreases to -210 K. It is clear that predicting BRs for these heavy molecules is unphysical, and *ab initio* data for a longer chain than 1-butene are required as a starting point. If it is assumed that a reliable scaling can be done when the effective temperature is at least 300 K, which is the lower limit of the 1-butene fit of the phenomenological rates, then for $C_{10}H_{20}O$ and $C_{20}H_{40}O$ reliable predictions can only be achieved above 600 K or 700 K, respectively. This is a good result, because the temperature range considered in combustion studies is usually above 700 K. The behavior at smaller temperature may be for instance extrapolated directly from the BRs. In fact, for the predictions of 1-pentene it was observed that the abrupt inversion of ISC and C_2H_5 channels at low T is avoided when the latter channel is scaled using a polynomial expression for the BR instead of the rate law for the kinetic constant. This may be done for all the channels and a smooth behavior would be obtained, however it might be not representative of the actual reactivity of the system.

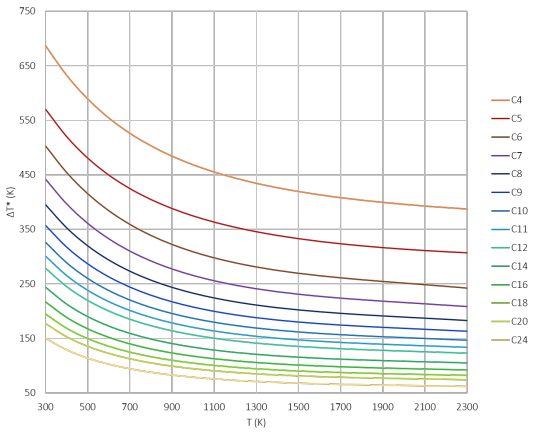

FIGURE 4.16: Plot of ΔT^* for $C_nH_{2n}O$ with n = $4 \div 24$

4.3 Conclusions

In this chapter, the results of the scaling of rate laws for $O(^3P)$ + alkenes were presented. First, the scaling from propylene to 1-butene was obtained. The two PES were compared and relations between reaction channels were established. Then, it was assessed that scaling factors can be determined using the heat capacity of the terminal carbon well only. The resulting predictions were not accurate due to both physical and computational differences. Corrective factors were calculated and imposed to make the predictions consistent, resulting in an error with respect to the calculated values within 5 %. This sets the validity of the approach and encourages further studies for heavier hydrocarbons.

An example of how the scaling of rate laws can be used to predict the BRs for heavier systems was provided applying the scaling to 1-pentene, whose heat capacity was computed *ab initio*, as in the other cases. The BRs were derived using the rate laws of both propylene and 1-butene, and it was concluded that the latter predictions should be more representative, for both the smaller scaling factor used and the larger fitting range of the original data. The predictions for 1-pentene allowed to make several considerations about the risks related to the scaling at low temperature and higher molecular weights. In particular, large scaling factors lead to effective temperatures which are either outside the original fitting range of data or even unphysical negative values. However, the scaling of 1-butene to longer chains may still be meaningful in the range of combustion temperatures. In fact, first estimates for the scaling to $C_{6\div24}$ were proposed, and it was observed that predictions above $600 \div 700$ K should be reliable for chain lengths in the range of diesel. If predictions at lower temperatures are needed, it would be required either to perform KMC-ME simulations for 1-butene below 300 K, or to perform full KMC-ME simulations for 1-pentene. The former option is certainly quicker, however attention must be paid to quantum effects and to the stronger variability with pressure. Furthermore, supposing that the reactivity of 1-butene is derived down to almost 0 K, this would still be insufficient to predict the behavior of $C_{10\div20}$ at room temperature. Therefore, the latter option is strongly encouraged. Calculated BRs for 1-pentene would also allow to further validate the method upon comparison with the predictions done in this work.

Thanks to the success in the predictions proposed, the method may be extended to the full PES, namely to the main singlet channels. In fact, ISC channel groups together all the singlet product branching, which shows similar correspondences between propylene and 1-butene to those observed on the triplet PES. In fact, ISC is followed by the formation of intermediate wells which have roughly the same relative energies with respect to the reactants in both systems, such that the same procedure would be followed. Clearly, this requires the computation of the heat capacities of the wells on the singlet surface. Finally, the global product branching obtained may be integrated in combustion modeling, and the effect of this reaction class on flame properties can be evaluated.

The prediction of rate laws with the scaling factors proposed is an innovative and promising simple way to derive the reactivity of systems which cannot be studied with the benchmark theoretical *ab initio* procedure. This scaling sets up several challenges, which will be faced more easily thanks to the increasing computational power. In this work, a first validation of this approach was provided, and guidelines for exciting future steps were suggested.

Chapter 5

Conclusions

In this thesis, the reaction class of $O(^3P)$ with alkenes was investigated in some of its multiple facets. In particular, a validation of the current theoretical *ab initio* methodology was conducted on the triplet PES and ISC channel of $O(^3P) + C_2H_4$. Then, a new approach for the scaling of kinetic constants determined *ab initio* to derive the reactivity of heavier molecules was proposed.

Concerning *ab initio* calculations for $O(^3P) + C_2H_4$, the same approach of previous studies of $O(^3P) + C_3H_6$ and $O(^3P) + C_4H_8$ was adopted [8, 16]. The final geometries, frequencies and energies were computed using CASPT2. It was shown how the active space must be selected appropriately for each pathway, so as to fully represent the reactive phenomenon. The computation of the energy barriers proved extremely sensitive to the level of theory used, especially in the case of the addition entrance channel. Nevertheless, the kinetic constant finally obtained was comparable to recommended values, with an estimated uncertainty smaller than 20 %. Variational kinetic constants were also computed, using DFT geometries and CC/CBS energies. The reaction rates obtained were smaller than the conventional ones by a factor of about 1.6 and 1.3 for H and CH_2O elimination, respectively. These factors were manually imposed as corrections on the input of the final KMC-ME simulations.

As regards ISC, the MECP was chosen as the geometry maximizing the H_{SO} of S0/T1 coupling. This MECP is about 0.2 kcal mol^{-1} above the well, and its H_{SO} is about 37 cm^{-1}, in accordance with the values found for propylene, 1-butene, and with literature recommendations. Interestingly, it was found that the geometry and energy of the MECP point strongly depend on the method used to localize it, as opposed to what generally stated in literature.

The global reactivity of $O(^3P) + C_2H_4$ was studied with KMC-ME simulations at different pressures in the $300 \div 2500$ K range. The branching ratios obtained showed how ISC prevails at room temperature, being as high as $60 \div 70$ %, and drops rapidly below 20 % at 1000 K. The channel to CH_2O is almost negligible at 300 K, and steadily increases up to $50 \div 60$ %, overcoming the contribution of H elimination at 1900 K. These trends are in agreement with the benchmark *ab initio* calculations of Li et al [10], setting the validity of the method. Instead, the discrepancy with experimental values for the ISC and H elimination channels is most likely due to a non-ergodic behavior of the system, as qualitatively shown in this work.

In the second part of this thesis, a new approach to derive the reactivity of heavier alkenes from that of smaller ones was proposed. The scaling factor was determined from an intrinsic temperature T^*, characteristic of each initial adduct. This T^* corresponds to the temperature needed to reach the internal energy of the well, and was calculated *ab initio* from the heat capacity. This approach was applied to scale the reactivity of the main triplet channels and ISC in propylene to derive that of 1-butene in the $500 \div 2100$ K range. The scaling factor obtained was $T^*_{C_4} - T^*_{C_3} = -180 \div -150$ K. The predictions did not fully correspond to *ab initio* calculations of 1-butene, due to both physical and computational differences in the two systems. Hence, corrective factors were applied and decreased the uncertainty in the predictions to less than 5 %. Furthermore, it was decided to scale the vinoxy channel directly from the central carbon fraction. The good agreement eventually obtained sets a first validation of the approach proposed, and encourages its extension to the full PES and to heavier alkenes.

Then, it was tried to scale kinetic constants of both propylene and 1-butene to 1-pentene. As expected for this heavier system, an increase in the ISC contribution was observed in the full temperature range. It was however noticed that scale factors of heavier hydrocarbons were extremely high in magnitude, especially at low temperature. Hence, the predicted kinetic constants fell outside of the original fitting range of data, resulting in different BRs from the calculated values. To face this issue, it is needed to either perform low temperature simulations for 1-butene, which would allow to extend the fitting range, or to complete *ab initio* KMC-ME simulations for 1-pentene, which would reduce the magnitude of the scaling factors and therefore broaden the validity range of the predictions.

Finally, first estimates for the heat capacities and T^* of $C_{6 \div 24}$ were proposed using a group additivity approach. It was shown that scaling the rate constants of 1-butene allows to obtain reliable predictions above $600 \div 700$ K, which would be useful for combustion studies. For instance, the scaling proposed might be for integrated in kinetic mechanisms of diesel combustion.

Overall, this new approach is extremely promising, and sets up several challenges. First of all, the scaling can be extended to the full singlet product branching using the same procedure; this requires the computation of *ab initio* heat capacities for the main singlet wells. Then, the method can be further validated with *ab initio* calculations for 1-pentene. Finally, an exciting applicative perspective is the integration of these predictions in combustion modeling for the estimation of flame properties, so as to evaluate the effect of this reaction class.

Appendix A

$O(^3P)+C_2H_4$ properties

TABLE A.1: Energies and frequencies of the reactive species of the addition reaction

	$O(^3P)$	**C_2H_4**	**$O(^3P)+C_2H_4$**	**TS**	**TS**	**well**	**well**
Lev of theory for geom, freq, ZPE	ωb97xd/ aug-cc-pVTZ	ωb97xd/ aug-cc-pVTZ	CASPT2(6e,5o)/ aug-cc-pVTZ	ωb97xd/ aug-cc-pVTZ	CASPT2(6e,5o)/ aug-cc-pVTZ	ωb97xd/ aug-cc-pVTZ	CASPT2(6e,5o)/ aug-cc-pVTZ
lev of theory for energy	CCSD(T)/ CBS	CCSD(T)/ CBS	CASPT2(6e,5o)/ aug-cc-pVTZ	CCSD(T)/ CBS	CASPT2(8e,7o)/ aug-cc-pVTZ	CCSD(T)/ CBS	CASPT2(8e,7o)/ aug-cc-pVTZ
E_{el} (Hartree)	-74.9964	-78.4667	-153.3760	-153.4612	-153.3751	-153.5009	-153.4151
ZPE (Hartree)	0	0.0513	0.0509	0.0520	0.0515	0.0512	0.0522
El degeneracy	3	1	3	3	3	3	3
Rot symmetry	1	4	1	2	2	1	1
Ix (GHz)		147.52	24.44	28.12	27.73	43.58	43.43
Iy (GHz)		30.51	0.62	8.69	8.39	10.56	10.52
Iz (GHz)		25.28	0.61	7.29	7.05	9.20	9.17
Freq (cm^{-1})							
1		839.0	i 23.6	i 226.5	i 311.1	152.9	169.5
2		989.3	-1.0	176.1	148.8	422.0	426.5
3		1002.9	32.4	324.1	304.8	514.4	551.9
4		1066.4	827.0	832.7	835.6	775.3	796.3
5		1249.0	918.8	959.0	911.3	928.6	922.5
6		1390.8	947.1	1001.2	960.9	1065.7	1068.5
7		1479.4	1005.3	1003.9	1109.1	1079.9	1100.9
8		1712.6	1198.9	1242.4	1246.2	1131.2	1146.0
9		3145.4	1375.8	1351.4	1339.7	1347.8	1359.6
10		3164.2	1484.0	1478.0	1483.2	1371.5	1407.0
11		3223.8	1669.3	1629.5	1620.3	1450	1467.0
12		3250.3	3180.4	3161.4	3193.3	2802.4	2902.4
13			3197.4	3173.2	3205.1	2987.4	3070.9
14			3266.5	3241.4	3299.3	3169.9	3202.4
15			3291.3	3268.7	3388.9	3285.6	3325.5

TABLE A.2: Energies and frequencies of the reactive species of the H elimination reaction

	well	**well**	**TS**	**TS**	**CH_2CHO**	**H**	**CH_2CHO+H**
Lev of theory for geom, freq, ZPE	ωb97xd/ aug-cc-pVTZ	CASPT2(4e,4o)/ aug-cc-pVTZ	ωb97xd/ aug-cc-pVTZ	CASPT2(4e,4o)/ aug-cc-pVTZ	ωb97xd/ aug-cc-pVTZ	ωb97xd/ aug-cc-pVTZ	CASPT2(4e,4o)/ aug-cc-pVTZ
lev of theory for energy	CCSD(T)/ CBS	CASPT2(10e,9o)/ aug-cc-pVTZ	CCSD(T)/ CBS	CASPT2(10e,9o)/ aug-cc-pVTZ	CCSD(T)/ CBS	CCSD(T)/ CBS	CASPT2(8e,7o)/ aug-cc-pVTZ
E_{el} (Hartree)	-153.5009	-153.4090	-153.4691	-153.3780	-152.9792	-0.4999	-153.3896
ZPE (Hartree)	0.0513	0.0519	0.0448	0.0455	0.0428	0.0000	0.0431
El degeneracy	3	3	3	3	2	2	3
Rot symmetry	1	1	1	1	1	1	1
Ix (GHz)	43.58	42.98	44.05	43.98	67.64	0.00	10.73
Iy (GHz)	10.56	10.45	10.81	10.62	11.56	0.00	4.48
Iz (GHz)	9.20	9.04	9.53	9.33	9.87	0.00	3.49
Freq (cm^{-1})							
1	193.3	188.6	i 986.34	i 973.97	447.4		i 4.66
2	424.4	428.6	400.8	407.3	510.5		i 1.91
3	520.6	547.3	484.6	484.4	763.7		7.2
4	774.9	800.4	533.1	561.6	983.7		459.8
5	927.7	924.0	568.5	616.8	990.9		503.1
6	1067.5	1068.5	747.1	752.6	1168.3		784.1
7	1079.8	1103.0	969.5	967.6	1407.9		983.2
8	1132.6	1142.4	1041.0	1068.1	1481.0		986.2
9	1348.2	1363.8	1168.2	1180.1	1601.5		1187.6
10	1371.3	1396.8	1360.2	1362.4	2971.4		1406.2
11	1449.3	1466.5	1467.4	1468.9	3163.5		1489.6
12	2801.8	2783.9	1491.2	1507.9	3279.6		1568.6
13	2987.2	3061.0	2988.3	3052.0			3040.9
14	3169.0	3200.8	3167.0	3197.0			3194.7
15	3284.8	3324.1	3283.2	3321.7			3318.5

Table A.3: Energies and frequencies of the reactive species of the CH_2O elimination reaction

	well	**well**	**TS**	**TS**	**CH_2**	**CH_2O**	**CH_2+CH_2O**
Lev of theory for geom, freq, ZPE	ωb97xd/ aug-cc-pVTZ	CASPT2(4e,4o)/ aug-cc-pVTZ	ωb97xd/ aug-cc-pVTZ	CASPT2(4e,4o)/ aug-cc-pVTZ	ωb97xd/ aug-cc-pVTZ	ωb97xd/ aug-cc-pVTZ	CASPT2(4e,4o)/ aug-cc-pVTZ
Lev of theory for energy	CCSD(T)/ CBS	CASPT2(10e,10o)/ aug-cc-pVTZ	CCSD(T)/ CBS	CASPT2(10e,10o)/ aug-cc-pVTZ	CCSD(T)/ CBS	CCSD(T)/ CBS	CASPT2(10e,10o)/ aug-cc-pVTZ
E_{el} (Hartree)	-153.5009	-153.4144	-153.4598	-153.3722	-39.0895	-114.3750	-153.3893
ZPE (Hartree)	0.0512	0.0521	0.0469	0.0474	0.0172	0.0268	0.0446
El degeneracy	3	3	3	3	3	1	3
Rot symmetry	1	1	1	1	2	2	1
Ix (GHz)	43.58	43.27	37.44	36.08	1683.72	284.69	30.97
Iy (GHz)	10.56	10.52	7.60	7.76	253.35	39.39	0.51
Iz (GHz)	9.20	9.14	6.63	6.73	220.21	34.60	0.50
Freq (cm^{-1})							
1	152.9	181.9	i 276.35	i 318.52	1066.5	1209.4	i 26.51
2	422.0	425.8	111.1	87.2	3134.1	1271.8	i 13.7
3	514.4	542.2	224.2	227.0	3364.3	1537.0	i 2.28
4	775.3	794.4	252.6	280.2		1851.9	11.9
5	928.6	923.3	430.0	416.6		2911.3	16.0
6	1065.7	1069.7	486.7	528.6		2971.6	20.5
7	1079.9	1090.0	1092.3	1096.3			1100.3
8	1131.2	1144.9	1123.1	1138.6			1183.7
9	1347.8	1361.1	1252.7	1253.8			1273.3
10	1371.5	1403.3	1506.5	1501.0			1545.4
11	1450.0	1466.7	1696.7	1641.7			1766.4
12	2802.4	2887.2	2913.0	2989.3			2991.7
13	2987.4	3062.4	2971.0	3069.3			3071.9
14	3169.9	3202.5	3138.9	3166.5			3178.2
15	3285.6	3325.7	3366.0	3398.2			3412.7

Table A.4: Energies, frequencies and H_{SO} of the MECP points of ISC

	S0/T1	**S0/T1**	**S1/T2**	**S1/T2**	**S1/T2**	**S1/T2**	**S1/T2**	**S0/T2**	**S0/T2**
optg	T1	T1	T1	T1	T1	S1	S1	T1	T1
MECP	max SOC	min S0/T1	max SOC	min S1/T2	min T1	min T1	min S1	min S0/T2	min T1
E_{el} (Hartree)	-153.4131	-153.4135	-153.4063	-153.4064	-153.4050	-153.4079	-153.4082	-153.4079	-153.4070
$E_{el,T1}$ (Hartree)	-153.4131	-153.4135	-153.4120	-153.4129	-153.4144	-153.4133	-153.4132	-153.4114	-153.4117
ZPE (Hartree)	0.0513	0.0523	0.0517	0.0518	0.0522	0.0518	0.0517	0.0504	0.0508
rot symmetry	1	1	1	1	1	1	1	1	1
H_{SO} (cm^{-1})	37.25	31.40	30.93	5.43	11.32	35.65	37.88	35.65	37.88
Ix (GHz)	9.32	9.38	9.50	9.36	9.12	9.05	9.09	9.32	9.40
Iy (GHz)	10.49	10.73	10.82	11.20	10.51	10.39	10.54	11.29	11.41
Iz (GHz)	40.66	40.11	38.54	40.19	43.60	42.95	42.41	40.02	39.42
Freq (cm^{-1})									
1	i 66.41	110.4	i 148.79	213.8	181.9	135.0	157.9	i 592.3	i 445.8
2	399.6	424.0	393.0	343.2	426.7	400.2	385.6	108.0	212.5
3	625.7	598.3	586.9	521.5	546.2	511.6	494.9	495.9	485.8
4	688.2	768.1	667.3	775.5	802.2	768.6	806.0	646.1	682.9
5	908.7	924.7	900.9	930.3	918.1	884.8	876.6	905.6	920.3
6	981.2	1049.2	956.3	978.4	1066.6	997.6	969.9	979.7	986.1
7	1085.4	1089.3	1079.8	1071.4	1101.9	1089.5	1092.9	1070.3	1064.5
8	1226.5	1153.3	1221.7	1146.8	1149.1	1137.8	1130.4	1169.0	1162.5
9	1331.1	1336.1	1307.6	1323.6	1360.6	1340.6	1330.1	1304.2	1319.8
10	1420.4	1420.2	1426.2	1440.1	1405.9	1415.8	1422.4	1452.6	1451.4
11	1484.1	1475.4	1481.7	1458.4	1465.8	1463.1	1461.2	1470.6	1479.5
12	3004.7	2972.0	3030.0	2922.8	2892.6	2985.1	2982.5	2963.1	2959.6
13	3089.9	3101.1	3107.0	3070.8	3062.1	3065.2	3059.3	3038.2	3050.8
14	3197.5	3201.0	3202.2	3197.8	3200.8	3205.5	3207.8	3199.7	3202.2
15	3314.2	3321.5	3321.4	3324.23	3323.95	3331.04	3334.12	3327.76	3331.37

Table A.5: Properties of MECP at different levels of theory

	this work	**MOLPRO**	**MOLPRO**	**NST**
Lev of theory for geom	CASSCF(6e,5o)/ aug-cc-pVTZ	CASSCF(6e,5o)/ aug-cc-pVTZ	CASSCF(6e,5o)/ 6-311+g(d,p)	mo62x/ 6-311+g(d,p)
lev of theory freq, energy	CASSCF(6e,5o)/ aug-cc-pVTZ	CASSCF(6e,5o)/ aug-cc-pVTZ	CASSCF(6e,5o)/ aug-cc-pVTZ	CASSCF(6e,5o)/ aug-cc-pVTZ
E_{T1} (Hartree)	-153.4131	-153.4119	-153.4115	-153.4136
E_{S0} (Hartree)	-153.4131	-153.4128	-153.4123	-153.4128
ΔE_{T1-S0} (kcal/mol)	0.000	0.578	0.510	-0.471
ZPE (Hartree)	0.051	0.059	0.051	0.052
$\Delta H_{T1-well}$ (kcal/mol)	0.251	5.673	1.047	0.333
H_{SO} (cm^{-1})	37.25	39.22	5.11	10.19
Geometry				
O-C1-C2 (°)	112.600	112.515	114.455	114.750
O-C1-C2-H2 (°)	84.500	-78.611	-23.419	28.432
O-C1 (Å)	1.401	1.440	1.419	1.487
Freq (cm^{-1})				
1	i 273.7	i 5473.2	i 347.6	347.3
2	388.7	i 582.88	361.5	446.2
3	453.0	383.0	469.8	604.7
4	652.8	674.7	537.4	829.8
5	879.4	831.4	837.3	914.1
6	946.8	1076.3	985.8	1076.3
7	1086.8	1139.0	1072.1	1098.5
8	1260.5	1291.5	1117.7	1171.3
9	1327.4	1429.4	1325.8	1377.9
10	1424.9	1482.1	1396.1	1409.8
11	1490.2	1675.2	1448.7	1475.5
12	3021.7	3057.3	3068.7	2767.7
13	3074.8	3123.5	3128.5	2916.5
14	3196.7	3234.8	3235.5	3100.4
15	3312.4	6348.0	3355.7	3220.2

Table A.6: Properties along the variational reaction pathway of the addition reaction

distance	**1.97**	**2.02**	**2.07**	**2.13**	**2.18**	**2.24**	**2.29**
Lev of theory	ωb97xd/ aug-cc-pVTZ	ωb97xd/ aug-cc-pVTZ	ωb97xd/ aug-cc-pVTZ	ωb97xd/ aug-cc-pVTZ	ωb97xd/ aug-cc-pVTZ	ωb97xd/ aug-cc-pVTZ	ωb97xd/ aug-cc-pVTZ
E_{el} (kcal/mol)	0.90	1.45	1.73	1.87	1.83	1.76	1.69
Freq (cm^{-1})							
1	i 226.48	i 226.48	i 226.48	i 226.48	i 226.48	i 226.48	i 226.48
2	242.4	220.5	199.4	171.1	156.8	145.6	139.3
3	379.1	364.2	346.9	318.4	299.8	283.7	269.5
4	821.4	826.6	829.9	833.3	834.5	835.5	836.3
5	894.6	918.9	938.8	963.2	973.2	980.9	986.4
6	957.2	972.3	987.0	1001.7	1001.2	1002.5	1004.0
7	1015.8	1006.2	1001.6	1007.3	1015.7	1022.8	1028.4
8	1240.8	1241.2	1241.6	1242.7	1243.4	1244.1	1244.8
9	1301.3	1319.6	1335.3	1354.7	1362.8	1368.9	1373.4
10	1474.5	1475.8	1476.8	1478.3	1478.9	1479.5	1479.9
11	1580.8	1595.7	1610.7	1633.9	1645.5	1655.3	1663.3
12	3162.0	3162.9	3162.5	3160.9	3160.1	3159.2	3158.4
13	3171.4	3172.0	3172.7	3173.1	3173.1	3172.9	3172.5
14	3239.0	3241.1	3241.8	3241.1	3240.4	3239.6	3238.8
15	3272.2	3270.9	3269.9	3268.2	3267.4	3266.5	3265.7

Table A.7: Properties along the variational reaction pathway of the H elimination reaction

distance	**1.30**	**1.50**	**1.70**	**1.75**	**1.85**	**2.00**	**2.10**	**2.20**
Lev of theory	ωb97xd/ aug-cc-pVTZ	ωb97xd/ aug-cc-pVTZ	ωb97xd/ aug-cc-pVTZ	ωb97xd/ aug-cc-pVTZ	ωb97xd/ aug-cc-pVTZ	ωb97xd/ aug-cc-pVTZ	ωb97xd/ aug-cc-pVTZ	ωb97xd/ aug-cc-pVTZ
E_{el} (kcal/mol)	14.74	15.63	15.89	15.90	15.80	15.51	15.08	14.56
Freq (cm^{-1})								
1	i 986.34	i 986.34	i 986.34	i 986.34	i 986.34	i 986.34	i 986.34	i 986.34
2	753.4	691.9	3284.0	3283.7	3283.0	3282.3	3281.8	3281.4
3	641.1	614.3	3167.7	3167.5	3166.8	3166.2	3165.7	3165.3
4	483.2	487.9	2987.4	2987.7	2988.5	2988.6	2988.2	2987.4
5	379.3	395.3	1488.7	1489.3	1492.5	1497.7	1504.3	1512.3
6	3286.2	3284.8	1464.2	1465.2	1468.4	1471.6	1474.0	1476.0
7	3170.0	3168.6	1354.3	1356.2	1362.2	1368.5	1374.2	1379.6
8	2983.0	2986.0	1167.8	1167.9	1168.4	1169.3	1170.5	1171.7
9	1487.5	1487.4	1056.0	1050.7	1037.1	1027.0	1014.7	1007.0
10	1457.8	1461.1	968.2	968.6	970.0	971.4	972.1	972.7
11	1341.2	1348.4	743.8	744.4	748.7	753.7	757.6	760.6
12	1169.4	1168.0	630.4	609.3	549.6	511.6	509.2	508.9
13	1097.0	1071.9	572.9	558.5	523.9	503.1	476.5	465.4
14	967.4	967.2	489.2	488.8	479.8	452.2	412.0	368.7
15	812.8	750.9	401.5	402.2	398.5	384.3	357.5	326.2

Table A.8: Properties along the variational reaction pathway of the CH_2O elimination reaction

distance	**1.9**	**2**	**2.1**	**2.2**	**2.3**	**2.4**	**2.6**	**2.8**
Lev of theory	ωb97xd/ aug-cc-pVTZ	ωb97xd/ aug-cc-pVTZ	ωb97xd/ aug-cc-pVTZ	ωb97xd/ aug-cc-pVTZ	ωb97xd/ aug-cc-pVTZ	ωb97xd/ aug-cc-pVTZ	ωb97xd/ aug-cc-pVTZ	ωb97xd/ aug-cc-pVTZ
E_{el} (kcal/mol)	22.37	22.60	22.81	22.97	23.04	22.98	22.73	22.43
Freq (cm^{-1})								
1	i 276.35	i 276.35	i 276.35	i 276.35	i 276.35	i 276.35	i 276.35	i 276.35
2	HR	HR	HR	HR	HR	HR	HR	HR
3	180.0	192.2	206.8	222.0	232.4	253.0	268.3	278.1
4	206.7	221.4	237.1	253.4	265.3	291.1	310.9	324.4
5	334.3	358.3	387.3	419.9	442.8	493.3	533.1	558.8
6	400.2	424.2	1095.2	477.8	496.5	536.1	568.1	591.8
7	1085.1	1090.5	1125.4	1095.2	1088.4	1065.1	1044.1	1028.9
8	1144.6	1134.6	1256.2	1121.8	1125.5	1141.7	1157.4	1169.6
9	1260.2	1258.3	1514.1	1253.8	1251.9	1247.8	1244.3	1241.8
10	1521.5	1518.3	1727.8	1508.9	1504.4	1492.3	1478.8	1466.8
11	1763.5	1747.1	2912.7	1705.0	1688.0	1650.4	1620.9	1602.3
12	2913.1	2912.9	2969.6	2912.5	2912.5	2912.7	2913.4	2914.2
13	2969.4	2969.4	3138.0	2970.2	2970.8	2973.0	2975.5	2977.7
14	3136.9	3137.5	3367.2	3138.8	3139.3	3140.2	3140.8	3141.2
15	3367.8	3367.6	450.1	3366.5	3365.7	3363.4	3360.7	3358.4

Appendix B

$O(^3P)+C_2H_4$ kinetic constants

TABLE B.1: High P kinetic constants for the addition reaction in $cm^3molec^{-1}s^{-1}$

T(K)	**Khaled et al**	**Baulch et al**	**Li et al**	**this work**	**this work(var)**	**corr$_{E_A}$**	**this work(var)$_{corr}$**
300	7.78E-13	7.52E-13	7.39E-13	9.03E-13	2.78E-13	2.56	7.10E-13
400	1.47E-12	1.39E-12	1.44E-12	1.69E-12	6.73E-13	2.02	1.36E-12
500	2.32E-12	2.22E-12	2.33E-12	2.64E-12	1.23E-12	1.76	2.15E-12
600	3.29E-12	3.22E-12	3.40E-12	3.74E-12	1.91E-12	1.60	3.06E-12
700	4.38E-12	4.40E-12	4.62E-12	4.97E-12	2.71E-12	1.50	4.06E-12
800	5.57E-12	5.76E-12	6.01E-12	6.33E-12	3.62E-12	1.42	5.15E-12
900	6.85E-12	7.27E-12	7.53E-12	7.80E-12	4.62E-12	1.37	6.31E-12
1000	8.21E-12	8.96E-12	9.19E-12	9.37E-12	5.70E-12	1.33	7.55E-12
1100	9.65E-12	1.08E-11	1.10E-11	1.10E-11	6.86E-12	1.29	8.86E-12
1200	1.12E-11	1.28E-11	1.29E-11	1.28E-11	8.09E-12	1.26	1.02E-11
1300	1.27E-11	1.50E-11	1.50E-11	1.46E-11	9.38E-12	1.24	1.16E-11
1400	1.44E-11	1.73E-11	1.71E-11	1.66E-11	1.07E-11	1.22	1.31E-11
1500	1.61E-11	1.98E-11	1.94E-11	1.85E-11	1.21E-11	1.21	1.47E-11
1600		2.24E-11	2.18E-11	2.06E-11	1.36E-11	1.19	1.62E-11
1700		2.52E-11	2.43E-11	2.28E-11	1.51E-11	1.18	1.78E-11
1800		2.82E-11	2.69E-11	2.50E-11	1.67E-11	1.17	1.95E-11
1900		3.13E-11	2.96E-11	2.72E-11	1.83E-11	1.16	2.12E-11
2000		3.45E-11	3.24E-11	2.96E-11	1.99E-11	1.15	2.29E-11
2100		3.79E-11	3.53E-11	3.20E-11	2.16E-11	1.14	2.47E-11
2200		4.15E-11	3.83E-11	3.44E-11	2.34E-11	1.14	2.66E-11
2300		4.52E-11	4.14E-11	3.69E-11	2.51E-11	1.13	2.84E-11
2400		4.90E-11	4.46E-11	3.95E-11	2.69E-11	1.12	3.03E-11
2500		5.30E-11	4.79E-11	4.21E-11	2.88E-11	1.12	3.22E-11

TABLE B.2: Kinetic constants for the H elimination reaction in s^{-1}

T (K)	**1 bar**	**10 bar**	**100 bar**	**1000 bar**	**10000 bar**	**high P limit**
300	8.14E+00	8.92E+00	9.04E+00	9.05E+00	9.05E+00	9.05E+00
400	4.61E+03	6.13E+03	6.53E+03	6.59E+03	6.59E+03	6.59E+03
500	1.88E+05	3.24E+05	3.86E+05	3.97E+05	3.99E+05	3.99E+05
600	1.91E+06	4.31E+06	6.07E+06	6.57E+06	6.63E+06	6.64E+06
700	8.73E+06	2.50E+07	4.30E+07	5.05E+07	5.17E+07	5.19E+07
800	2.49E+07	8.56E+07	1.80E+08	2.37E+08	2.49E+08	2.50E+08
900	5.33E+07	2.10E+08	5.26E+08	7.86E+08	8.60E+08	8.71E+08
1000	9.52E+07	4.14E+08	1.19E+09	2.04E+09	2.35E+09	2.40E+09
1100		7.07E+08	2.27E+09	4.38E+09	5.38E+09	5.57E+09
1200		1.09E+09	3.80E+09	8.18E+09	1.08E+10	1.14E+10
1300			5.81E+09	1.37E+10	1.94E+10	2.09E+10
1400			8.30E+09	2.12E+10	3.21E+10	3.55E+10
1500				3.06E+10	4.95E+10	5.64E+10
1600				4.20E+10	7.23E+10	8.51E+10
1700				5.55E+10	1.01E+11	1.23E+11
1800				7.09E+10	1.35E+11	1.70E+11
1900				8.81E+10	1.75E+11	2.29E+11
2000					2.22E+11	2.99E+11
2100					2.74E+11	3.82E+11
2200					3.31E+11	4.79E+11
2300					3.94E+11	5.88E+11
2400					4.62E+11	7.12E+11
2500					5.35E+11	8.50E+11

TABLE B.3: Variational kinetic constants for the H elimination reaction in s^{-1}

T (K)	**1 bar**	**10 bar**	**100 bar**	**1000 bar**	**10000 bar**	**high P limit**
300	7.39E+00	8.05E+00	8.15E+00	8.16E+00	8.16E+00	8.16E+00
400	4.26E+03	5.58E+03	5.91E+03	5.96E+03	5.96E+03	5.96E+03
500	1.76E+05	2.97E+05	3.49E+05	3.58E+05	3.59E+05	3.60E+05
600	1.81E+06	3.98E+06	5.49E+06	5.89E+06	5.94E+06	5.95E+06
700	8.36E+06	2.33E+07	3.90E+07	4.51E+07	4.60E+07	4.61E+07
800	2.40E+07	8.06E+07	1.64E+08	2.10E+08	2.20E+08	2.21E+08
900	5.16E+07	1.99E+08	4.82E+08	6.98E+08	7.55E+08	7.63E+08
1000	9.24E+07	3.94E+08	1.10E+09	1.81E+09	2.05E+09	2.09E+09
1100		6.75E+08	2.10E+09	3.90E+09	4.67E+09	4.81E+09
1200		1.04E+09	3.54E+09	7.29E+09	9.30E+09	9.72E+09
1300			5.43E+09	1.23E+10	1.67E+10	1.78E+10
1400			7.77E+09	1.90E+10	2.75E+10	2.99E+10
1500			1.06E+10	2.75E+10	4.24E+10	4.73E+10
1600				3.79E+10	6.19E+10	7.08E+10
1700				5.01E+10	8.62E+10	1.01E+11
1800				6.40E+10	1.15E+11	1.40E+11
1900				7.97E+10	1.50E+11	1.87E+11
2000				9.71E+10	1.89E+11	2.43E+11
2100					2.34E+11	3.08E+11
2200					2.83E+11	3.83E+11
2300					3.36E+11	4.69E+11
2400					3.94E+11	5.64E+11
2500					4.56E+11	6.69E+11

TABLE B.4: Kinetic constants for the CH_2O elimination reaction in s^{-1}

T (K)	**1 bar**	**10 bar**	**100 bar**	**1000 bar**	**10000 bar**	**high P limit**
300	9.95E-05	1.13E-04	1.16E-04	1.16E-04	1.16E-04	1.16E-04
400	2.17E+00	3.03E+00	3.30E+00	3.34E+00	3.34E+00	3.35E+00
500	7.45E+02	1.34E+03	1.64E+03	1.71E+03	1.72E+03	1.72E+03
600	3.06E+04	7.02E+04	1.02E+05	1.13E+05	1.15E+05	1.15E+05
700	3.67E+05	1.05E+06	1.87E+06	2.27E+06	2.34E+06	2.36E+06
800	2.04E+06	7.13E+06	1.55E+07	2.12E+07	2.27E+07	2.30E+07
900	6.93E+06	2.84E+07	7.45E+07	1.18E+08	1.33E+08	1.36E+08
1000	1.71E+07	7.90E+07	2.44E+08	4.51E+08	5.46E+08	5.66E+08
1100	3.40E+07	1.72E+08	6.08E+08	1.30E+09	1.72E+09	1.82E+09
1200	5.85E+07	3.18E+08	1.25E+09	3.05E+09	4.42E+09	4.83E+09
1300		5.21E+08	2.22E+09	6.07E+09	9.71E+09	1.11E+10
1400		7.85E+08	3.56E+09	1.07E+10	1.88E+10	2.25E+10
1500			5.28E+09	1.72E+10	3.31E+10	4.16E+10
1600			7.41E+09	2.57E+10	5.35E+10	7.14E+10
1700				3.62E+10	8.10E+10	1.15E+11
1800				4.89E+10	1.16E+11	1.75E+11
1900				6.36E+10	1.60E+11	2.56E+11
2000					2.11E+11	3.61E+11
2100					2.71E+11	4.91E+11
2200					3.39E+11	6.50E+11
2300					4.15E+11	8.40E+11
2400					4.99E+11	1.06E+12
2500					5.91E+11	1.32E+12

TABLE B.5: Variational kinetic constants for the CH_2O elimination reaction in s^{-1}

T (K)	**1 bar**	**10 bar**	**100 bar**	**1000 bar**	**10000 bar**	**high P limit**
300	9.52E-05	1.08E-04	1.10E-04	1.10E-04	1.10E-04	1.10E-04
400	2.08E+00	2.86E+00	3.08E+00	3.12E+00	3.12E+00	3.12E+00
500	7.17E+02	1.26E+03	1.52E+03	1.57E+03	1.57E+03	1.57E+03
600	2.96E+04	6.60E+04	9.35E+04	1.02E+05	1.03E+05	1.03E+05
700	3.56E+05	9.95E+05	1.70E+06	2.01E+06	2.06E+06	2.07E+06
800	1.99E+06	6.76E+06	1.41E+07	1.86E+07	1.96E+07	1.97E+07
900	6.79E+06	2.71E+07	6.79E+07	1.02E+08	1.13E+08	1.14E+08
1000	1.67E+07	7.56E+07	2.24E+08	3.90E+08	4.56E+08	4.67E+08
1100	3.34E+07	1.66E+08	5.60E+08	1.13E+09	1.42E+09	1.48E+09
1200	5.75E+07	3.06E+08	1.15E+09	2.64E+09	3.61E+09	3.85E+09
1300		5.04E+08	2.06E+09	5.28E+09	7.87E+09	8.65E+09
1400		7.60E+08	3.32E+09	9.35E+09	1.52E+10	1.73E+10
1500			4.94E+09	1.51E+10	2.66E+10	3.15E+10
1600			6.95E+09	2.26E+10	4.30E+10	5.31E+10
1700				3.20E+10	6.51E+10	8.41E+10
1800				4.33E+10	9.34E+10	1.26E+11
1900				5.64E+10	1.28E+11	1.82E+11
2000				7.14E+10	1.70E+11	2.52E+11
2100					2.18E+11	3.39E+11
2200					2.73E+11	4.43E+11
2300					3.35E+11	5.65E+11
2400					4.02E+11	7.06E+11
2500					4.76E+11	8.66E+11

Appendix C

CH_2 pathway: high level AS

In this section, the alternative active spaces tried for the CH_2O elimination reaction are presented. A possible single-state AS with 10 electrons in 10 orbitals is shown in Figure C.1. In this case, instead of including the C-H bonds of the CH_2O group, those of CH_2 are included. This indeed results in a more consistent representation of the C1-O bonding. However, this active space applied to the well resulted in the intrusion of Rydberg orbital, therefore calculations using the same AS were also performed on the product at a fixed distance of 10 Å. The resulting high level energies are in Table C.1. Due to the inconsistency of the CASPT2 results for the well (in red), the energy of the backward reaction was computed first as $E_{A,BW} = (E_{TS} + ZPE_{TS})_{CASPT2} - (E_{prod1})_{CASPT2} - (ZPE_{prod1})_{CC}$. The CASPT2 ZPE was not used for the product as it is meaningless. IPEA shift was used for CASPT2 energies. Then, the forward activation energy was simply computed as $E_{A,FW} = E_{A,BW} + \Delta H_{CC}$. The values found are extremely close to those of the active space presented in the results.

Alternatively, a two-state averaged active space was tried, as it was done for the high level of H elimination. Only in this way the lone pair was included. The AS contained one orbital and two electrons more, resulting in a CASPT2(12e,11o)/aug-cc-pVTZ. The space was opened using two states since the beginning and the larger basis set. Two orbital rotations were necessary. The result is shown in Figure C.2: orbitals 10.1-14.1 and 12.1-13.1 correspond to the electrons included in the level1 AS, although the occupancy of 12.1 is higher because of the partial inclusion of the lone pair on oxygen. The remaining part of the lone pair is on orbital 11.1. Then, 7.1 clearly captures the C1-O σ bond, whereas the anti-bond is captured together with the anti-bond of C2-H (bond at 9.1), in the orbitals 16.1-17.1. Finally, 9.1-15.1 show electron density associated with a C-H bond on CH_2. The $E_{A,FW}$ was computed from CIPT2 energies (CIPT2 is a multi-reference method used only in this case because the others did not converge), and it resulted in an underestimation of the barriers of about 0.7 kcal mol^{-1}, leading to comparable values to those obtained at coupled cluster level. The results with a single state were considered more representative of the reaction. Nevertheless, the extreme sensitivity of the energies to the AS used is an indication of the actual uncertainty of all the barriers obtained.

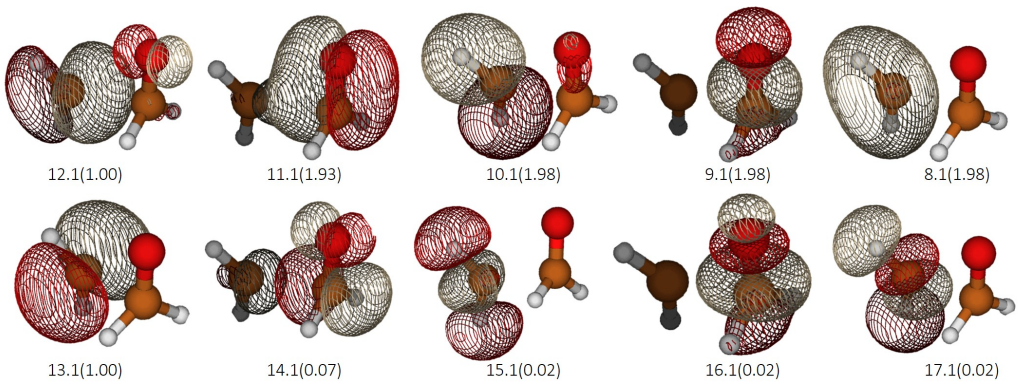

FIGURE C.1: Electron density and orbital occupancy at high level for the TS of CH_2O elimination at CASPT2(10e,10o)

TABLE C.1: High level energies for the CH_2O elimination step with 10e,10o including C-H bonds of CH_2

high level energies (Hartree)						
	RS2	**shift=0.2**	**IPEA=0.25**	**CC**	**ZPE_{CC}**	**ZPE_{CASPT2}**
well	-153.4249	-153.4165	-153.4106	-153.5009	0.0513	0.0521
TS	-153.3853	-153.3776	-153.3720	-153.4598	0.0469	0.0474
prod1	-153.3893	-153.3812	-153.3768	-114.3750	0.0268	0.0446
prod2				-39.0895	0.0172	
Final energies						
	ΔE_{CC}	**ΔH_{CC}**	**$E_{A,FW}$**	**E_{A,FW_CC}**	**$E_{A,BW}$**	**E_{A,BW_CC}**
(Hartree)	0.0364	0.0291	0.0373	0.0366	0.0082	0.0075
(kcal/mol)	22.86	18.26	23.39	22.98	5.13	4.73

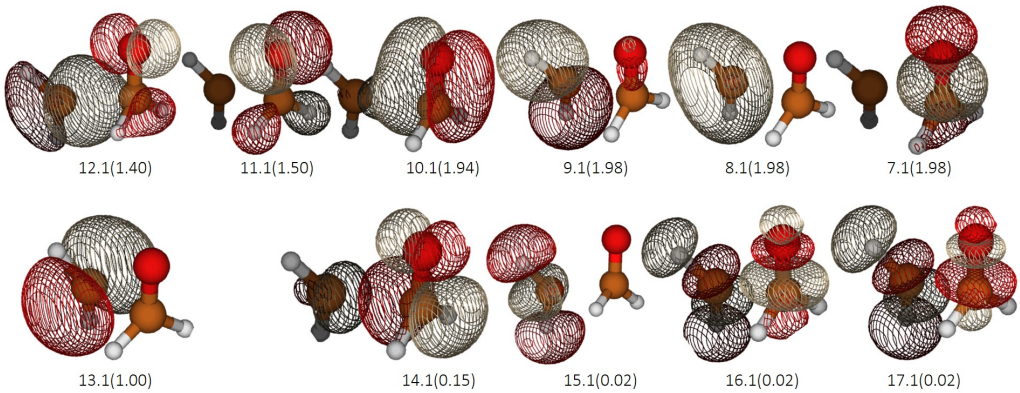

FIGURE C.2: Electron density and orbital occupancy at high level for the TS of CH_2O elimination at CASPT2(12e,11o)/aug-cc-pVTZ with 2 state averaging

TABLE C.2: High level energies for the CH_2O elimination step with 12e,11o and 2-state averaging

high level energies (Hartree)						
	RS2	**shift=0.2**	**IPEA=0.25**	**CC**	**ZPE_{CC}**	**ZPE_{CASPT2}**
well	-153.4229	-153.4186	-153.4114	-153.5009	0.0513	0.0521
TS	-153.3792	-153.3780	-153.3704	-153.4598	0.0469	0.0474
prod1				-114.3750	0.0268	
prod2				-39.0895	0.0172	
Final energies						
	ΔE_{CC}	**ΔH_{CC}**	**$E_{A,FW}$**	**E_{A,FW_CC}**	**$E_{A,BW}$**	**E_{A,BW_CC}**
(Hartree)	0.0364	0.0291	0.0363	$0.036\bar{6}$	0.0073	$0.007\bar{5}$
(kcal/mol)	22.86	18.26	22.81	22.98	4.55	4.73

Appendix D

$O(^3P)+C_2H_4$ ISC

In this section, the calculations done for the S0/T2 and S1/T2 intersections are presented in detail. As anticipated, the level of geometry optimization was T1 rather than the analyzed PES (S0, S1 or T2). This choice derives from the need of consistency with the initial state of the molecule, which lies on T1 PES. Also geometry optimizations at S0, T2 and S1 levels were tried: the AS was selected on the well geometry at T1 using CASSCF with two-state averaging; then, RS2 was applied on the excited state for optimization at T2; for the singlet states, the CASSCF was modified to singlet and then RS2 applied on either the ground or the excited state for S0 and S1, respectively. However, optimization at T2 never converged, S0 optimization resulted in no S0/T2 crossing, whereas S1 optimization was the only one actually used to find S1/T2 crossing points as an alternative to T1.

The PES and corresponding isoenergy lines for S0/T2 crossing are shown in Figure D.1, and the corresponding data with respect to S0 minimum energy are in Tables D.3 and D.6. The MECP region is localized around a small region of aabs1=106 ÷ 107° and babs1=0°. The energies of the states T1 and T2 along the intersection line (whose coordinates are in Table D.2) are plotted in Figure D.2: two points were analyzed further, namely the one minimizing T1 energy at 106° and the one minimizing T2 energy at 107°, whose structures are shown on the right. As reported in Table D.1, both points have similar H_{SO}, and the only significant difference is the barrier with respect to the well, 1 kcal mol^{-1} higher at 106°. In both cases, a negative frequency was found, corresponding to O-C1-C2 bending. For consistency, the final MECP point would be taken as that minimizing T1, considering that it also maximizes the hopping probability.

As regards S1/T2, the two-dimensional PES for the two states with geometry optimized at level T1 is shown in Figure D.3, together with the isoenergy lines corresponding to (T2-S1). The data of the two PES are in Table D.4 and D.6. In this case, asymmetric points were investigated due to the increase in the T1 energy in the central crossing region at smaller angles. However, also the central symmetric point was considered, as it was found to maximize the coupling. The coordinates along the intersection line are in Table D.2, and the energies of T1 and T2 along this line are plotted in Figure D.4 together with the structures of the corresponding energy minima. In the asymmetric structures, the H_{SO} is extremely small, resulting in a

small contribution to the total hopping probability. The symmetric high energy point yielded instead a high coupling of about 30 cm^{-1}. Trials with optimization at S1 level led to distorted geometries and higher H_{SO}, as reported in Table D.1. The only structure resulting in a similar H_{SO} as Li et Al [10] is the symmetric one, which is however characterized by a barrier smaller by 1 kcal mol^{-1}. The final structures considered would correspond to the one maximizing H_{SO}, also in light of the negative frequency found. However, the contribution from S1/T2 crossing would be indeed mitigated by the high barrier found.

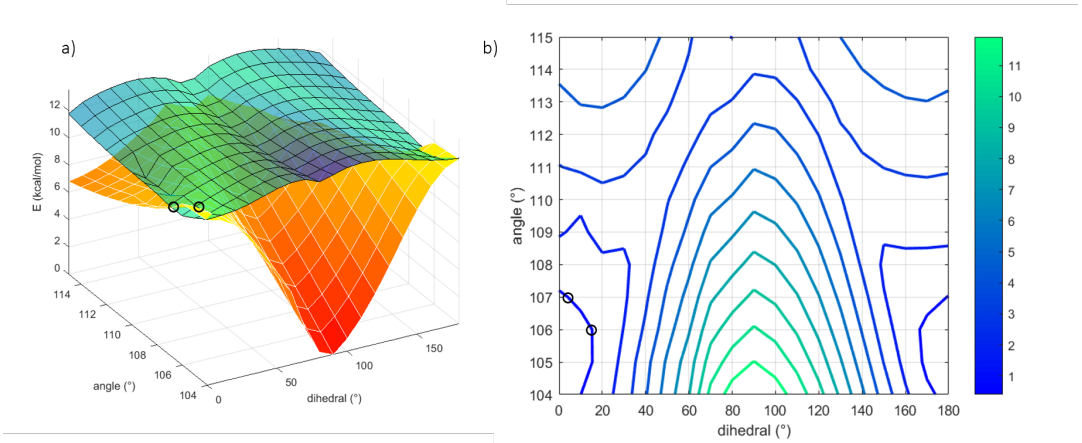

FIGURE D.1: a) PES around MECP as a function of C2-C1-O angle and O-C1-C2-H2 dihedral (S0 in red and T2 in blue) b) Isoenergy level lines for (T2-S0) around MECP

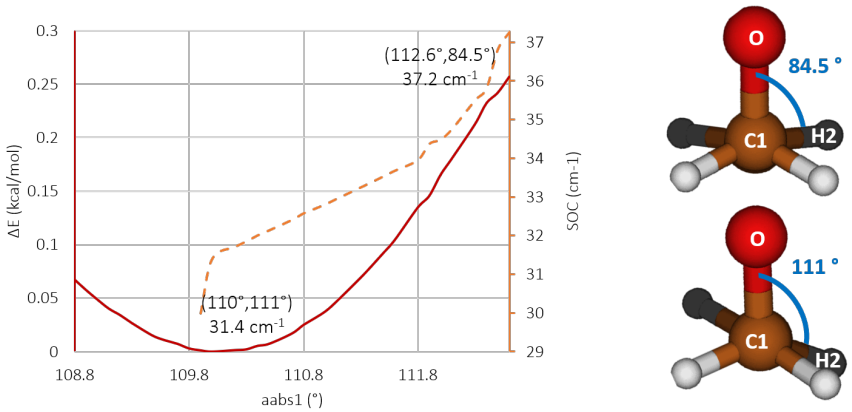

FIGURE D.2: MEP and H_{SO} around to find the MECP for S0T2 and relative structures considered

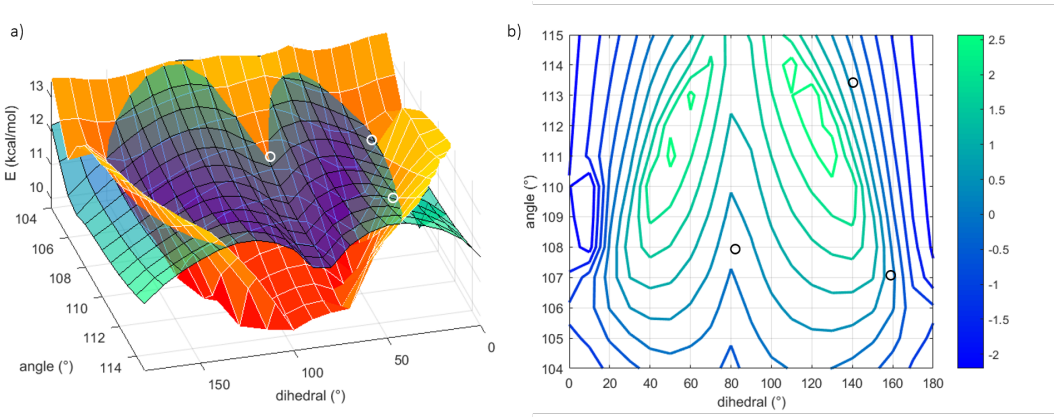

FIGURE D.3: a) PES around MECP as a function of C2-C1-O angle and O-C1-C2-H2 dihedral (S1 in red and T2 in blue) b) Isoenergy level lines for (T2-S1) around MECP

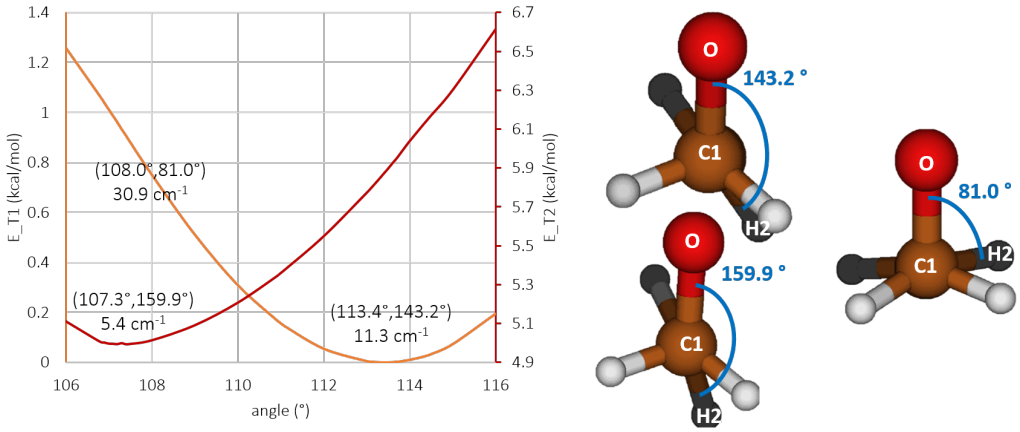

FIGURE D.4: MEP and H_{SO} around to find the MECP for S1T2 and relative structures considered

Table D.1: MECP points found for different couplings in detail

aabs1 (∘)	**b1** (∘)	**states** -	**optg** -	**MECP** -	**neg freq** -	**H** **(hartree)**	$\mathbf{H_{T1}}$ **(hartree)**	$\mathbf{\Delta H_{(T1-well)}}$ **(kcal/mol)**	$\mathbf{\Delta H_{well}}$ **(kcal/mol)**	$\mathbf{\Delta H_{well}}$[10] **(kcal/mol)**	$\mathbf{H_{SO}}$ $\mathbf{cm^{-1}}$	$\mathbf{H_{SO}}$[10] $\mathbf{cm^{-1}}$
112.6	84.5	S0/T1	T1	max SOC	Y (babs1)	-153.3618	-153.3618	0.251	0.251	0	37.3	19.0
110	111	S0/T1	T1	min S0/T1	N	-153.3615	-153.3615	0.449	0.449	0	31.4	19.0
108	81	S1/T2	T1	max SOC	Y (babs1)	-153.3546	-153.3603	1.196	4.771	3.4	30.9	30.0
107.3	159.9	S1/T2	T1	min S1/T2	N	-153.3551	-153.3611	0.658	4.421	3.4	5.4	30.0
113.4	143.2	S1/T2	T1	min T1	N	-153.3533	-153.3622	-0.009	5.603	3.4	11.3	30.0
113.3	136.5	S1/T2	S1	min T1	N	-153.3564	-153.3615	0.414	3.606	3.4	23.8	30.0
112.1	143	S1/T2	S1	min S1	N	-153.3568	-153.3614	0.483	3.368	3.4	22.7	30.0
107	1.5	S0/T2	T1	min S0/T2	Y (aabs1)	-153.3574	-153.3610	0.730	2.980	3.8	35.6	6.7
106	9.4	S0/T2	T1	min T1	Y (aabs1)	-153.3562	-153.3609	0.822	3.768	3.8	37.9	6.7

TABLE D.2: (angle,dihedral) of MECP for different S/T configurations

S0T1		**S0T2**		**S1T2**	
angle(°)	**dihedral**(°)	**angle**(°)	**dihedral**(°)	**angle**(°)	**dihedral**(°)
108.8	119.9	105.0	10.5	116.0	130.0
108.9	119.2	105.7	10.5	115.0	135.7
109.0	118.5	105.8	10.3	114.5	138.5
109.1	117.8	105.9	10.0	114.4	139.0
109.2	117.0	106.0	9.4	114.3	139.5
109.3	116.3	106.1	8.6	114.0	141.0
109.4	115.6	106.2	7.8	113.9	141.4
109.5	114.9	106.3	6.7	113.8	141.7
109.6	114.1	106.4	5.6	113.7	142.0
109.7	113.3	106.5	4.4	113.6	142.4
109.8	112.6	106.6	3.1	113.5	142.8
109.9	111.8	106.7	1.6	113.4	143.2
110.0	111.0	106.8	-0.5	113.3	143.6
110.1	110.1	106.9	0.6	113.2	144.0
110.2	109.3	107.0	1.5	113.1	144.4
110.3	108.5			113.0	144.8
110.4	107.6			112.0	148.2
110.5	106.8			111.1	150.9
110.6	105.9			111.0	151.2
110.7	105.0			110.9	151.5
110.8	104.0			110.0	153.9
110.9	103.1			109.0	156.5
111.0	102.2			108.0	158.7
111.1	101.2			107.5	159.6
111.2	100.2			107.4	159.8
111.3	99.2			107.3	159.9
111.4	98.2			107.2	160.1
111.5	97.2			107.1	160.2
111.6	96.2			107.0	160.3
111.7	95.1			106.9	160.4
111.8	94.0			106.8	160.5
111.9	93.1			106.0	160.5
112.0	91.8				
112.1	90.7				
112.2	89.6				
112.3	88.4				
112.4	87.0				
112.5	86.0				
112.6	84.5				

TABLE D.3: ISC - PES data for (S0-$S0_{min}$) (kcal/mol)

dih\ang	**115**	**114**	**113**	**112**	**111**	**110**	**109**	**108**	**107**	**106**	**105**	**104**
0	6.79	7.11	7.46	7.87	8.32	8.82	9.37	9.98	10.73	11.84	11.96	12.11
10	7.00	7.31	7.66	8.06	8.50	8.61	9.13	9.85	10.76	11.36	11.72	11.83
20	7.31	7.60	7.93	8.31	8.75	9.23	9.77	10.35	10.87	11.10	11.11	11.24
30	7.75	8.01	8.31	8.68	9.10	9.60	10.18	10.62	10.62	10.43	10.28	10.27
40	8.36	8.58	8.86	9.21	9.72	10.44	10.39	10.00	9.62	9.29	8.84	8.75
50	9.03	9.22	9.48	10.27	10.26	9.62	9.19	8.65	8.16	7.74	7.22	7.05
60	9.74	9.98	10.73	9.99	9.26	8.55	8.00	7.36	6.77	6.20	5.63	5.36
70	10.81	10.47	9.67	8.84	8.00	7.17	6.34	5.52	4.70	3.90	3.12	2.37
80	10.37	9.61	8.76	7.88	6.99	6.09	5.17	4.25	3.32	2.37	1.42	0.44
90	10.00	9.15	8.26	7.36	6.44	5.52	4.60	3.69	2.76	1.84	0.92	0.00
100	10.66	9.82	8.93	8.04	7.17	6.28	5.39	4.50	3.61	2.72	1.83	0.94
110	10.08	10.55	9.70	8.87	8.04	7.21	6.38	5.55	4.71	3.87	3.03	2.19
120	9.44	9.57	10.55	9.79	9.04	8.29	7.54	6.79	6.03	5.27	4.50	3.73
130	8.89	9.07	9.33	9.99	10.20	9.51	8.85	8.19	7.52	6.85	6.17	5.48
140	8.33	8.56	8.85	9.21	9.73	10.46	10.18	9.63	9.07	8.50	7.92	7.33
150	7.80	8.06	8.37	8.74	9.17	9.68	10.26	10.60	10.41	10.01	9.56	9.12
160	7.31	7.60	7.93	8.31	8.74	9.22	9.75	10.33	10.84	11.01	10.85	10.63
170	6.91	7.21	7.56	7.94	8.38	8.86	9.40	9.99	10.64	11.29	11.61	11.67
180	6.67	6.96	7.29	7.67	8.10	8.57	9.09	9.68	10.46	11.82	11.96	12.11

Table D.4: ISC - PES data for (S1-$S0_{min}$) (kcal/mol)

dih\ang	**115**	**114**	**113**	**112**	**111**	**110**	**109**	**108**	**107**	**106**	**105**	**104**
0	14.21	13.99	13.80	13.64	13.50	13.36	13.21	13.00	12.57	12.00	12.75	13.56
10	14.31	13.99	13.73	13.46	13.23	13.22	13.28	13.17	12.30	12.18	12.67	13.51
20	14.10	13.73	13.36	13.02	12.69	12.38	12.08	11.79	11.62	11.87	12.51	13.39
30	13.74	13.28	12.83	12.39	11.96	11.52	11.06	10.82	11.11	11.71	12.44	13.31
40	13.23	12.66	12.10	11.51	10.84	10.01	10.17	10.64	11.20	11.83	12.52	13.32
50	12.67	12.00	11.29	10.12	9.81	10.19	10.58	11.04	11.56	12.13	12.77	13.50
60	12.05	11.19	9.88	10.12	10.39	10.71	11.06	11.48	11.95	12.48	13.07	13.76
70	10.73	10.34	10.44	10.61	10.84	11.11	11.43	11.80	12.22	12.70	13.24	13.83
80	10.68	10.61	10.68	10.81	11.00	11.24	11.53	11.86	12.25	12.68	13.17	13.70
90	10.57	10.56	10.64	10.77	10.95	11.18	11.46	11.78	12.16	12.59	13.07	13.59
100	10.33	10.36	10.47	10.63	10.83	11.08	11.39	11.74	12.14	12.59	13.09	13.65
110	11.20	9.99	10.15	10.35	10.58	10.87	11.20	11.58	12.01	12.50	13.04	13.63
120	12.02	11.27	9.72	9.96	10.23	10.55	10.92	11.34	11.81	12.34	12.92	13.55
130	12.69	12.02	11.33	10.28	9.74	10.14	10.57	11.04	11.56	12.13	12.76	13.44
140	13.29	12.72	12.15	11.56	10.85	9.99	10.19	10.71	11.28	11.91	12.59	13.34
150	13.82	13.36	12.90	12.45	11.99	11.51	10.99	10.78	11.15	11.77	12.49	13.30
160	14.22	13.86	13.51	13.18	12.87	12.55	12.24	11.93	11.72	11.92	12.54	13.36
170	14.43	14.15	13.90	13.68	13.47	13.27	13.06	12.84	12.58	12.40	12.73	13.50
180	14.30	14.10	13.93	13.79	13.68	13.58	13.47	13.30	12.84	12.01	12.74	13.55

TABLE D.5: ISC - PES data for (T1-$S0_{min}$) (kcal/mol)

dih\ang	**115**	**114**	**113**	**112**	**111**	**110**	**109**	**108**	**107**	**106**	**105**	**104**
0	7.63	7.60	7.61	7.68	7.79	7.94	8.13	8.34	8.55	8.63	8.68	8.77
10	7.37	7.32	7.32	7.37	7.46	8.25	8.47	8.70	8.20	8.42	8.58	8.72
20	7.11	7.05	7.04	7.07	7.15	7.28	7.44	7.65	7.88	8.13	8.38	8.61
30	6.91	6.84	6.83	6.85	6.93	7.05	7.21	7.41	7.66	7.93	8.22	8.51
40	6.82	6.76	6.74	6.77	6.84	6.96	7.12	7.33	7.58	7.87	8.19	8.52
50	6.86	6.81	6.80	6.83	6.91	7.04	7.20	7.42	7.68	7.98	8.32	8.69
60	7.01	6.97	6.97	7.02	7.11	7.24	7.42	7.65	7.92	8.24	8.61	9.01
70	7.22	7.20	7.21	7.27	7.37	7.52	7.71	7.95	8.24	8.57	8.95	9.38
80	7.45	7.43	7.46	7.53	7.64	7.80	8.00	8.25	8.54	8.87	9.26	9.69
90	7.45	7.43	7.45	7.51	7.62	7.77	7.96	8.20	8.48	8.81	9.19	9.62
100	7.26	7.23	7.24	7.30	7.40	7.54	7.73	7.97	8.26	8.59	8.98	9.41
110	7.07	7.04	7.04	7.09	7.19	7.33	7.52	7.75	8.04	8.38	8.76	9.20
120	6.93	6.89	6.88	6.93	7.01	7.15	7.33	7.56	7.84	8.17	8.55	8.98
130	6.84	6.79	6.78	6.81	6.89	7.02	7.19	7.42	7.68	8.00	8.36	8.77
140	6.82	6.76	6.74	6.77	6.84	6.96	7.13	7.34	7.59	7.89	8.23	8.60
150	6.88	6.82	6.80	6.82	6.89	7.01	7.16	7.36	7.60	7.87	8.18	8.51
160	7.05	6.99	6.97	7.00	7.07	7.19	7.34	7.53	7.75	8.00	8.25	8.52
170	7.32	7.27	7.26	7.30	7.39	7.51	7.68	7.87	8.08	8.28	8.47	8.64
180	7.64	7.61	7.63	7.69	7.80	7.96	8.14	8.35	8.55	8.62	8.68	8.77

Table D.6: ISC - PES data for (T2-$S0_{min}$) (kcal/mol)

dih\ang	**115**	**114**	**113**	**112**	**111**	**110**	**109**	**108**	**107**	**106**	**105**	**104**
0	11.75	11.57	11.42	11.32	11.24	11.18	11.14	11.09	10.95	10.96	11.53	12.17
10	12.35	12.11	11.95	11.78	11.68	10.49	10.61	10.70	11.43	11.41	11.59	12.22
20	12.68	12.46	12.26	12.11	11.98	11.90	11.84	11.80	11.78	11.82	11.96	12.32
30	12.89	12.67	12.48	12.33	12.22	12.14	12.09	12.08	12.10	12.15	12.28	12.56
40	13.04	12.84	12.67	12.54	12.44	12.38	12.32	12.33	12.37	12.46	12.64	12.87
50	13.05	12.86	12.71	12.60	12.53	12.50	12.48	12.53	12.62	12.75	12.94	13.17
60	12.90	12.74	12.61	12.52	12.47	12.47	12.50	12.58	12.71	12.88	13.10	13.37
70	12.61	12.45	12.33	12.26	12.24	12.25	12.32	12.42	12.58	12.79	13.05	13.36
80	12.04	11.88	11.77	11.71	11.70	11.73	11.81	11.93	12.11	12.33	12.61	12.93
90	12.11	11.99	11.92	11.89	11.89	11.94	12.03	12.18	12.37	12.60	12.87	13.20
100	12.70	12.57	12.48	12.42	12.35	12.37	12.45	12.56	12.71	12.92	13.17	13.47
110	12.98	12.82	12.71	12.63	12.60	12.60	12.65	12.74	12.88	13.06	13.29	13.57
120	13.13	12.96	12.82	12.73	12.67	12.66	12.69	12.76	12.88	13.05	13.26	13.52
130	13.13	12.94	12.79	12.68	12.61	12.58	12.59	12.65	12.75	12.90	13.10	13.36
140	13.00	12.80	12.63	12.51	12.42	12.38	12.37	12.41	12.50	12.64	12.83	13.10
150	12.78	12.56	12.39	12.25	12.15	12.09	12.07	12.09	12.16	12.29	12.49	12.80
160	12.51	12.29	12.10	11.95	11.84	11.76	11.72	11.72	11.76	11.88	12.12	12.51
170	12.18	11.96	11.78	11.63	11.52	11.44	11.38	11.35	11.35	11.45	11.75	12.29
180	11.71	11.51	11.36	11.24	11.16	11.10	11.05	10.99	10.83	10.95	11.52	12.16

Appendix E

KMC-ME simulations

In this section, a more detailed explanation of the KMC-ME simulations is provided together with the inputs. The presentation of the calculations is done only for $O(^3P) + C_2H_4$, whereas for the multi-well PES of propylene and 1-butene only the scheme of the ME input is provided at the end of this appendix.

The scheme of the species for $O(^3P)+C_2H_4$ with the indexes for paths, wells and products used in the input is shown in Figure E.1, whereas the full input is listed in Tables E.1, E.2 and E.3. The reaction pathways are numbered from 0 to 4, and also the reverse addition pathway is considered. As far as the wells are concerned, they are all the reactants and wells undergoing stabilization, so in this case only C_2H_4O is considered. The entrance well is numbered twice, since it is considered as either the starting well for all reaction pathways 0 or the reactant for the reverse pathway 1. The arrival wells instead refer to the product species of every reaction, as in Table E.3, and they are counted starting from the last main well.

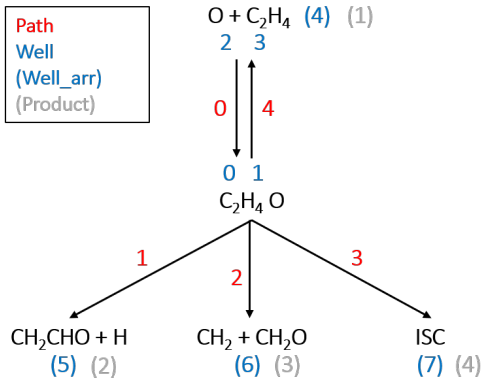

FIGURE E.1: Species considered for the $O(^3P) + C_2H_4$ PES and names given in the KMC-ME input

In Table E.1, the first part of the input is shown. The main parameters are the seed number, which is set to 0 so as to ensure that at every added molecule the random number generator starts with no memory of what previously happened. The number of reacted molecules is set to 10000, as anticipated in the methods. The maximum number of cycles indicates the number of maximum steps undertaken, such as a collision, a reaction or an energetic transition. The number of energy levels considered is instead 100000, with a step of 1 cm^{-1} between successive levels. The

other parameters are related to other energy and angular momentum steps. The pressure was set to 0.0076 torr, which is almost void conditions, so as to reproduce the single collision conditions of CMB experiments. Also higher pressure simulations were performed. In this input, the temperature was set to 300 K, however the full $300 \div 2500$ K range was considered. Then, the Lennard-Jones parameters for Ar, which is the bath gas, are put, together with the molecular weight. Finally, the number of wells is set to 4, which are 0 1 2 and 3, namely the reactants and the entrance well, and the number of products is set to 4, and in fact in the row below the product energies are found, in the order of Figure E.1. All the energies are referred to the reactants and computed as explained in the results. The number of paths is set to 5. Finally, the kind of reaction is set to bimolecular, and the reactants are specified as 2 and 3, together with the energy difference with respect to the well.

In Table E.2, the properties of the wells are listed. The Lennard-Jones parameters were taken from the appendixes of "Properties of gases and liquids" [69]. The exponentials are set as explained in the methods. Symmetry numbers and electronic degeneracies are put appropriately, and inertia moments and frequencies were taken from the optimized CASPT2 structures for the well, and from the DFT level for the reactants. The "numhind_rot" indicates the file associated to the HR eigenvalues, to be put in the same folder. Considering the HRs implies the deletion of the lowest frequency values, set to 99999 so as to give null contribution to the partition function.

Finally, in Table E.3 the input for the TS of the various reaction pathways is found. In this case, all the properties were taken from the CASPT2 calculations with the respective active spaces. Imaginary frequencies are reported as negative, and it is evident that only the HR on the CH_2O elimination step was considered, as explained in the results. It is also noted that the "HSO" parameter is only set in case of the ISC path, and it is converted from 37.2 cm^{-1} to 0.106 kcal mol^{-1}. An important remark is needed with regards to the symmetry number. This corresponds to the rotational symmetry of the molecule divided by the number of optical isomers. The partition function will then be divided by this "symm". The transition state of H elimination has an optical isomer, therefore the symmetry number is divided by 2. In the case of CH_2O elimination instead, the symmetry number is set to 2: the reason is that the TS actually has an optical isomer, which is however already accounted for by the 1DHR considered, as during the torsion both isomers are captured in a rotation of a single period. Therefore, the inclusion of the optical isomer is unneeded. Furthermore, the periodicity of the rotor was set to 2, hence the 1DHR actually captures the optical isomers twice. Hence, the symmetry number actually has to be multiplied by two.

A final point to be highlighted is the introduction of variational effects. Since in these simulations no variational pathways were considered, at every temperature a scaling factor for the H and CH_2O elimination pathways was put: in particular, this was computed as the ratio between the high pressure variational and non variational constants listed in Table B.2, B.3, B.4, B.5 in Appendix B. The results of all the simulations are listed in Appendix F.

TABLE E.1: Part 1 of KMC-ME input for $O(^3P) + C_2H_4$

seed_number	0			
num_molecules	10000			
MaxCycles	1.00E+008			
averaging_it	5000000000			
Energy_vector_dimension	100000			
J_max	350			
Estep(1/cm)	1			
Egrain/Estep	100			
J_step	10			
energy_threshold(1/cm)	0			
stabilization_threshold(1/cm)	1000			
tunneling_threshold(1/cm)	3500			
2DME	0			
2D_yEJ_parameter	1			
Not_ME	0			
JumpMax	100			
restart	no			
Pressure(torr)	0.0076			
Temperature(K)	300			
LJ_Inert_Bath_Diameter(A)	3.33			
LJ_Energy_parameter(1/cm)	79.1			
Inert_Bath_Molecular_Mass(g/mol)	39.95			
Number_of_wells	4			
Number_of_Products	4			
Products_energy	0	-15.2	-5.2	-23.5
Number_of_reaction_paths	5			
BIMOL_RRKM	2	3	23.5	

TABLE E.2: Part 2 of KMC-ME input for $O(^3P) + C_2H_4$

Wells				
index	**0**	**1**	**2**	**3**
stabil	NO	NO	NO	NO
PM(g/mol)	44	44	28	16
LJ_Diameter_(A)	4.53	4.53	4.163	3.567
LJ_energy(1/cm)	251.7539	251.7539	156.0097	74.0820
pre-dedown	260	260	260	260
exp-dedown	0.875	0.875	0.875	0.875
Djloss	0	0	0	0
Energy	-23.5	-23.5	0	0
rot_dim	3	3	3	0
symm	2	2	4	1
Ix_(GHz)	9.17	9.17	25.13	999999
Iy_(GHz)	10.52	10.52	30.32	999999
Iz_(GHz)	43.43	43.43	146.85	0
deg_elec	3	3	1	6.74
numhind_rot	1	1	0	0
numfreqs	15	15	12	0
1	99999	99999	839	
2	428.67	428.67	989.34	
3	543.71	543.71	1002.9	
4	799.86	799.86	1066.4	
5	924.13	924.13	1249	
6	1068.3	1068.3	1390.8	
7	1103.3	1103.3	1479.4	
8	1142.6	1142.6	1712.6	
9	1364	1364	3145.4	
10	1396.5	1396.5	3164.2	
11	1466.5	1466.5	3223.8	
12	2784.1	2784.1	3250.3	
13	3061.2	3061.2		
14	3201	3201		
15	3324.5	3324.5		

TABLE E.3: Part 2 of KMC-ME input for $O(^3P) + C_2H_4$

Paths					
index	**0**	**1**	**2**	**3**	**4**
type	chem_bar	chem_bar	chem_bar	chem_bar	bimol-chem_bar
w_start	**0**	**0**	**0**	**0**	**1**
w_arr	**(4)**	**(5)**	**(6)**	**(7)**	**(4)**
numProd	1	1	1	1	1
Energy	1.7	-7.75	-0.0773	-23.3	1.7
rot_dim	3	3	3	3	3
symm	1	0.5	2	1	2
Ix_(GHz)	7.053	9.492	6.745	9.297	7.053
Iy_(GHz)	8.393	10.766	7.773	10.397	8.393
Iz_(GHz)	27.729	44.741	36.222	41.256	27.729
deg_elec	3	3	3	3	3
numhr	0	0	2	0	0
HSO	0	0	0	0.107	0
Ima_fr	-311.07	-972.89	-318.63	-273.73	-311.07
Qtunn_rmass	0	0	0	0	1
numfreq	14	14	14	14	14
1	148.85	407.34	99999	388.73	148.85
2	304.76	484.4	226.99	453.01	304.76
3	835.61	561.61	279.22	652.78	835.61
4	911.32	616.76	416.63	879.36	911.32
5	960.86	752.61	528.39	946.79	960.86
6	1109.1	967.58	1096.4	1086.8	1109.1
7	1246.2	1068.1	1138.7	1260.5	1246.2
8	1339.7	1180.1	1254	1327.4	1339.7
9	1483.2	1362.4	1501.2	1424.9	1483.2
10	1620.3	1468.9	1642.2	1490.2	1620.3
11	3193.3	1507.9	2989.5	3021.7	3193.3
12	3205.1	3052	3069.6	3074.8	3205.1
13	3299.3	3197	3166.7	3196.7	3299.3
14	3388.9	3321.7	3398.6	3312.4	3388.9

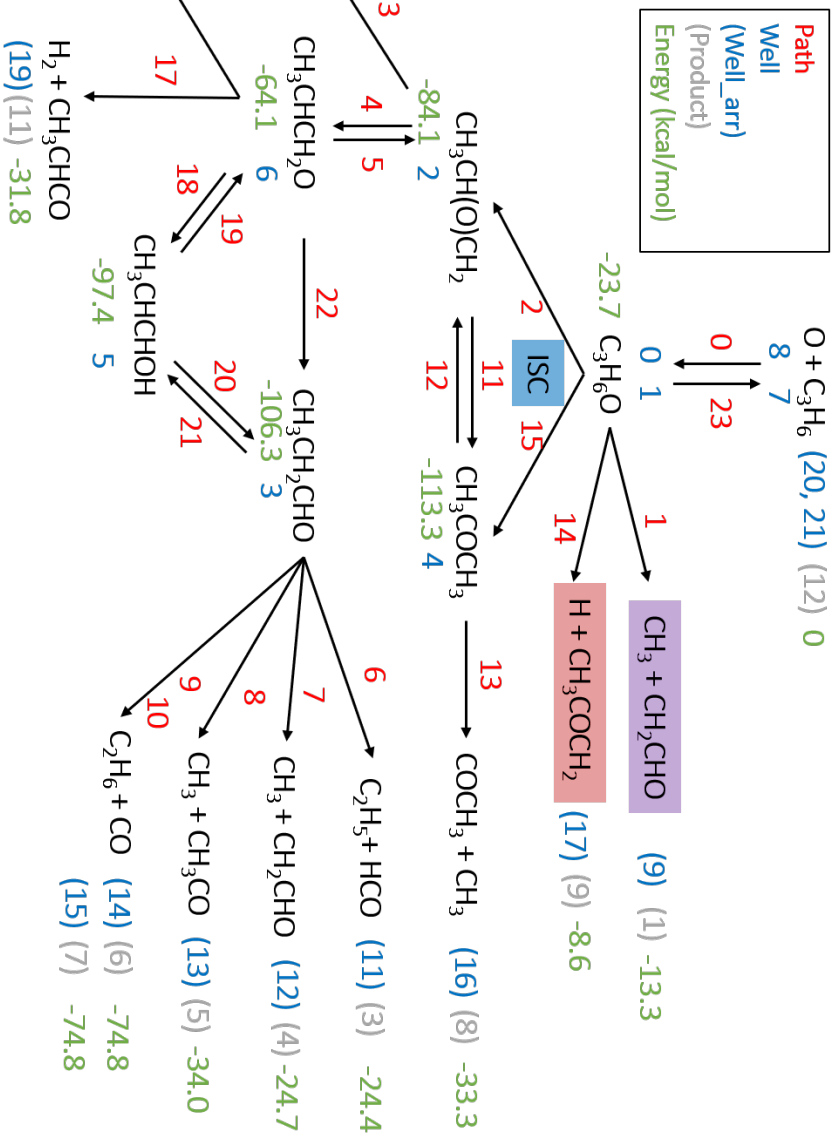

FIGURE E.2: KMC-ME input sketch for the $O(^3P) + C_3H_6$ PES of the central carbon addition

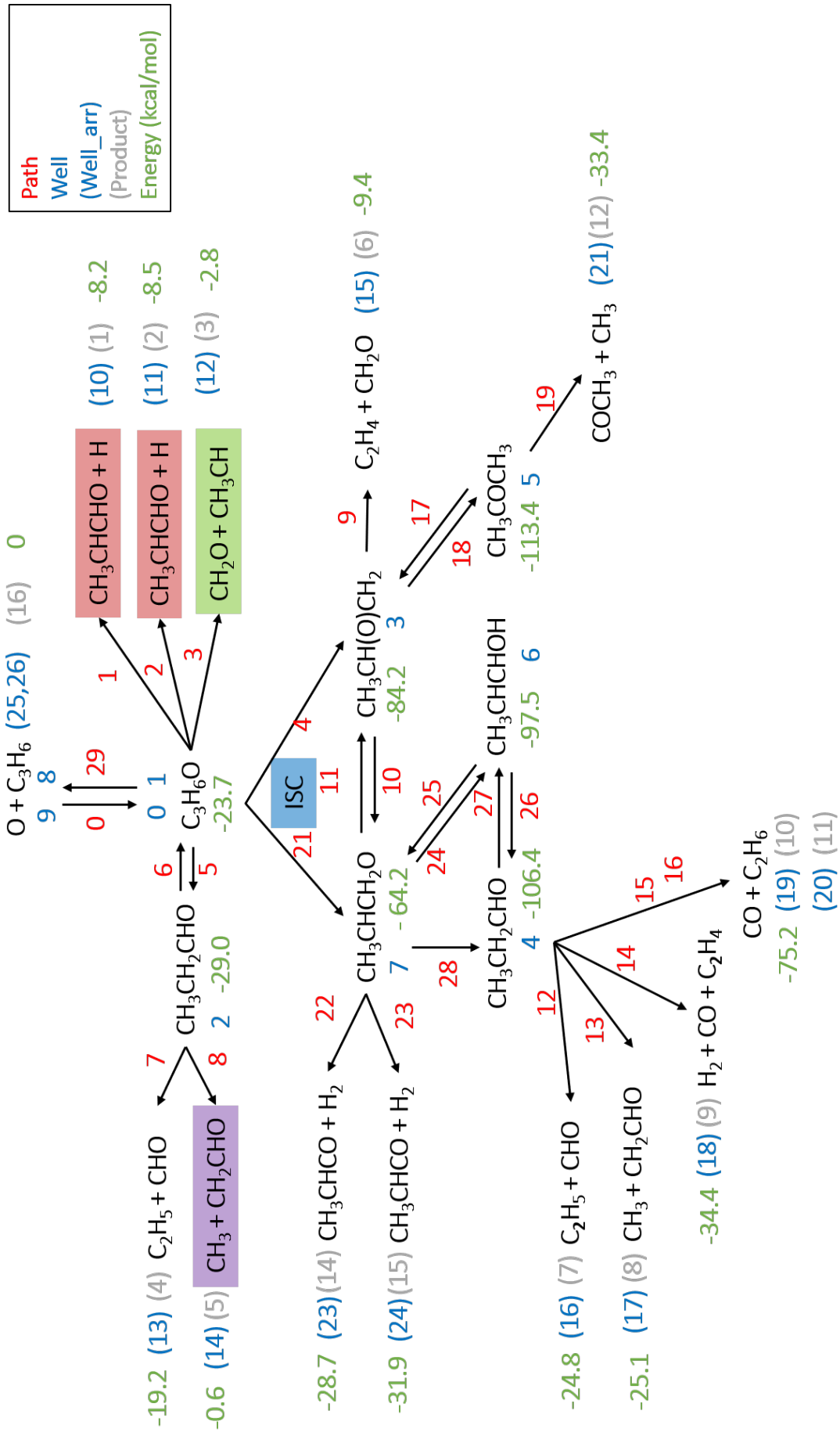

FIGURE E.3: KMC-ME input sketch for the $O(^3P) + C_3H_6$ PES of the terminal carbon addition

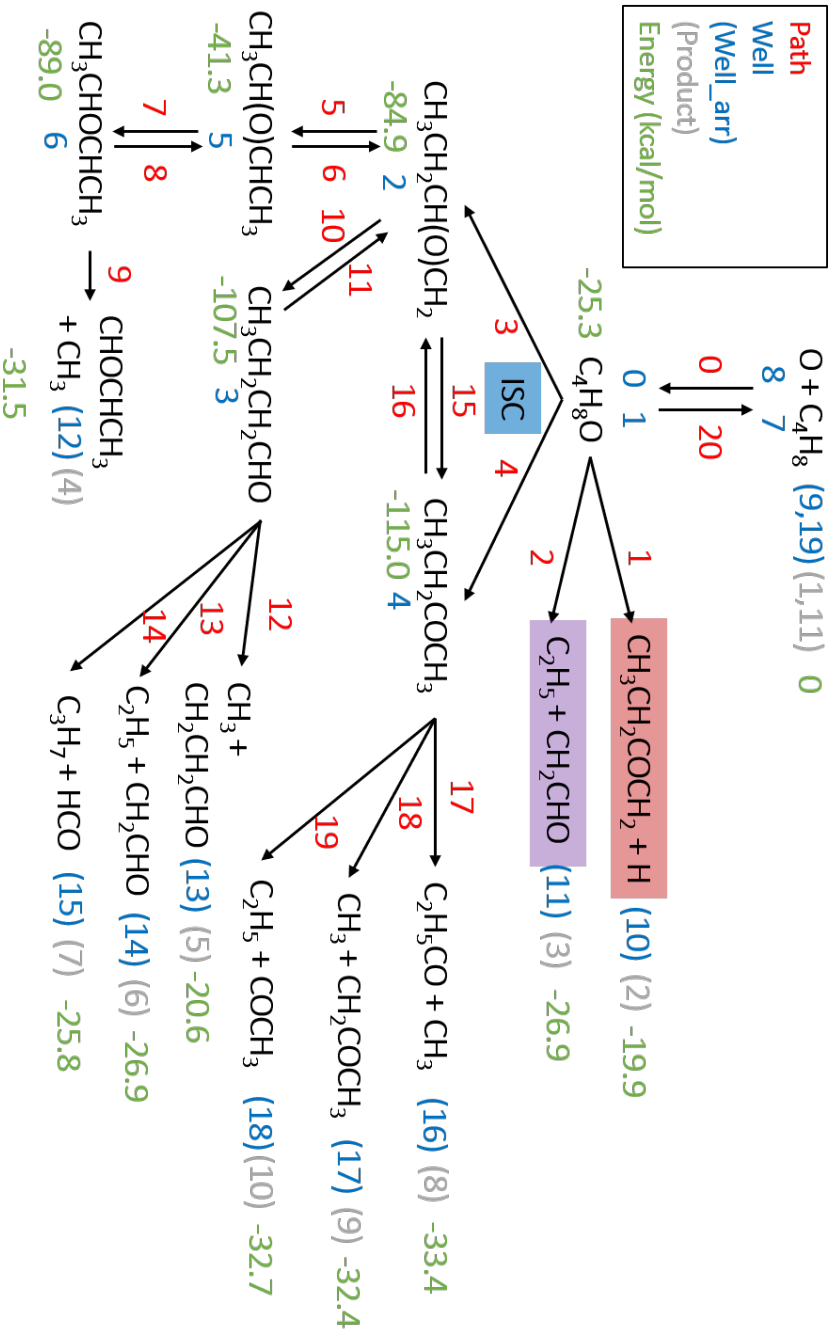

FIGURE E.4: KMC-ME input sketch for the $O(^3P) + C_4H_8$ PES of the central carbon addition

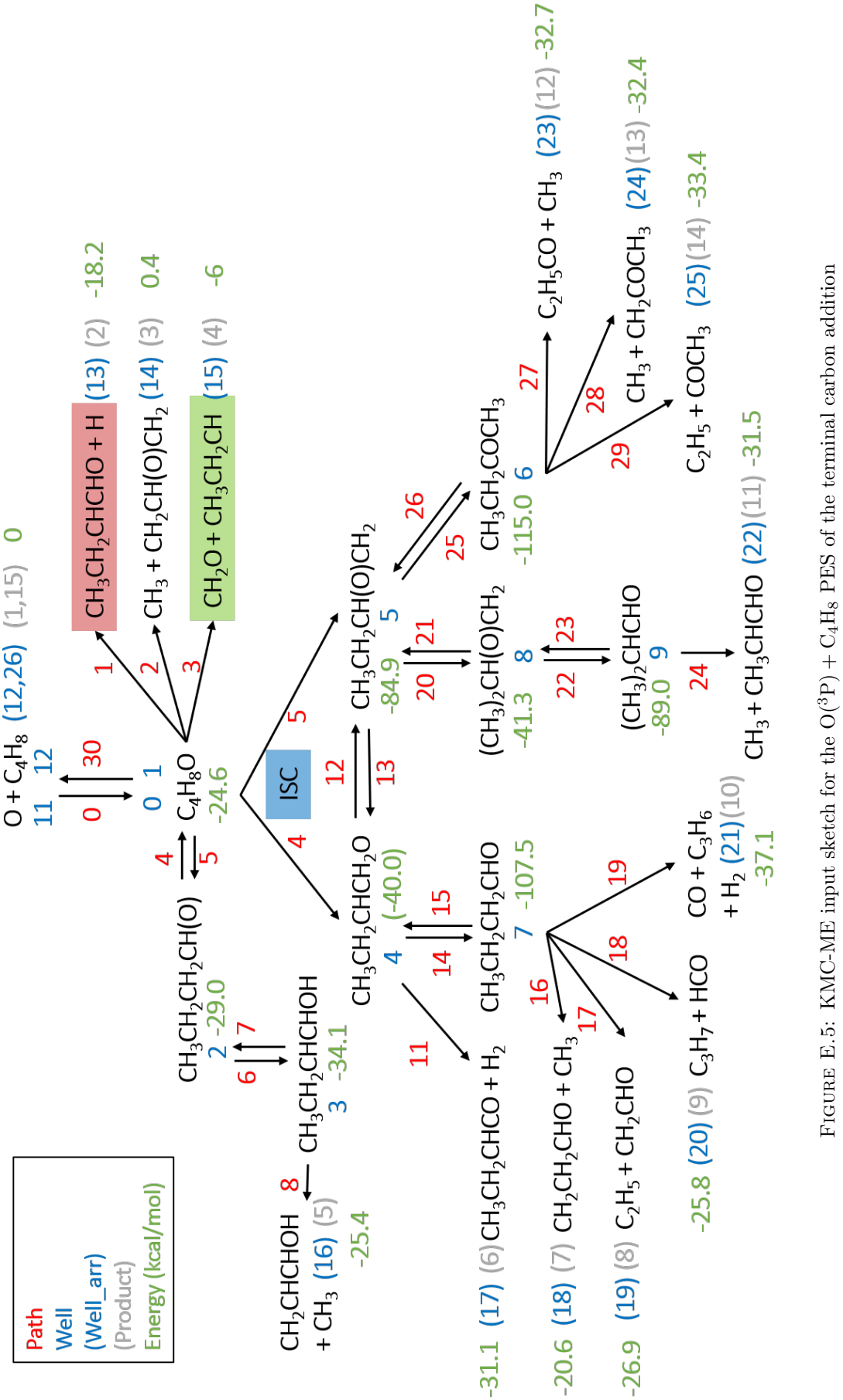

FIGURE E.5: KMC-ME input sketch for the $O(^3P) + C_4H_8$ PES of the terminal carbon addition

Appendix F

Branching Ratios

TABLE F.1: BRs and fitting parameters for $O(^3P) + C_2H_4$

	Li et Al [10]			This work		
T	**ISC**	**H**	**CH_2O**	**ISC**	**H**	**CH_2O**
300	0.687	0.302	0.011	0.562	0.410	0.028
400	0.615	0.357	0.028	0.472	0.469	0.058
500	0.530	0.415	0.055	0.387	0.524	0.090
600	0.444	0.466	0.090	0.322	0.555	0.123
700	0.366	0.503	0.131	0.264	0.572	0.164
800	0.299	0.527	0.174	0.223	0.581	0.196
900	0.242	0.539	0.218	0.187	0.583	0.230
1000	0.196	0.543	0.261	0.157	0.583	0.260
1100	0.160	0.539	0.302	0.128	0.574	0.298
1200	0.130	0.530	0.339	0.109	0.565	0.327
1300	0.107	0.519	0.374	0.087	0.551	0.362
1400	0.088	0.505	0.407	0.074	0.539	0.386
1500	0.073	0.491	0.436	0.060	0.526	0.413
1600	0.061	0.476	0.463	0.048	0.517	0.435
1700	0.052	0.461	0.488	0.041	0.503	0.456
1800	0.044	0.446	0.510	0.035	0.493	0.472
1900	0.037	0.431	0.531	0.028	0.484	0.488
2000	0.032	0.417	0.551	0.026	0.473	0.501
2100	0.028	0.404	0.569	0.022	0.466	0.513
2200	0.024	0.391	0.585	0.019	0.458	0.523
2300	0.021	0.379	0.600	0.016	0.449	0.534
2400	0.018	0.367	0.615	0.014	0.442	0.543
2500	0.016	0.356	0.628	0.013	0.435	0.552
	Fitting parameters					
k0 $\left(\frac{cm^3}{molec\ s}\right)$	9.76E-07	2.49E-13	6.53E-16	3.15E-06	2.19E-14	2.24E-17
α	-1.72E+00	9.48E-01	1.99E+00	-1.91E+00	8.97E-01	1.83E+00
$\mathbf{E_A}$ $\left(\frac{kcal}{mol}\right)$	2.89E+00	1.72E+00	2.86E+00	3.43E+00	1.89E+00	2.56E+00

TABLE F.2: BRs for $O(^3P) + C_2H_4$ ad different pressures

	1 bar			**10 bar**			**30 bar**			**100 bar**		
T(K)	**ISC**	**H**	**CH_2O**	**ISC**	**H**	**CH_2O**	**ISC**	**H**	**CH_2O**	**ISC**	**H**	**CH_2O**
300	0.566	0.406	0.027	0.580	0.391	0.028	0.616	0.363	0.021	0.715	0.269	0.016
500	0.390	0.518	0.092	0.398	0.518	0.084	0.420	0.494	0.086	0.483	0.444	0.073
750	0.240	0.582	0.178	0.253	0.563	0.184	0.265	0.562	0.173	0.309	0.530	0.160
1000	0.157	0.585	0.257	0.156	0.577	0.268	0.160	0.577	0.263	0.186	0.558	0.256
1250	0.095	0.564	0.341	0.095	0.560	0.345	0.099	0.552	0.349	0.111	0.551	0.337
1500	0.057	0.526	0.416	0.060	0.519	0.420	0.061	0.531	0.408	0.065	0.527	0.408
1750	0.038	0.498	0.463	0.039	0.487	0.474	0.038	0.507	0.455	0.040	0.499	0.461
2000	0.027	0.474	0.499	0.027	0.459	0.514	0.026	0.468	0.506	0.027	0.478	0.495
2250	0.017	0.440	0.542	0.020	0.448	0.531	0.018	0.446	0.535	0.017	0.453	0.530

TABLE F.3: BR at 0.1 bar and high P kinetic constants for $O(^3P) + C_3H_6$

Branching Ratios					k $\left(\frac{cm^3}{molec\ s}\right)$		Fractions	
T (K)	**ISC**	**H**	**CH_2O**	**CH_3**	**term**	**centr**	**term**	**centr**
500	0.408	0.217	0.164	0.210	5.50E-12	2.93E-12	0.653	0.347
750	0.202	0.233	0.292	0.273	8.59E-12	5.13E-12	0.626	0.374
1000	0.098	0.225	0.371	0.306	1.21E-11	7.54E-12	0.617	0.383
1250	0.053	0.208	0.416	0.323	1.61E-11	1.03E-11	0.609	0.391
1500	0.031	0.198	0.441	0.329	2.03E-11	1.33E-11	0.604	0.396
1750	0.020	0.198	0.453	0.329	2.50E-11	1.66E-11	0.600	0.400
2000	0.014	0.196	0.464	0.327	2.99E-11	2.01E-11	0.598	0.402
2250	0.010	0.201	0.465	0.323	3.49E-11	2.38E-11	0.594	0.406
Fitting Parameters								
ln k0 $\left(\frac{cm^3}{molec\ s}\right)$	-11.893	-33.771	-30.591	-32.479				
α	-2.069	1.108	0.868	1.035				
Ea $\left(\frac{kcal}{mol}\right)$	1.612	0.122	2.093	1.008				
$\mathbf{R^2}$	0.995	0.996	1.000	1.000				

TABLE F.4: BR at 0.1 bar and high P kinetic constants for $O(^3P) + C_4H_8$

Branching Ratios					k $\left(\frac{cm^3}{molec\ s}\right)$		Fractions	
T (K)	**ISC**	**H**	**CH_2O**	**C_2H_5**	**term**	**centr**	**term**	**centr**
300	0.728	0.031	0.006	0.235	3.40E-12	1.45E-12	0.701	0.299
400	0.684	0.043	0.016	0.257	3.56E-12	1.61E-12	0.689	0.311
500	0.610	0.073	0.046	0.271	3.91E-12	1.85E-12	0.679	0.321
600	0.513	0.104	0.092	0.291	4.35E-12	2.14E-12	0.670	0.330
700	0.426	0.124	0.149	0.302	4.85E-12	2.47E-12	0.662	0.338
800	0.330	0.141	0.215	0.313	5.39E-12	2.83E-12	0.656	0.344
900	0.252	0.154	0.271	0.324	5.95E-12	3.21E-12	0.649	0.351
1000	0.185	0.158	0.329	0.329	6.53E-12	3.61E-12	0.644	0.356
1100	0.127	0.160	0.381	0.332	7.12E-12	4.03E-12	0.639	0.361
1200	0.101	0.154	0.409	0.336	7.73E-12	4.46E-12	0.634	0.366
1300	0.070	0.147	0.443	0.340	8.36E-12	4.91E-12	0.630	0.370
1400	0.051	0.143	0.464	0.342	8.99E-12	5.38E-12	0.626	0.374
1500	0.040	0.140	0.476	0.344	9.65E-12	5.85E-12	0.622	0.378
1600	0.034	0.136	0.486	0.344	1.03E-11	6.34E-12	0.619	0.381
1700	0.026	0.133	0.495	0.347	1.10E-11	6.84E-12	0.616	0.384
1800	0.022	0.131	0.501	0.345	1.17E-11	7.36E-12	0.614	0.386
1900	0.017	0.129	0.507	0.348	1.24E-11	7.89E-12	0.612	0.388
2000	0.013	0.133	0.508	0.347	1.32E-11	8.43E-12	0.609	0.391
2100	0.013	0.128	0.513	0.347	1.39E-11	8.98E-12	0.608	0.392

Fitting Parameters				
ln k0 $\left(\frac{cm^3}{molec\ s}\right)$	-0.469	-28.426	-30.160	-36.199
α	-3.624	0.299	0.770	1.377
Ea $\left(\frac{kcal}{mol}\right)$	3.204	1.784	3.375	-0.491
$\mathbf{R^2}$	0.990	0.991	0.993	0.999

TABLE F.5: BR for $O(^3P)+C_3H_6$: central and terminal additions

	Terminal				Central		
T (K)	**ISC**	**H**	**CH_2O**	**CH_3**	**ISC**	**H**	**CH_3**
500	0.425	0.324	0.251	0.000	0.378	0.017	0.605
750	0.182	0.351	0.467	0.000	0.235	0.037	0.728
1000	0.069	0.329	0.601	0.000	0.144	0.058	0.798
1250	0.029	0.286	0.683	0.001	0.089	0.085	0.825
1500	0.012	0.257	0.730	0.001	0.061	0.109	0.830
1750	0.006	0.240	0.752	0.003	0.041	0.134	0.825
2000	0.003	0.223	0.770	0.004	0.029	0.155	0.816
2250	0.002	0.218	0.774	0.006	0.023	0.176	0.801

TABLE F.6: BR for $O(^3P)+C_4H_8$: central and terminal additions

	Terminal				Central		
T (K)	**ISC**	**H**	**CH_2O**	**CH_3**	**ISC**	**H**	**C_2H_5**
300	0.949	0.042	0.009	0.000	0.209	0.004	0.787
400	0.918	0.060	0.023	0.000	0.167	0.007	0.826
500	0.830	0.102	0.068	0.000	0.145	0.010	0.845
600	0.713	0.150	0.137	0.000	0.107	0.010	0.883
700	0.597	0.179	0.224	0.000	0.092	0.015	0.894
800	0.466	0.205	0.329	0.000	0.071	0.021	0.907
900	0.359	0.223	0.416	0.000	0.053	0.025	0.922
1000	0.261	0.227	0.510	0.001	0.048	0.032	0.920
1100	0.176	0.225	0.595	0.001	0.040	0.043	0.916
1200	0.140	0.212	0.644	0.001	0.032	0.052	0.915
1300	0.095	0.199	0.703	0.001	0.028	0.056	0.914
1400	0.067	0.187	0.740	0.002	0.023	0.067	0.908
1500	0.053	0.179	0.762	0.003	0.020	0.074	0.904
1600	0.043	0.167	0.782	0.003	0.020	0.083	0.894
1700	0.031	0.158	0.800	0.005	0.016	0.090	0.891
1800	0.026	0.151	0.813	0.006	0.015	0.098	0.881
1900	0.019	0.142	0.824	0.007	0.012	0.105	0.879
2000	0.013	0.147	0.828	0.006	0.012	0.109	0.873
2100	0.014	0.133	0.838	0.008	0.010	0.117	0.865

TABLE F.7: Comparison of BR and relative fractions of ISC from central and terminal carbon in propylene and butene

	Propylene (BR)		**1-Butene (BR)**		**Propylene (FR)**		**1-Butene (FR)**	
T (K)	**term**	**centr**	**term**	**centr**	**term**	**centr**	**term**	**centr**
500	0.277	0.131	0.564	0.047	0.679	0.321	0.924	0.076
750	0.114	0.088	0.395	0.031	0.565	0.435	0.927	0.073
1000	0.043	0.055	0.168	0.017	0.436	0.564	0.908	0.092
1250	0.018	0.035	0.089	0.012	0.338	0.662	0.882	0.118
1500	0.007	0.024	0.033	0.007	0.236	0.764	0.814	0.186
1750	0.004	0.016	0.019	0.006	0.181	0.819	0.754	0.246
2000	0.002	0.012	0.008	0.005	0.147	0.853	0.635	0.365
2250	0.001	0.009	0.008	0.004	0.112	0.888	0.675	0.325

TABLE F.8: Predictions for constants and BRs of $O(^3P) + C_4H_8$

Temperature (K)		**Constants** $\left(\frac{\mathbf{cm^3}}{\mathbf{molec\ s}}\right)$				**Branching ratios**			
T	$\mathbf{\Delta T^*_{C4-C3}}$	**ISC**	**H**	$\mathbf{CH_2O}$	$\mathbf{C_2H_5}$	**ISC**	**H**	$\mathbf{CH_2O}$	$\mathbf{C_2H_5}$
300	-183.35	3.45E-13	2.49E-13	3.85E-16	1.39E-14	0.568	0.409	0.001	0.023
400	-178.67	2.46E-12	6.48E-13	4.81E-14	2.12E-13	0.731	0.192	0.014	0.063
500	-173.72	3.59E-12	1.09E-12	3.11E-13	6.61E-13	0.635	0.193	0.055	0.117
600	-168.91	3.69E-12	1.55E-12	8.69E-13	1.29E-12	0.499	0.210	0.117	0.174
700	-164.47	3.40E-12	2.03E-12	1.69E-12	2.03E-12	0.372	0.222	0.185	0.222
800	-160.47	3.01E-12	2.52E-12	2.71E-12	2.84E-12	0.272	0.227	0.245	0.256
900	-156.92	2.64E-12	3.02E-12	3.89E-12	3.71E-12	0.199	0.228	0.293	0.280
1000	-153.81	2.30E-12	3.52E-12	5.17E-12	4.61E-12	0.148	0.226	0.332	0.295
1100	-151.08	2.02E-12	4.03E-12	6.54E-12	5.54E-12	0.111	0.222	0.361	0.306
1200	-148.71	1.77E-12	4.54E-12	7.96E-12	6.48E-12	0.085	0.219	0.384	0.312
1300	-146.64	1.57E-12	5.06E-12	9.43E-12	7.45E-12	0.067	0.215	0.401	0.317
1400	-144.84	1.39E-12	5.58E-12	1.09E-11	8.42E-12	0.053	0.212	0.415	0.320
1500	-143.28	1.24E-12	6.10E-12	1.24E-11	9.41E-12	0.043	0.209	0.426	0.322
1600	-141.91	1.12E-12	6.63E-12	1.40E-11	1.04E-11	0.035	0.206	0.435	0.324
1700	-140.72	1.01E-12	7.16E-12	1.55E-11	1.14E-11	0.029	0.204	0.442	0.325
1800	-139.67	9.14E-13	7.70E-12	1.71E-11	1.24E-11	0.024	0.202	0.448	0.326
1900	-138.75	8.32E-13	8.23E-12	1.87E-11	1.34E-11	0.020	0.200	0.453	0.326
2000	-137.94	7.60E-13	8.77E-12	2.02E-11	1.45E-11	0.017	0.198	0.457	0.327
2100	-137.22	6.97E-13	9.32E-12	2.18E-11	1.55E-11	0.015	0.197	0.461	0.327
2200	-136.57	6.41E-13	9.86E-12	2.34E-11	1.65E-11	0.013	0.196	0.464	0.328
2300	-135.99	5.92E-13	1.04E-11	2.49E-11	1.75E-11	0.011	0.195	0.466	0.328
2400	-135.46	5.48E-13	1.10E-11	2.65E-11	1.86E-11	0.010	0.194	0.468	0.328
2500	-134.98	5.08E-13	1.15E-11	2.81E-11	1.96E-11	0.009	0.193	0.470	0.329

TABLE F.9: Predictions for constants and BRs of $O(^3P) + C_4H_8$ corrected with variational effects

Temperature (K)		**Constants** $\left(\frac{\mathbf{cm^3}}{\mathbf{molec\ s}}\right)$				**Branching ratios**			
T	$\mathbf{\Delta T^*_{C4-C3}}$	**ISC**	**H**	$\mathbf{CH_2O}$	$\mathbf{C_2H_5}$	**ISC**	**H**	$\mathbf{CH_2O}$	$\mathbf{C_2H_5}$
300	-183.35	3.45E-13	1.51E-13	3.85E-16	1.39E-14	0.676	0.296	0.001	0.027
400	-178.67	2.46E-12	4.08E-13	4.81E-14	2.12E-13	0.787	0.130	0.015	0.068
500	-173.72	3.59E-12	6.98E-13	3.11E-13	6.61E-13	0.682	0.133	0.059	0.126
600	-168.91	3.69E-12	1.00E-12	8.69E-13	1.29E-12	0.539	0.146	0.127	0.188
700	-164.47	3.40E-12	1.31E-12	1.69E-12	2.03E-12	0.404	0.155	0.200	0.241
800	-160.47	3.01E-12	1.62E-12	2.71E-12	2.84E-12	0.296	0.159	0.266	0.279
900	-156.92	2.64E-12	1.94E-12	3.89E-12	3.71E-12	0.217	0.159	0.319	0.305
1000	-153.81	2.30E-12	2.26E-12	5.17E-12	4.61E-12	0.161	0.157	0.361	0.321
1100	-151.08	2.02E-12	2.57E-12	6.54E-12	5.54E-12	0.121	0.154	0.392	0.332
1200	-148.71	1.77E-12	2.89E-12	7.96E-12	6.48E-12	0.093	0.151	0.417	0.339
1300	-146.64	1.57E-12	3.21E-12	9.43E-12	7.45E-12	0.072	0.148	0.435	0.344
1400	-144.84	1.39E-12	3.53E-12	1.09E-11	8.42E-12	0.057	0.145	0.450	0.347
1500	-143.28	1.24E-12	3.85E-12	1.24E-11	9.41E-12	0.046	0.143	0.462	0.349
1600	-141.91	1.12E-12	4.17E-12	1.40E-11	1.04E-11	0.038	0.141	0.471	0.351
1700	-140.72	1.01E-12	4.50E-12	1.55E-11	1.14E-11	0.031	0.139	0.479	0.352
1800	-139.67	9.14E-13	4.83E-12	1.71E-11	1.24E-11	0.026	0.137	0.485	0.352
1900	-138.75	8.32E-13	5.15E-12	1.87E-11	1.34E-11	0.022	0.135	0.490	0.353
2000	-137.94	7.60E-13	5.48E-12	2.02E-11	1.45E-11	0.019	0.134	0.494	0.353
2100	-137.22	6.97E-13	5.81E-12	2.18E-11	1.55E-11	0.016	0.133	0.498	0.354
2200	-136.57	6.41E-13	6.14E-12	2.34E-11	1.65E-11	0.014	0.132	0.501	0.354
2300	-135.99	5.92E-13	6.48E-12	2.49E-11	1.75E-11	0.012	0.131	0.503	0.354
2400	-135.46	5.48E-13	6.81E-12	2.65E-11	1.86E-11	0.010	0.130	0.505	0.354
2500	-134.98	5.08E-13	7.15E-12	2.81E-11	1.96E-11	0.009	0.129	0.507	0.354

TABLE F.10: Predictions for constants and BRs of $O(^3P) + C_4H_8$ with fixed central BR

Temperature (K)		**Constants** $\left(\frac{\mathbf{cm^3}}{\mathbf{molec\ s}}\right)$				**Branching ratios**			
T	$\mathbf{\Delta T^*_{C4-C3}}$	**ISC**	**H**	$\mathbf{CH_2O}$	$\mathbf{C_2H_5}$	**ISC**	**H**	$\mathbf{CH_2O}$	$\mathbf{C_2H_5}$
300	-183.35	3.45E-13	1.55E-13	3.85E-16		0.474	0.213	0.001	0.312
400	-178.67	2.46E-12	4.05E-13	4.81E-14		0.567	0.093	0.011	0.329
500	-173.72	3.59E-12	6.81E-13	3.11E-13		0.516	0.098	0.045	0.341
600	-168.91	3.69E-12	9.71E-13	8.69E-13		0.433	0.114	0.102	0.351
700	-164.47	3.40E-12	1.27E-12	1.69E-12		0.343	0.128	0.171	0.358
800	-160.47	3.01E-12	1.58E-12	2.71E-12		0.263	0.138	0.237	0.362
900	-156.92	2.64E-12	1.89E-12	3.89E-12		0.199	0.142	0.294	0.365
1000	-153.81	2.30E-12	2.20E-12	5.17E-12		0.151	0.144	0.339	0.366
1100	-151.08	2.02E-12	2.52E-12	6.54E-12		0.116	0.144	0.375	0.366
1200	-148.71	1.77E-12	2.84E-12	7.96E-12		0.090	0.143	0.403	0.364
1300	-146.64	1.57E-12	3.16E-12	9.43E-12		0.071	0.142	0.425	0.362
1400	-144.84	1.39E-12	3.49E-12	1.09E-11		0.056	0.141	0.442	0.360
1500	-143.28	1.24E-12	3.81E-12	1.24E-11		0.046	0.140	0.457	0.358
1600	-141.91	1.12E-12	4.14E-12	1.40E-11		0.037	0.139	0.469	0.355
1700	-140.72	1.01E-12	4.48E-12	1.55E-11		0.031	0.138	0.479	0.352
1800	-139.67	9.14E-13	4.81E-12	1.71E-11		0.026	0.137	0.487	0.350
1900	-138.75	8.32E-13	5.15E-12	1.87E-11		0.022	0.136	0.494	0.348
2000	-137.94	7.60E-13	5.48E-12	2.02E-11		0.019	0.136	0.500	0.346
2100	-137.22	6.97E-13	5.82E-12	2.18E-11		0.016	0.135	0.505	0.344
2200	-136.57	6.41E-13	6.17E-12	2.34E-11		0.014	0.134	0.509	0.342
2300	-135.99	5.92E-13	6.51E-12	2.49E-11		0.012	0.134	0.513	0.341
2400	-135.46	5.48E-13	6.85E-12	2.65E-11		0.011	0.134	0.516	0.339
2500	-134.98	5.08E-13	7.20E-12	2.81E-11		0.009	0.133	0.520	0.338

TABLE F.11: Predictions for constants and BRs of $O(^3P) + C_4H_8$ with calculated C_2H_5 BR

Temperature (K)		**Constants** $\left(\frac{\mathbf{cm^3}}{\mathbf{molec\ s}}\right)$				**Branching ratios**			
T	$\mathbf{\Delta T^*_{C4-C3}}$	**ISC**	**H**	$\mathbf{CH_2O}$	$\mathbf{C_2H_5}$	**ISC**	**H**	$\mathbf{CH_2O}$	$\mathbf{C_2H_5}$
300	-183.35	3.45E-13	1.55E-13	3.85E-16		0.474	0.213	0.001	0.312
400	-178.67	2.46E-12	4.05E-13	4.81E-14		0.567	0.093	0.011	0.329
500	-173.72	3.59E-12	6.81E-13	3.11E-13		0.516	0.098	0.045	0.341
600	-168.91	3.69E-12	9.71E-13	8.69E-13		0.433	0.114	0.102	0.351
700	-164.47	3.40E-12	1.27E-12	1.69E-12		0.343	0.128	0.171	0.358
800	-160.47	3.01E-12	1.58E-12	2.71E-12		0.263	0.138	0.237	0.362
900	-156.92	2.64E-12	1.89E-12	3.89E-12		0.199	0.142	0.294	0.365
1000	-153.81	2.30E-12	2.20E-12	5.17E-12		0.151	0.144	0.339	0.366
1100	-151.08	2.02E-12	2.52E-12	6.54E-12		0.116	0.144	0.375	0.366
1200	-148.71	1.77E-12	2.84E-12	7.96E-12		0.090	0.143	0.403	0.364
1300	-146.64	1.57E-12	3.16E-12	9.43E-12		0.071	0.142	0.425	0.362
1400	-144.84	1.39E-12	3.49E-12	1.09E-11		0.056	0.141	0.442	0.360
1500	-143.28	1.24E-12	3.81E-12	1.24E-11		0.046	0.140	0.457	0.358
1600	-141.91	1.12E-12	4.14E-12	1.40E-11		0.037	0.139	0.469	0.355
1700	-140.72	1.01E-12	4.48E-12	1.55E-11		0.031	0.138	0.479	0.352
1800	-139.67	9.14E-13	4.81E-12	1.71E-11		0.026	0.137	0.487	0.350
1900	-138.75	8.32E-13	5.15E-12	1.87E-11		0.022	0.136	0.494	0.348
2000	-137.94	7.60E-13	5.48E-12	2.02E-11		0.019	0.136	0.500	0.346
2100	-137.22	6.97E-13	5.82E-12	2.18E-11		0.016	0.135	0.505	0.344
2200	-136.57	6.41E-13	6.17E-12	2.34E-11		0.014	0.134	0.509	0.342
2300	-135.99	5.92E-13	6.51E-12	2.49E-11		0.012	0.134	0.513	0.341
2400	-135.46	5.48E-13	6.85E-12	2.65E-11		0.011	0.134	0.516	0.339
2500	-134.98	5.08E-13	7.20E-12	2.81E-11		0.009	0.133	0.520	0.338

TABLE F.12: Predictions for constants and BRs of $O(^3P) + C_5H_{10}$ from C_3H_6

Temperature (K)		**Constants** $\left(\frac{\mathbf{cm^3}}{\mathbf{molec\ s}}\right)$				**Branching ratios**			
T	$\mathbf{\Delta T^*_{C5-C3}}$	**ISC**	**H**	$\mathbf{CH_2O}$	$\mathbf{C_2H_5}$	**ISC**	**H**	$\mathbf{CH_2O}$	$\mathbf{C_2H_5}$
300	-299.93	0.00E+00	0.00E+00	0.00E+00		-	-	-	0.208
400	-291.20	2.42E-13	1.38E-13	1.89E-16		0.487	0.279	0.000	0.233
500	-282.26	2.40E-12	3.96E-13	4.38E-14		0.630	0.104	0.012	0.255
600	-273.74	3.59E-12	6.81E-13	3.11E-13		0.569	0.108	0.049	0.273
700	-265.96	3.69E-12	9.80E-13	8.88E-13		0.472	0.125	0.114	0.289
800	-259.03	3.38E-12	1.29E-12	1.74E-12		0.368	0.140	0.189	0.302
900	-252.94	2.99E-12	1.60E-12	2.79E-12		0.278	0.149	0.260	0.313
1000	-247.62	2.61E-12	1.91E-12	4.00E-12		0.207	0.152	0.318	0.322
1100	-243.00	2.27E-12	2.23E-12	5.31E-12		0.155	0.153	0.363	0.329
1200	-238.99	1.98E-12	2.55E-12	6.70E-12		0.118	0.151	0.397	0.334
1300	-235.50	1.74E-12	2.88E-12	8.15E-12		0.090	0.149	0.422	0.338
1400	-232.45	1.54E-12	3.21E-12	9.63E-12		0.071	0.147	0.442	0.341
1500	-229.78	1.37E-12	3.53E-12	1.11E-11		0.056	0.145	0.457	0.343
1600	-227.43	1.22E-12	3.87E-12	1.27E-11		0.045	0.143	0.468	0.344
1700	-225.33	1.10E-12	4.20E-12	1.42E-11		0.037	0.141	0.478	0.345
1800	-223.47	9.91E-13	4.53E-12	1.58E-11		0.030	0.139	0.485	0.345
1900	-221.79	8.98E-13	4.87E-12	1.74E-11		0.025	0.138	0.491	0.345
2000	-220.26	8.18E-13	5.21E-12	1.89E-11		0.021	0.136	0.496	0.346
2100	-218.87	7.47E-13	5.55E-12	2.05E-11		0.018	0.135	0.500	0.347
2200	-217.58	6.85E-13	5.89E-12	2.21E-11		0.016	0.134	0.502	0.349
2300	-216.40	6.31E-13	6.23E-12	2.37E-11		0.013	0.132	0.503	0.351
2400	-215.29	5.82E-13	6.58E-12	2.53E-11		0.012	0.131	0.503	0.354
2500	-214.25	5.39E-13	6.93E-12	2.68E-11		0.010	0.129	0.502	0.359

TABLE F.13: Predictions for constants and BRs of $O(^3P) + C_5H_{10}$ from C_4H_8

Temperature (K)		**Constants** $\left(\frac{\mathbf{cm^3}}{\mathbf{molec\ s}}\right)$				**Branching ratios**			
T	$\mathbf{\Delta T^*_{C5-C4}}$	**ISC**	**H**	$\mathbf{CH_2O}$	$\mathbf{C_2H_5}$	**ISC**	**H**	$\mathbf{CH_2O}$	$\mathbf{C_2H_5}$
300	-116.57	5.95E-13	1.61E-14	4.19E-16		0.771	0.021	0.001	0.208
400	-112.54	2.81E-12	1.08E-13	1.69E-14		0.735	0.028	0.004	0.233
500	-108.54	4.08E-12	2.72E-13	1.03E-13		0.683	0.046	0.017	0.255
600	-104.83	4.12E-12	4.72E-13	3.06E-13		0.611	0.070	0.045	0.273
700	-101.49	3.64E-12	6.83E-13	6.41E-13		0.521	0.098	0.092	0.289
800	-98.56	3.04E-12	8.93E-13	1.10E-12		0.422	0.124	0.152	0.302
900	-96.01	2.49E-12	1.10E-12	1.66E-12		0.326	0.143	0.218	0.313
1000	-93.82	2.02E-12	1.29E-12	2.31E-12		0.244	0.155	0.279	0.322
1100	-91.92	1.64E-12	1.47E-12	3.03E-12		0.179	0.160	0.331	0.329
1200	-90.28	1.34E-12	1.64E-12	3.81E-12		0.132	0.161	0.374	0.334
1300	-88.86	1.10E-12	1.80E-12	4.64E-12		0.097	0.158	0.407	0.338
1400	-87.61	9.15E-13	1.95E-12	5.50E-12		0.072	0.154	0.433	0.341
1500	-86.50	7.64E-13	2.10E-12	6.38E-12		0.054	0.149	0.454	0.343
1600	-85.52	6.42E-13	2.24E-12	7.29E-12		0.041	0.144	0.471	0.344
1700	-84.62	5.43E-13	2.37E-12	8.22E-12		0.032	0.139	0.484	0.345
1800	-83.80	4.62E-13	2.49E-12	9.16E-12		0.025	0.135	0.495	0.345
1900	-83.04	3.96E-13	2.61E-12	1.01E-11		0.020	0.130	0.505	0.345
2000	-82.32	3.41E-13	2.72E-12	1.11E-11		0.016	0.126	0.512	0.346
2100	-81.65	2.96E-13	2.82E-12	1.20E-11		0.013	0.122	0.519	0.347
2200	-81.01	2.57E-13	2.93E-12	1.30E-11		0.010	0.118	0.523	0.349
2300	-80.41	2.25E-13	3.03E-12	1.40E-11		0.008	0.114	0.527	0.351
2400	-79.83	1.98E-13	3.12E-12	1.50E-11		0.007	0.110	0.528	0.354
2500	-79.27	1.75E-13	3.21E-12	1.59E-11		0.006	0.107	0.529	0.359

Appendix G

Heat Capacities

G.1 Properties of the wells and resulting ΔT^*

TABLE G.1: Properties of the wells for the computation of Cv

	C_2H_4O	C_3H_6O	C_4H_8O	$C_5H_{10}O$
Lev of theory	wb97xd/	wb97xd/	wb97xd/	wb97xd/
geom/freq	aug-cc-pVTZ	aug-cc-pVTZ	aug-cc-pVTZ	aug-cc-pVTZ
HR	6-311+g(d,p)	6-311+g(d,p)	6-311+g(d,p)	6-311+g(d,p)
Ix (GHz)	9.22	4.47	2.64	1.76
Iy (GHz)	10.57	5.32	3.10	2.13
Iz (GHz)	43.77	17.18	9.54	5.84
Freq (cm^{-1})				
1	193.8 (HR)	61.8 (HR)	44.2 (HR)	34.4 (HR)
2	419.3	119.9 (HR)	108.1 (HR)	82.3 (HR)
3	511.9	277.2	224.0 (HR)	142.4 (HR)
4	773.2	391.6	281.3	215.4 (HR)
5	928.8	545.4	307.0	240.4
6	1068.0	806.8	462.0	311.2
7	1079.8	885.5	568.8	371.5
8	1131.0	987.5	781.6	486.1
9	1349.3	1009.7	811.4	554.8
10	1370.6	1072.2	885.5	772.4
11	1449.9	1134.4	981.6	807.8
12	2802.4	1164.8	1022.9	837.3
13	2988.5	1316.0	1057.7	906.3
14	3169.7	1362.9	1096.6	933.0
15	3285.4	1383.5	1122.3	1024.5
16		1420.7	1172.1	1066.9
17		1476.1	1270.2	1079.7
18		1488.1	1319.6	1106.1
19		2813.2	1343.2	1124.6
20		3001.8	1368.3	1177.9
21		3008.6	1403.7	1239.9
22		3068.0	1421.8	1279.9
23		3119.6	1484.5	1321.9
24		3201.4	1501.3	1352.9
25			1510.8	1363.9
26			2803.3	1383.6
27			3000.9	1420.8
28			3024.3	1429.2
29			3048.1	1473.6
30			3079.6	1496.0
31			3121.6	1501.9
32			3134.0	1508.0
33			3186.7	2798.3
34				2987.2
35				2996.8
36				3040.8
37				3045.9
38				3067.4
39				3082.5
40				3117.9
41				3122.8
42				3182.1

TABLE G.2: Heat capacities computed *ab initio* and intrinsic temperature differences ΔT^*

	Heat Capacities (cal/mol/K)				ΔT^* (K)			
T (K)	**C_2H_4O**	**C_3H_6O**	**C_4H_8O**	**$C_5H_{10}O$**	**C_2H_4O**	**C_3H_6O**	**C_4H_8O**	**$C_5H_{10}O$**
300	7.02	10.97	16.32	21.99	1181.27	869.71	686.36	569.78
400	10.24	15.56	22.46	29.60	1121.52	810.92	632.30	519.72
500	13.09	19.83	28.06	36.48	1071.80	762.64	588.90	480.38
600	15.51	23.53	32.86	42.36	1030.30	723.13	554.20	449.39
700	17.59	26.71	36.95	47.36	995.36	690.60	526.10	424.64
800	19.40	29.47	40.48	51.68	965.74	663.62	503.20	404.59
900	21.01	31.89	43.57	55.45	940.49	641.10	484.20	388.17
1000	22.44	34.02	46.29	58.78	918.88	622.20	468.40	374.57
1100	23.73	35.92	48.69	61.71	900.32	606.24	455.20	363.24
1200	24.89	37.60	50.83	64.32	884.32	592.70	444.00	353.71
1300	25.94	39.11	52.73	66.63	870.49	581.16	434.50	345.66
1400	26.90	40.46	54.42	68.70	858.48	571.26	426.40	338.81
1500	27.78	41.68	55.95	70.55	848.01	562.73	419.50	332.95
1600	28.58	42.78	57.33	72.22	838.84	555.34	413.40	327.92
1700	29.33	43.79	58.58	73.72	830.79	548.90	408.20	323.57
1800	30.02	44.71	59.72	75.09	823.69	543.27	403.60	319.80
1900	30.67	45.56	60.77	76.32	817.40	538.31	399.60	316.52
2000	31.28	46.35	61.74	77.45	811.81	533.92	396.00	313.66
2100	31.85	47.08	62.64	78.49	806.82	530.02	392.80	311.16
2200	32.39	47.77	63.47	79.44	802.35	526.55	390.00	308.96
2300	32.91	48.42	64.26	80.32	798.34	523.43	387.40	307.04
2400	33.41	49.03	64.99	81.13	794.72	520.63	385.20	305.34
2500	33.89	49.61	65.69	81.89	791.45	518.10	383.10	303.85

TABLE G.3: Comparison of properties and T^* of central and terminal C_4H_8O wells

Properties		
	term	**centr**
Lev of theory	ωb97xd/	ωb97xd/
geom/freq	aug-cc-pVTZ	aug-cc-pVTZ
HR	6-311+g(d,p)	6-311+g(d,p)
Ix (GHz)	2.64	2.80
Iy (GHz)	3.10	3.61
Iz (GHz)	9.54	9.06
Freq (cm^{-1})		
1	44.2 (HR)	107.33 (HR)
2	108.1 (HR)	161.72 (HR)
3	224.0 (HR)	225.41 (HR)
4	281.3	248.4
5	307.0	385.3
6	462.0	441.3
7	568.8	484.9
8	781.6	550.7
9	811.4	782.4
10	885.5	827.7
11	981.6	932.6
12	1022.9	1002.2
13	1057.7	1024.2
14	1096.6	1057.3
15	1122.3	1066.2
16	1172.1	1146.9
17	1270.2	1191.4
18	1319.6	1233.7
19	1343.2	1309.5
20	1368.3	1360.9
21	1403.7	1421.4
22	1421.8	1444.9
23	1484.5	1490.6
24	1501.3	1502.6
25	1510.8	1511.9
26	2803.3	2767.8
27	3000.9	3046.6
28	3024.3	3050.4
29	3048.1	3090.5
30	3079.6	3120.8
31	3121.6	3137.0
32	3134.0	3166.7
33	3186.7	3284.0

T* (K)			
T (K)	**term**	$\frac{\text{centr}}{23.7\ \frac{\text{kcal}}{\text{mol}}}$	$\frac{\text{centr}}{24.7\ \frac{\text{kcal}}{\text{mol}}}$
300	986.4	952.7	974.0
400	1032.3	1004.4	1025.3
500	1088.9	1066.5	1086.9
600	1154.2	1136.2	1156.1
700	1226.1	1211.7	1231.1
800	1303.2	1291.5	1310.5
900	1384.2	1374.7	1393.3
1000	1468.4	1460.6	1478.9
1100	1555.2	1548.7	1566.7
1200	1644.0	1638.6	1656.3
1300	1734.5	1729.9	1747.4
1400	1826.4	1822.5	1839.7
1500	1919.5	1916.1	1933.1
1600	2013.4	2010.5	2027.4
1700	2108.2	2105.6	2122.4
1800	2203.6	2201.3	2217.9
1900	2299.6	2297.5	2314.0
2000	2396.0	2394.2	2410.6
2100	2492.8	2491.2	2507.5
2200	2590.0	2588.5	2604.7
2300	2687.4	2686.1	2702.2
2400	2785.2	2784.0	2800.0
2500	2883.1	2882.0	2898.0

TABLE G.4: Approximated heat capacities for $C_nH_{2n}O$ with n > 5

Heat capacities												
T (K)	**6**	**7**	**8**	**9**	**10**	**11**	**12**	**14**	**16**	**18**	**20**	**24**
300	27.66	33.33	39.00	44.67	50.34	56.01	61.68	73.02	84.35	95.69	107.03	129.71
400	36.73	43.86	51.00	58.13	65.26	72.40	79.53	93.79	108.06	122.33	136.59	165.13
500	44.90	53.32	61.74	70.16	78.58	87.00	95.41	112.25	129.09	145.93	162.76	196.44
600	51.86	61.35	70.85	80.35	89.85	99.35	108.85	127.85	146.85	165.84	184.84	222.84
700	57.77	68.18	78.60	89.01	99.42	109.83	120.25	141.07	161.89	182.72	203.54	245.19
800	62.88	74.08	85.27	96.47	107.67	118.87	130.07	152.46	174.86	197.25	219.65	264.44
900	67.34	79.22	91.10	102.99	114.87	126.75	138.64	162.40	186.17	209.93	233.70	281.23
1000	71.26	83.75	96.23	108.72	121.20	133.69	146.18	171.15	196.12	221.09	246.06	296.00
1100	74.73	87.75	100.77	113.78	126.80	139.82	152.84	178.87	204.91	230.95	256.98	309.06
1200	77.81	91.29	104.78	118.27	131.76	145.25	158.74	185.72	212.70	239.68	266.66	320.61
1300	80.54	94.45	108.35	122.26	136.17	150.08	163.98	191.80	219.61	247.42	275.24	330.87
1400	82.98	97.26	111.53	125.81	140.09	154.36	168.64	197.19	225.75	254.30	282.85	339.96
1500	85.16	99.76	114.36	128.97	143.57	158.18	172.78	201.99	231.19	260.40	289.61	348.02
1600	87.11	102.00	116.89	131.78	146.68	161.57	176.46	206.24	236.02	265.81	295.59	355.15
1700	88.87	104.01	119.15	134.30	149.44	164.58	179.73	210.01	240.30	270.59	300.87	361.45
1800	90.45	105.81	121.17	136.54	151.90	167.26	182.63	213.35	244.08	274.80	305.53	366.98
1900	91.88	107.43	122.98	138.53	154.09	169.64	185.19	216.30	247.40	278.51	309.61	371.82
2000	93.17	108.88	124.60	140.31	156.03	171.74	187.46	218.89	250.32	281.75	313.18	376.04
2100	94.34	110.19	126.05	141.90	157.75	173.61	189.46	221.16	252.87	284.58	316.28	379.69
2200	95.41	111.38	127.34	143.31	159.28	175.25	191.22	223.15	255.09	287.02	318.96	382.83
2300	96.38	112.44	128.51	144.57	160.63	176.69	192.76	224.88	257.01	289.13	321.26	385.51
2400	97.27	113.41	129.55	145.69	161.83	177.97	194.11	226.38	258.66	290.94	323.22	387.78
2500	98.09	114.29	130.49	146.68	162.88	179.08	195.28	227.68	260.08	292.48	324.88	389.67
Fitting parameters for Cv = a1 + a2 T a3 T^2 + a4 T^3												
a1	-1.4E+00	-2.1E-01	9.6E-01	2.1E+00	3.3E+00	4.5E+00	5.7E+00	8.0E+00	1.0E+01	1.3E+01	1.5E+01	2.0E+01
a2	1.1E-01	1.3E-01	1.5E-01	1.7E-01	1.9E-01	2.0E-01	2.2E-01	2.6E-01	2.9E-01	3.3E-01	3.6E-01	4.3E-01
a3	-4.9E-05	-5.7E-05	-6.4E-05	-7.2E-05	-8.0E-05	-8.7E-05	-9.5E-05	-1.1E-04	-1.3E-04	-1.4E-04	-1.6E-04	-1.9E-04
a4	7.8E-09	9.0E-09	1.0E-08	1.1E-08	1.3E-08	1.4E-08	1.5E-08	1.7E-08	2.0E-08	2.2E-08	2.4E-08	2.9E-08

Table G.5: Approximated ΔT^* for $C_nH_{2n}O$ with n > 5

T (K)	**6**	**7**	**8**	**9**	**10**	**11**	**12**	**14**	**16**	**18**	**20**	**24**
300	502.73	441.62	394.43	356.76	325.93	300.21	278.38	243.28	216.24	194.73	177.19	150.26
400	454.16	396.48	352.21	317.05	288.44	264.68	244.60	212.51	187.95	168.54	152.81	128.82
500	415.35	360.88	319.29	286.42	259.78	237.74	219.18	189.66	167.19	149.51	135.23	113.58
600	384.26	332.66	293.44	262.56	237.61	217.05	199.77	172.38	151.62	135.34	122.22	102.40
700	359.23	310.14	272.97	243.79	220.27	200.93	184.72	159.08	139.70	124.54	112.36	93.98
800	338.97	292.05	256.61	228.86	206.55	188.23	172.89	148.68	130.43	116.17	104.73	87.50
900	322.49	277.42	243.45	216.90	195.58	178.10	163.48	140.45	123.11	109.58	98.74	82.43
1000	309.02	265.51	232.78	207.23	186.75	169.96	155.94	133.87	117.27	104.34	93.97	78.41
1100	297.96	255.78	224.09	199.38	179.58	163.37	149.84	128.57	112.58	100.12	90.15	75.18
1200	288.84	247.78	216.97	192.96	173.74	158.01	144.89	124.26	108.77	96.72	87.07	72.59
1300	281.28	241.19	211.11	187.69	168.95	153.62	140.84	120.75	105.67	93.95	84.56	70.48
1400	274.99	235.72	206.27	183.35	165.01	150.02	137.52	117.88	103.14	91.68	82.51	68.76
1500	269.70	231.15	202.25	179.75	161.75	147.04	134.78	115.52	101.06	89.83	80.84	67.36
1600	265.21	227.29	198.87	176.74	159.03	144.57	132.50	113.56	99.35	88.30	79.46	66.21
1700	261.32	223.98	195.98	174.18	156.73	142.48	130.59	111.92	97.91	87.02	78.31	65.25
1800	257.88	221.08	193.47	171.97	154.75	140.69	128.95	110.53	96.70	85.94	77.34	64.44
1900	254.73	218.46	191.22	170.00	153.00	139.11	127.52	109.31	95.64	85.01	76.50	63.75
2000	251.73	215.99	189.13	168.18	151.39	137.66	126.21	108.21	94.69	84.17	75.75	63.13
2100	248.77	213.57	187.09	166.42	149.85	136.29	124.97	107.17	93.80	83.39	75.06	62.56
2200	245.73	211.11	185.03	164.65	148.30	134.91	123.73	106.15	92.92	82.63	74.38	62.01
2300	242.51	208.52	182.86	162.80	146.68	133.48	122.45	105.09	92.01	81.84	73.68	61.44
2400	239.02	205.71	180.52	160.80	144.94	131.94	121.07	103.95	91.04	81.00	72.94	60.84
2500	235.19	202.61	177.94	158.60	143.02	130.24	119.54	102.69	89.97	80.07	72.11	60.17

G.2 Plots of the hindered rotors

G.2.1 C_3H_6

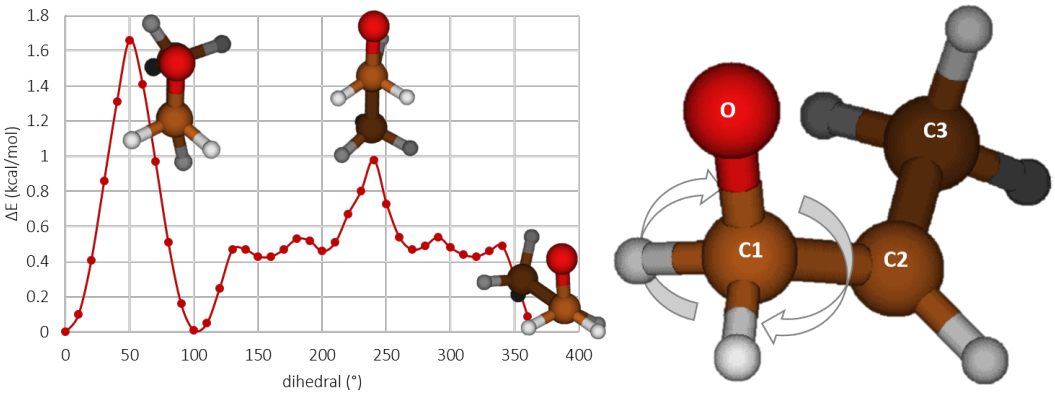

FIGURE G.1: Potential of HR O-C1-C2-C3 of C_3H_6O and relevant structures shown on the PES

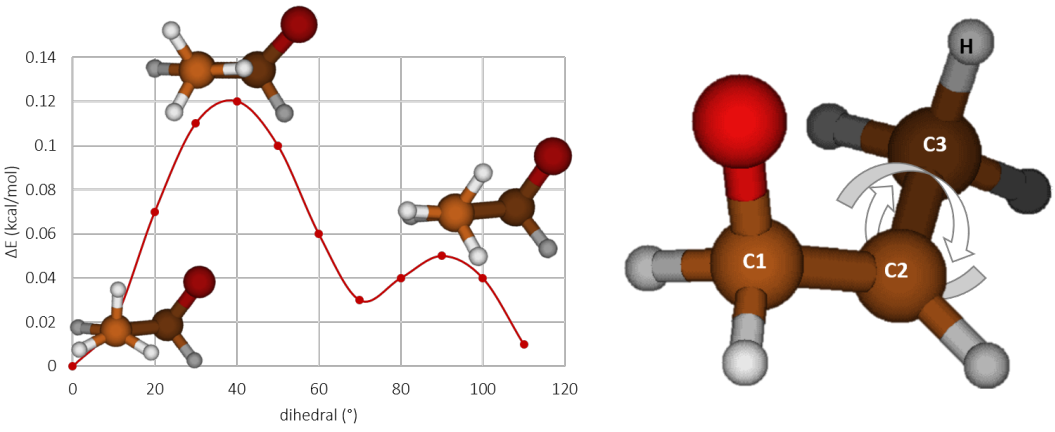

FIGURE G.2: Potential of HR C1-C2-C3-H of C_3H_6O and relevant structures shown on the PES

G.2.2 C_4H_8

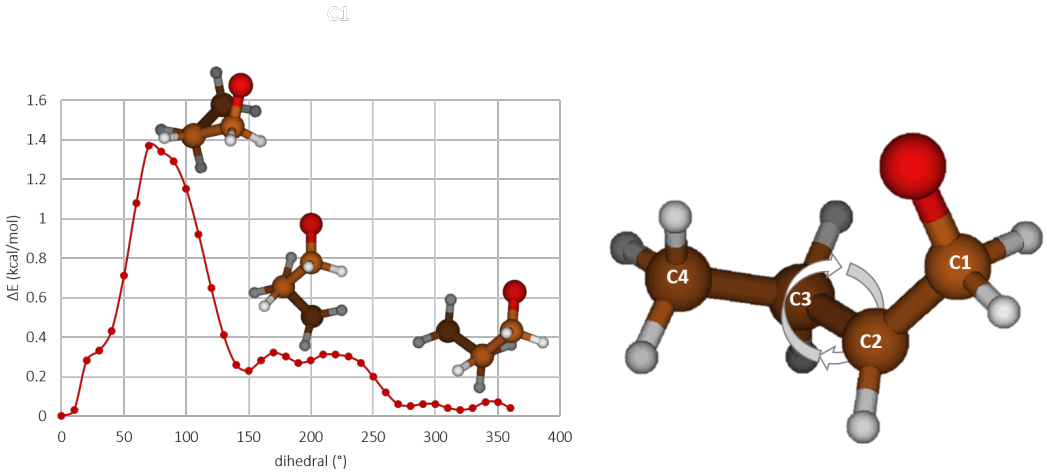

FIGURE G.3: Potential of HR C1-C2-C3-C4 of C_4H_8O and relevant structures shown on the PES

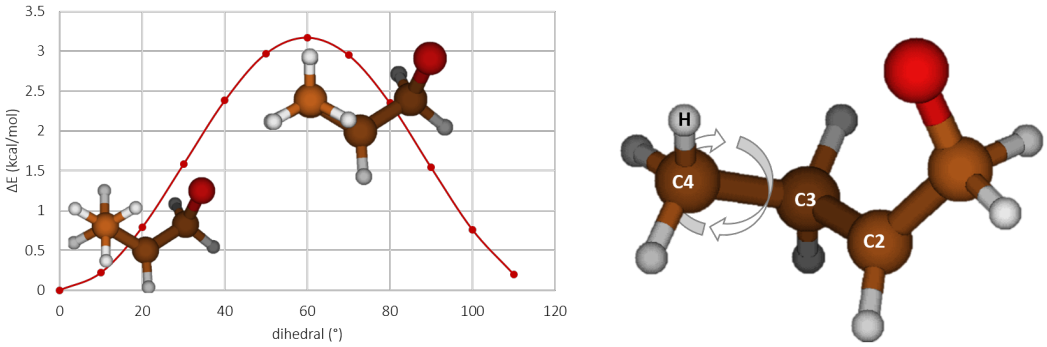

FIGURE G.4: Potential of HR C2-C3-C4-H of C_4H_8O and relevant structures shown on the PES

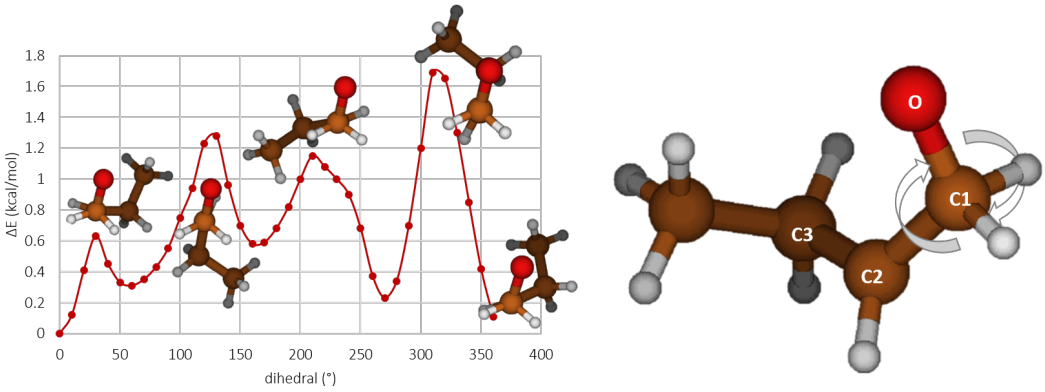

FIGURE G.5: Potential of HR O-C1-C2-C3 of C_4H_8O and relevant structures shown on the PES

G.2.3 C_5H_{10}

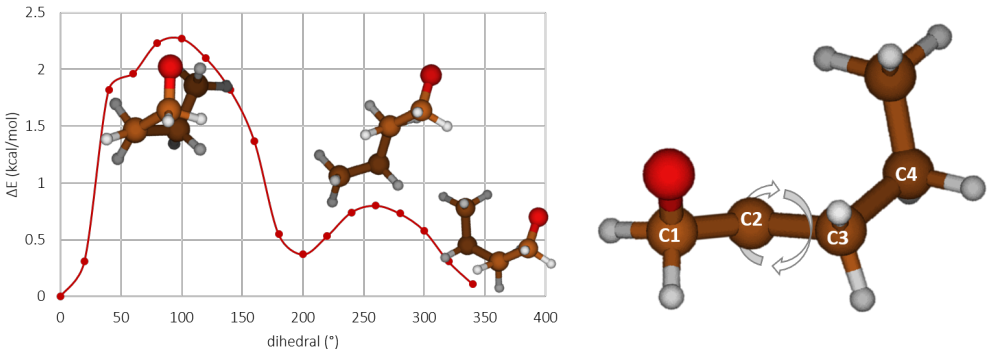

FIGURE G.6: Potential of HR C1-C2-C3-C4 of C_5H_10O and relevant structures shown on the PES

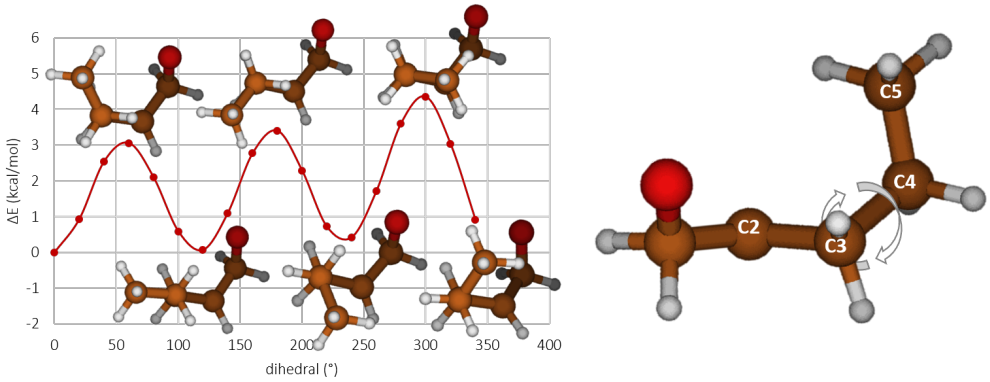

FIGURE G.7: Potential of HR C2-C3-C4-C5 of C_5H_10O and relevant structures shown on the PES

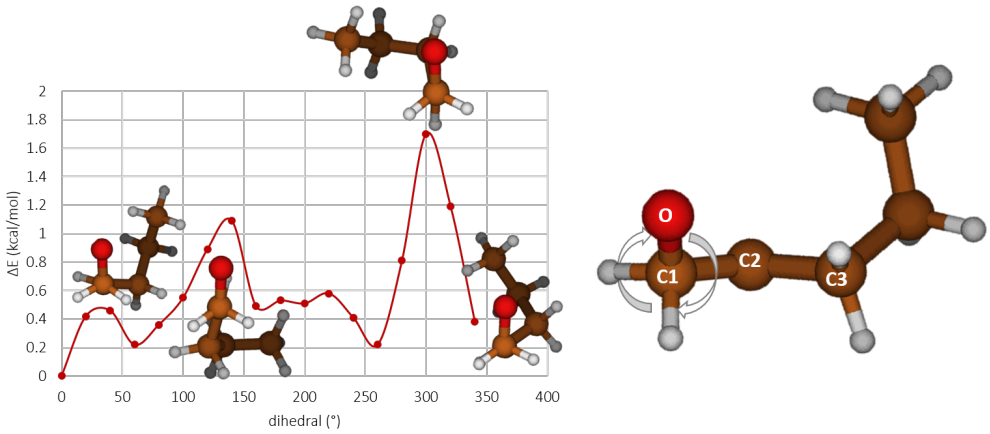

FIGURE G.8: Potential of HR O-C1-C2-C3 of C_5H_10O and relevant structures shown on the PES

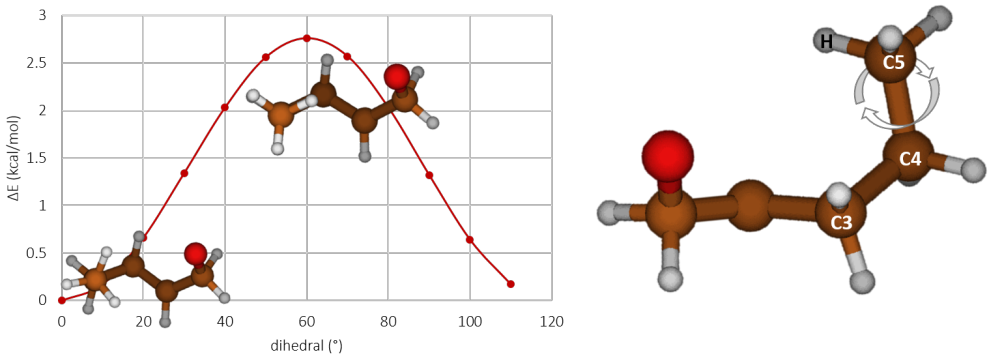

FIGURE G.9: Potential of HR C3-C4-C5-H of C_5H_10O and relevant structures shown on the PES

Bibliography

[1] S. E. Paulson, R. C. Flagan, and J. H. Seinfeld. "Atmospheric photooxidation of isoprene part I: The hydroxyl radical and ground state atomic oxygen reactions". In: *International Journal of Chemical Kinetics* 24.1 (1992), pp. 79–101. DOI: 10.1002/kin.550240109.

[2] H. Sabbah et al. "Understanding Reactivity at Very Low Temperatures: The Reactions of Oxygen Atoms with Alkenes". In: *Science* 317.5834 (2007), pp. 102–105. DOI: 10.1126/science.1142373.

[3] M. Pelucchi. "H-Abstraction reactions by OH, HO_2, O, O_2 and benzyl radical addition to O2 and their implications for kinetic modelling of toluene oxidation". In: *Physical Chemistry Chemical Physics* 20.16 (2018), pp. 10607–10627. DOI: 10.1039/c7cp07779c.

[4] R.J. Cvetanovic. "Evaluated chemical kinetic data for the reactions of atomic oxygen O (^{3}P) with unsaturated hydrocarbons". In: *J. Phys. Chem. Ref. Data* 16.2 (1987), pp. 261–326. DOI: 10.1063/1.555783.

[5] J. T. Herron and R. E. Huie. "Rate constants for the reactions of atomic oxygen with organic compounds in the gas phase". In: *J. Phys. Chem. Ref. Data* 2 (1973), pp. 467–518. DOI: 10.1063/1.3253125.

[6] A. M. Schmoltner et al. "Crossed molecular beam study of the reaction O(3P)+C2H4". In: *The Journal of Chemical Physics* 91.11 (1989), pp. 6926–6936. ISSN: 00219606. DOI: 10.1063/1.457309.

[7] I. Gimondi et al. "Reaction Dynamics of O(^{3}P) + Propyne: II. Primary Products, Branching Ratios, and Role of Intersystem Crossing". In: *Journal of Physical Chemistry A* 120.27 (2016), pp. 4619–4633. DOI: 10.1021/acs.jpca.6b01564.

[8] C. Cavallotti et al. "Relevance of the channel leading to formaldehyde + triplet ethylidene in the O(^{3}P) + propene reaction under combustion conditions". In: *Journal of Physical Chemistry Letters* 5.23 (2014), pp. 4213–4218. DOI: 10.1021/jz502236y.

[9] P. Casavecchia, F. Leonori, and N. Balucani. "Reaction dynamics of oxygen atoms with unsaturated hydrocarbons from crossed molecular beam studies: primary products, branching ratios and role of intersystem crossing". In: *International Reviews in Physical Chemistry* 34.2 (2015), pp. 161–204. DOI: 10.1080/0144235X.2015.1039293.

[10] X. Li et al. "Theoretical kinetics of O + C_2H_4". In: *Proceedings of the Combustion Institute* 36.1 (2017), pp. 219–227. DOI: 10.1016/j.proci.2016.06.053.

[11] J. N. Harvey. "Understanding the kinetics of spin-forbidden chemical reactions". In: *physical chemistry chemical physics* 9 (2007), pp. 331–343. DOI: 10.1039/b614390c.

[12] A. Barbato, C. Seghi, and C. Cavallotti. "An *ab initio* Rice-Ramsperger-Kassel-Marcus/master equation investigation of SiH_4 decomposition kinetics using a kinetic Monte Carlo approach". In: *The Journal of Chemical Physics* 130.7 (2009), p. 074108. DOI: 10.1063/1.3077561.

[13] D. Polino, A. Barbato, and C. Cavallotti. "Theoretical investigation of germane and germylene decomposition kinetics". In: *Physical Chemistry Chemical Physics* 12.35 (2010), pp. 10622–10632. DOI: 10.1039/c002221g.

[14] D. Polino and C. Cavallotti. "Fulvenallene decomposition kinetics". In: *Journal of Physical Chemistry A* 115.37 (2011), pp. 10281–10289. DOI: 10.1021/jp202756s.

[15] F. Leonori et al. "Experimental and Theoretical Studies on the Dynamics of the O(^{3}P) + Propene Reaction: Primary Products, Branching Ratios, and Role of Intersystem Crossing". In: *Journal of Physical Chemistry C* 119.26 (2015), pp. 14632–14652. DOI: 10.1021/jp512670y.

[16] C. Cavallotti and P. Casavecchia. "Experimental and theoretical study of O(^{3}P) + 1-butene". In: *still unpublished* (2018).

[17] R. A. Friesner. "Ab initio quantum chemistry: Methodology and applications". In: *Proceedings of the National Academy of Sciences* 102.19 (2005), pp. 6648–6653. DOI: 10.1073/pnas.0408036102.

[18] Jonathan R. et al. "Strategies for quantum computing molecular energies using the unitary coupled cluster ansatz". In: *Quantum Science and Technology* (2018). DOI: 10.1088/2058-9565/aad3e4.

[19] N. J. Labbe, R. Sivaramakrishnan, and S. J. Klippenstein. "The role of radical + fuel-radical well-skipping reactions in ethanol and methylformate low-pressure flames". In: *Proceedings of the Combustion Institute* 35.1 (2015), pp. 447–455. DOI: 10.1016/j.proci.2014.05.107.

[20] C. F. Goldsmith et al. "Effect of non-thermal product energy distributions on ketohydroperoxide decomposition kinetics". In: *Proceedings of the Combustion Institute* 35.1 (2015), pp. 283–290. DOI: 10.1016/j.proci.2014.05.006.

[21] M. Singla et al. "Ab initio calculations and kinetic modeling of thermal conversion of methyl chloride: implications for gasification of biomass". In: *Physical Chemistry Chemical Physics* 20 (2018), pp. 10741–10752. DOI: 10.1039/C7CP07552A.

[22] J. C. Tully. "Nonadiabatic Processes in Molecular Collisions". In: *Dynamics of Molecular Collisions: Part B*. Ed. by William H. Miller. Boston, MA: Springer US, 1976, pp. 217–267. DOI: 10.1007/978-1-4757-0644-4_5.

[23] Laura Gagliardi. "Relativistic Electronic Structure Theory. Part 1. Fundamentals. By Peter Schwerdtfeger." In: *Angewandte Chemie International Edition* 43.20 (), pp. 2599–2600. DOI: 10.1002/anie.200385079.

[24] E. Epifanovsky et al. "Spin-orbit couplings within the equation-of-motion coupled-cluster framework : Theory , implementation , and benchmark calculations". In: *The Journal of chemical physics* 143.6 (2015). DOI: 10.1063/1.4927785.

[25] Zener C. "Non-adiabatic crossing of energy levels". In: *Proceedings of the Royal Society of London A: Mathematical, Physical and Engineering Sciences* 137.833 (1932), pp. 696–702. DOI: 10.1098/rspa.1932.0165.

[26] L. D. Landau. "On the theory of transfer of energy at collisions". In: *Phys. Z. Sowjetunion* 2 (1932), p. 46.

[27] Y. T. Lee. "Molecular Beam Studies of Elementary Chemical Processes". In: *Science* 236.4803 (1987), pp. 793–798. DOI: 10.1126/science.236.4803.793.

[28] M. Alagia et al. "Reactive scattering of atoms and radicals". In: *Journal of the Chemical Society, Faraday Transactions* 91.4 (1995), pp. 575–596. DOI: 10.1039/FT9959100575.

[29] A. M. Schmoltner et al. "Crossed molecular beam study of the reaction $O(^3P)+C_2H_4$". In: *The Journal of Chemical Physics* 91.11 (1989), pp. 6926–6936. DOI: 10.1063/1.457309.

[30] P. Casavecchia et al. "Probing the dynamics of polyatomic multichannel elementary reactions by crossed molecular beam experiments with soft electron-ionization mass spectrometric detection". In: *Physical Chemistry Chemical Physics* 11.1 (2009), pp. 46–65. DOI: 10.1039/b814709d.

[31] B. Fu et al. "Intersystem crossing and dynamics in O(3P) + C2H4 multichannel reaction: Experiment validates theory". In: 109.25 (2012), pp. 9733–9738. DOI: 10.1073/pnas.1202672109.

[32] B. Fu et al. "Experimental and theoretical studies of the $O(^3P) + C_2H_4$ reaction dynamics: Collision energy dependence of branching ratios and extent of intersystem crossing". In: *The Journal of Chemical Physics* 137.22 (2012), 22A532. DOI: 10.1063/1.4746758.

[33] J. C. Tully. "Molecular dynamics with electronic transitions". In: *The Journal of Chemical Physics* 93.2 (1990), pp. 1061–1071. DOI: 10.1063/1.459170.

[34] S. J. Klippenstein. "From theoretical reaction dynamics to chemical modeling of combustion". In: 36.1 (2016), pp. 77–111. DOI: 10.1016/j.proci.2016.07.100.

[35] J. N. Harvey et al. "The singlet and triplet states of phenyl cation . A hybrid approach for locating minimum energy crossing points between non-interacting potential energy surfaces". In: *Theor. Chem. Acc.* 99.2 (1998), pp. 95–99. DOI: 10.1007/s002140050309.

[36] K. M. Smith, M. Poli, and J. N. Harvey. "Ligand dissociation accelerated by spin state change : locating the minimum energy crossing point for phosphine exchange in $CpMoCl_2(PR_3)_2$ complexes". In: *New J. Chem* 24 (2000), pp. 77–80. DOI: 10.1039/A909646I.

[37] T. L. Nguyen et al. "Potential energy surfaces, product distributions and thermal rate coefficients of the reaction of $O(^3P)$ with C_2H_4(X1Ag): A comprehensive theoretical study". In: *Journal of Physical Chemistry A* 109.33 (2005), pp. 7489–7499. DOI: 10.1021/jp052970k.

[38] N. Balucani et al. "Crossed Molecular Beams and Quasiclassical Trajectory Surface Hopping Studies of the Multichannel Nonadiabatic $O(^3P)$ + Ethylene Reaction at High Collision Energy". In: *Journal of Physical Chemistry A* 119.50 (2015), pp. 12498–12511. DOI: 10.1021/acs.jpca.5b07979.

[39] A. Bhargava and P. R. Westmoreland. "MBMS analysis of a fuel-lean ethylene flame". In: *Combustion and Flame* 115.4 (1998), pp. 456–467. DOI: https://doi.org/10.1016/S0010-2180(98)00018-2.

[40] R.D. Wilk et al. "Propene oxidation at low and intermediate temperatures: A detailed chemical kinetic study". In: *Combustion and Flame* 77.2 (1989), pp. 145–170. DOI: 10.1016/0010-2180(89)90034-5.

[41] W. Hu et al. "Trajectory surface hopping study of the $O(^3P)$ + ethylene reaction dynamics". In: *Journal of Physical Chemistry A* 112.10 (2008), pp. 2093–2103. DOI: 10.1021/jp076716z.

[42] D. L. Baulch et al. "Evaluated Kinetic Data for Combustion Modeling: Supplement II". In: *Journal of Physical and Chemical Reference Data* 34.3 (2005), pp. 757–1397. DOI: 10.1063/1.1748524.

[43] P. Casavecchia et al. "Dynamics of the $O(^3P)$ + C_2H_4 Reaction: Identification of Five Primary Product Channels (Vinoxy, Acetyl, Methyl, Methylene, and Ketene) and Branching Ratios by the Crossed Molecular Beam Technique with Soft Electron Ionization". In: *The Journal of Physical Chemistry A letters* 109 (2005), pp. 3527–3530. DOI: 10.1021/jp050627.

[44] Y. Endo et al. "Microwave kinetic spectroscopy of reaction intermediates: O + ethylene reaction at low pressure". In: *The Journal of Chemical Physics* 85.8 (1986), pp. 4446–4452. DOI: 10.1063/1.451765.

[45] A. Miyoshi et al. "Product branching fractions for the reaction of O(3P) with ethene". In: *Physical Chemistry Chemical Physics* 11.33 (2009), pp. 7318–7323. DOI: 10.1039/b905787k.

[46] J.D. Savee et al. "New mechanistic insights to the O(^{3}P)+propene reaction from multiplexed photoionization mass spectrometry". In: *Phys. Chem. Chem. Phys.* 14.30 (2012), pp. 10410–10423. DOI: 10.1039/C2CP41200D.

[47] H. Deslauriers and G. J. Collin. "The relative rate constants of oxygen, O(3P), atoms with different gaseous unsaturated compounds at room temperature". In: *Canadian Journal of Chemistry* 64.9 (1986), pp. 1925–1929. DOI: 10.1139/v86-317.

[48] T. Oguchi et al. "Mechanism of the Reactions of Butenes with O(^{3}P): The Yields of CH_3 and C_2H_5". In: *The Journal of Physical Chemistry A* 108.8 (2004), pp. 1409–1416. DOI: 10.1021/jp035251j.

[49] H. Zhao, Lu Pan, and W. Bian. "A theoretical study on the reaction mechanisms of O(^{3}P)+1-butene". In: *International Journal of Quantum Chemistry* 112.3 (2012), pp. 858–872. DOI: 10.1002/qua.23078.

[50] A. Caracciolo et al. "Observation of H displacement and H_2 elimination channels in the reaction of O(^{3}P) with 1-butene from crossed beams and theoretical studies". In: *Chemical Physics Letters* 683 (2017), pp. 105–111. DOI: doi.org/10.1016/j.cplett.2017.02.036.

[51] A. Szabo and N.S. Ostund. *Modern quantum chemistry. Introduction to advanced electronic structure theory.* USA: McGraw-Hill, 1989. ISBN: 0486691861.

[52] F. Jensen. *Introduction to Computational Chemistry.* 3rd. USA: John Wiley Sons, Inc., 2006. ISBN: 0470011874.

[53] K. Andersson et al. "Second-Order Perturbation Theory with a CASSCF Reference Function". In: *The Journal of Physical Chemistry* 94.14 (1990), pp. 5483–5488. DOI: 10.1021/j100377a012.

[54] B. O. Roos and K. Andersson. "Multiconfigurational perturbation theory with level shift - the Cr 2 potential revisited". In: *Chemical Physics Letters* 245.2-3 (1995), pp. 215–223. DOI: 10.1016/0009-2614(95)01010-7.

[55] G. Ghigo and O Roos. "A modified definition of the zeroth-order Hamiltonian in multiconfigurational perturbation theory (CASPT2)". In: *Chemical Physics Letters* 396.1-3 (2004), pp. 142–149. DOI: 10.1016/j.cplett.2004.08.032.

[56] F. Eckert, P. Pulay, and H. J. Werner. "Ab initio geometry optimization for large molecules". In: *Journal of Computational Chemistry* 18.12 (1997), pp. 1473–1483. DOI: 10.1002/(SICI)1096-987X(199709)18:12<1473::AID-JCC5>3.0.CO;2-G.

[57] M. J. Frisch and L. Xiasong. "Energy-represented DIIS within a hybrid geometry optimization method". In: *J. Chem. Theory and Comput.* 2 (2006), pp. 835–839. DOI: 10.1021/ct050275a.

[58] M.G. Evans and M. Polanyi. "Some Applications of the Transition State Method To the Calculation O F Reaction Velocities , Especially in Solution ." In: *Trans. Faraday Soc.* 31 (1935), pp. 875–894.

[59] H. Eyring. "The Activated Complex in Chemical Reactions". In: *The Journal of Chemical Physics* 3.2 (1935), pp. 107–115. DOI: 10.1063/1.1749604.

[60] D. G. Truhlar and B. C. Garrett. "Variational Transition-State Theory". In: *Accounts of Chemical Research* 13.12 (1980), pp. 440–448. DOI: 10.1021/ar50156a002.

[61] S. Fascella et al. "The Peculiar Kinetics of the Reaction between Acetylene and the Cyclopentadienyl Radical". In: *The Journal of Physical Chemistry A* 109.33 (2005), pp. 7546–7557. DOI: 10.1021/jp051508x.

[62] A. L. L. East and L. Radom. "*Ab initio* statistical thermodynamical models for the computation of third-law entropies". In: *The Journal of Chemical Physics* 106.16 (1997), pp. 6655–6674. DOI: 10.1063/1.473958.

[63] J. I. Steinfeld, J. S. Francisco, and W. L. Hase. *Chemical Kinetics and Dynamics*. USA: Prentice-Hall, 1989. ISBN: 0137371233.

[64] Y. Georgievskii et al. "Reformulation and solution of the master equation for multiple-well chemical reactions". In: *Journal of Physical Chemistry A* 117.46 (2013), pp. 12146–12154. ISSN: 10895639. DOI: 10.1021/jp4060704.

[65] C. Cavallotti et al. "EStokTP:Electronic Structure to Temperature and Pressure Dependent Rate Constants; A Code for Automatically Predicting the Thermal Kinetics of Reactions". In: *The Journal of Chemical Physics - submitted* (2018).

[66] A. Miyoshi. "Molecular size dependent falloff rate constants for the recombination reactions of alkyl radicals with O2 and implications for simplified kinetics of alkylperoxy radicals". In: *International Journal of Chemical Kinetics* 44.1 (2012), pp. 59–74. DOI: 10.1002/kin.20623.

[67] D. A. McQuarrie and J. D. Simon. *Molecular Thermodynamics*. USA: University Science Books, 1999.

[68] K. Mahamud, P. Marshall, and A. Fontijn. "A High-Temperature Photochemistry Kinetics Study of the Reaction of O(3P) Atomos with Ethylene from 290 to 1510 K". In: *J. Phys. Chem* 91.1 (1987), pp. 1568–1573. DOI: 10.1021/j100290a056.

[69] R.C. Reid, J.M. Prausnitz, and B.E. Poling. *The properties of gases and liquids*. Mc Graw Hill, 1987.